Distribution Enhanced Methods of Homogenization for Heterogeneous Materials and Multi-scale Crystal Plasticity Modeling

by

Coleman Alleman

A dissertation submitted to The Johns Hopkins University in conformity with the requirements for the degree of Doctor of Philosophy.

Baltimore, Maryland

August, 2015

Abstract

Ductile rupture is the dominant failure mechanism in body centered cubic (BCC) tantalum (Ta) loaded at high strain rates. Existing material models and simulation techniques are insufficient to provide the desired level of fidelity and accuracy in representing the plasticity and damage evolution in this dynamic failure process. Significant advancement is required to model the effects of the contributing physical processes, which play out over a range of length and timescales covering multiple orders of magnitude, and to incorporate these effects into a single coherent simulation framework.

In this study, the authors propose a novel multiscale framework for modeling ductile failure with crystal plasticity and damage. Within this framework, the single crystal plasticity constitutive behavior is derived from the results of molecular dynamics simulations, where the atomistic process of slip is modeled explicitly. These results are used to establish a physically meaningful functional form and parameterization for a continuum-scale crystal plasticity flow rule that captures the effects of loading orientation, strain rate, and temperature.

ABSTRACT

At the intermediate scale, slip and hardening and the coupling of these phenomena to the evolution of damage in the material are studied. Finite element simulations of damage evolution are performed with the atomistically-informed flow model coupled to dislocation density based crystal plasticity. Rates of slip and hardening are directly linked to dislocation kinetics and dislocation density evolution and structure formation at this scale. The spatial discretization at this scale includes an explicit geometric representation of damage as an initially spherical void that evolves during deformation. The effects of damage on the evolving plasticity are quantified, and an understanding of the role of crystal plasticity and stress triaxiality on damage evolution is obtained.

At the highest scale, finite element simulations employ a homogenized constitutive law that couples crystal plasticity and damage evolution. The heterogeneous stress field induced by the damage is handled within the newly developed distribution enhanced homogenization framework, where evolving measures of microscale stress distributions are explicitly included as new internal variables in the homogenized constitutive relation. This model accurately represents the material behavior observed at the intermediate continuum scale without explicit geometric representation of the damage. A novel damage evolution law is introduced to model void growth, and this model accurately represents the effects of the microscale stress field on the plastic evolution of the void and the surrounding material.

ABSTRACT

Advisor: Professor Somnath Ghosh

Thesis Readers: Professor Lori Graham-Brady, Professor Jaafar El-Awady, Dr. Curt Bronkhorst

Acknowledgments

I would like to begin by acknowledging my PhD advisor, Professor Somnath Ghosh, for his guidance and constant support. His drive and deep passion for research are essential ingredients in this work. He has helped me to develop as a researcher from a student in his Mechanics of Materials class years ago, through a Master's degree, this PhD, and I am sure for years to come. The benefits I have gotten from his vast experience and wisdom are too great to be measured.

I am very grateful to Professor Lori Graham-Brady and Professor Jafaar El-Awady for serving as members of my committee, and for the many valuable insights that I gained from the courses I took from them. My sincerest thanks to Dr. D. J. Luscher and Dr. Curt Bronkhorst at Los Alamos National Laboratory for their invaluable contributions to this work through their constant encouragement and enlightening discussions.

Thank you also to the many past and current lab members and friends in the Computational Mechanics Research Laboratory to whom I have so often turned for technical discussions and moral support throughout the course of my study.

ACKNOWLEDGMENTS

I would like to express my heartfelt gratitude to Joanna Alleman–my best friend, my partner, and my wife. Your support means more to me than I can express. My sincerest love and gratitude to my parents and parents-in-law, my sister and my brothers-in law for their unwavering support and patience.

This work has been supported by the Advanced Simulations and Computing Program at Los Alamos National Laboratory. This sponsorship is gratefully acknowledged. Computer support by the Homewood High Performance Computing Center is also gratefully acknowledged.

Dedication

To Nora and Josie,

In the end, this is all for you.

Contents

CONTENTS

List of Tables

List of Figures

Chapter 1

Introduction

Multi-scale modeling is a theme integral to the modeling of heterogeneous multi-phase materials. It offers a tractable means to model sufficiently large spatial domains of heterogeneous media without being impeded by the exorbitant computational overhead incurred due to detailed high-resolution modeling of variations in material morphology at the lower microscopic scale. The ability of these powerful computational methods to resolve material behavior at different scales and communicate across them is fostering unprecedented advances in multi-scale modeling. These models provide in-depth understanding of material deformation and failure that brings new insights to the integrated computational structure-material engineering paradigm.

The ability to accurately model material behavior at disparate scales within a consistent framework is also critical to the challenge of integrating the wide array of

existing and emerging experimental results into a coherent understanding of material behavior. For example, the study of individual dislocation behavior in nano-pillar or thin film tests is a promising area of experimental investigation, but incorporating understanding of this behavior in interpreting macroscale experimental and modeling results requires robust, detailed methods for transferring information across spatial scales. Multiscale modeling enables this transfer via a number of different paths, as discussed below.

Multi-scale modeling can also be an invaluable tool in leveraging combinations of simulation and experimental results to focus new work on mutually beneficial areas. A multi-scale model which incorporates microscale behavior in computing macroscale response is in a unique position to evaluate the validity or applicability of the microscale model. If the macroscale behavior predicted by a multi-scale model does not agree with macroscale experimental observations, the microscale behavior assumed by the model is called into question, and the model can suggest appropriate further modeling and experiments to assess the origin of the discrepancy. Ideally, this process supplants the classical problem of empirical fitting of macroscale models to macroscale experimental results, and allows advances in understanding at any scale to inform predictions of macroscale response.

Within the domain of computational multi-spatial scale analyses, two categories

of methods have emerged, depending on the nature of coupling between the scales, namely, "hierarchical" and "concurrent" models. Hierarchical models enable bottom-up coupling for unidirectional transfer of information from lower to higher scales. The information transferred is usually in the form of effective material properties. This type of model is depicted in Figure 1.1, where information about the polycrystalline microstructure would be used at the macroscale to determine the effective material response at a point in the macroscopic domain.

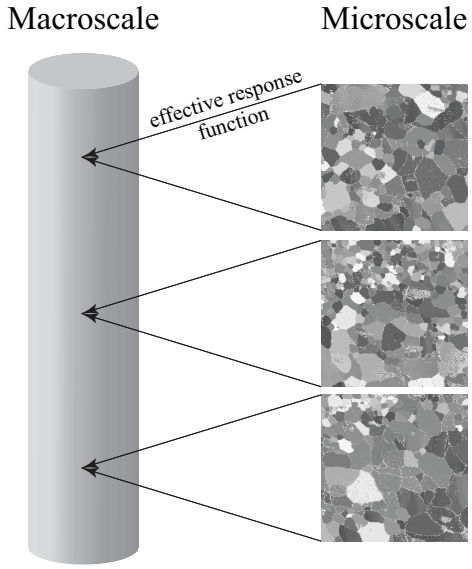

Figure 1.1: Schematic representation of a hierarchical multi-scale model.

A number of different methods to achieve this transfer have been developed in the literature. Analytical models have been developed, e.g. for linear elasticity, to evaluate effective constitutive quantities at the macroscale based on characterization of the microstructure. However, microscale solutions are known analytically only for

a very limited class of problems. The canonical example of this type of homogenization is the effective medium theory introduced by [7] to deal with isotropic ellipsoidal inclusions in an otherwise homogeneous isotropic medium. Other methods based on this approach can provide good approximations of certain material properties for simple microstructures, e.g. [8, 9]. These approaches are applicable to linear constitutive relations and simple inclusion/matrix morphologies. Extensions to a limited class of nonlinear materials have been achieved in the variational framework proposed in [10, 11]. This approach establishes absolute bounds for some nonlinear composites. The self-consistent method, originally developed by [12] and [13] has been extended to the polycrystalline problems in [14], which simultaneously satisfies compatibility and equilibrium between each phase of a material and its surrounding homogeneous medium.

A subset of the hierarchical models has been branded as the "FE^2 multi-scale methods" by [15, 16], where micro-mechanical RVE or unit cell models are solved in every increment to obtain homogenized properties for macroscopic analysis. The model does not require a closed form macroscale constitutive relation, rather, this relationship is implicit in the transfer of information from the microscale to the macroscale. However, this method can be very expensive, as it entails solving the RVE micromechanical problem for every element integration point in the computational domain. The macroscale discretization must be sufficiently coarse to achieve

a computational advantage over a fully microscale discretization of the entire domain.

To overcome the limitations of prohibitive computational overhead, explicit forms for the macroscale constitutive relations have been developed in [17, 18] from homogenization of RVE response at microscopic scales. This requires determination of the functional forms of the macroscale constitutive parameters with respect to the microstructure, and is referred to as *parametric homogenization*. The constitutive models represent the effect of morphological features and evolving microstructural mechanisms through evolving, anisotropic homogenized parameters. Reduced-order constitutive models based on parametric homogenization are significantly more efficient than the FE^2-type models since they carry the minimum sufficient information on the microstructural morphology and do not have to solve the RVE problem in every step. Macroscale constitutive relations based on parametric homogenization are valid as long as the effective material behavior is well-represented by an homogeneous effective medium. This is the case when, for example, there exists a wide separation between the lower and higher scales.

For hierarchical multi-scale models that employ explicit macroscale constitutive relations, it is common, e.g. in [16, 19–22] to incorporate asymptotic homogenization theory, originally developed in [23, 24], in conjunction with computational micromechanics models. This homogenization theory is based on complete scale separa-

tion with an implicit assumption that the macroscopic gradient length-scale is much greater than the characteristic microstructural length scale, leading to macroscopic uniformity. Uncoupling of the governing equations at different scales is often achieved through incorporation of uniform displacement, traction, or periodicity boundary conditions on the microscopic representative volume elements (RVEs). For non-uniform microstructures, a statistically equivalent representative volume element or SERVE has been defined in [25] as the smallest volume element such that the effective material properties and morphological parameters of the SERVE are statistically equivalent to the entire microstructure, independent of location and applied loading. Computational homogenization typically proceeds from SERVE-based simulations to obtain effective constitutive relationships that connect macroscopic quantities such as the average stress and average strain in a way that includes the effects of microscale heterogeneity at the macroscale.

While the volume average microscopic strain is commonly taken as the macroscale descriptor of kinematics in a two-scale model, including the effects of the strain-gradient fields, as in [26–28] increases the fidelity of the kinematic description at higher scales, and can be nested at multiple levels to provide an increasingly fine description. This approach extends the microscale framework to a macroscale description in which the non-uniformity of the microscale kinematics is explicitly represented. This is one way in which the macroscale description allows for behavior that is

not well-represented by an homogeneous effective medium described within the same framework as the microscale, specifically, the microscale kinematic framework.

Additionally, the macroscale constitutive behavior may not be well-represented by an homogeneous effective medium, for example in heterogeneous materials involving high solution gradients. In this case, *concurrent* multi-scale models have been developed to treat the heterogeneity explicitly. This second main category of multi-scale modeling methods employ bottom-up and top-down coupling, where different parts of the computational domain represent different scales and the relevant information is passed across an explicitly resolved interface in a bidirectional fashion. Concurrent methods can be successful for problems where a limited region of interest needs to be evaluated, and the rest of the domain is governed by well-understood constitutive relations. If the region of interest is too large compared to the overall domain, or if the macroscale constitutive relations are not well-understood, concurrent multi-scaling schemes may not reduce the complexity of the underlying problem. Hierarchical and concurrent multi-scale methods can be combined by applying each to different parts of the computational domain to exploit the strength of each method while mitigating their inherent limitations. A powerful adaptive hierarchical and concurrent multi-scale framework has been developed in [17, 29, 30]. In this method, efficient macroscale constitutive relations are hierarchically constructed by parametric homogenization in the bulk of the material, and high-fidelity concurrent microscale

simulations are conducted in limited regions where the inherent assumptions of homogenization are invalidated due to lack of scale separation.

The present study proposes a novel alternative approach to homogenization, where the macroscale constitutive behavior is not assumed a priori, as in homogeneous effective medium theory. Rather, the macroscale constitutive relations involve higher-order descriptors of the microscale fields in addition to the commonly used volume averages. This *distribution-enhanced homogenization framework* (DEHF) associates a non-uniform microscale field variable to a macroscopic material region by incorporating higher-order moments of microscale field variable distributions in the constitutive calculations. Macroscale constitutive relations are formulated by constructing series expansions in terms of these moments. The truncated expansions result in well-behaved approximations of the macroscopic response that converge with increasing order of approximations of the underlying field variables. Using DEHF, it is possible to derive a set of macroscale constitutive relations that represent the microscale behavior exactly in the limit, without constructing effective macroscale parameters by fitting the macroscopic behavior to the average microscopic behavior.

The layout of this document is as follows. In Chapter 2, the theory of DEHF is derived, and the methodology is applied to a set of sample problems that demonstrate the effectiveness of the approach. In Chapter 3, the material model for tantalum is

given in some detail, especially the non-Schmid formulation of the thermally-activated slip mechanism. In Chapter 5, the application of DEHF to the crystal plasticity formulation is outlined, and DEHF is combined with a novel damage evolution relation in order to simulate coupled crystal plasticity and ductile damage.

Chapter 2

The Distribution Enhanced Homogenization Framework

This work proposes a novel alternative approach to homogenization, where the macroscale constitutive behavior is not assumed a priori, as in homogeneous effective medium theory. Rather, the macroscale constitutive relations involve higher-order descriptors of the microscale fields in addition to the commonly used volume averages. This *distribution-enhanced homogenization framework*, or DEHF, associates a non-uniform microscale field variable to a macroscopic material region by incorporating higher-order moments of microscale field variable distributions in the constitutive calculations. Macroscale constitutive relations are formulated by constructing series expansions in terms of these moments. The truncated expansions result in well-behaved approximations of the macroscopic response that converge with increasing

order of approximations of the underlying field variables. Using DEHF, it is possible to derive a set of macroscale constitutive relations that represent the microscale behavior exactly in the limit, without constructing effective macroscale parameters by fitting the macroscopic behavior to the average microscopic behavior. A discussion of the microscale boundary value problem is given in section 2.4, followed by a detailed development of DEHF for the macroscale problem in 2.5. Section 2.6 summarizes the numerical implementation of the DEHF and numerical examples are conducted in section 2.7 with this model.

2.1 Relevant Aspects of Distribution Theory

The distribution-enhanced homogenization framework includes macroscale moment-based descriptors of microscale distributions of field variables in the representation of macroscopic constitutive relations. Standard homogenization frameworks, which typically include only moments of order one, are extended here to include moments of arbitrary order. Conceptually, this extension relaxes the assumption that the microscale response is represented by a set of constitutive relations operating on a uniform microscale. Instead, DEHF accounts for microscale inhomogeneity by including moments of arbitrary order as explicit, quantitative descriptions of this inhomogeneity and formulates constitutive relations for the evolution of this inhomogeneity in

terms of the evolution of the moment variables. Distributions that represent microscale fields in the neighborhood of a macroscale point are assigned to the point. The moments of these distributions quantify the effects of the nonuniform microscale field variables on the macroscale constitutive response.

This type of description is analogous to familiar concepts from statistics, where moments can be used as descriptors of statistical distributions from which random variables are sampled. For example, a normal distribution $\mathcal{N}(\mu, \sigma^2)$ is characterized by the parameters μ and σ^2 that correspond to the first moment (mean) and second moment (variance), respectively. While the definition of moments in DEHF is analogous to the statistical definition, it is emphasized that the underlying distributions are of a fundamentally different nature. In statistics, distributions characterize probability of events arising from stochastic processes, while in DEHF, the distributions arise from deterministic, thermomechanical processes operating on known inhomogeneous microscale configurations. Additionally, the moments rather than the distributions themselves are the mathematical objects in the theory. There is no attempt to identify distributions that give rise to the moments that appear in the problems, as the theory operates directly on the moments themselves. Aspects of distribution theory are outlined next.

2.1.1 Distributions or Generalized Functions

A *distribution* or *generalized function* is defined as a linear functional acting on the space of test functions $\mathcal{D}(\Omega) = C_0^\infty(\Omega)$ defined for the open set $\Omega \subset \mathbb{R}^n$ [31]. A test function $\phi \in \mathcal{D}(\Omega)$ is infinitely differentiable and compactly supported in Ω; that is, $\phi \in C_0^\infty(\Omega)$. The space of distributions $\mathcal{D}'(\Omega)$ is a space in which locally integrable functions can be mapped onto infinitely differentiable distributions [32]. For example, the distribution $\langle f, \phi \rangle \in \mathcal{D}'(\Omega)$ for a locally integrable function f is defined as:

$$\langle f, \phi \rangle = \int_{-\infty}^{\infty} f(\mathbf{x})\phi(\mathbf{x})d\mathbf{x} \tag{2.1}$$

The space $\mathcal{D}'(\Omega)$ also includes generalized functions such as the Dirac distribution $\langle \delta, \phi \rangle = \phi(0)$, which cannot, strictly speaking, be written in the form of (2.1).

The test functions used may be taken from a larger space $\mathcal{S}(\mathbb{R}^n)$ of *rapidly decreasing functions*, each of which is infinitely differentiable, but not necessarily compactly supported; that is, $C_0^\infty(\mathbb{R}^n) \subset \mathcal{S}(\mathbb{R}^n) \subset C^\infty(\mathbb{R}^n)$. This space $\mathcal{S}$ has the property that each member of $\mathcal{S}$ has a Fourier transform in $\mathcal{S}$, a property that will be used in this development. The dual space of distributions $\mathcal{S}'$ defined for functions in $\mathcal{S}$ is known as the space of *tempered distributions*, with $\mathcal{S}' \subset \mathcal{D}'$. *Density functions* are defined in this work as members of a subspace $U(\mathbb{R}^n) \subset \mathcal{S}(\mathbb{R}^n)$ of the space of rapidly decreasing functions. The density functions used in this work can be thought of as representing the volume fraction ϕ_Ω of material in a neighborhood $\Omega(\mathbf{x})$ of a point $\mathbf{x}$, at which a given field variable of interest has a value $\mathbf{q} \in \mathbb{R}^n$. These functions satisfy

the conditions:

$$\langle 1, \phi_\Omega(\mathbf{q}) \rangle = \int_{\mathbb{R}^n} \phi_\Omega(\mathbf{q})\, dq_1 \cdots dq_n = 1 \tag{2.2}$$

$$\langle q_1^{p_1} \cdots q_n^{p_n}, \phi_\Omega(\mathbf{q}) \rangle = \int_{\mathbb{R}^n} q_1^{p_1} \cdots q_n^{p_n} \phi_\Omega(\mathbf{q})\, dq_1 \cdots dq_n = \mu^k_{q_1^{p_1} \cdots q_n^{p_n}} \tag{2.3}$$

for $\sum_{i=1}^n p_i = k$. The quantity $\mu^k_{q_1^{p_1} \cdots q_n^{p_n}}$ defined in equation (2.3) is the k-th moment of the field variable $q_1^{p_1} \cdots q_n^{p_n}$ in Ω. These moments represent the distributions of microscale field variables and can be identified with macroscale field variables in solving the macroscale problem. For example, if $k = 1$, Ω is the extent of the microscale domain, and q corresponds to the stress component σ_{ij}, equation (2.3) yields the volume average of σ_{ij} in the microscale BVP, i.e.

$$\mu^1_{\sigma_{ij}} = \langle \sigma_{ij}, \phi_\Omega(\sigma_{ij}) \rangle \tag{2.4}$$

If field variables $\mathbf{r}$ and $\mathbf{q}$ in the microscale boundary value problem have a functional dependence through the kinematic and constitutive relations, then the homogenization problem requires a corresponding relation between the macroscale representations of those field variables. Conventional homogenization methods relate the first moments $\mu^1_{r_i}$ and $\mu^1_{q_j}$ by the same function operating at the microscale, extended by a microstructural parametrization function M. For example, the stress-strain relation $\sigma = f(\boldsymbol{\epsilon}^e)$ in equation (2.67) can be homogenized to $\mu^1_{\boldsymbol{\sigma}} = f(\mu^1_{\boldsymbol{\epsilon}^e}; \mathrm{M})$ by representing the homogenized elastic tensor $\mathbb{C}^{\text{eff}}$ as a function of the effective microstructural parameters M, to yield the macroscale constitutive relation:

$$\mu^1_{\boldsymbol{\sigma}} = \mathbb{C}^{\text{eff}}(\mathrm{M}) : \mu^1_{\boldsymbol{\epsilon}^e} \tag{2.5}$$

Satisfaction of equation (2.5) implies the applicability of the parametric function M for a given microstructure. However, this does not answer the question of whether the parametric function M is sufficient to guarantee the uniqueness of $\mathbb{C}^{\text{eff}}$. That is, it is possible that two microstructures admitting the same M may have different macroscale elastic responses. For example, two porous microstructures may contain the same volume fraction of voids, but the shapes and locations of the voids could result in two $\mathbb{C}^{\text{eff}}$ tensors that do not have the same symmetry. In this case, the two material responses could agree under uniaxial tension loading, while differing under bi-axial or shear loads. Furthermore, even a parametrization M that guarantees a unique $\mathbb{C}^{\text{eff}}$ may not guarantee the existence of a unique relation that homogenizes a different constitutive relation, such as the plastic flow rule in equation (2.75). To solve this general problem, the role of higher-order moments in homogenized constitutive relations is examined in following sections.

2.2 Moment Expansion

For the homogenized domain, functions of the fundamental quantities are most appropriately considered as distributions,

The characteristic function $\phi_{\boldsymbol{X}}$ of a vector random variable $\boldsymbol{X}$ is defined as the Fourier transform of the distribution $f_{\boldsymbol{X}}$ which maps $\mathbb{R}^n \to \mathbb{R}$,

$$\phi_{\boldsymbol{X}}(\boldsymbol{\xi}) = \int_{\mathbb{R}^n} \exp(i\boldsymbol{\xi} \cdot \boldsymbol{x}) f_{\boldsymbol{X}}(\boldsymbol{x}) \, d\boldsymbol{x} \tag{2.6}$$

The distribution $f_{\boldsymbol{X}}$ can then be expressed as the inverse transform of the characteristic function $\phi_{\boldsymbol{X}}$,

$$f_{\boldsymbol{X}}(\boldsymbol{x}) = \frac{1}{(2\pi)^n} \int_{\mathbb{R}^n} \exp(-i\boldsymbol{\xi} \cdot \boldsymbol{x}) \, \phi_{\boldsymbol{X}}(\boldsymbol{\xi}) \, d\boldsymbol{\xi} \tag{2.7}$$

$$\phi_{\boldsymbol{g}(\boldsymbol{X})}(\boldsymbol{\xi}) = \int_{\mathbb{R}^n} \exp(i\boldsymbol{\xi} \cdot \boldsymbol{g}(\boldsymbol{x})) \, f_{\boldsymbol{X}}(\boldsymbol{x}) \, d\boldsymbol{x} \tag{2.8}$$

The derivatives of the characteristic function are given by

$$\frac{\partial}{\partial \xi_{j_1} \cdots \partial \xi_{j_h}} \left[\phi_{\boldsymbol{g}(\boldsymbol{X})}(\boldsymbol{\xi}) \right] = \int_{\mathbb{R}^n} i^h \left[g_{j_1}(\boldsymbol{x}) \cdots g_{j_h}(\boldsymbol{x}) \right] \exp(i\boldsymbol{\xi} \cdot \boldsymbol{g}(\boldsymbol{x})) \, f_{\boldsymbol{X}}(\boldsymbol{x}) \, d\boldsymbol{x} \tag{2.9}$$

Now, the h-th moments of $\boldsymbol{g}$ are given by

$$\mu^h_{g_{j_1} \cdots g_{j_h}} = \int_{\mathbb{R}^n} \left[g_{j_1}(\boldsymbol{x}) \cdots g_{j_h}(\boldsymbol{x}) \right] \exp(i\boldsymbol{\xi} \cdot \boldsymbol{g}(\boldsymbol{x})) \, f_{\boldsymbol{X}}(\boldsymbol{x}) \, d\boldsymbol{x} \tag{2.10}$$

so that

$$\mu^h_{g_{j_1} \cdots g_{j_h}} = \left\{ \frac{1}{i^h} \frac{\partial}{\partial \xi_{j_1} \cdots \partial \xi_{j_h}} \left[\phi_{\boldsymbol{g}(\boldsymbol{X})}(\boldsymbol{\xi}) \right] \right\}_{\boldsymbol{\xi}=0} \tag{2.11}$$

This enables the Taylor expansion of the characteristic function as

$$\phi_{\boldsymbol{g}(\boldsymbol{X})}(\boldsymbol{\xi}) = 1 + i\xi_j \mu^1_{g_j} + \frac{1}{2} i^2 \xi_{j_1} \xi_{j_2} \mu^2_{g_{j_1} g_{j_2}} + \frac{1}{k!} i^k \xi_{n_1} \cdots \xi_{n_h} \mu^k_{g_{n_1} \cdots g_{n_k}} + \mathcal{O}\left(|\boldsymbol{\xi}|^{k+1} \right) \tag{2.12}$$

where summation is implied on repeated indices. The utility of this expansion is that it allows for the moments of $\boldsymbol{g}(\boldsymbol{X})$ to be expressed as a function of the moments of $\boldsymbol{X}$, as follows. For example, the first moment of $\boldsymbol{g}(\boldsymbol{X})$ is given by

$$\mu^1_{\boldsymbol{g}(\boldsymbol{X})} = \int_{\mathbb{R}^n} \boldsymbol{g}(\boldsymbol{x}) \, f_{\boldsymbol{X}}(\boldsymbol{x}) \, d\boldsymbol{x} \tag{2.13}$$

Substituting the expression for the distribution $f_{\boldsymbol{X}}$ in terms of its characteristic function $\phi_{\boldsymbol{X}}$ from Equation (2.7),

$$\mu^1_{\boldsymbol{g}(\boldsymbol{X})} = \frac{1}{(2\pi)^n} \int_{\mathbb{R}^n} \boldsymbol{g}(\boldsymbol{x}) \int_{\mathbb{R}^n} \exp(-i\boldsymbol{\xi}\cdot\boldsymbol{x})\, \phi_{\boldsymbol{X}}(\boldsymbol{\xi})\, d\boldsymbol{\xi} d\boldsymbol{x} \tag{2.14}$$

Then, substituting the expansion for $\phi_{\boldsymbol{X}}$ from Equation (2.12),

$$\begin{aligned}\mu^1_{\boldsymbol{g}(\boldsymbol{X})} =& \frac{1}{(2\pi)^n} \int_{\mathbb{R}^n} \boldsymbol{g}(\boldsymbol{x}) \int_{\mathbb{R}^n} \exp(-i\boldsymbol{\xi}\cdot\boldsymbol{x}) \left[1 + i\xi_j \mu^1_{g_j} + \frac{1}{2} i^2 \xi_{j_1}\xi_{j_2}\mu^2_{g_{j_1}g_{j_2}}\right. \\ &\left. + \frac{1}{k!} i^k \xi_{n_1}\cdots\xi_{n_h}\mu^k_{g_{n_1}\cdots g_{n_k}} + \mathcal{O}\left(|\boldsymbol{\xi}|^{k+1}\right)\right] d\boldsymbol{\xi} d\boldsymbol{x}\end{aligned} \tag{2.15}$$

Integrating over $\boldsymbol{\xi}$,

$$\begin{aligned}\mu^1_{\boldsymbol{g}(\boldsymbol{X})} = \int_{\mathbb{R}^n} \boldsymbol{g}(\boldsymbol{x}) \left\{ \prod_{j=1}^n \delta(x_j) - \mu^1_{X_j} \delta'(x_j) \prod_{l=1, l\neq j}^n \delta(x_l) \right. \\ \left. + \frac{(-1)^k}{k!} \mu^k_{X_{j_1}\cdots X_{j_k}} \left[\prod_{m=1}^p \delta^{(q_m)}(x_{j_m})\right] \prod_{l=1, l\neq j_m}^n \delta(x_l) \right\} d\boldsymbol{x}\end{aligned} \tag{2.16}$$

Here, p is the number of unique components of $\boldsymbol{X}$ appearing in $\mu^k_{X_{j_1}\cdots X_{j_k}}$, and q_m is the multiplicity of the m-th component. Next, integrating over $\boldsymbol{x}$,

$$\mu^1_{\boldsymbol{g}(\boldsymbol{X})} = \boldsymbol{g}(\boldsymbol{0}) + \mu^1_{X_j} \boldsymbol{g}_{,j}(\boldsymbol{0}) + \frac{1}{k!} \mu^k_{X_{j_1}\cdots X_{j_k}} \boldsymbol{g}_{,j_1\cdots j_k}(\boldsymbol{0}) \tag{2.17}$$

Similarly, the second moments of $\boldsymbol{g}(\boldsymbol{X})$ are given by

$$\mu^2_{\boldsymbol{g}(\boldsymbol{X})} = \int_{\mathbb{R}^n} \boldsymbol{g}(\boldsymbol{x})\, \boldsymbol{g}^{\mathrm{T}}(\boldsymbol{x})\, f_{\boldsymbol{X}}(\boldsymbol{x})\, d\boldsymbol{x} \tag{2.18}$$

A derivation similar to that given for the first moment shows that

$$\begin{aligned}\mu^2_{\boldsymbol{g}(\boldsymbol{X}),\boldsymbol{g}(\boldsymbol{X})} =& \boldsymbol{g}(\boldsymbol{0})\, \boldsymbol{g}^{\mathrm{T}}(\boldsymbol{0}) + \mu^1_{X_j} \left[\boldsymbol{g}_{,j}(\boldsymbol{0})\, \boldsymbol{g}^{\mathrm{T}}(\boldsymbol{0}) + \boldsymbol{g}(\boldsymbol{0})\, \boldsymbol{g}^{\mathrm{T}}_{,j}(\boldsymbol{0})\right] \\ &+ \frac{1}{k!} \mu^k_{X_{j_1}\cdots X_{j_k}} \sum_A \left[\boldsymbol{g}_{,j_{a_1}\cdots j_{a_r}}(\boldsymbol{0})\, \boldsymbol{g}^{\mathrm{T}}_{,j_{b_1}\cdots j_{b_s}}(\boldsymbol{0}) + \boldsymbol{g}_{,j_{b_1}\cdots j_{b_s}}(\boldsymbol{0})\, \boldsymbol{g}^{\mathrm{T}}_{,j_{a_1}\cdots j_{a_r}}(\boldsymbol{0})\right]\end{aligned} \tag{2.19}$$

Here, the k-th term involves a sum $\sum_A$ over all the subsets $A \subset \{1, \ldots, k\}$ with,

$$\begin{gathered} A = \{a_1, \ldots, a_r\} \subset \{1, \ldots, k\} \\ B = \{b_1, \ldots, b_s\} = \{1, \ldots, k\} \setminus A \\ A \cup B = \{1, \ldots, k\} \\ k = r + s \end{gathered} \tag{2.20}$$

Similar derivations yield moments of $\boldsymbol{g}$ of arbitrary order in terms of the moments of $\boldsymbol{X}$.

The moment expansion can be taken about an arbitrary value $\boldsymbol{x} = \boldsymbol{x}_0$ by considering the following transformation. Let

$$\boldsymbol{X} = \boldsymbol{Y} + \boldsymbol{x}_0 \tag{2.21}$$

Then, we have the result that, for an increasing function $\boldsymbol{X} = \boldsymbol{g}(\boldsymbol{Y})$, the cumulative distribution functions $F_{\boldsymbol{X}}$ and $F_{\boldsymbol{Y}}$ have the relationship,

$$\begin{aligned} F_{\boldsymbol{X}}(\boldsymbol{x}) =& P_{\boldsymbol{X}}(\boldsymbol{X} \leq \boldsymbol{x}) \\ =& P_{\boldsymbol{X}}(\boldsymbol{g}(\boldsymbol{Y}) \leq \boldsymbol{x}) \\ =& P_{\boldsymbol{Y}}\left(\boldsymbol{Y} \leq \boldsymbol{g}^{-1}(\boldsymbol{x})\right) \\ =& F_{\boldsymbol{Y}}\left(\boldsymbol{g}^{-1}(\boldsymbol{x})\right) \end{aligned} \tag{2.22}$$

That is, the probability that $\boldsymbol{X} \leq \boldsymbol{x}$ is the same as the probability that $\boldsymbol{Y} \leq \boldsymbol{g}^{-1}(\boldsymbol{x})$. The probability density function $f_{\boldsymbol{X}}$ is defined as the derivative of the cumulative

distribution function $F_{\boldsymbol{X}}$, so that

$$\begin{aligned} f_{\boldsymbol{X}}(\boldsymbol{x}) =& \frac{\partial^n}{\partial x_1 \cdots \partial x_n} F_{\boldsymbol{X}}(\boldsymbol{x}) \\ =& \frac{\partial^n}{\partial y_1 \cdots \partial y_n} F_{\boldsymbol{Y}}\left(\boldsymbol{g}^{-1}(\boldsymbol{x})\right) \left| \frac{\partial}{\partial \boldsymbol{x}} \boldsymbol{g}^{-1}(\boldsymbol{x}) \right| \\ =& f_{\boldsymbol{Y}}\left(\boldsymbol{g}^{-1}(\boldsymbol{x})\right) \left| \frac{\partial}{\partial \boldsymbol{x}} \boldsymbol{g}^{-1}(\boldsymbol{x}) \right| \end{aligned} \tag{2.23}$$

Combining Equations (2.21) and (2.23), we have

$$f_{\boldsymbol{X}}(\boldsymbol{x}) = f_{\boldsymbol{Y}}(\boldsymbol{x} - \boldsymbol{x}_0) \tag{2.24}$$

From Equation (2.6) and (2.24)

$$\begin{aligned} \phi_{\boldsymbol{X}}(\boldsymbol{\xi}) =& \int_{\mathbb{R}^n} \exp(i\boldsymbol{\xi} \cdot \boldsymbol{x}) f_{\boldsymbol{Y}}(\boldsymbol{x} - \boldsymbol{x}_0) d\boldsymbol{x} \\ =& \int_{\mathbb{R}^n} \exp(i\boldsymbol{\xi} \cdot (\boldsymbol{y} + \boldsymbol{x}_0)) f_{\boldsymbol{Y}}(\boldsymbol{y}) d\boldsymbol{x} \\ =& \exp(i\boldsymbol{\xi} \cdot \boldsymbol{x}_0) \int_{\mathbb{R}^n} \exp(i\boldsymbol{\xi} \cdot \boldsymbol{y}) f_{\boldsymbol{Y}}(\boldsymbol{y}) d\boldsymbol{x} \\ =& \exp(i\boldsymbol{\xi} \cdot \boldsymbol{x}_0) \int_{\mathbb{R}^n} \exp(i\boldsymbol{\xi} \cdot \boldsymbol{y}) f_{\boldsymbol{Y}}(\boldsymbol{y}) d\boldsymbol{y} \\ =& \exp(i\boldsymbol{\xi} \cdot \boldsymbol{x}_0) \phi_{\boldsymbol{Y}}(\boldsymbol{\xi}) \\ =& \exp(i\boldsymbol{\xi} \cdot \boldsymbol{x}_0) \phi_{\boldsymbol{X}-\boldsymbol{x}_0}(\boldsymbol{\xi}) \end{aligned} \tag{2.25}$$

Combining Equations (2.7) and (2.25),

$$\begin{aligned} f_{\boldsymbol{X}}(\boldsymbol{x}) =& \frac{1}{(2\pi)^n} \int_{\mathbb{R}^n} \exp(-i\boldsymbol{\xi} \cdot \boldsymbol{x}) \exp(i\boldsymbol{\xi} \cdot \boldsymbol{x}_0) \phi_{\boldsymbol{X}-\boldsymbol{x}_0}(\boldsymbol{\xi}) d\boldsymbol{\xi} \\ =& \frac{1}{(2\pi)^n} \int_{\mathbb{R}^n} \exp(-i\boldsymbol{\xi} \cdot (\boldsymbol{x} - \boldsymbol{x}_0)) \phi_{\boldsymbol{X}-\boldsymbol{x}_0}(\boldsymbol{\xi}) d\boldsymbol{\xi} \end{aligned} \tag{2.26}$$

Now, the derivatives of the shifted characteristic function are

$$\frac{\partial}{\partial\xi_{j_1}\cdots\partial\xi_{j_h}}\left[\phi_{\boldsymbol{X}-\boldsymbol{x}_0}\left(\boldsymbol{\xi}\right)\right]=\int_{\mathbb{R}^n} i^h\left[\left(\boldsymbol{x}-\boldsymbol{x}_0\right)_{j_1}\cdots\left(\boldsymbol{x}-\boldsymbol{x}_0\right)_{j_h}\right]\exp\left(i\boldsymbol{\xi}\cdot\left(\boldsymbol{x}-\boldsymbol{x}_0\right)\right)f_{\boldsymbol{X}}\left(\boldsymbol{x}\right)d\boldsymbol{x} \tag{2.27}$$

and

$$\mu^h_{(\boldsymbol{X}-\boldsymbol{x}_0)_{j_1}\cdots(\boldsymbol{X}-\boldsymbol{x}_0)_{j_h}}=\int_{\mathbb{R}^n}\left[\left(\boldsymbol{x}-\boldsymbol{x}_0\right)_{j_1}\cdots\left(\boldsymbol{x}-\boldsymbol{x}_0\right)_{j_h}\right]\exp\left(i\boldsymbol{\xi}\cdot\left(\boldsymbol{x}-\boldsymbol{x}_0\right)\right)f_{\boldsymbol{X}}\left(\boldsymbol{x}\right)d\boldsymbol{x} \tag{2.28}$$

so that

$$\mu^h_{(\boldsymbol{X}-\boldsymbol{x}_0)_{j_1}\cdots(\boldsymbol{X}-\boldsymbol{x}_0)_{j_h}}=\left\{\frac{1}{i^h}\frac{\partial}{\partial\xi_{j_1}\cdots\partial\xi_{j_h}}\left[\phi_{\boldsymbol{X}-\boldsymbol{x}_0}\left(\boldsymbol{\xi}\right)\right]\right\}_{\boldsymbol{\xi}=0} \tag{2.29}$$

This enables the Taylor expansion of the characteristic function as

$$\begin{aligned}\phi_{\boldsymbol{X}-\boldsymbol{x}_0}\left(\boldsymbol{\xi}\right)=&1+i\xi_j\mu^1_{(\boldsymbol{X}-\boldsymbol{x}_0)}+\frac{1}{2}i^2\xi_{j_1}\xi_{j_2}\mu^2_{(\boldsymbol{X}-\boldsymbol{x}_0)_{j_1}(\boldsymbol{X}-\boldsymbol{x}_0)_{j_2}}\\&+\frac{1}{k!}i^k\xi_{n_1}\cdots\xi_{n_h}\mu^k_{(\boldsymbol{X}-\boldsymbol{x}_0)_{n_1}\cdots(\boldsymbol{X}-\boldsymbol{x}_0)_{n_k}}+\mathcal{O}\left(\left|\boldsymbol{\xi}\right|^{k+1}\right)\end{aligned} \tag{2.30}$$

The first moment of $\boldsymbol{g}\left(\boldsymbol{X}\right)$ is given by

$$\begin{aligned}\mu^1_{\boldsymbol{g}(\boldsymbol{X})}=&\int_{\mathbb{R}^n}\boldsymbol{g}\left(\boldsymbol{x}\right)f_{\boldsymbol{X}}\left(\boldsymbol{x}\right)d\boldsymbol{x}\\=&\frac{1}{\left(2\pi\right)^n}\int_{\mathbb{R}^n}\boldsymbol{g}\left(\boldsymbol{x}\right)\int_{\mathbb{R}^n}\exp\left(-i\boldsymbol{\xi}\cdot\left(\boldsymbol{x}-\boldsymbol{x}_0\right)\right)\phi_{\boldsymbol{X}-\boldsymbol{x}_0}\left(\boldsymbol{\xi}\right)d\boldsymbol{\xi}d\boldsymbol{x}\\=&\frac{1}{\left(2\pi\right)^n}\int_{\mathbb{R}^n}\boldsymbol{g}\left(\boldsymbol{x}\right)\int_{\mathbb{R}^n}\exp\left(-i\boldsymbol{\xi}\cdot\left(\boldsymbol{x}-\boldsymbol{x}_0\right)\right)\left[1+i\xi_j\mu^1_{(\boldsymbol{X}-\boldsymbol{x}_0)}+\frac{1}{2}i^2\xi_{j_1}\xi_{j_2}\mu^2_{(\boldsymbol{X}-\boldsymbol{x}_0)_{j_1}(\boldsymbol{X}-\boldsymbol{x}_0)_{j_2}}\right.\\&\left.+\frac{1}{k!}i^k\xi_{n_1}\cdots\xi_{n_h}\mu^k_{(\boldsymbol{X}-\boldsymbol{x}_0)_{n_1}\cdots(\boldsymbol{X}-\boldsymbol{x}_0)_{n_k}}+\mathcal{O}\left(\left|\boldsymbol{\xi}\right|^{k+1}\right)\right]d\boldsymbol{\xi}d\boldsymbol{x}\end{aligned} \tag{2.31}$$

Integrating over $\boldsymbol{\xi}$,

$$\mu^1_{\boldsymbol{g}(\boldsymbol{X})} = \int_{\mathbb{R}^n} \boldsymbol{g}(\boldsymbol{x}) \left\{ \prod_{j=1}^{n} \delta\left((\boldsymbol{x}-\boldsymbol{x}_0)_j \right) - \mu^1_{(\boldsymbol{X}-\boldsymbol{x}_0)_j} \delta'\left((\boldsymbol{x}-\boldsymbol{x}_0)_j \right) \prod_{l=1, l\neq j}^{n} \delta\left((\boldsymbol{x}-\boldsymbol{x}_0)_l \right) \right.$$
$$\left. + \frac{(-1)^k}{k!} \mu^k_{(\boldsymbol{X}-\boldsymbol{x}_0)_{j_1}\cdots(\boldsymbol{X}-\boldsymbol{x}_0)_{j_k}} \left[\prod_{m=1}^{p} \delta^{(q_m)}\left((\boldsymbol{x}-\boldsymbol{x}_0)_{j_m} \right) \right] \prod_{l=1, l\neq j_m}^{n} \delta\left((\boldsymbol{x}-\boldsymbol{x}_0)_l \right) \right\} d\boldsymbol{x} \tag{2.32}$$

Next, integrating over $\boldsymbol{x}$,

$$\mu^1_{\boldsymbol{g}(\boldsymbol{X})} = \boldsymbol{g}(\boldsymbol{x}_0) + \mu^1_{(\boldsymbol{X}-\boldsymbol{x}_0)_j} \boldsymbol{g}_{,j}(\boldsymbol{x}_0) + \cdots + \frac{1}{k!} \mu^k_{(\boldsymbol{X}-\boldsymbol{x}_0)_{j_1}\cdots(\boldsymbol{X}-\boldsymbol{x}_0)_{j_k}} \boldsymbol{g}_{,j_1\cdots j_k}(\boldsymbol{x}_0) \tag{2.33}$$

Now, we expand $\boldsymbol{g}$ about the mean of $\boldsymbol{X}$; that is, we take $(\boldsymbol{x}_0)_j = \mu^1_{X_j}$. Then, $\mu^1_{(\boldsymbol{X}-\boldsymbol{x}_0)_j} = 0$, and

$$\mu^1_{\boldsymbol{g}(\boldsymbol{X})} = \boldsymbol{g}\left(\mu^1_{\boldsymbol{X}}\right) + \frac{1}{2} \mu^2_{\left(\boldsymbol{X}-\mu^1_{\boldsymbol{X}}\right)_{j_1}\left(\boldsymbol{X}-\mu^1_{\boldsymbol{X}}\right)_{j_2}} \boldsymbol{g}_{,j_1 j_2}\left(\mu^1_{\boldsymbol{X}}\right) + \cdots + \frac{1}{k!} \mu^k_{\left(\boldsymbol{X}-\mu^1_{\boldsymbol{X}}\right)_{j_1}\cdots\left(\boldsymbol{X}-\mu^1_{\boldsymbol{X}}\right)_{j_k}} \boldsymbol{g}_{,j_1\cdots j_k}\left(\mu^1_{\boldsymbol{X}}\right) \tag{2.34}$$

Using the notation, $\mu^k_{\left(\boldsymbol{X}-\mu^1_{\boldsymbol{X}}\right)_{j_1},\ldots,\left(\boldsymbol{X}-\mu^1_{\boldsymbol{X}}\right)_{j_k}} = \hat{\mu}^k_{X_{j_1},\ldots,X_{j_k}}$ for $k > 1$,

$$\mu^1_{\boldsymbol{g}(\boldsymbol{X})} = \boldsymbol{g}\left(\mu^1_{\boldsymbol{X}}\right) + \frac{1}{2} \hat{\mu}^2_{X_{j_1},X_{j_1}} \boldsymbol{g}_{,j_1 j_2}\left(\mu^1_{\boldsymbol{X}}\right) + \cdots + \frac{1}{k!} \hat{\mu}^k_{X_{j_1},\ldots,X_{j_k}} \boldsymbol{g}_{,j_1\cdots j_k}\left(\mu^1_{\boldsymbol{X}}\right) \tag{2.35}$$

Now,

$$\begin{aligned}
\hat{\mu}^2_{\boldsymbol{g}(\boldsymbol{X}),\boldsymbol{g}(\boldsymbol{X})} &= \int_{-\infty}^{\infty} \left[\boldsymbol{g}(\boldsymbol{x}) - \mu^1_{\boldsymbol{g}(\boldsymbol{x})}\right] \left[\boldsymbol{g}(\boldsymbol{x}) - \mu^1_{\boldsymbol{g}(\boldsymbol{x})}\right]^{\mathrm{T}} f_{\boldsymbol{X}}(\boldsymbol{x})\, d\boldsymbol{x} \\
&= \int_{-\infty}^{\infty} \boldsymbol{g}(\boldsymbol{x}) \left[\boldsymbol{g}(\boldsymbol{x})\right]^{\mathrm{T}} f_{\boldsymbol{X}}(\boldsymbol{x})\, d\boldsymbol{x} \\
&\quad - \left[\int_{-\infty}^{\infty} \boldsymbol{g}(\boldsymbol{x}) f_{\boldsymbol{X}}(\boldsymbol{x})\, d\boldsymbol{x}\right] \left[\mu^1_{\boldsymbol{g}(\boldsymbol{x})}\right]^{\mathrm{T}} \\
&\quad - \mu^1_{\boldsymbol{g}(\boldsymbol{x})} \left[\int_{-\infty}^{\infty} \boldsymbol{g}(\boldsymbol{x}) f_{\boldsymbol{X}}(\boldsymbol{x})\, d\boldsymbol{x}\right]^{\mathrm{T}}
\end{aligned}$$

$$
\begin{aligned}
&+ \int_{-\infty}^{\infty} \mu^1_{\boldsymbol{g}(\boldsymbol{x})} \left[\mu^1_{\boldsymbol{g}(\boldsymbol{x})}\right]^{\mathrm{T}} f_{\boldsymbol{X}}(\boldsymbol{x})\, d\boldsymbol{x} \\
&= \mu^2_{\boldsymbol{g}(\boldsymbol{X}),\boldsymbol{g}(\boldsymbol{X})} - \mu^1_{\boldsymbol{g}(\boldsymbol{X})} \left[\mu^1_{\boldsymbol{g}(\boldsymbol{x})}\right]^{\mathrm{T}} - \mu^1_{\boldsymbol{g}(\boldsymbol{x})} \left[\mu^1_{\boldsymbol{g}(\boldsymbol{X})}\right]^{\mathrm{T}} + \mu^1_{\boldsymbol{g}(\boldsymbol{x})} \left[\mu^1_{\boldsymbol{g}(\boldsymbol{x})}\right]^{\mathrm{T}} \\
&= \mu^2_{\boldsymbol{g}(\boldsymbol{X}),\boldsymbol{g}(\boldsymbol{X})} - \mu^1_{\boldsymbol{g}(\boldsymbol{x})} \left[\mu^1_{\boldsymbol{g}(\boldsymbol{x})}\right]^{\mathrm{T}}
\end{aligned} \tag{2.36}
$$

$$
\begin{aligned}
\mu^2_{\boldsymbol{g}(\boldsymbol{X}),\boldsymbol{g}(\boldsymbol{X})} =& \boldsymbol{g}\left(\mu^1_{\boldsymbol{X}}\right) \boldsymbol{g}^{\mathrm{T}}\left(\mu^1_{\boldsymbol{X}}\right) \\
&+ \frac{1}{2}\hat{\mu}^2_{X_{j_1},X_{j_2}} \left[\boldsymbol{g}_{,j_1 j_2}\left(\mu^1_{\boldsymbol{X}}\right) \boldsymbol{g}^{\mathrm{T}}\left(\mu^1_{\boldsymbol{X}}\right) + \boldsymbol{g}_{,j_1}\left(\mu^1_{\boldsymbol{X}}\right) \boldsymbol{g}^{\mathrm{T}}_{,j_2}\left(\mu^1_{\boldsymbol{X}}\right)\right. \\
&\qquad \left. + \boldsymbol{g}_{,j_2}\left(\mu^1_{\boldsymbol{X}}\right) \boldsymbol{g}^{\mathrm{T}}_{,j_1}\left(\mu^1_{\boldsymbol{X}}\right) + \boldsymbol{g}\left(\mu^1_{\boldsymbol{X}}\right) \boldsymbol{g}^{\mathrm{T}}_{,j_1 j_2}\left(\mu^1_{\boldsymbol{X}}\right)\right] \\
&+ \cdots \\
&+ \frac{1}{k!}\hat{\mu}^k_{X_{j_1}\cdots X_{j_k}} \sum_A \left[\boldsymbol{g}_{,j_{a_1}\cdots j_{a_r}}\left(\mu^1_{\boldsymbol{X}}\right) \boldsymbol{g}^{\mathrm{T}}_{,j_{b_1}\cdots j_{b_s}}\left(\mu^1_{\boldsymbol{X}}\right) + \boldsymbol{g}_{,j_{b_1}\cdots j_{b_s}}\left(\mu^1_{\boldsymbol{X}}\right) \boldsymbol{g}^{\mathrm{T}}_{,j_{a_1}\cdots j_{a_r}}\left(\mu^1_{\boldsymbol{X}}\right)\right]
\end{aligned} \tag{2.37}
$$

$$
\begin{aligned}
\hat{\mu}^2_{\boldsymbol{g}(\boldsymbol{X}),\boldsymbol{g}(\boldsymbol{X})} =& \frac{1}{2}\hat{\mu}^2_{X_{j_1},X_{j_2}} \left[\boldsymbol{g}_{,j_1}\left(\mu^1_{\boldsymbol{X}}\right) \boldsymbol{g}^{\mathrm{T}}_{,j_2}\left(\mu^1_{\boldsymbol{X}}\right) + \boldsymbol{g}_{,j_2}\left(\mu^1_{\boldsymbol{X}}\right) \boldsymbol{g}^{\mathrm{T}}_{,j_1}\left(\mu^1_{\boldsymbol{X}}\right)\right] \\
&+ \cdots \\
&+ \frac{1}{k!}\hat{\mu}^k_{X_{j_1}\cdots X_{j_k}} \sum_{j_1=1}^{k} \left[\boldsymbol{g}_{,j_1}\left(\mu^1_{\boldsymbol{X}}\right) \boldsymbol{g}^{\mathrm{T}}_{,j_2\cdots j_k}\left(\mu^1_{\boldsymbol{X}}\right) + \boldsymbol{g}_{,j_2\cdots j_k}\left(\mu^1_{\boldsymbol{X}}\right) \boldsymbol{g}^{\mathrm{T}}_{,j_1}\left(\mu^1_{\boldsymbol{X}}\right)\right]
\end{aligned} \tag{2.38}
$$

2.2.1 Moment Expansions for Mechanical Variables

In general, it is not feasible to determine exact expressions of relevant distributions and their density functions for field variables in the microscale problem. Instead,

microscale distributions can be approximately represented by a set of moments defined in equation (2.3). Consequently, if a microscale quantity r depends on other microscale quantities $\{q_1, \ldots, q_n\}$ through the constitutive relation $r(q_1, \ldots, q_n)$, the macroscale constitutive relation will require expressions for the moments μ_r^k, as functions of the moments $\mu_{q_1}^k, \ldots, \mu_{q_n}^k$ of the field variables $q_1, \ldots, q_n$. For example, if r is the plastic strain rate $\dot{\epsilon}_{22}$, and the q variables are $\sigma_{11}, \sigma_{22}, \sigma_{33}, \sigma_{12}, \sigma_{13}, \sigma_{23}$, an expression is required for the average strain rate $\mu_{\dot{\epsilon}_{22}}^1$ as a function of the set of moments $\{\mu_{\sigma_{ij}}^1, \mu_{\sigma_{ij}\sigma_{kl}}^2, \mu_{\sigma_{ij}\sigma_{kl}\sigma_{mn}}^3, \ldots\}$ where i, j, k, l, m, n range over 1,2,3. A general expression is derived here for providing the functional dependence of μ_r^1 on a (possibly infinite) series involving the moments $\mu_{q_1}^k, \ldots, \mu_{q_n}^k (k = 1, \ldots, n, \ldots)$. The development of this expansion is based on the properties of the density function $\phi(q_1, \ldots, q_n)$, as discussed next.

The characteristic function $\tilde{\phi} \in U$ is defined as the Fourier transform of a density function $\phi \in U$ as:

$$\tilde{\phi}(\boldsymbol{\xi}) = \langle \exp(i\boldsymbol{\xi} \cdot \mathbf{q}), \phi \rangle = \int_{\mathbb{R}^n} \exp(i\boldsymbol{\xi} \cdot \mathbf{q}) \phi(\mathbf{q}) \, dq_1 \cdots dq_n \tag{2.39}$$

The inverse transform of $\tilde{\phi}$ yields the density function ϕ, i.e.

$$\phi(\mathbf{q}) = \left\langle \frac{1}{2\pi} \exp(-i\boldsymbol{\xi} \cdot \mathbf{q}), \tilde{\phi} \right\rangle = \frac{1}{2\pi} \int_{\mathbb{R}^n} \exp(-i\boldsymbol{\xi} \cdot \mathbf{q}) \tilde{\phi}(\boldsymbol{\xi}) \, d\xi_1 \cdots d\xi_n \tag{2.40}$$

The derivatives of the characteristic function are given as:

$$\frac{\partial^k \tilde{\phi}}{\partial \boldsymbol{\xi}_1^{p_1} \cdots \partial \boldsymbol{\xi}_n^{p_n}} = \int_{\mathbb{R}^n} i^k q_1^{p_1} \cdots q_n^{p_n} \exp(i\boldsymbol{\xi} \cdot \mathbf{q}) \phi(\mathbf{q}) \, dq_1 \cdots dq_n \tag{2.41}$$

where $\sum_{i=1}^{n} p_i = k$. Comparing equations (2.3) and (2.41), the moments of $\mathbf{q}$ can be represented in terms of the derivatives of $\tilde{\phi}$ as:

$$\mu^k_{q_1^{p_1}\cdots q_n^{p_n}} = \frac{1}{i^k} \left. \frac{\partial^k \tilde{\phi}}{\partial \xi_1^{p_1} \cdots \partial \xi_n^{p_n}} \right|_{\boldsymbol{\xi}=0} \tag{2.42}$$

This representation enables the Taylor expansion of the characteristic function in terms of the moments,

$$\tilde{\phi}(\boldsymbol{\xi}) = \sum_{k=0}^{\infty} \frac{i^k}{k!} \boldsymbol{\xi}^k \odot \mu^k_{\mathbf{q}} \tag{2.43}$$

where $\odot$ is the appropriate scalar product. The density function $\phi(\mathbf{q})$ can then be written, from equations (2.40) and (2.43) as:

$$\phi(\mathbf{q}) = \sum_{k=0}^{\infty} \left\langle \frac{1}{2\pi} \exp(-i\boldsymbol{\xi} \cdot \mathbf{q}), \frac{i^k}{k!} \boldsymbol{\xi}^k \odot \mu^k_{\mathbf{q}} \right\rangle = \sum_{k=0}^{\infty} \frac{i^k}{k!} \mu^k_{\mathbf{q}} D^k_{\boldsymbol{\xi}} \delta \tag{2.44}$$

where δ is the Dirac-distribution, and $D^k\delta$ is the k-th derivative of δ. The utility of this expansion is that it allows for the moments of $r(\mathbf{q})$ to be expressed as a function of the moments of $\mathbf{q}$, as follows. For example, the first moment of $\mathbf{r}(\mathbf{q})$ is given by

$$\mu^1_{\mathbf{r}} = \langle \mathbf{r}, \phi \rangle = \int_{\mathbb{R}^n} \mathbf{r}(\mathbf{q}) \phi(\mathbf{q}) \, d\mathbf{q} \tag{2.45}$$

Substituting equation (2.44) in equation (2.45) yields:

$$\mu^1_{\mathbf{r}} = \left\langle \mathbf{r}, \sum_{k=0}^{\infty} \frac{i^k}{k!} \mu^k_{\mathbf{q}} D^k_{\boldsymbol{\xi}} \delta \right\rangle = \sum_{k=0}^{\infty} \left\langle \mathbf{r}, \frac{i^k}{k!} \mu^k_{\mathbf{q}} D^k_{\boldsymbol{\xi}} \delta \right\rangle = \sum_{k=0}^{\infty} \frac{1}{k!} \mu^k_{\mathbf{q}} \odot \left. \frac{\partial^k \mathbf{r}}{\partial \mathbf{q}^k} \right|_{\mathbf{q}=0} \tag{2.46}$$

Equation (2.46) is a prescription for writing the moments of r as a series involving the moments of the constituents $\mathbf{q}$ and the derivatives of the constitutive relation $r(\mathbf{q})$. Substituting $\hat{\mathbf{q}} = \mathbf{q} - \mathbf{q}_0$ in the preceding derivation, an equivalent expression

is obtained as:

$$\mu_{\mathbf{r}}^1 = \sum_{k=0}^{\infty} \frac{1}{k!} \mu_{\hat{\mathbf{q}}}^k \odot \left. \frac{\partial^k \mathbf{r}}{\partial \hat{\mathbf{q}}^k} \right|_{\hat{\mathbf{q}}=\mathbf{0}} = \sum_{k=0}^{\infty} \frac{1}{k!} \mu_{\hat{\mathbf{q}}}^k \odot \left. \frac{\partial^k r}{\partial \mathbf{q}^k} \right|_{\mathbf{q}=\mathbf{q}_0} \tag{2.47}$$

For the special case where $\mathbf{q}_0 = \mu_{\mathbf{q}}^1$,

$$\mu_{\mathbf{r}}^1 = \sum_{k=0}^{\infty} \frac{1}{k!} \hat{\mu}_{\mathbf{q}}^k \left. \frac{\partial^k \mathbf{r}}{\partial \mathbf{q}^k} \right|_{\mathbf{q}=\mu_{\mathbf{q}}^1} \tag{2.48}$$

where $\hat{\mu}_{\mathbf{q}}^k$ is the k-th central moment, given by

$$\hat{\mu}_x^k = \left\langle \left(\mathbf{q} - \mu_{\mathbf{q}}^1\right)^k, \phi\left(\mathbf{q}\right) \right\rangle \tag{2.49}$$

Equations (2.46) and (2.48) represent the moment expansions of $\mu_{\mathbf{r}}^1$ about $\mathbf{q} = \mathbf{0}$ and $\mathbf{q} = \mu_{\mathbf{q}}^1$ respectively. In the infinite sum, the two representations are equivalent. However, approximations of the sum by a truncated series will generally cause difference between the two. Since the k-th moment $\mu_{\mathbf{r}}^k$ of $\mathbf{r}$ may be interpreted as the first moment $\mu_{\mathbf{r}^k}^1$ of the k-th power of $\mathbf{r}$, equation (2.46) is a recipe for any moment of $\mathbf{r}$ in terms of the moments of $\mathbf{q}$. This prescription enables the development of homogenization methods with sufficient flexibility to represent the microscale behavior to a desired degree of accuracy at the macroscale by choosing an appropriate set of moments of $\mathbf{q}$.

It should be noted that the averaging theorems in equations (2.46) and (2.48) assign no special status to the field variables $\mathbf{q}$ as kinematic, material property, or otherwise. For example, if the constitutive equation is given as $\mathbf{r}\left(\mathrm{P};\mathrm{M}\right)$ where P are

mechanical field variables, and M are material parameters, then

$$\mu^1_{\mathbf{r}} = \sum_{k=0}^{\infty} \frac{1}{k_1!k_2!} \mu^k_{\mathrm{P}^{k_1}\mathrm{M}^{k_2}} \odot \left. \frac{\partial^k \mathbf{r}}{\partial \mathrm{P}^{k_1} \partial \mathrm{M}^{k_2}} \right|_{\mathrm{P}=\mathbf{0},\mathrm{M}=\mathbf{0}} \tag{2.50}$$

with $k_1+k_2 = k$. Mathematically, this is equivalent to taking $\mathbf{q} = \{\mathrm{P}; \mathrm{M}\}$ in Equation (2.46). Thus, the DEHF treats the heterogeneity of all microscale spatial fields in the same way through their effects on the constitutive relations, allowing the study of the effects of heterogeneity in material properties, as well as thermal, mechanical and other fields. Additionally, the quantities that appear in the macroscale constitutive relations are generally descriptors of arbitrary order of the microscale problem. While this does not guarantee uniqueness of the resulting macroscale constitutive equations, it does provide a means to extend a given constitutive relation to include a finer description of the microscale heterogeneity when necessary.

2.3 Examples: Time-Invariant Ordinary Differential Equations

To analyze the performance of DEHF, two mathematical examples of ordinary differential equations (ODEs) governing the evolution of an inhomogeneous field are considered. In the first, the governing equations are linear, and it is seen that no difference appears when applying DEHF, validating the model with respect to a standard homogenization scheme. In the second example, the nonlinear governing equations

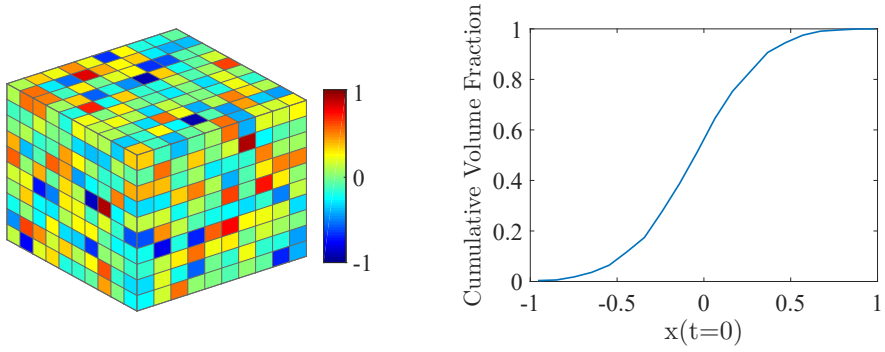

(a) (b)

Figure 2.1: Initial conditions: (a) a contour of the initial values; (b) the cumulative volume fraction measure of x.

result in a qualitatively different response of the ensemble average. It is shown that DEHF is able to capture this response to an arbitrary degree of accuracy, while the standard method predicts a response that is both quantitatively and qualitatively inaccurate.

Figure 2.1 shows the initial conditions for the example problems. In Figure 2.1a, the initial values of the variable x at time $t = 0$ are plotted within a three-dimensional geometric representation for visualization. In Figure 2.1, the distribution of x at time $t = 0$ is represented by the cumulative volume fraction, which gives for each value of x the volume fraction of material that has a value $x' < x$. The behavior of this field is studied under evolution equations of the form

$$\dot{x} = f(x) \tag{2.51}$$

The first moment μ_x^1 of x is the quantity of interest; its evolution is given by

$$\frac{d}{dt}\mu_x^1 = \mu_f^1 \tag{2.52}$$

Applying the moment expansion to μ_f^1 in Equation (2.52) yields

$$\frac{d}{dt}\mu_x^1 = f\left(\mu_x^1\right) + \sum_{k=2}^{\infty} \frac{1}{k!} \left.\frac{d^k f}{dx^k}\right|_{x=\mu_x^1} \mu_{x-\mu_x^1}^k \tag{2.53}$$

Taking f to be a linear function of x, Equations (2.51) and (2.53) respectively become

$$\dot{x} = a_1 x \tag{2.54}$$

$$\frac{d}{dt}\mu_x^1 = f\left(\mu_x^1\right) = a_1 \mu_x^1 \tag{2.55}$$

For the linear case, the higher-order derivatives in Equation (2.53) are identically zero, so that the evolution of the field average is obtained by substituting the average into the original evolution equation, as shown in Figure 2.2.

The equivalence of these two approaches is not general; in fact, it only holds for the linear case. To demonstrate this, take f to be a quadratic function of x, so that

$$\dot{x} = a_1 x + a_2 x^2 \tag{2.56}$$

$$\frac{d}{dt}\mu_x^1 = f\left(\mu_x^1\right) + \frac{1}{2} \left.\frac{d^2 f}{dx^2}\right|_{x=\mu_x^1} \mu_{x-\mu_x^1}^k = a_1 \mu_x^1 + a_2 \left(\mu_x^1\right)^2 + a_2 \mu_{x-\mu_x^1}^2 \tag{2.57}$$

Equation (2.57) introduces a new variable, $\mu_{x-\mu_x^1}^2$ whose evolution has not been specified. Applying the moment expansion to this new variable, the evolution is derived:

$$\dot{x} = a_1 x + a_2 x^2 \tag{2.58}$$

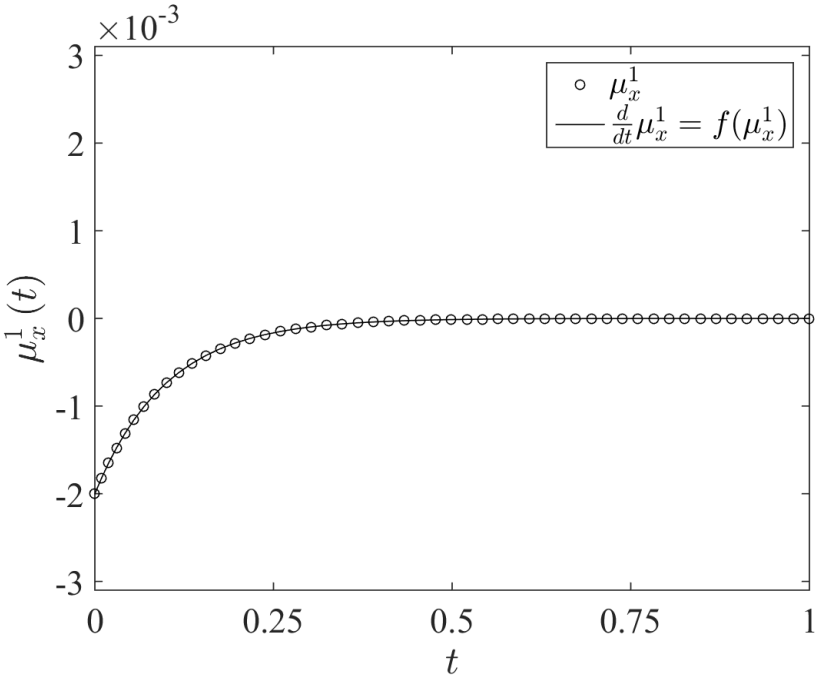

Figure 2.2

$$\frac{d}{dt}\mu^2_{x-\mu_x^1} = 4a_2\mu_x^1\mu^2_{x-\mu_x^1} + 2a_1\mu^2_{x-\mu_x^1} + 2a_2\mu^3_{x-\mu_x^1} \tag{2.59}$$

Again, Equation (2.59) introduces a new variable $\mu^3_{x-\mu_x^1}$. The evolution of this variable can be derived in terms of moments of order four, and so on. If the system of equations is closed at order n by ignoring the terms of order $n+1$ and higher, an approximate solution can be found. Increasing the order of the approximation increases the fidelity of the solution, as shown in Figure 2.3 For the approximation of order 14, the evolution is plotted as the solid line in Figure 2.4. It is clear that the agreement with the full field evolution (open circles) is quite good.

Unlike the linear case, it is clear from Figure 2.4 that the approximation resulting

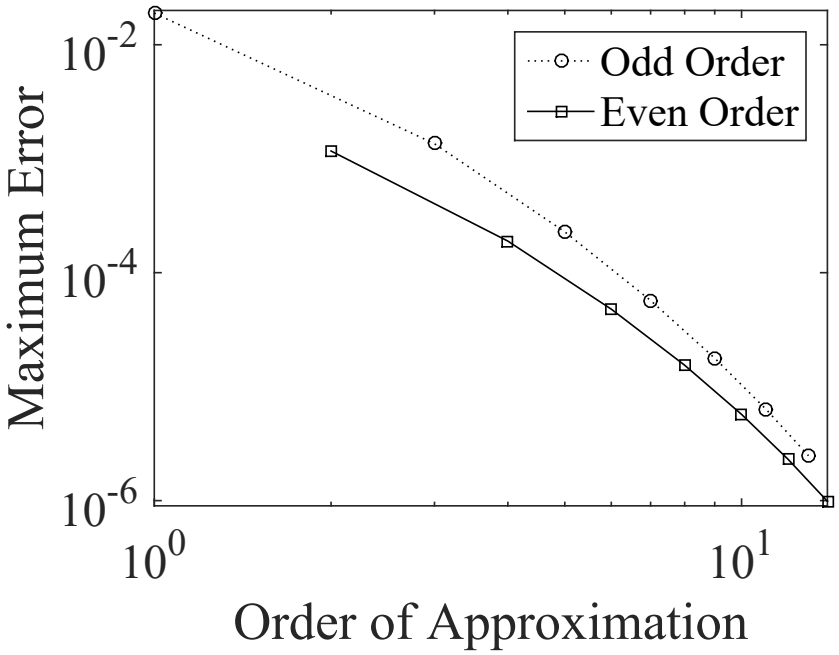

Figure 2.3: Error in the moment expansion approximations of the evolution of the field x.

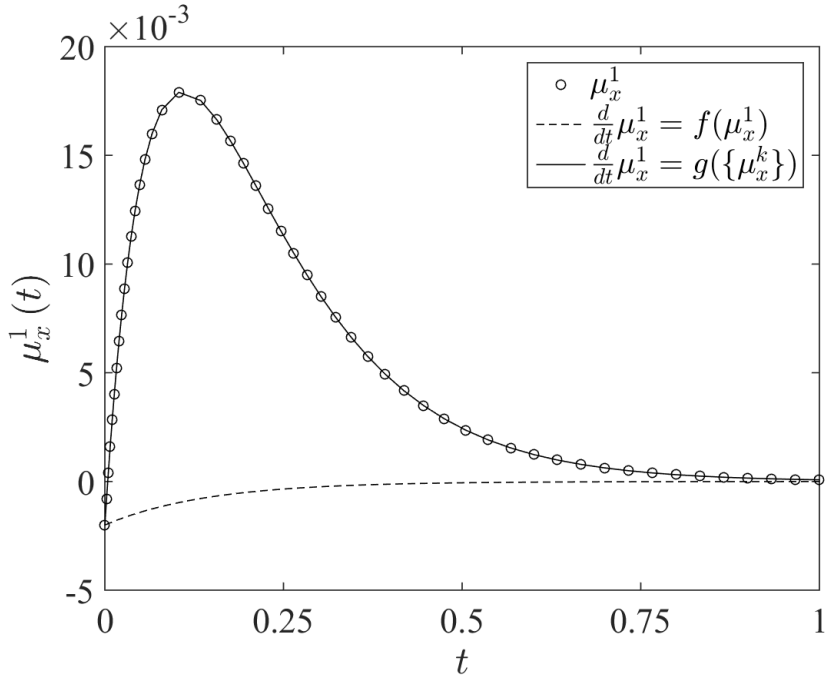

Figure 2.4

from substituting the average of x into the original evolution equation (dashed line) does not even qualitatively match the full field evolution. In fact, no parameter fitting of $a_1^{\text{effective}}$ and $a_2^{\text{effective}}$ could possibly produce the correct curve, as the same value of x produces different derivatives at different points in the evolution. This is a crucial point: for heterogeneous fields that evolve pointwise by a nonlinear time-invariant differential equation, it is not generally possible to derive an effective time-invariant differential equation that governs the evolution of the field average. On the other hand, it is possible in some such cases to construct a system of coupled equations that will approximate the evolution of the field average via distribution enhanced homogenization.

2.4 The Microscale Boundary Value Problem

Next, the application of DEHF to the mechanics of elasto-plasticity is studied. The two-scale homogenization problem derives effective *macroscale* constitutive relations and a kinematic framework that is consistent with the underlying *microscale* mechanics. *Microscale*, in this context, represents the scale at which heterogeneities with different material properties and nonuniform material geometry are explicitly represented, whereas *macroscale* corresponds to a scale at which the microscale heterogeneities are not explicitly resolved, but are represented through parametric forms in the constitutive relation. Explicit microscale boundary value problems need to be solved to obtain macroscale constitutive relations using classical homogenization procedures and serve as a reference solution for evaluating the DEHF results. These are discussed next.

2.4.1 Governing Equations for the Microscale Problem

The boundary value problem for the microscale domain Ω, in the absence of body forces and inertial effects, is governed by the equilibrium equations in terms of the

Cauchy stress $\boldsymbol{\sigma}$, given as:

$$\operatorname{div}(\boldsymbol{\sigma}) = \mathbf{0} \quad \forall\ \mathbf{x} \in \Omega \tag{2.60}$$

along with the boundary conditions on $\partial\Omega$, expressed as:

$$\mathbf{t} = \mathbf{t}_0 \quad \forall\ \mathbf{x} \in \Gamma_t \subset \partial\Omega \ \text{ and } \ \mathbf{u} = \mathbf{u}_0 \quad \forall\ \mathbf{x} \in \Gamma_u \subset \partial\Omega \tag{2.61}$$

where $\mathbf{t} = \boldsymbol{\sigma}\cdot\mathbf{n}$ is the traction on a surface with normal $\mathbf{n}$, $\mathbf{t}_0$ is the prescribed traction vector on the traction boundary Γ_t, and $\mathbf{u}_0$ is the prescribed displacement vector on the displacement boundary Γ_u. The principle of energy conservation for infinitesimal strain-rate $\dot{\boldsymbol{\epsilon}} = \frac{1}{2}\left[\nabla\mathbf{v} + (\nabla\mathbf{v})^{\mathrm{T}}\right]$ is stated in terms of the balance of power as:

$$p^{\text{ext}} \triangleq \int_{\partial\Omega} \mathbf{t}\cdot\mathbf{v}\,dA = \int_{\Omega} \boldsymbol{\sigma} : \dot{\boldsymbol{\epsilon}}\,dV \triangleq p^{\text{int}} \tag{2.62}$$

For an isothermal problem with constant stored defect energy, the rate of change of the Helmholtz free energy density is

$$\rho\dot{\psi} = \boldsymbol{\sigma} : \dot{\boldsymbol{\epsilon}}^e \tag{2.63}$$

The non-negative mechanical dissipation per unit volume, expressed as [33]:

$$d = p^{\text{int}} - \rho\dot{\psi} \geq 0 \tag{2.64}$$

can be written in terms of the plastic strain-rate, i.e.

$$d = \boldsymbol{\sigma} : (\dot{\boldsymbol{\epsilon}} - \dot{\boldsymbol{\epsilon}}^e) = \boldsymbol{\sigma} : \dot{\boldsymbol{\epsilon}}^p \tag{2.65}$$

where the plastic strain rate is defined as $\dot{\boldsymbol{\epsilon}}^p = \dot{\boldsymbol{\epsilon}} - \dot{\boldsymbol{\epsilon}}^e$. The microscale constitutive relations are then defined with reference to these quantities, as follows.

2.4.2 Microscale Constitutive Relations

The elastic constitutive relation is expressed in terms of a strain energy function W as:

$$\boldsymbol{\sigma} = \frac{\partial W}{\partial \boldsymbol{\epsilon}^e} \tag{2.66}$$

where $\boldsymbol{\epsilon}^e$ is the elastic strain. For isothermal conditions, the strain energy and free energy are identified, since $\boldsymbol{\sigma} = \left(\frac{\partial \psi}{\partial \boldsymbol{\epsilon}^e}\right)_\theta$. The linear elastic constitutive relation is consequently defined as:

$$\boldsymbol{\sigma} = \left(\frac{\partial^2 \psi}{\partial \left(\boldsymbol{\epsilon}^e\right)^2}\right)_\theta : \boldsymbol{\epsilon}^e = \mathbb{C} : \boldsymbol{\epsilon}^e \tag{2.67}$$

where $\mathbb{C} = \left(\frac{\partial^2 \psi}{\partial (\boldsymbol{\epsilon}^e)^2}\right)_\theta$ is the elasticity tensor. Assuming that the defect energy at the microscale is negligible, the free energy naturally takes on the form,

$$\psi\left(\boldsymbol{\epsilon}^e\right) = \frac{1}{2}\boldsymbol{\epsilon}^e : \mathbb{C} : \boldsymbol{\epsilon}^e \tag{2.68}$$

where $\mathbb{C}$ is the elasticity tensor. The microscale complementary Helmholtz free energy $\hat{\psi}$ is similarly identified with the complementary strain energy, as:

$$\hat{\psi}\left(\boldsymbol{\sigma}\right) = \frac{1}{2}\boldsymbol{\sigma} : \mathbb{S} : \boldsymbol{\sigma} \tag{2.69}$$

where $\mathbb{S}$ is the elastic compliance tensor. For the examples in this study, the material is assumed to be isotropic at the microscale. Correspondingly, the elastic stiffness tensor is given by the expression:

$$\mathbb{C} = \frac{E}{(1-2\nu)(1+\nu)}\left[\nu \mathbf{I}^{(2)} \otimes \mathbf{I}^{(2)} + (1-2\nu)\mathbf{I}^{(4)}\right] \tag{2.70}$$

where $\mathbf{I}^{(2)}$ and $\mathbf{I}^{(4)}$ are the second- and fourth-order identity tensors, respectively. The compliance tensor is:

$$\mathbb{S} = \mathbb{C}^{-1} = \frac{1}{E}\left[-\nu \mathbf{I}^{(2)} \otimes \mathbf{I}^{(2)} + (1+\nu)\,\mathbf{I}^{(4)}\right] \tag{2.71}$$

The microscale plastic constitutive relation is derived to be consistent with the principle of maximum plastic dissipation at the microscale, as follows. Assuming no material hardening, the maximum dissipation for viscoplastic flow can be formulated as an unconstrained minimization problem following [34], as:

$$\boldsymbol{\sigma} = \underset{\bar{\boldsymbol{\sigma}} \in \int}{\arg\min} \left\{ -d\left(\bar{\boldsymbol{\sigma}}; \dot{\boldsymbol{\epsilon}}^p\right) + \frac{1}{\eta} g\left(f\left(\bar{\boldsymbol{\sigma}}\right)\right) \right\} \tag{2.72}$$

where g is a penalization function with $g \geq 0$ and $g(f) = 0 \leftrightarrow f \leq 0$, $\eta \in]0, \infty[$ is a penalty parameter, and $\int$ is the space of admissible stresses, such that

$$\int = \{\bar{\sigma} | \mathrm{div}\,(\bar{\sigma}) = 0\} \tag{2.73}$$

From equation (2.72), the viscoplastic flow rule is derived to be:

$$\frac{\partial}{\partial \boldsymbol{\sigma}} \left[d\left(\boldsymbol{\sigma}; \dot{\boldsymbol{\epsilon}}^p\right) - \frac{1}{\eta} g\left(f\left(\boldsymbol{\sigma}\right)\right) \right] = \dot{\boldsymbol{\epsilon}}^p - \frac{1}{\eta} \frac{\partial g}{\partial f} \frac{\partial f}{\partial \boldsymbol{\sigma}} = 0 \tag{2.74}$$

which implies

$$\dot{\boldsymbol{\epsilon}}^p \triangleq \mathbf{h}^p\left(\boldsymbol{\sigma}\right) = \frac{1}{\eta} \frac{\partial g}{\partial f} \frac{\partial f}{\partial \boldsymbol{\sigma}} \tag{2.75}$$

The flow rule given by Equation (2.75) guarantees the regularization of the maximum microscale dissipation in equation (2.72).

The loading function f is chosen as a function of the equivalent stress

$$\sigma^e = \|\mathbf{s}\| = \sqrt{\|\boldsymbol{\sigma}\|^2 - \frac{1}{3}\left[\mathrm{tr}\left(\boldsymbol{\sigma}\right)\right]^2} \tag{2.76}$$

as:

$$f\left(\boldsymbol{\sigma}\right) = \sigma^e - \sigma_0 \tag{2.77}$$

where $\mathbf{s}$ is the deviatoric stress, and the flow direction is given as $\mathbf{n} = \frac{\partial f}{\partial \boldsymbol{\sigma}} = \frac{\mathbf{s}}{\|\mathbf{s}\|}$. Assuming an exponential form for $g(f)$ with the requirement that $\mathbf{h}^p(\mathbf{0}) = \mathbf{0}$, the penalty function g may be defined as:

$$g(f) = \beta\left[\exp\left(\alpha f\right) - \frac{1}{\alpha} f \exp\left(-\alpha\sigma_0\right) - 1\right] \tag{2.78}$$

with $\alpha = \frac{1}{\eta}$. Correspondingly, the right hand side in the flow rule of equation (2.75) is given as:

$$\mathbf{h}^p\left(\boldsymbol{\sigma}\right) = \beta\left[\exp\left(\alpha\left(\sigma^e\left(\boldsymbol{\sigma}\right) - \sigma_0\right)\right) - \exp\left(-\alpha\sigma_0\right)\right]\mathbf{n}\left(\boldsymbol{\sigma}\right) \tag{2.79}$$

This flow rule has an exponential form, similar to the thermally activated crystal plasticity models in [2,18,35,36], with the parameter α identified with the activation energy of slip. The parameter α may be adjusted to control the rate sensitivity of the material, such that the rate-independent limit is approached for $\alpha \to \infty$. The parameter β is a reference strain rate, and σ_0 is a measure of flow resistance. The flow rule (2.79) is capable of approximating a wide range of realistic behaviors with a model that is simple enough to analyze fully in the discussion of the homogenization problem.

CHAPTER 2. THE DISTRIBUTION ENHANCED HOMOGENIZATION FRAMEWORK

Successful application of any homogenization framework should, at a minimum, preserve the power balance relation written in terms of the microscale quantities in equation (2.62) when p^{int} and p^{ext} are written in terms of macroscale quantities. Typically, this requirement is met by applying boundary conditions that ensure satisfaction of Hill's lemma [37], in which the power balance may be written entirely in terms of the volume averages of the microscale stress and strain. Satisfying Hill's lemma, however, is not a sufficient condition for a consistent partition of the internal energy into free and dissipative energy parts at the macroscale. In the literature, the macroscale constitutive relations are typically homogenized through averaging the stress-strain responses for a number of microscale test problems. This process often incorporates fitting of macroscopic parameters to the averaged microscopic response variables. This may render the macroscopic constitutive relations non-unique, as consistency with the microscale response is enforced over a finite load-response regime rather than in a pointwise-valid form. In what follows, higher-order descriptors of the microscale response are used to derive homogenized constitutive relations for the macroscale that do not exhibit these limitations.

2.5 Distribution Enhanced Homogenization Method for the Macroscale Problem

The DEHF equations are developed in this section to solve the homogenized macroscale problem. The moment-based descriptors of the microscale fields are evaluated in the macroscale constitutive response.

2.5.1 Macroscale Quantities in the Distribution Enhanced Homogenization Framework

Macroscale quantities in DEHF are distributions on the space of microscale density functions. The macroscale stress may thus be defined in terms of the microscale stress density functions as:

$$\Sigma_1 \triangleq \mu^1_{\boldsymbol{\sigma}} = \langle \boldsymbol{\sigma}, \phi_\Omega(\boldsymbol{\sigma}) \rangle \tag{2.80}$$

where $\phi_\Omega(\boldsymbol{\sigma}) \in \hat{U}$ approximates the volume fraction or density $f(\boldsymbol{\sigma})$ of the microscale stress $\boldsymbol{\sigma}$ in a microscale neighborhood Ω of $\mathbf{x}$. From equation (2.3), this defines Σ_1 as the average or first moment of the microscale stress field. For the problems considered in this study, this is analogous to the more familiar definition of homogenized stress $\boldsymbol{\Sigma} = \frac{1}{|\Omega|}\int_\Omega \boldsymbol{\sigma} dV$. Correspondingly, the macroscale stress defined by equation (2.80) is

governed by the equilibrium equation:

$$\operatorname{div}(\boldsymbol{\Sigma}_1) = 0 \tag{2.81}$$

Additional macroscale stresses are defined in terms of the higher order moments of the microscale stresses as:

$$\Sigma_k \triangleq \mu^k_{\boldsymbol{\sigma}^k} \circ \left(\mu^{k-1}_{\boldsymbol{\sigma}^{k-1}}\right)^{-1} \tag{2.82}$$

where $\circ$ represents the appropriate tensor product that produces a second order tensor. For a uniform microscale stress $\boldsymbol{\sigma}(\mathbf{x}) = \boldsymbol{\sigma}$, equation (2.80) shows that $\boldsymbol{\Sigma_1} = \boldsymbol{\sigma}$, since the stress density function approximates the indicator function $1_{\{\boldsymbol{\Sigma_1}\}}$. Then, $\mu^k_{\boldsymbol{\sigma}^k} = \boldsymbol{\sigma}^k$ and

$$\boldsymbol{\Sigma}_k = \boldsymbol{\sigma}^k \circ \left(\boldsymbol{\sigma}^{k-1}\right)^{-1} = \boldsymbol{\Sigma}_1 \tag{2.83}$$

Thus for a uniform microscale stress, the higher-order macroscale stress description is equivalent to that in a parametric homogenization framework. For a nonuniform microscale stress, the DEHF extends this description by introducing a set of macroscale stress descriptors derived from the higher-order moments of the microscale stress field. The macroscale strain rate is similarly defined as:

$$\dot{\boldsymbol{\Xi}}_1 \triangleq \langle \dot{\boldsymbol{\epsilon}}, \phi_\Omega(\dot{\boldsymbol{\epsilon}}) \rangle = \frac{1}{|\Omega|} \int_\Omega \dot{\boldsymbol{\epsilon}} dV = \frac{1}{2}\left[\nabla \mathbf{V} + (\nabla \mathbf{V})^{\mathrm{T}}\right] \tag{2.84}$$

where $\mathbf{V}$ is the macroscale velocity.

In DEHF, the macroscale Helmholtz free energy distribution is derived from the

microscale free energy density function, as:

$$\Psi \triangleq \langle \psi, \phi_\Omega(\psi) \rangle \tag{2.85}$$

Substituting equation (2.68) and the moment expansions (2.46) and (2.48) in equation (2.85) yields

$$\Psi = \frac{1}{2}\mu^3_{\boldsymbol{\epsilon}^e:\mathbb{C}:\boldsymbol{\epsilon}^e} = \frac{1}{2}\left(\mu^1_{\boldsymbol{\epsilon}^e} : \mu^1_{\mathbb{C}} : \mu^1_{\boldsymbol{\epsilon}^e} + \hat{\mu}^2_{\boldsymbol{\epsilon}^e\otimes\boldsymbol{\epsilon}^e} \odot \mu^1_{\mathbb{C}} + \mu^1_{\boldsymbol{\epsilon}^e} : \hat{\mu}^2_{\mathbb{C}:\boldsymbol{\epsilon}^e} + \hat{\mu}^3_{\boldsymbol{\epsilon}^e:\mathbb{C}:\boldsymbol{\epsilon}^e}\right) \tag{2.86}$$

where $\odot$ is the scalar product for fourth-rank tensors. The first equality in equation (2.86) gives an interpretation of the macroscale free energy in terms of the third-order moment involving the elastic strain and stiffness tensor. This could be taken as a fundamental quantity, or the second equality in equation (2.86) can be used to write the macroscale free energy equivalently in terms of parts due to the average microscale elastic strain and stiffness fields and their microscale fluctuations. For a uniform $\mathbb{C} \equiv \mu^1_{\mathbb{C}}$

$$\Psi = \frac{1}{2}\mathbb{C} \odot \mu^2_{\boldsymbol{\epsilon}^e\otimes\boldsymbol{\epsilon}^e} = \frac{1}{2}\mathbb{C} \odot \left(\mu^1_{\boldsymbol{\epsilon}^e} \otimes \mu^1_{\boldsymbol{\epsilon}^e} + \hat{\mu}^2_{\boldsymbol{\epsilon}^e\otimes\boldsymbol{\epsilon}^e}\right) \tag{2.87}$$

Accordingly, the macroscale complementary free energy is expressed in terms of the microscale stress field as:

$$\hat{\Psi} \triangleq \left\langle \hat{\psi}, \phi_\Omega\left(\hat{\psi}\right) \right\rangle = \frac{1}{2}\mu^3_{\boldsymbol{\sigma}:\mathbb{S}:\boldsymbol{\sigma}} \tag{2.88}$$

A set of macroscopic variables are defined as

$$\Lambda_{km} \triangleq \mu^k_{\boldsymbol{\sigma}^{k-m}\mathrm{M}^m} \circ \left(\mu^{k-1}_{\boldsymbol{\sigma}^{k-m-1}\mathrm{M}^m}\right)^{-1} \tag{2.89}$$

where M is a set of material parameters appearing in the microscale constitutive relations. For $m = 0$, these variables are stress-like, and correspond to the variables defined in equation (2.82). From equation (2.80), $\Lambda_{10} \triangleq \Sigma_1$, and the higher-order variables $\Lambda_{k0} \triangleq \Sigma_k$ are derived from higher moments of the microscale stress. Under the condition of uniform $\mathbb{S} \equiv \mu^1_{\mathbb{S}}$, equation (2.88) reduces to:

$$\hat{\Psi} = \frac{1}{2}\left[\mu^2_{\boldsymbol{\sigma}\otimes\boldsymbol{\sigma}} : \left(\mu^1_{\boldsymbol{\sigma}}\right)^{-1}\right] : \mathbb{S} : \mu^1_{\boldsymbol{\sigma}} = \frac{1}{2}\Sigma_2 : \mathbb{S} : \Sigma_1 \tag{2.90}$$

For a uniform microscale stress, $\Sigma_2 = \Sigma_1$, and the standard definition of the complimentary free energy is recovered. For the elastic strain, defined as $\Xi^e_1 \triangleq \langle \boldsymbol{\epsilon}^e, \phi_\Omega(\boldsymbol{\epsilon}^e)\rangle$, the elastic constitutive relation is

$$\Xi^e_1 = \mathbb{S}^{\text{eff}} : \Sigma_1 \quad \text{where} \quad \mathbb{S}^{\text{eff}} = \frac{\partial^2 \hat{\Psi}}{\partial\Sigma_1 \otimes \partial\Sigma_1} = \frac{1}{2}\frac{\partial^2 \Lambda_{21}}{\partial\Sigma_1 \otimes \partial\Sigma_1} \tag{2.91}$$

For a uniform (constant) compliance $\mathbb{S}$,

$$\mathbb{S}^{\text{eff}} = \frac{\partial^2 \hat{\Psi}}{\partial\Sigma_1 \otimes \partial\Sigma_1} = \mathbb{S} : \frac{\partial\Sigma_2}{\partial\Sigma_1} + \frac{1}{2}\Sigma_1 : \mathbb{S} : \frac{\partial^2\Sigma_2}{\partial\Sigma_1 \otimes \partial\Sigma_1} \tag{2.92}$$

It can be verified that for a uniform microscale stress, equation (2.92) leads to $\mathbb{S}^{\text{eff}} = \mathbb{S}$, as expected. From the additive decomposition of the total strain and the linearity property of the distribution, the plastic strain may be expressed as:

$$\Xi^p_1 \triangleq \langle \boldsymbol{\epsilon}^p, \phi_\Omega(\boldsymbol{\epsilon}^p)\rangle = \Xi_1 - \Xi^e_1 \tag{2.93}$$

The macroscale BVP can then be formulated as one whose governing equations result from equations (2.81), (2.84), (2.91) and (2.93). Given boundary conditions on terms

of U or V, a constitutive relation between Ξ^e or Σ and Ξ^p is then sufficient to close the system of equations for solution of the macroscale problem.

The macroscale internal power density is expressed as:

$$\mathcal{P}^{\text{int}} = \left\langle p^{\text{int}}, \phi_\Omega \left(p^{\text{int}} \right) \right\rangle = \mu^2_{\boldsymbol{\sigma}:\dot{\boldsymbol{\epsilon}}} = \mu^1_{\boldsymbol{\sigma}} : \mu^1_{\dot{\boldsymbol{\epsilon}}} + \hat{\mu}^2_{\boldsymbol{\sigma}:\dot{\boldsymbol{\epsilon}}} \tag{2.94}$$

As for the macroscale free energy, the macroscale internal power is composed of a part due to the product of the averages of the stress and strain rate and an additional term due to the average of the product of these terms. For the internal power, there is a classical treatment of the higher order term based on Hill's Lemma [37], which guarantees that the internal power at the macroscale can be formulated as a function of the averages of microscale quantities under the application of one of a particular set of boundary conditions. Boundary conditions may include known displacement, uniform traction, or periodic boundary conditions. If the set of effective quantities are taken as just the averages of the microscale quantities, then the last equality in equation (2.94) requires,

$$\hat{\mu}^2_{\boldsymbol{\sigma}:\dot{\boldsymbol{\epsilon}}} = 0 \quad \text{which implies that} \quad \mu^2_{\boldsymbol{\sigma}:\dot{\boldsymbol{\epsilon}}} = \mu^1_{\boldsymbol{\sigma}} : \mu^1_{\dot{\boldsymbol{\epsilon}}} \tag{2.95}$$

From the microscale power balance,

$$\mu^2_{\boldsymbol{\sigma}:\dot{\boldsymbol{\epsilon}}} = \frac{1}{|\Omega|} \int_{\partial\Omega} \mathbf{t} \cdot \mathbf{v} dA \tag{2.96}$$

For applied boundary conditions of (i) uniform stress: $\mathbf{t} = \mu^1_{\boldsymbol{\sigma}} \cdot \mathbf{n}$, (ii) uniform strain-rate: $\mathbf{v} = \mu^1_{\dot{\boldsymbol{\epsilon}}} \cdot \mathbf{x}$, or (iii) periodicity $\mathbf{t}\left(\tilde{\mathbf{x}}\right) = -\mathbf{t}\left(\mathbf{x}\right), \mathbf{v}\left(\tilde{\mathbf{x}}\right) = \mathbf{v}\left(\mathbf{x}\right) + \mu^1_{\dot{\boldsymbol{\epsilon}}} \cdot \left(\tilde{\mathbf{x}} - \mathbf{x}\right)$ with

$\tilde{\mathbf{x}}$ as the periodic image of $\mathbf{x}$,

$$\frac{1}{|\Omega|}\int_{\partial\Omega}\mathbf{t}\cdot\mathbf{v}dA=\mu^1_{\boldsymbol{\sigma}}:\mu^1_{\dot{\boldsymbol{\epsilon}}} \tag{2.97}$$

that satisfies equation (2.95). For elastic problems, where $\boldsymbol{\epsilon}=\boldsymbol{\epsilon}^e$, the effective elasticity tensor can be estimated from the relation between $\mu^1_{\boldsymbol{\sigma}}$ and $\mu^1_{\boldsymbol{\epsilon}}$. However, there is no simple way to eliminate the higher order terms in equation (2.87) for the general case, since boundary conditions are not typically applied for $\boldsymbol{\epsilon}^e$. In the DEHF, equations (2.86) and (2.94) consistently treat all the higher order terms. This approach permits solutions for a much larger class of problems and also allows the application of a much larger set of admissible boundary conditions.

The expression for macroscale internal power density in equation (2.94) is expanded as:

$$\begin{aligned}\mathcal{P}^{\text{int}}=&\mu^2_{\boldsymbol{\sigma}:\dot{\boldsymbol{\epsilon}}^e}+\mu^2_{\boldsymbol{\sigma}:\dot{\boldsymbol{\epsilon}}^p}=\frac{1}{2}\mathbb{S}\odot\frac{d}{dt}\mu^2_{\boldsymbol{\sigma}\otimes\boldsymbol{\sigma}}+\mu^2_{\boldsymbol{\sigma}:\dot{\boldsymbol{\epsilon}}^p}\\ =&\frac{1}{2}\left(\frac{d}{dt}\left(\Sigma_2\right):\mathbb{S}:\Sigma_1+\Sigma_2:\mathbb{S}:\frac{d}{dt}\Sigma_1\right)+\mu^2_{\boldsymbol{\sigma}:\dot{\boldsymbol{\epsilon}}^p}\end{aligned} \tag{2.98}$$

The macroscale dissipation is then expressed as:

$$\mathcal{D}^p=\mathcal{P}^{\text{int}}-\dot{\Psi}=\mu^2_{\boldsymbol{\sigma}:\dot{\boldsymbol{\epsilon}}^p} \tag{2.99}$$

which is consistent with the macroscale definition as a distribution, since

$$\mathcal{D}^p\triangleq\left\langle d^p,\phi_\Omega\left(d^p\right)\right\rangle=\mu^2_{\boldsymbol{\sigma}:\dot{\boldsymbol{\epsilon}}^p} \tag{2.100}$$

Analogous to equation (2.87) for the macroscale free energy, the macroscale dissipation can be written using equation (2.48) as:

$$\mathcal{D}^p = \langle d^p, \phi_\Omega\left(d^p\right)\rangle = \mu^1_{\boldsymbol{\sigma}} : \mu^1_{\dot{\boldsymbol{\epsilon}}^p} + \hat{\mu}^2_{\boldsymbol{\sigma}:\dot{\boldsymbol{\epsilon}}^p} \tag{2.101}$$

Thus, the macroscale dissipation may be formulated as the sum of the product of the averages of the microscale stress and plastic strain rate fields and a correction due to the microscale fluctuations of these fields. This form of the macroscale dissipation highlights a very important conjecture that the product of the average stress with the average plastic strain rate is different from the effective dissipation by an arbitrary relative difference. For example, the loading of a heterogeneous microstructure under a macroscale hydrostatic stress would make the product $\mu^1_{\boldsymbol{\sigma}} : \mu^1_{\dot{\boldsymbol{\epsilon}}^p} = 0$, while the local deviatoric plastic strain-rate could be non-zero due to microscale fluctuations in the stress field. In such a case, the macroscale dissipation should obviously be different from zero, due to the higher-order term $\hat{\mu}^2_{\sigma:\dot{\boldsymbol{\epsilon}}^p}$. Since it is not obvious that there is any advantage from considering the decomposition (2.101), as it is for the purely elastic case, the macroscale dissipation is developed from equation (2.100).

Using the moment expansion in equation (2.46), the macroscale dissipation can be expanded in terms of the moments of the microscale stress $\boldsymbol{\sigma}$ and the microscale material properties M as:

$$\mathcal{D}^p = \sum_{k=0}^{\infty}\sum_{m=0}^{k} \frac{1}{(k-m)!m!}\mu^k_{\boldsymbol{\sigma}^{k-m}\mathrm{M}^m} \circ \frac{\partial^k}{\partial\boldsymbol{\sigma}^{k-m}\partial\mathrm{M}^m}\left[\boldsymbol{\sigma} : \mathbf{h}^p\left(\boldsymbol{\sigma};\mathrm{M}\right)\right]\Big|_{\boldsymbol{\sigma}=\mathbf{0},\mathrm{M}=\mathbf{0}} \tag{2.102}$$

Since the expansion is about $\boldsymbol{\sigma} = \mathbf{0}$, the derivatives in equation (2.102) can be simplified to obtain

$$\mathcal{D}^p = \sum_{k=2}^{\infty} \sum_{m=0}^{k-1} \frac{1}{(k-m)!m!} \mu^k_{\boldsymbol{\sigma}^{k-m}\mathrm{M}^m} \circ \left. \frac{\partial^{k-1}\mathbf{h}^p}{\partial \boldsymbol{\sigma}^{k-m-1}\partial \mathrm{M}^m} \right|_{\boldsymbol{\sigma}=\mathbf{0},\mathrm{M}=\mathbf{0}} \tag{2.103}$$

The index k starts at 2, since the $k = 1$ term involves $\mathbf{h}^p(\mathbf{0};\mathbf{0}) = \mathbf{0}$. The macroscopic plastic strain-rate variables are defined as:

$$\dot{\Xi}^p_{km} = \frac{1}{(k-m-1)!m!} \mu^{k-1}_{\boldsymbol{\sigma}^{k-m-1}\mathrm{M}^m} \odot \left. \frac{\partial^{k-1}\mathbf{h}^p}{\partial \boldsymbol{\sigma}^{k-m-1}\partial \mathrm{M}^m} \right|_{\boldsymbol{\sigma}=\mathbf{0},\mathrm{M}=\mathbf{0}} \tag{2.104}$$

for $k \geq 2$. Substituting equation (2.104) into equation (2.103), the macroscopic plastic dissipation becomes:

$$\mathcal{D}^p = \sum_{k=2}^{\infty} \sum_{m=0}^{k-1} \mu^k_{\boldsymbol{\sigma}^{k-m}\mathrm{M}^m} \circ \left(\mu^{k-1}_{\boldsymbol{\sigma}^{k-m-1}\mathrm{M}^m}\right)^{-1} \odot \dot{\Xi}^p_{km} \tag{2.105}$$

Using definitions in equation (2.89), the macroscale dissipation is written as:

$$\mathcal{D}^p = \sum_{k=2}^{\infty} \sum_{m=0}^{k-1} \Lambda_{km} : \dot{\Xi}^p_{km} \tag{2.106}$$

The macroscale plastic strain rate variable $\dot{\Xi}^p_1$ does not enter explicitly into the calculation of the macroscale dissipation, and hence the term $\mu^1_{\sigma_{ij}} \mu^1_{\dot{\epsilon}^p_{ij}}$ does not appear in the macroscale plastic dissipation . On the other hand, the macroscopic plastic strain rate is given by

$$\dot{\Xi}^p_1 = \sum_{k=2}^{\infty} \frac{1}{(k-1)!} \mu^{k-1}_{\boldsymbol{\sigma}} \left. \frac{\partial^{k-1}\mathbf{h}^p}{\partial \boldsymbol{\sigma}^{k-1}} \right|_{\boldsymbol{\sigma}=\mathbf{0}} = \sum_{k=2}^{\infty} \dot{\Xi}^p_k \tag{2.107}$$

and the macroscopic plastic constitutive relation is obtained from equations (2.104) and (2.107). For a uniform microscale stress field,

$$\mathcal{D}^p = \Sigma_1 : \sum_{k=1}^{\infty} \dot{\Xi}^p_k = \Sigma_1 : \dot{\Xi}^p \tag{2.108}$$

It should be emphasized that the relation (2.107) is generally not of the form $\mathbf{h}^p(\Sigma; \mathrm{M})$ which is an extension of the microscale $\mathbf{h}^p$ by assigning a functional dependence of the material parameters in $\mathbf{h}^p$ on M, as in equation (2.5). Rather, the present formulation introduces a new functional form based on the nonzero derivatives of $\mathbf{h}^p$, and a set of new macroscale quantities $\mathbf{\Sigma}_k$ that represent the heterogeneity of the microscale stress field.

The plastic strain-rate variables at the macroscale are functions of the macroscale stress-like state variables $\{\Sigma_1, \ldots, \Sigma_k\}$ from the above formulation. New equations are required to govern the evolution of these variables. To form the basis for these equations it is noted that the k-th moment of the microscopic stress field is

$$\mu^k_{\boldsymbol{\sigma}} = \int_{\mathbb{R}^6} \boldsymbol{\sigma}^k \phi_\Omega(\boldsymbol{\sigma})\, d\boldsymbol{\sigma} \tag{2.109}$$

Assuming a negligible change in volume, the time derivatives of the k-th moment of the microscopic stress is given as:

$$\frac{d}{dt}\mu^k_{\boldsymbol{\sigma}} = k \int_{\mathbb{R}^6} \boldsymbol{\sigma}^{k-1} \otimes \dot{\boldsymbol{\sigma}} \phi_\Omega(\boldsymbol{\sigma})\, d\boldsymbol{\sigma} \tag{2.110}$$

With the trajectories in equation (2.110), the macroscale stress variables $\mathbf{\Sigma}_k$ can be calculated, and a solution to the macroscale BVP may be found. For the applications considered in section 2.7, relationships between the $\mathbf{\Sigma}_k$ that are required for microscale equilibrium are used to derive specific forms from (2.110). Before presenting these examples, a general strategy is outlined for the numerical solution of these types of

equations.

2.6 Numerical Implementation for the DEHF Macroscale Problem

This section discusses the implementation of the DEHF framework and strategies for the macroscale constitutive updates. For the problems considered, the primary focus is on the evaluation of macroscale constitutive relations corresponding to the constitutive relation (2.75) relating plastic strain rate $\dot{\boldsymbol{\epsilon}}^p$ and stress $\boldsymbol{\sigma}$ at the microscale. The discussion below focuses on this particular relation with the understanding that this process can be adapted for a general constitutive relation.

At the microscale, solutions are required for the governing equation

$$\dot{\boldsymbol{\sigma}} - \mathbb{C} : \left[\dot{\boldsymbol{\epsilon}} - \dot{\boldsymbol{\epsilon}}^p \left(\boldsymbol{\sigma}\right)\right] = 0 \tag{2.111}$$

From developments in section 2.5, the corresponding equations at the macroscale are:

$$\dot{\boldsymbol{\Sigma}}_1 - \mathbb{C} : \left[\dot{\boldsymbol{\Xi}}_1 - \dot{\boldsymbol{\Xi}}_1^p \left(\boldsymbol{\Sigma}_1, \ldots, \boldsymbol{\Sigma}_k, \mathrm{M}\right)\right] = 0 \tag{2.112}$$

where M is the microstructural parametrization. The macroscale system in the DEHF also requires the closure

$$\dot{\boldsymbol{\Sigma}}_k - \mathbf{f}\left(\boldsymbol{\Xi}_1, \ldots, \boldsymbol{\Xi}_n, \boldsymbol{\Sigma}_1, \ldots, \boldsymbol{\Sigma}_n, \mathrm{M}\right) = 0 \tag{2.113}$$

Here, the evolution of the higher-order stresses are related to the current values of the set of quantities (up to order n) that are considered in the macroscale problem and the microstructural parametrization function M. The numerical implementation and solution strategy for these equations are presented next.

2.6.1 The Microscale Problem Solution

The backward Euler integration scheme is employed to obtain microscale stresses at step $n+1$ by solving equations (2.111), using variables at step n, as:

$$\boldsymbol{\sigma}_{n+1} = \mathbb{C} : [\boldsymbol{\epsilon}_{n+1} - \boldsymbol{\epsilon}^p_n - \dot{\boldsymbol{\epsilon}}^p (\boldsymbol{\sigma}_{n+1}) \Delta t] \tag{2.114}$$

A residual is defined as:

$$\mathbf{R}\left(\boldsymbol{\sigma}^{(k)}_{n+1}\right) = \boldsymbol{\sigma}^{(k)}_{n+1} - \mathbb{C} : \left[\boldsymbol{\epsilon}_{n+1} - \boldsymbol{\epsilon}^p_n - \dot{\boldsymbol{\epsilon}}^p \left(\boldsymbol{\sigma}^{(k)}_{n+1}\right) \Delta t\right] \approx \mathbf{0} \tag{2.115}$$

The solution algorithm proceeds by finding the root of $\mathbf{R}$ based on a Newton update of the stress $\boldsymbol{\sigma}_{n+1}$

$$\boldsymbol{\sigma}^{(k+1)}_{n+1} = \boldsymbol{\sigma}^{(k)}_{n+1} - \left[\frac{\partial \mathbf{R}}{\partial \boldsymbol{\sigma}_{n+1}}\left(\boldsymbol{\sigma}^{(k)}_{n+1}\right)\right]^{-1} : \mathbf{R}\left(\boldsymbol{\sigma}^{(k)}_{n+1}\right) \tag{2.116}$$

for which the derivative is derived as:

$$\frac{\partial \mathbf{R}}{\partial \boldsymbol{\sigma}}\left(\boldsymbol{\sigma}^{(k)}_{n+1}\right) = \mathbf{I}^{(4)} + \mathbb{C} : \left[\frac{\partial \dot{\boldsymbol{\epsilon}}^p}{\partial \sigma^e}(\boldsymbol{\sigma}_{n+1}) \otimes \mathbf{n}_{n+1}\right] \Delta t \tag{2.117}$$

where $\mathbf{n}_{n+1} = \frac{\mathbf{s}_{n+1}}{\|\mathbf{s}_{n+1}\|}$, where $\boldsymbol{s}$ is the deviatoric stress. Substituting the expression for the plastic flow from equation (2.79) in (2.117) leads to

$$\frac{\partial \mathbf{R}}{\partial \boldsymbol{\sigma}}\left(\boldsymbol{\sigma}_{n+1}^{(k)}\right) = \mathbf{I}^{(4)} + \alpha\beta \exp\left(\alpha\left(\sigma_{n+1}^{e} - \sigma_0\right)\right)\Delta t \mathbb{C} : (\mathbf{n}_{n+1} \otimes \mathbf{n}_{n+1}) \tag{2.118}$$

Defining the iterative stress-update as:

$$\boldsymbol{\sigma}_{n+1}^{(k+1)} = \boldsymbol{\sigma}_{n+1}^{(k)} - \mathbb{C} : \Delta\boldsymbol{\epsilon}_{n+1}^{p(k+1)} \tag{2.119}$$

the iterative increment of the plastic strain is given as:

$$\Delta\boldsymbol{\epsilon}_{n+1}^{p(k+1)} = \mathbb{C}^{-1} : \left[\frac{\partial \mathbf{R}}{\partial \boldsymbol{\sigma}_{n+1}}\left(\boldsymbol{\sigma}_{n+1}^{(k)}\right)\right]^{-1} : \mathbf{R}\left(\boldsymbol{\sigma}_{n+1}^{(k)}\right) \tag{2.120}$$

The iteration stops when $\left\|\Delta\boldsymbol{\epsilon}_{n+1}^{p(k+1)}\right\| < \text{TOL}$, and the updated plastic strain is

$$\boldsymbol{\epsilon}_{n+1}^{p} = \boldsymbol{\epsilon}_{n+1}^{p(k+1)} \tag{2.121}$$

2.6.2 Macroscale Stress-Update Algorithm in the DEHF

For the parametric homogenization procedure, the macroscale constitutive update solving (2.112) proceeds in a manner analogous to the microscale problem, the only difference being in the effective constants appearing in the homogenized macroscale constitutive relations. However in the DEHF, an adaptation of these computational procedures is required for the solution of the macroscale problem, since the equations are written in terms of a set of macroscale constituents that extend those appearing in

the microscale problem. In DEHF, solutions are sought to the system of macroscale equations

$$\frac{d}{dt}[\mu_{\boldsymbol{\sigma}}] = \mathrm{A}\left[\mu_{\boldsymbol{\sigma}}\right] + \mathrm{v}\left([\mu_{\boldsymbol{\sigma}}], t\right) \tag{2.122}$$

where $[\mu_{\boldsymbol{\sigma}}]$ is an array of stress moments, and A and v are the corresponding problem-specific arrays. The solution of this system is given as:

$$[\mu_{\boldsymbol{\sigma}}] = \exp\left(\mathrm{A}t\right)\left[[\mu_{\boldsymbol{\sigma}}]_{t=0} + \int_0^t \exp\left(-\mathrm{A}\tau\right)\mathrm{v}\left([\mu_{\boldsymbol{\sigma}}], \tau\right) d\tau\right] \tag{2.123}$$

In some cases, it is feasible to determine the solution of this equation in closed form, or to numerically approximate the integral. In general, solutions are obtained directly from (2.122) via the following numerical scheme.

The stress moments at step $n+1$ in the backward Euler integration scheme are obtained as:

$$[\mu_{\boldsymbol{\sigma}}]_{n+1} = [\mu_{\boldsymbol{\sigma}}]_n + \Delta t \frac{d}{dt}[\mu_{\boldsymbol{\sigma}}]_{n+1} = [\mu_{\boldsymbol{\sigma}}]_n + \Delta t\left[\mathrm{A}\left[\mu_{\boldsymbol{\sigma}}\right]_{n+1} + \mathrm{v}\left([\mu_{\boldsymbol{\sigma}}]_{n+1}, t_{n+1}\right)\right] \tag{2.124}$$

for which a residual is defined as:

$$\mathbf{R} = [\mu_{\boldsymbol{\sigma}}]^{(k)}_{n+1} - [\mu_{\boldsymbol{\sigma}}]_n - \Delta t\left[\mathrm{A}\left[\mu_{\boldsymbol{\sigma}}\right]^{(k)}_{n+1} + \mathrm{v}\left([\mu_{\boldsymbol{\sigma}}]^{(k)}_{n+1}, t_{n+1}\right)\right] \tag{2.125}$$

The iterative solution algorithm performs a Newton update of the stress moments as:

$$[\mu_{\boldsymbol{\sigma}}]^{(k+1)}_{n+1} = [\mu_{\boldsymbol{\sigma}}]^{(k)}_{n+1} - \left[\frac{\partial \mathbf{R}}{\partial [\mu_{\boldsymbol{\sigma}}]^{(k)}_{n+1}}\left([\mu_{\boldsymbol{\sigma}}]^{(k)}_{n+1}\right)\right]^{-1} \mathbf{R}\left([\mu_{\boldsymbol{\sigma}}]^{(k)}_{n+1}\right) \tag{2.126}$$

where the derivative for the tangent matrix is

$$\frac{\partial \mathbf{R}}{\partial [\mu_{\boldsymbol{\sigma}}]^{(k)}_{n+1}}\left([\mu_{\boldsymbol{\sigma}}]^{(k)}_{n+1}\right) = \mathbf{I}^{(a)} - \Delta t\left[\mathrm{A} + \frac{\partial \mathrm{v}}{\partial [\mu_{\boldsymbol{\sigma}}]^{(k)}_{n+1}}\left([\mu_{\boldsymbol{\sigma}}]^{(k)}_{n+1}\right)\right] \tag{2.127}$$

Here, a is the order of the approximation and $\mathbf{I}^{(a)}$ is the a-dimensional identity matrix. The update can then be written as

$$[\mu_{\boldsymbol{\sigma}}]_{n+1}^{(k+1)} = [\mu_{\boldsymbol{\sigma}}]_{n+1}^{(k)} - \left[\mathbf{I}^{(a)} - \Delta t \left(\mathrm{A} + \frac{\partial \mathrm{v}}{\partial [\mu_{\boldsymbol{\sigma}}]_{n+1}^{(k)}} \left([\mu_{\boldsymbol{\sigma}}]_{n+1}^{(k)}\right)\right)\right]^{-1} \tag{2.128}$$

$$\times \left\{[\mu_{\boldsymbol{\sigma}}]_{n+1}^{(k)} - [\mu_{\boldsymbol{\sigma}}]_n - \Delta t \left[\mathrm{A}\,[\mu_{\boldsymbol{\sigma}}]_{n+1}^{(k)} + \mathrm{v}\left([\mu_{\boldsymbol{\sigma}}]_{n+1}^{(k)}\right)\right]\right\} \tag{2.129}$$

The iterative increment of the stress-moment vector is expressed as:

$$\Delta[\mu_{\boldsymbol{\sigma}}]_{n+1}^{(k+1)} = [\mu_{\boldsymbol{\sigma}}]_{n+1}^{(k+1)} - [\mu_{\boldsymbol{\sigma}}]_{n+1}^{(k)} \tag{2.130}$$

The iteration stops when $\left\|\Delta[\mu_{\boldsymbol{\sigma}}]_{n+1}^{(k+1)}\right\| < \mathrm{TOL}$, and the updated stress-moment vector is

$$[\mu_{\boldsymbol{\sigma}}]_{n+1} = [\mu_{\boldsymbol{\sigma}}]_{n+1}^{(k+1)} \tag{2.131}$$

2.7 Numerical Examples Elucidating the Significance of Distribution-Enhanced Homogenization Framework

In this section, the DEHF is applied to solve a set of problems involving tensile deformation, for which the resulting microscale mechanical fields exhibit some degree of non-uniformity. Two types of heterogeneous problems are solved, viz. (i) for which non-uniformity in microscale fields is related to the specimen geometry, and

(ii) for which microscale non-uniformity is related to spatially varying material properties. For each problem, detailed microscale simulations are performed to obtain the reference solution. Parametric homogenization is conducted for the problem (i) to compare with results from the DEHF model. Finally, the DEHF is applied separately for elastic, viscoplastic, and combined elasto-viscoplastic responses of both types of specimens to investigate various features of the modeling framework.

2.7.1 Direct Numerical Simulation of the Microscale BVP

In the first problem, microscale heterogeneity in mechanical fields is induced by the specimen geometry. Consider a tensile specimen loaded in uniaxial stress, with geometry shown in in figure 2.5a. The geometry for all the microscale simulations is $D_A = 2cm$, $L = 10cm$. The quantities D_B and R are varied for different scenarios. The domain of the specimen is discretized into 5760 hexahedral elements, as shown in figure 2.5a. The simulations are performed with the commercial code Abaqus Standard with constitutive relations implemented in a user material subroutine (UMAT). The loading is displacement controlled, so that the planar ends of the tensile bar remain planar and parallel and the rate of logarithmic strain $\ln\left(1 + \frac{\Delta L}{L}\right)$ remains constant.

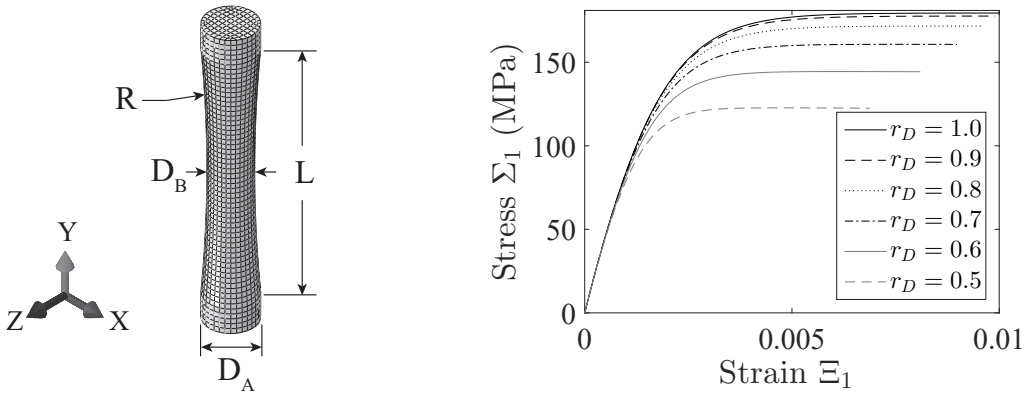

(a) (b)

Figure 2.5: (a) Finite element model and mesh of the tensile bar with geometric specifications. (b) Macroscale stress-strain response obtained by averaging the corresponding microscale fields for various gauge diameter ratios $r_D = \frac{D_B}{D_A}$.

Results of the microscale simulations with $\beta = 1\text{s}^{-1}$, $\alpha = 0.01MPa^{-1}$, $\sigma_0 = 100MPa$, $E = 100GPa$, $\nu = 0.3$, and $D_B = (0.5, \ldots, 1.0)\, D_A$ are shown in Figure 2.5b. The stress is highest for any point in the strain history for $D_B = D_A$, where the stress is uniform. For the nonuniform geometries, the stress for any given strain decreases monotonically with decreasing gauge diameter. The microstructural parameter controlling the heterogeneity of the microscale field is the gauge diameter D_B. Qualitatively, it can be inferred that the heterogeneity in the stress field enhances the plasticity, and hence the amount of plasticity is higher for a given average stress with increasing heterogeneity. It is worth noting that while the specimens were all strained to an equal one-dimensional strain $\epsilon_L = \ln\left(1 + \frac{\Delta L}{L}\right) = 0.01$, the volume

averaged strain is different for each case. The volume average of the strain tensor is calculated as:

$$\begin{aligned}\Xi_1 &= \frac{1}{|\Omega|}\int_\Omega \boldsymbol{\epsilon} dV = \frac{1}{|\Omega|}\int_\Omega \frac{1}{2}\left[\nabla\mathbf{u} + (\nabla\mathbf{u})^{\mathrm{T}}\right] dV \\ &= \frac{1}{|\Omega|}\int_{\partial\Omega} \frac{1}{2}\left(\mathbf{u}\otimes\mathbf{n} + \mathbf{n}\otimes\mathbf{u}\right) dA\end{aligned} \tag{2.132}$$

The strain component along the longitudinal axis of the tensile bar is $(\Xi_1)_{22} = \frac{1}{|\Omega|}\int_{\partial\Omega} u_2 n_2 dA$. With the origin at the center of the specimen, integration over the planar ends of the bar produces a value $(\Xi_1)_{22} = 0.01$. However along the gauge cutout, the 2-component of the normal n_2 is always opposite in sign to the 2-component of the displacement u_2, thus guaranteeing that the final value of the strain $(\Xi_1)_{22} \leq 0.01$. The homogenization scheme will have to account for this effect.

2.7.2 Parametric Homogenization

Since the microstructure of the microscale problem has a uniform modulus, the effective elastic constitutive relations is expressed as:

$$\Sigma_1 = \frac{1}{|\Omega|}\int_\Omega \mathbb{C} : \boldsymbol{\epsilon} dV = \mathbb{C} : \frac{1}{|\Omega|}\int_\Omega \boldsymbol{\epsilon}^e dV = \mathbb{C} : \Xi_1^e \triangleq \mathbb{C}^{\text{eff}} : \Xi_1^e \tag{2.133}$$

Thus $\mathbb{C}^{\text{eff}} = \mathbb{C}$. For this particular microstructure, parametric homogenization of the elastic constitutive relation uniquely determines $\mathbb{C}^{\text{eff}}$ from the physics of the microscale problem, although this is not generally the case. The parametrization of the effective plastic constitutive parameters is not as straightforward. However, one set of effective plastic parameters can be determined by considering the effects of the

microstructure on the strain-rate and flow stress, as follows.

In the microscale problem, for uniaxial tension under a homogeneous deformation, the uniform state of stress is

$$\boldsymbol{\sigma} = \begin{bmatrix} 0 & 0 & 0 \\ 0 & \sigma_{22} & 0 \\ 0 & 0 & 0 \end{bmatrix} \tag{2.134}$$

From equation (2.76) the equivalent stress is $\sigma^e = \sqrt{\frac{2}{3}}\sigma_{22}$ and the flow direction $\mathbf{n} = \frac{\mathbf{s}}{\|\mathbf{s}\|}$ is thus

$$\mathbf{n} = \frac{1}{\sqrt{6}} \begin{bmatrix} -1 & 0 & 0 \\ 0 & 2 & 0 \\ 0 & 0 & -1 \end{bmatrix} \tag{2.135}$$

The component $\dot{\epsilon}^p_{22}$ of the plastic strain rate from equation (2.79) is

$$\dot{\epsilon}^p_{22} = \sqrt{\frac{2}{3}}\beta \left[\exp\left(\alpha\left(\sigma^e - \sigma_0\right)\right) - \exp\left(-\alpha\sigma_0\right)\right] \tag{2.136}$$

At steady state, $\dot{\epsilon}^p_{22} = \dot{\epsilon}_{22}$ and hence from equation (2.136)

$$\sigma_{22} = \sigma_0^{'} + \frac{1}{\alpha^{'}} \ln\left(\frac{1}{\beta^{'}}\dot{\epsilon}_{22} + \exp\left(-\alpha^{'}\sigma_0^{'}\right)\right) \tag{2.137}$$

where

$$\alpha^{'} = \sqrt{\frac{2}{3}}\alpha \quad , \quad \beta^{'} = \sqrt{\frac{2}{3}}\beta \quad , \quad \sigma_0^{'} = \sqrt{\frac{3}{2}}\sigma_0 \tag{2.138}$$

Thus, the flow stress can be written as a function of the material parameters and the applied strain rate. If this relationship can be inverted, the material parameters can

be written as a function of the microstructural and loading parameters through the dependence of the flow stress on these parameters. Note that this inverse will not be unique.

To determine the sensitivity of the flow stress with respect to the microstructural descriptor D_B, the results of the microscale direct numerical simulations (DNS) are analyzed, where D_B varies from $0.5D_A$ to $1.0D_A$. The flow stress is plotted as a function of the ratio $r_D = D_B/D_A$ across this range of values in figure 2.6.

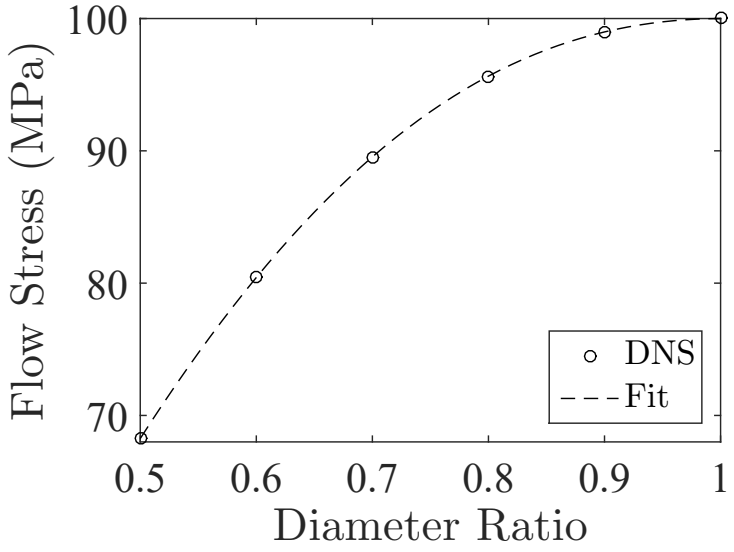

Figure 2.6: Flow stress as a function of gauge diameter from the DNS results and the empirical fit for the classical homogenization procedure.

The classical parametric homogenization proceeds by fitting a curve to the representative simulation data, so that the flow stress may be written as a function

$g(D_B)$ of the microstructural parameter D_B. With the assumption that $g(0) = 0$, a fourth-order polynomial provides a reasonable estimate of the flow stress for the microstructures simulated, as shown in figure 2.6. Define

$$r_g(D_B) = \frac{g(D_B)}{g(1)} \quad \text{and} \quad r_{\dot{\epsilon}}(D_B) = \frac{\left\langle \left(\dot{\Xi}_1\right)_{22}(D_B) \right\rangle}{\left\langle \left(\dot{\Xi}_1\right)_{22}(1) \right\rangle} \tag{2.139}$$

where $\left\langle \dot{\Xi}_1 \right\rangle$ is the time average of the volume-averaged microscale strain rate over the entire microscale evolution. Adjusting the parameters in Equation (2.137) as:

$$\begin{aligned} \alpha^{\text{eff}}(D_B) =& r_g^{-1}(D_B)\,\alpha' \\ \beta^{\text{eff}}(D_B) =& r_{\dot{\epsilon}}(D_B)\,\beta' \\ \sigma_0^{\text{eff}}(D_B) =& r_g(D_B)\,\sigma_0' \end{aligned} \tag{2.140}$$

to produce the macroscale plastic constitutive relation,

$$\dot{\mathbf{\Xi}}^p = \beta^{\text{eff}} \left[\exp\left(\alpha^{\text{eff}}\left(\Sigma_1^e - \sigma_0^{\text{eff}}\right)\right) - \exp\left(-\alpha^{\text{eff}}\sigma_0^{\text{eff}}\right)\right] \mathbf{n} \tag{2.141}$$

guarantees that the homogenized problem will exhibit the correct flow stress.

The homogenized solution is obtained by implementing the macroscale constitutive relations (2.133) and (2.141) with the parameters taken as a function of microstructure through the relations (2.133) and (2.140). It is noted that the volume average of the strain-rate is input to the homogenized model from the microscale simulations. Thus, the fact that $r_{\dot{\epsilon}} \leq 1$ is naturally taken into account in matching the flow stress. However, the macroscopic strain-rate will generally be different than

the volume average of the microscale strain-rate.

As an example, the parameters corresponding to the specimen with $D_B = 0.5D_A$ are used in the homogenized problem. The stress-strain responses of the microscale and homogenized calculations are plotted in figure 2.7a. An error is defined as $\frac{\left|\Sigma_1^{\text{hom}} - \Sigma_1(\boldsymbol{\sigma})\right|}{\sigma_0'}$ and plotted in figure 2.7b. Although good agreement is seen in the stress-strain response, the error plot shows a localized maximum error in the predicted stress of $\approx 10\%$ of the microscale flow resistance.

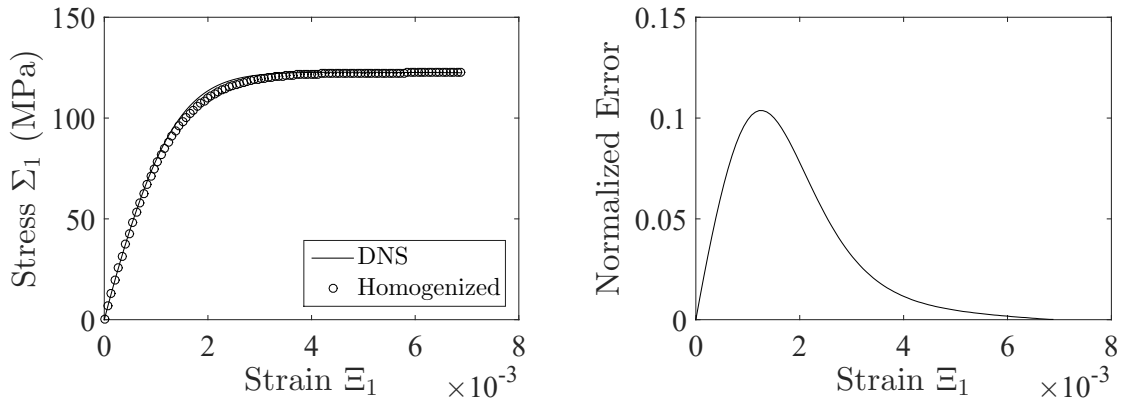

(a) (b)

Figure 2.7: (a) Comparison of stress-strain response from classical parametric homogenization with microscale results, (b) error in units of the parameter σ_0 for the homogenized problem.

This error could be corrected locally, for example, by matching the yield stress in the homogenization procedure. However, this flexibility in the parametrization is

evidence that the values of the parameters in the polynomial fit to the DNS flow stress are not determined uniquely from the underlying physics of the problem. This implies that the parametrization of $\alpha^{\text{eff}}(D_B)$, $\beta^{\text{eff}}(D_B)$, and $\sigma_0^{\text{eff}}(D_B)$ is dependent on the choice of what characteristics of the DNS stress-strain profile (flow stress, initial yield, etc.) are to be be used in calibrating parameters (3 in this case). The homogenized constitutive law will thus depend on this choice.

Furthermore, writing the homogenized constitutive relations in terms of the average quantities enforces a lower bound on the error that is related to how well the macroscale behavior can be represented by an homogeneous effective medium. That is, it may not be possible to parametrize the macroscale constitutive relations to qualitatively match the microscale behavior, leading to some amount of error that cannot be eliminated. To circumvent this limitation, it is necessary to include other macroscale variables to capture the microscale behavior. In the following sections, a natural choice for these additional variables is described within the DEHF. Choosing an appropriate set of these variables leads to macroscale constitutive relations that approximate the microscale behavior to numerical precision, since the macroscale behavior can be made to match the microscale behavior qualitatively and quantitatively in the limit. The results of this section can be compared to the results of the DEHF analysis in section 2.7.3.3, where it is shown that the agreement with the microscale flow stress is a natural outcome of the macroscale development, rather than an input

to the process. First, details of the DEHF procedure for this problem are examined.

2.7.3 DEHF Solution of the Geometry-Induced Variation in Stress Field

Application of the DEHF to the microscale problem in Section 2.7.1 is considered, where the material parameters are uniform, but the geometry induces non-uniform microscale mechanical fields. The radius of the circular cross-section of the bar is a function of the longitudinal position x, given as $r(x) = R + r - \sqrt{R^2 - x^2}$. The cross-sectional area is a function of longitudinal position $x \in [-L/2, L/2]$, given as

$$A(x) = \pi \left(R + r - \sqrt{R^2 - x^2} \right) \tag{2.142}$$

Assuming that the stress is uniaxial and constant through the circular cross-section, the stress field is characterized by a scalar variable $\sigma(x,t) = \sigma_{22}(x,t)$, and the macroscale stress from equation (2.109) is:

$$\Sigma_1(t) = \frac{1}{|\Omega|} \int_L \sigma(x,t) A(x,t) \, dL \tag{2.143}$$

From equilibrium, the force $f(x,t) = \sigma(x,t) A(x,t) = f(t)$ is constant through the length of the bar, so that

$$\Sigma_1(t) = \frac{L}{|\Omega|} \sigma(x,t) A(x,t) \tag{2.144}$$

Thus, the microscale stress can be written as a function of the position through the inverse area,

$$\sigma(x,t) = \Sigma_1(t) A^{-1}(x) \frac{|\Omega|}{L} \tag{2.145}$$

Assuming negligible changes in the cross-sectional area, the stress-rate is the time derivative of equation (2.145),

$$\dot{\sigma}(x,t) = \mu_{\dot{\sigma}}^1(t) A^{-1}(x) \frac{|\Omega|}{L} \tag{2.146}$$

The effects of the inhomogeneous microscale stress due to the specimen geometry on the evolution of the stress moments can be evaluated using equations (2.109) and (2.145). The effects of this heterogeneity under various loading conditions is considered in the following sections.

First, the relation between an applied displacement and the corresponding volume-averaged strain-rate is examined. The average strain-rate, taken over the length of the bar, is

$$\begin{aligned}
\dot{\boldsymbol{\epsilon}}_L =& \frac{1}{L}\int_L \dot{\boldsymbol{\epsilon}}(x)\, dL \\
=& \frac{1}{L}\int_\Omega \left[\mathbb{S} : \dot{\boldsymbol{\sigma}}(x) + \dot{\boldsymbol{\epsilon}}^p(x)\right] A^{-1}(x)\, dV \\
=& \mathbb{S} : \dot{\Sigma}_1 \mu_{A^{-2}}^2 \left(\frac{|\Omega|}{L}\right)^2 \mathbf{I}^{(2)} + \sum_{j=1}^{k} \left.\frac{\partial^{j-1}\mathbf{h}^p}{\partial \boldsymbol{\sigma}^{j-1}}\right|_{\boldsymbol{\sigma}=\mathbf{0}} \mu_{\boldsymbol{\sigma}}^j \left(\Sigma_1\right)^{-1}
\end{aligned} \tag{2.147}$$

where substitutions have been made from equations (2.145), (2.146), and (2.46). The

volume average of the strain-rate, on the other hand, is

$$\mu^1_{\dot{\boldsymbol{\epsilon}}} = \frac{1}{|\Omega|}\int_\Omega \dot{\boldsymbol{\epsilon}}\,(x)\,dV = \mathbb{S} : \dot{\Sigma}_1 + \sum_{j=1}^{k} \left.\frac{\partial^j \mathbf{h}^p}{\partial \boldsymbol{\sigma}^j}\right|_{\boldsymbol{\sigma}=\mathbf{0}} \mu^j_{\boldsymbol{\sigma}}\,(\Sigma_1)^{-1} \tag{2.148}$$

which can be written as:

$$\begin{aligned}\mu^1_{\dot{\boldsymbol{\epsilon}}} =& \mathbb{S} : \dot{\Sigma}_1 \mu^2_{A^{-2}} \left(\frac{|\Omega|}{L}\right)^2 + \sum_{j=1}^{k} \left.\frac{\partial^{j-1} \mathbf{h}^p}{\partial \boldsymbol{\sigma}^{j-1}}\right|_{\boldsymbol{\sigma}=\mathbf{0}} \mu^j_{\boldsymbol{\sigma}}\,(\Sigma_1)^{-1} \\ &\times \left[\mathbb{S} : \dot{\Sigma}_1 \mathbf{I}^{(2)} + \sum_{j=1}^{k} \left.\frac{\partial^j \mathbf{h}^p}{\partial \boldsymbol{\sigma}^j}\right|_{\sigma=\mathbf{0}} \mu^j_{\boldsymbol{\sigma}}\,(\Sigma_1)^{-1}\right]^{-1} \dot{\boldsymbol{\epsilon}}_L\end{aligned} \tag{2.149}$$

This expression allows the displacement-control of the microscale DNS to be translated into the average strain-rate control of the homogenized simulation.

2.7.3.1 Elastic Response

For a purely elastic response, substituting the expressions (2.145) and (2.146) into equation (2.110) yields

$$\frac{d}{dt}\mu^k_\sigma = k\left(\mu^1_\sigma\right)^{k-1}\left(\frac{|\Omega|}{L}\right)^k \mu^k_{A^{-1}}\mu^1_{\dot{\sigma}}\,(t) \tag{2.150}$$

This system of differential equations has the form:

$$\frac{d}{dt}\left[\mu_\sigma\right] = \mathrm{v}\,(t) \tag{2.151}$$

where the vector $\mathrm{v}\,(t)$ can be explicitly formulated. For constant strain rate elastic loading, the rate form of the constitutive relation

$$\dot{\boldsymbol{\sigma}} = \mathbb{C} : (\dot{\boldsymbol{\epsilon}} - \dot{\boldsymbol{\epsilon}}^p) \tag{2.152}$$

where $\dot{\boldsymbol{\epsilon}}$ is the total strain-rate and $\dot{\boldsymbol{\epsilon}}^p$ is the plastic strain-rate, reduces to

$$\dot{\boldsymbol{\sigma}} = \mathbb{C} : \dot{\boldsymbol{\epsilon}} \rightarrow \boldsymbol{\sigma} = \mathbb{C} : \dot{\boldsymbol{\epsilon}} t \tag{2.153}$$

Substituting equation (2.153) into equation (2.150), yields

$$\frac{d}{dt}\mu_\sigma^k = k t^{k-1} E^k \circ \left(\mu_{\dot{\epsilon}}^1\right)^k \left(\frac{|\Omega|}{L}\right)^k \mu_{A^{-1}}^k \tag{2.154}$$

where $\dot{\epsilon}(x,t) = \dot{\epsilon}_{22}(x,t)$. From equation (2.149), the constant volume-averaged strain rate is $\mu_{\dot{\epsilon}}^1 = \mu_{A^{-2}}^2 \left(\frac{|\Omega|}{L}\right)^2 \dot{\epsilon}_L$, and equation (2.154) can be integrated to obtain:

$$\mu_\sigma^k(t) = t^k E^k \left(\mu_{\dot{\epsilon}}^1\right)^k \left(\frac{|\Omega|}{L}\right)^k \mu_{A^{-1}}^k \tag{2.155}$$

The stress contour computed by the DNS for the microscale problem with $D_B = 0.8D_A$, $E = 100$GPa, and $\nu = 0.3$, is shown in Figure 2.8a.

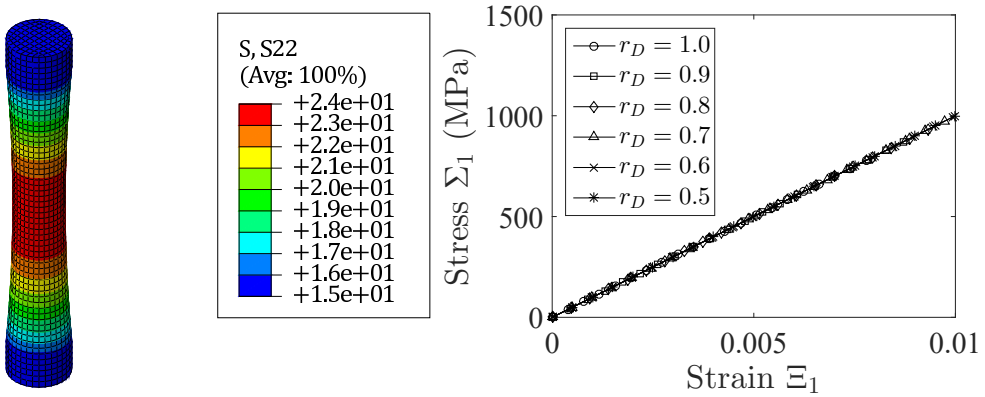

(a) (b)

Figure 2.8: Results of the microscale simulation of the elastic response: (a) stress contour at $\Xi_1 = 0.01$ for $D_B = 0.8D_A$, (b) stress-strain plot for different diameter ratios.

In figure 2.8b, the stress-strain response for the microscale simulations are shown for a range of values of D_B. The effective modulus is independent of the microstructure, as expected. For the homogenized response, the average stress μ^1_σ is considered. From equation (2.155),

$$\mu^1_\sigma = tE\mu^1_\epsilon \frac{|\Omega|}{L}\mu^1_{A^{-1}} = tE\mu^1_\epsilon \tag{2.156}$$

where the relation $\mu^1_{A^{-1}} = \frac{L}{|\Omega|}$ implies the second equality in equation (2.156). Thus, the average stress is given exactly by a homogenized constitutive law of order one. The DNS results are compared to the order-one DEHF solution in figure 2.9. The agreement is very good, with errors on the order of numerical precision.

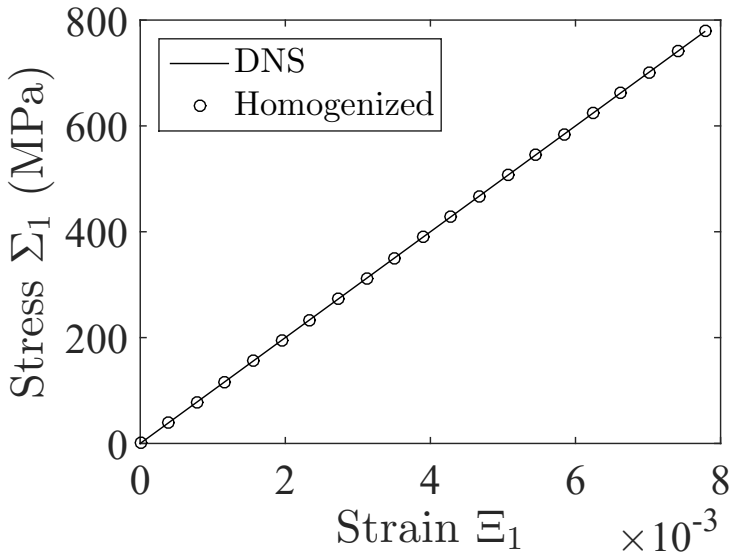

Figure 2.9: Stress-strain response for elastic loading from the microscale DNS and the homogenized macroscale simulations corresponding to the microstructure with $D_B = 0.5D_A$.

2.7.3.2 Stress Relaxation Test

In the stress-relaxation test, the total strain ϵ_L is held constant. For a non-evolving strain, the k-th moment of σ decays from its initial value of $\mu_\sigma^k(t=0) = \left(\mu_\sigma^1(t=0)\right)^k \mu_{A^{-k}}^k \left(\mu_{A^{-1}}^1\right)^{-k}$ at a rate

$$\frac{d}{dt}\mu_\sigma^k = -k\mu_{\sigma^{k-1}}^{k-1} E\dot{\Xi}_1^p \tag{2.157}$$

where $\dot{\Xi}_1^p = \left(\dot{\boldsymbol{\Xi}}_1^p\right)_{22}$. The plastic part of the constitutive relation relates the rate of plastic strain to the stress through $\mathbf{h}^p(\boldsymbol{\sigma})$, for which the moment expansion of $\mathbf{h}^p$ about $\boldsymbol{\sigma} = \mathbf{0}$ is constructed to obtain,

$$\frac{d}{dt}\mu_\sigma^k = -k\mu_{\sigma^{k-1}}^{k-1} E \sum_{j=0}^{\infty} \frac{1}{j!} \left.\frac{d^j h^p}{d\sigma^j}\right|_{\sigma=0} \mu_{\sigma^j}^j = -kE \sum_{j=1}^{\infty} \frac{1}{j!} \left.\frac{d^j h^p}{d\sigma^j}\right|_{\sigma=0} \circ \mu_\sigma^{j+k-1} \tag{2.158}$$

where $h^p = (\mathbf{h}^p)_{22}$. Define an array of moment variables as:

$$[\mu_\sigma] = [\mu_\sigma^1 \mu_\sigma^2 \cdots \mu_\sigma^n]^{\mathrm{T}} \tag{2.159}$$

If the moment expansion is truncated at order-n, the evolution of the array of moment variables can be written as a matrix equation as:

$$\frac{d}{dt}[\mu_\sigma] = -E \begin{bmatrix} a_1 & a_2 & \cdots\cdots\cdots & a_n \\ 0 & 2a_1 & 2a_2 & \cdots\cdots & 2a_n \\ 0 & 0 & 3a_1 & 3a_2 & \cdots & 3a_n \\ \cdots & \cdots & \cdots & \cdots & \cdots & \cdots \\ 0 & 0 & 0 & 0 & 0 & na_n \end{bmatrix} [\mu_\sigma] = A[\mu_\sigma] \tag{2.160}$$

where $a_j = \frac{d^j h^p}{d\sigma^j}\Big|_{\sigma=0}$. The solution to this system of linear ODEs is obtained in the closed form:

$$[\mu_\sigma] = \exp(At)\,[\mu_\sigma]_{t=0} \tag{2.161}$$

The microscale DNS is carried out in ABAQUS Standard. The parameters are $\beta = 1\text{s}^{-1}$, $\alpha = 0.01MPa^{-1}$, $\sigma_0 = 100MPa$, $E = 100GPa$, and $\nu = 0.3$ with the boundary condition $u = \pm 0.003$cm at the bar ends. The contour of the stresses at time $t = 0.01$s is plotted in figure 2.10a. The stress history is plotted for the microscale DNS in figure 2.10b.

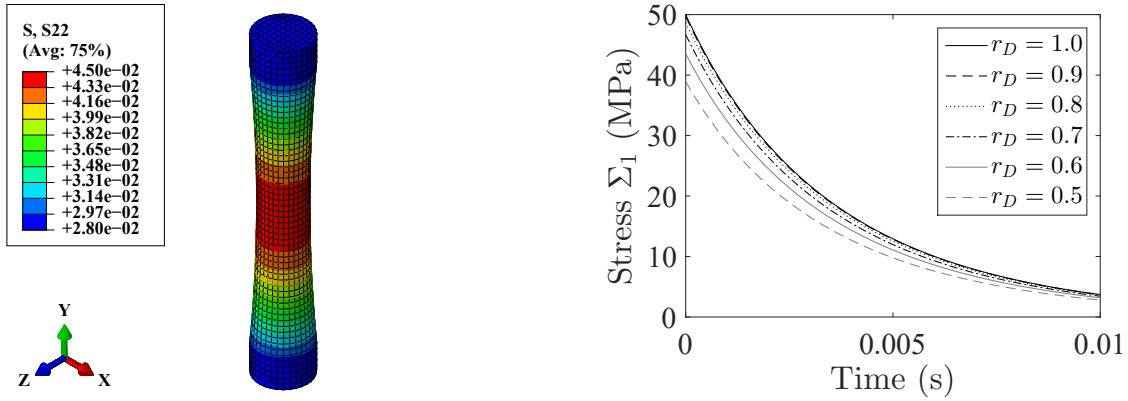

(a) (b)

Figure 2.10: Stress-strain response for a stress relaxation test based on the microscale DNS, (a) stress contour at $t = 0.01$, (b) stress-time plot for different diameter ratios.

The DNS results are compared with the homogenized solution in figure 2.11a. The results of the tenth-order homogenization and the DNS agree very well, indicating

that the macroscale response is well-characterized by a finite subset of the spectrum of relaxation times represented by the values in the matrix A appearing in (2.161).

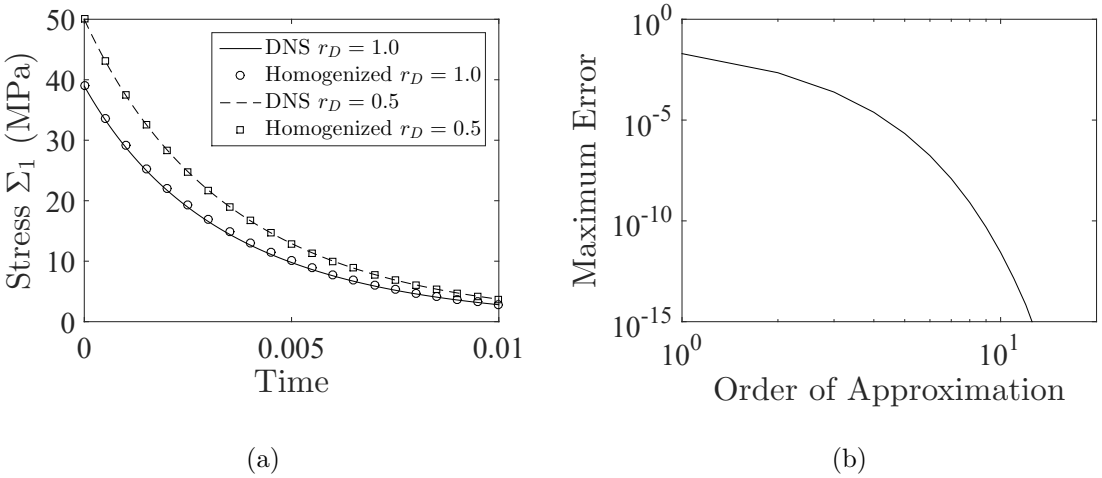

(a) (b)

Figure 2.11: Results of the macroscale stress relaxation simulation in DEHF: (a) Comparison of the microscale DNS and DEHF macroscale stress-strain response corresponding to the microstructures with $D_B = D_A$ and $D_B = 0.5D_A$; (b) convergence of the moment approximations for the DEHF macroscale simulation.

Convergence of the homogenized response with respect to the order of the approximation is shown in figure 2.11b. The maximum error is defined as the maximum difference between the stress Σ_1 for an expansion of order k and an expansion of order 21, for which the results of the approximation are found not to change with increasing k within the accepted machine tolerance. This figure also clearly indicates that the error associated with approximating the macroscopic response by an homogeneous

effective medium–as in the order 1 approximation–can be mitigated by including a higher-order moment representation of the microscale heterogeneity. The magnitude of the error for a given order of approximation is problem-specific, but analysis of the DEHF approximation such as that in equation (2.161) can be used to gauge the contribution of the terms of an order k to determine a cutoff in the number of terms corresponding to a given level of accuracy.

2.7.3.3 Uniaxial Tension Test

A uniaxial tension test is simulated in this example. For the microscale DNS, the discretized bars are loaded at a constant longitudinal strain rate $\dot{\epsilon}_L$ in a way that the ends remain planar and parallel throughout the simulation. The stress contour of $(\Sigma_1)_{22}$ at the final strain $\epsilon_L = 0.01$ is plotted for a diameter ratio $D_B = 0.5D_A$ in figure 2.12a. The stress-strain responses for various gauge diameters are plotted in figure 2.12b.

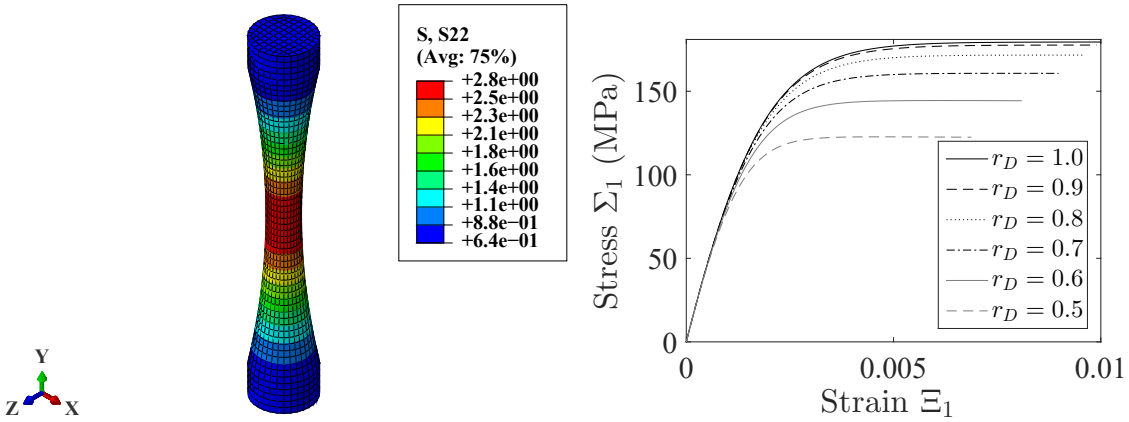

(a) (b)

Figure 2.12: Stress-strain response for a uniaxial tension test based on the microscale DNS: (a) stress contour and (b) stress-strain plot for different diameter ratios.

The stress value for any given strain decreases monotonically with decreasing gauge diameter, leading to the inference that heterogeneity in mechanical fields enhances the plasticity in this test. To quantitatively analyze this observation, the first moments in equation (2.152) are expressed as:

$$\mu_{\dot{\sigma}}^1 = E\left(\mu_{\dot{\epsilon}}^1 - \mu_{\dot{\epsilon}^p}^1\right) \tag{2.162}$$

Substituting equation (2.162) into equation (2.150) yields,

$$\begin{aligned}\frac{d}{dt}\mu_\sigma^k =& k\left(\frac{|\Omega|}{L}\right)^k \mu_{A^{-1}}^k \left(\mu_\sigma^1\right)^{k-1} E\left(\mu_{\dot{\epsilon}}^1 - \mu_{\dot{\epsilon}^p}^1\right) \\ =& k\left(\frac{|\Omega|}{L}\right)^k \mu_{A^{-1}}^k \left(\mu_\sigma^1\right)^{k-1} E\mu_{\dot{\epsilon}}^1 - k\left(\frac{|\Omega|}{L}\right)^k \mu_{A^{-1}}^k \left(\mu_\sigma^1\right)^{k-1} E\mu_{\dot{\epsilon}^p}^1\end{aligned} \tag{2.163}$$

Equation (2.163) is a combination of results in the previous sections, i.e.

$$\frac{d}{dt}[\mu_\sigma] = \mathrm{A}\left[\mu_\sigma\right] + \mathrm{v}\left(t\right) \tag{2.164}$$

The solution of this system of equations is

$$[\mu_\sigma] = \exp(\mathrm{A}t)\left([\mu_\sigma]_{t=0} + \int_0^t \exp(-\mathrm{A}\tau)\,\mathrm{v}(\tau)d\tau\right) \tag{2.165}$$

With the eigen-decomposition $\mathrm{A} = \mathrm{PDP}^{-1}$, where P is a matrix of columns of the eigenvectors of A and D is a diagonal matrix of the corresponding eigenvalues, the solution can be rewritten as:

$$[\mu_\sigma] = \exp(\mathrm{A}t)\,[\mu_\sigma]_{t=0} + \mathrm{P}\exp(\mathrm{D}t)\int_0^t \exp(-\mathrm{D}\tau)\,\mathrm{P}^{-1}\mathrm{v}(\tau)d\tau \tag{2.166}$$

The solution to the macroscale problem can be obtained by numerical approximation of the integral in (2.166). In this study, however, the more general approach of applying the scheme in 2.6.2 is used. From equation (2.126), it can be seen that the expense of the macroscale update algorithm is governed by the inversion of a matrix of size $k \times k$ for an approximation of order k.

The tenth-order moment approximation is compared to the DNS results in figure 2.13a, where it is seen that the macroscale DEHF results are in very good agreement with the macroscale average of the DNS results. The convergence profile is plotted in figure 2.13b.

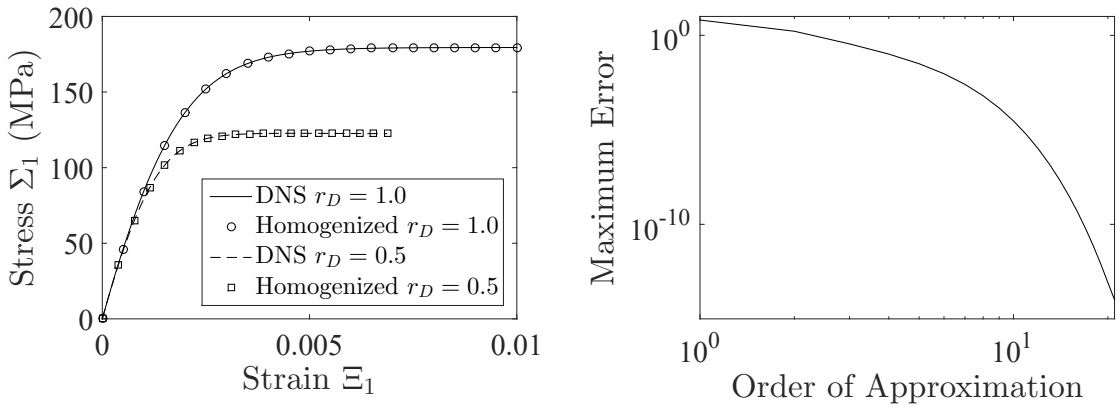

(a) (b)

Figure 2.13: Results of macroscale tension test simulations: (a) Comparison of macroscale stress-strain response for $D_B = D_A$ and $D_B = 0.5D_A$ generated by microscale DNS and the DEHF simulations. (b)convergence of the moment approximations for the DEHF simulations.

The flow stress, required as an input for the macroscale simulations with the parametric homogenization procedure in section 2.7.2, can be easily obtained from the results of the macroscale DEHF simulations. The normalized flow stress is plotted as a function of the normalized gauge diameter in figure 2.14.

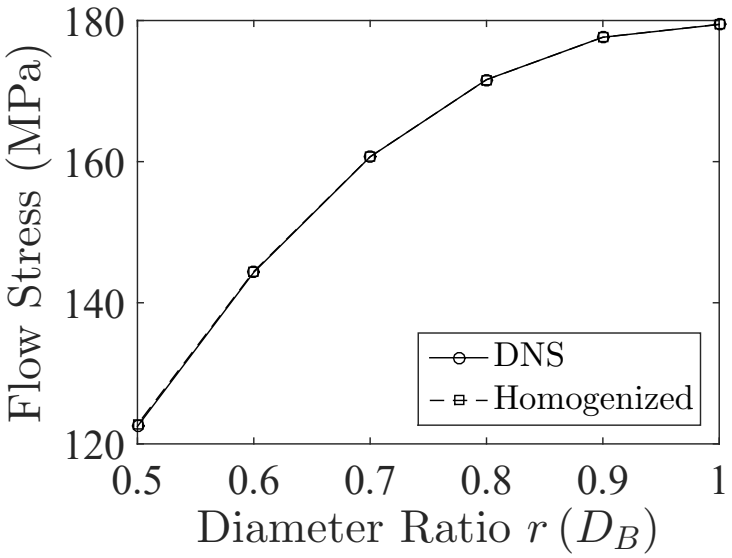

Figure 2.14: Flow stress as a function of normalized gauge diameter D_B in units of D_A.

The agreement between the flow stresses in the DEHF and DNS simulations is very good. More important, this agreement is a natural outcome of the homogenization process, i.e. the matching of a particular feature of a stress-strain profile like those plotted in the figure is a result of approximating the correct macroscale constitutive relations.

2.7.4 DEHF Solution of the Material-Induced Variation in Stress Field

The distribution-enhanced homogenization framework is next applied to a microscale problem with heterogeneity in material properties. Consider the tensile bar of section 2.7.1, with $D_B = D_A = 2.0cm$, but with E and ν in equation (2.70) and σ_0 in equation (2.77) varying along the length of the bar. The microstructures are numerically generated according to the formula

$$q(y) = \text{erf}^{-1}\left(\text{erf}\left(\frac{1}{\sqrt{2}}\right)\frac{y}{L/2}\right)\sqrt{2\hat{\mu}_q^2} + \mu_q^1 \tag{2.167}$$

where the variable y corresponds to the location along the length of the bar, or the centroid of each element in the microscale discretization, and $q = E, \sigma_0$. This choice is essentially arbitrary except for its general nonlinearity. It corresponds to values of the density function for a normal distribution $\mathcal{N}\left(\mu_q^1, \sqrt{\hat{\mu}_q^2}\right)$ on the interval $\left(\mu_q^1 - \sqrt{\hat{\mu}_q^2}, \mu_q^1 + \sqrt{\hat{\mu}_q^2}\right)$. The Poisson's ratio ν is given in terms of E as $\nu(y) = \mu_\nu^1 \frac{E(y)}{\mu_E^1}$ to ensure $\epsilon_{11}^e(y) = \epsilon_{33}^e(y) = -\mu_\nu^1 \mu_{\epsilon_{22}^e}^1$. Thus, the parameters that characterize this microstructure are μ_E^1, $\hat{\mu}_E^2$, μ_ν^1, $\mu_{\sigma_0}^1$, and $\hat{\mu}_{\sigma_0}^2$. For comparison of the results, the characteristic ratios are defined as:

$$r_E = \frac{\hat{\mu}_E^2}{\left(\mu_E^1\right)^2} \quad \text{and} \quad r_{\sigma_0} = \frac{\hat{\mu}_{\sigma_0}^2}{\left(\mu_{\sigma_0}^1\right)^2} \tag{2.168}$$

Figures 2.15(a,b) show the variation in the properties along the length of the specimen for $r_E = r_{\sigma_0} = 0.5$.

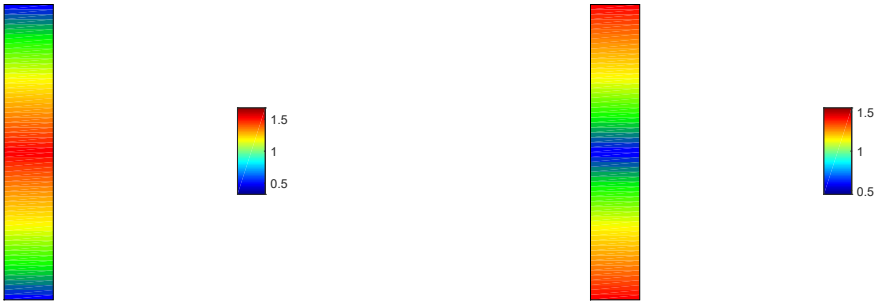

(a) (b)

Figure 2.15: Contours of microscale modulus and flow resistance fields for $r_E = r_{\sigma_0} = 0.5$: (a) modulus and (b) flow resistance. The color maps indicate the values of the material parameters normalized by their averages.

Procedures described in section 2.7.1 are applied to the microscale BVPs with these microstructures, and the DEHF is used to provide macroscale results.

2.7.4.1 Elastic Response

Microscale simulations of the elastic response are performed for $\mu_E^1 = 100\text{GPa}$, $\mu_\nu^1 = 0.3$, and a range of r_E, with the results plotted in figure 2.16.

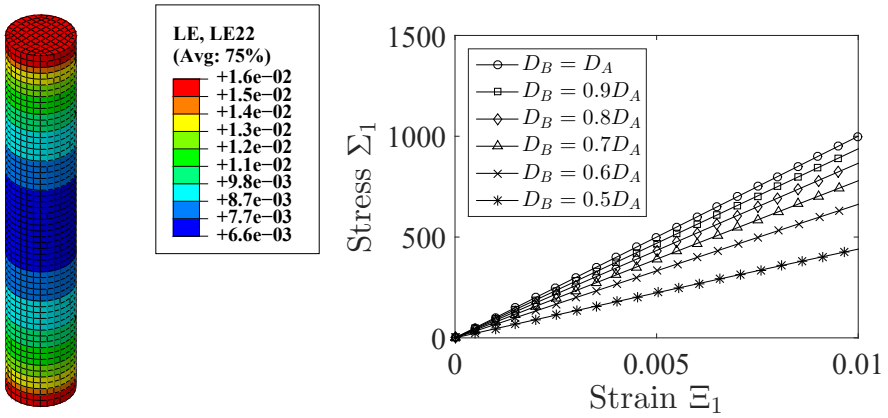

(a) (b)

Figure 2.16: Elastic response for microscale simulations with various values of r_E: (a) strain contour and (b) stress-strain plots.

Qualitatively, figure 2.16a shows that the strain is maximum at the ends of the bar where the stiffness is minimum, and figure 2.16b shows that the the stress decreases monotonically with increasing r_E. Homogenization of the elastic problem proceeds by determining the appropriate $\mathbb{C}^{\text{eff}}$. For elastic loading, the rate form of the linear elastic constitutive relation $\dot{\boldsymbol{\epsilon}}^e = \mathbb{C}^{-1} : \dot{\boldsymbol{\sigma}}$ along with the equilibrium condition that $\boldsymbol{\sigma}$ is uniform throughout the bar, i.e. $\dot{\boldsymbol{\sigma}}(x) = \mu^1_{\dot{\boldsymbol{\sigma}}}$ yields the relation:

$$\dot{\boldsymbol{\epsilon}}^e = \mathbb{C}^{-1} : \mu^1_{\dot{\boldsymbol{\sigma}}} \tag{2.169}$$

The first moment of the elastic strain may be written as:

$$\mu^1_{\dot{\boldsymbol{\epsilon}}^e} = \mu^1_{\mathbb{C}^{-1}} : \mu^1_{\dot{\boldsymbol{\sigma}}} \tag{2.170}$$

The inverse relation $\mu^1_{\dot{\boldsymbol{\sigma}}} = \left(\mu^1_{\mathbb{C}^{-1}}\right)^{-1} : \mu^1_{\dot{\boldsymbol{\epsilon}}^e}$ results in the effective modulus

$$\mathbb{C}^{\text{eff}} = \left(\mu^1_{\mathbb{C}^{-1}}\right)^{-1} \tag{2.171}$$

The macroscale problem is simulated using this effective modulus, and the results are compared to the microscale results in figure 2.17, showing excellent agreement.

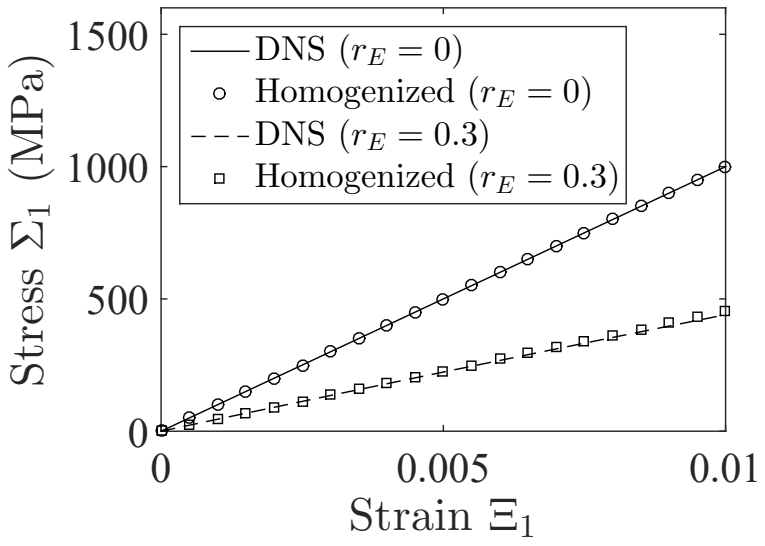

Figure 2.17: Comparison of the elastic response for the microscale and DEHF based macroscale simulations for various distributions of the modulus E.

Additionally, the modulus estimated from the microscale simulations is compared to the value determined by equation (2.171) in figure 2.18.

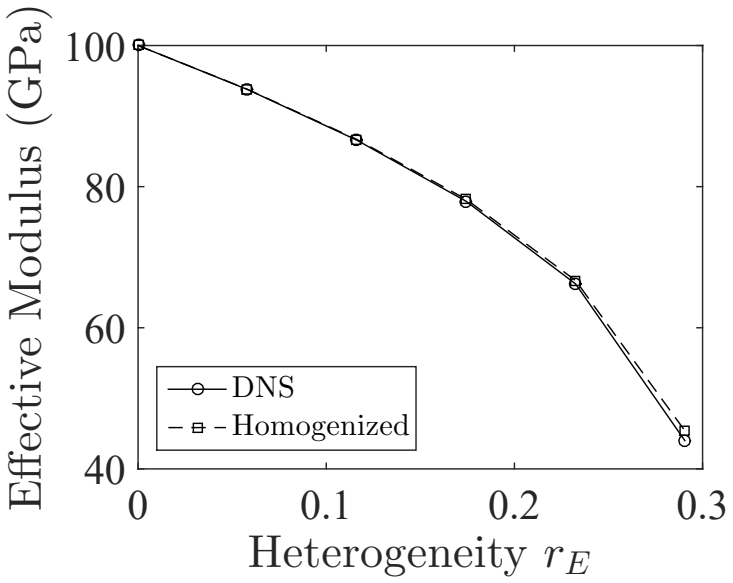

Figure 2.18: Effective modulus as a function of the heterogeneity in the local modulus represented through r_E.

2.7.4.2 Elasto-Viscoplastic Response

The elasto-viscoplastic microscale problem is simulated next for a range of r_{σ_0} with $r_E = 10^{-2}$ and the microscale stress-strain responses are plotted in figure 2.19.

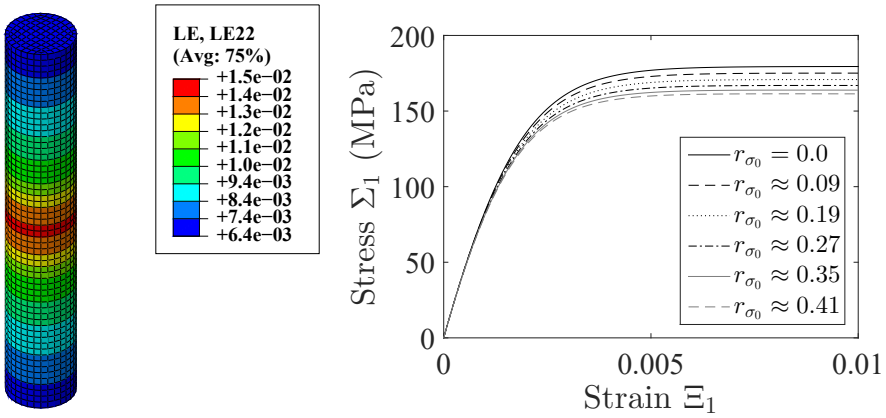

(a) (b)

Figure 2.19: Microscale stress-strain response for various values of r_{σ_0}: (a) strain contour for $r_{\sigma_0} = 0.06$ at $\Xi_1 = 0.01$, and (b) stress-strain plots.

In contrast to the elastic case, the strain is now maximum at the center of the bar where the flow resistance is minimum. The heterogeneity in the flow resistance parameter σ_0 has the effect of enhancing plasticity in the domain, causing the stress to decrease monotonically with increasing r_{σ_0} for a fixed value of $\mu^1_{\sigma_0}$. In deriving the DEHF models, it is noted that for the general elasto-viscoplastic case, the stress-rate may be written in terms of the total and plastic strain-rates as:

$$\mu^1_{\dot{\boldsymbol{\sigma}}} = \left(\mu^1_{\mathbb{C}^{-1}}\right)^{-1} : \mu^1_{\dot{\boldsymbol{\epsilon}}} - \left(\mu^1_{\mathbb{C}^{-1}}\right)^{-1} : \mu^1_{\dot{\boldsymbol{\epsilon}}^p} \tag{2.172}$$

From the averaging theorem (2.46), the expression for the first moment of the plastic strain rate is:

$$\mu^1_{\dot{\boldsymbol{\epsilon}}^p} = \sum_{k=0}^{\infty} \frac{1}{k!} \sum_{j=0}^{k} \mu^k_{\boldsymbol{\sigma}^j \sigma_0^{k-j}} \left. \frac{\partial^k \mathbf{h}^p}{\partial \boldsymbol{\sigma}^j \partial \sigma_0^{k-j}} \right|_{\boldsymbol{\sigma}=\mathbf{0}, \sigma_0=0} \tag{2.173}$$

which in a simplified form is:

$$\mu^1_{\dot{\boldsymbol{\epsilon}}^p} = \sum_{k=0}^{\infty} \frac{1}{k!} \sum_{j=0}^{k} \left(\mu^1_{\sigma}\right)^j \mu^{k-j}_{\sigma_0} \left. \frac{\partial^k \mathbf{h}^p}{\partial \boldsymbol{\sigma}^j \partial \sigma_0^{k-j}} \right|_{\boldsymbol{\sigma}=\mathbf{0},\sigma_0=0} \tag{2.174}$$

Substituting from the microscale plastic constitutive relation (2.79),

$$\mu^1_{\dot{\boldsymbol{\epsilon}}^p} = \sum_{k=0}^{\infty} \frac{1}{k!} \sum_{j=1}^{k} \left(\mu^1_{\boldsymbol{\sigma}}\right)^j \mu^{k-j}_{\sigma_0} \, \alpha^j \left(-\alpha\right)^{k-j} \beta \exp\left(\alpha\left(\sigma^e - \sigma_0\right)\right) \mathbf{n}^k \Big|_{\boldsymbol{\sigma}=\mathbf{0},\sigma_0=0} \tag{2.175}$$

reduces to

$$\mu^1_{\dot{\boldsymbol{\epsilon}}^p} = \sum_{k=0}^{\infty} \frac{1}{k!} \sum_{j=1}^{k} \left(\mu^1_{\boldsymbol{\sigma}}\right)^j \mu^{k-j}_{-\sigma_0} \alpha'^k \beta = \sum_{k=1}^{n} \sum_{j=1}^{k} B_{kj} w_j \tag{2.176}$$

where

$$B_{kj}\left(\mu^{i-j}_{\sigma_0}\right) = \frac{\alpha'^k \beta}{k!} \mu^{k-j}_{-\sigma_0} \quad \text{and} \quad w_j\left(\mu^1_{\boldsymbol{\sigma}}\right) = \left(\mu^1_{\boldsymbol{\sigma}}\right)^j \tag{2.177}$$

The macroscale stress-rate corresponding to the first moment of the microscale stress-rate is then written as

$$\mu^1_{\dot{\boldsymbol{\sigma}}} = \mathbb{C}^{\text{eff}} : \left[\mu^1_{\dot{\boldsymbol{\epsilon}}} - \sum_{i=1}^{k} \sum_{j=1}^{i} B_{ij} w_j\right] \tag{2.178}$$

and the evolution of the higher-order moments is

$$\frac{d}{dt}\mu^k_{\boldsymbol{\sigma}} = k\left(\mu^1_{\boldsymbol{\sigma}}\right)^{k-1} \mu^1_{\dot{\boldsymbol{\sigma}}} \tag{2.179}$$

The microscale DNS and macroscale homogenized stress-strain responses are plotted in figure 2.20 showing excellent agreement.

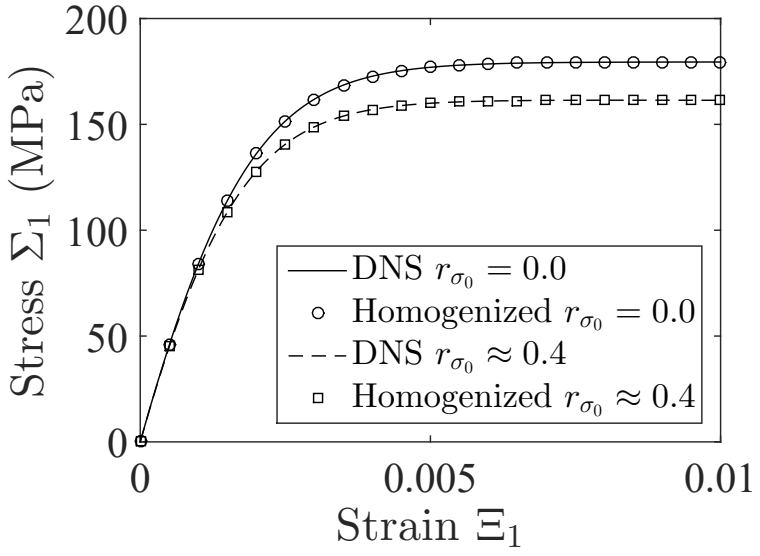

Figure 2.20: Stress-strain response for a uniaxial tension test based on the microscale DNS and the DEHF macroscale simulations.

The flow stress is plotted as a function of the normalized second moment of the flow resistance in figure 2.21. The DEHF based simulations again produce a good estimate of the macroscale flow stress without any fitting of the microscale response.

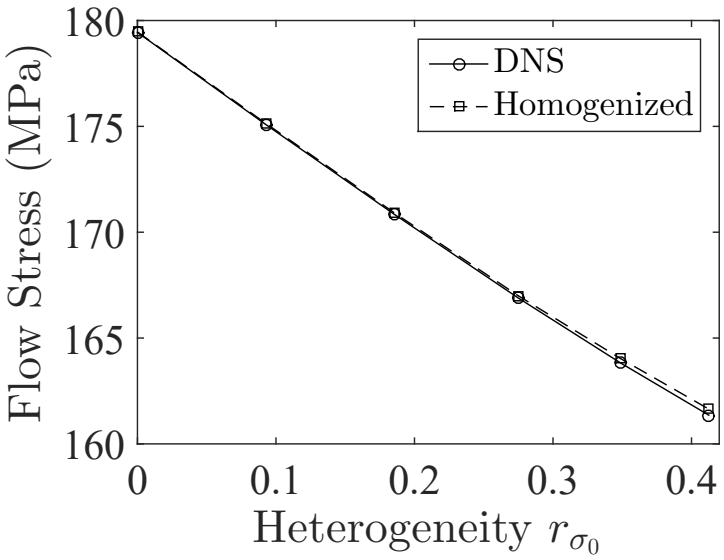

Figure 2.21: Flow stress as a function of the heterogeneity in flow resistance, measured as the normalized magnitude of the second central moment of that quantity.

2.8 Observations From DEHF Theory and Application to Example Problems

The DEHF-based results in these examples may be summarized with the following major observations.

1. Constitutive parameters from the microscale are used directly in the DEHF, so no separate calibration is required for the macroscale problem.

2. In DEHF, the homogenized response approximates the microscale behavior,

rather than being constructed to match certain features such as the flow stress of the macroscale response.

3. In some cases, DEHF naturally leads to closed-form analytical series solutions that can be well-approximated numerically in an homogenized macroscale setting.

4. The parameters required for parametric homogenization can be obtained by postprocessing of the DEHF results, if desired.

5. Material and geometric nonlinearity are treated similarly in DEHF, as the theory handles microscale distributions of material properties and response variables in the same manner.

In this chapter, a new approach to hierarchical multi-scale modeling in the form of the *distribution-enhanced homogenization framework* or DEHF is proposed. The framework does not make any a priori assumption on the macroscale constitutive behavior being represented by a homogeneous effective medium theory. Instead, the evolution of macroscale variables are governed by the moments of microscale distribution of evolving field variables. The macroscale constitutive relations are formulated in terms of a series expansion that is based on the microscale constitutive relations and the moments (of arbitrary order) of microscale field variables. This approach demonstrates excellent accuracy in representing the microscale fields through their distributions. Also, an approximate characterization of the microscale heterogeneity

is accounted for explicitly in the macroscale constitutive behavior. Increasing the order of this approximation results in increased fidelity of the macroscale approximation of the microscale constitutive behavior.

In the following chapters, DEHF equations are developed to simulate the macroscopic constitutive behavior of a damaged material, for which the microscale constitutive behavior of the undamaged material is represented by the thermally-activated crystal plasticity formulation in [36]. This analysis extends the DEHF treatment of the flow rule (2.79) in this chapter to a physically meaningful form for dislocation glide on a three-dimensional geometry of slip systems. The microscale constitutive model is developed in Chapter 3, and the microscale behavior of the voided microstructure is analyzed directly with a unit cell micromechanics model in Chapter 4. The application of DEHF to this model is investigated in Chapter 5. Additionally, the relations that connect the higher-order macroscale variables depend on an evolving voided microstructure, extend the framework to handle a microstructural characterization which is not constant. The theory and application of a novel damage evolution model coupled to the DEHF macroscale constitutive behavior is presented in Section 5.3 at the end of Chapter 5.

Chapter 3

Tantalum Material Model

The material studied in the remainder of this work is body-centered cubic (BCC) tantalum. In this chapter, the microscale material model is developed in detail. This material model has an anisotropic thermo-elastic constitutive relation that exhibits cubic symmetry in the stress-strain relationship, and isotropy in the strain-temperature relationship. The mathematical details are given next, in Section 3.1. The tantalum material model also employs a nonlinear viscoplastic constitutive relation based on thermally-activated glide governed by a non-Schmid formulation of the effective resolved shear stress. The development of this novel formulation is presented in Sections 3.2, 3.3, 3.5, and 3.6. Additionally, a new hardening law in the crystal plasticity model governed by the evolution of dislocation densities is described in Section 3.7.

3.1 Thermoelasticity

The thermoelastic constitutive relation gives the second Piola-Kirchhoff stress referred to the intermediate configuration $\mathbf{T}^*$ in terms of the Green-Lagrange strain in the same configuration $\mathbf{E}^*$ as:

$$\mathbf{T}^* = \mathbb{L} : (\mathbf{E}^* - \alpha\theta\mathbf{I}) \tag{3.1}$$

Here, $\mathbb{L}$ is the temperature-dependent elasticity tensor, α is the coefficient of thermal expansion, θ is the absolute temperature, and $\mathbf{I}$ is the second-rank identity tensor.

The temperature-dependence of the single crystal elastic response is modeled by fitting linear temperature dependence of the anisotropic moduli and isotropic thermal expansion to the data in [38]. The data and fits are shown in Figure 3.1. The elastic constants are given the temperature dependence:

$$C_{ij}(\theta) = C_{ij}^0 + m_{ij}\theta \tag{3.2}$$

where C_{ij}^0 is the modulus at 0K, θ is the temperature in Kelvin, and $ij = 11, 12, 44$. The coefficient of thermal expansion α is obtained via:

$$\rho(\theta) = \rho_0 (1 - \alpha\theta)^3 \tag{3.3}$$

where ρ_0 is the density of the material at 0 K. The fit of the parameter α in Equation (3.3) to the experimental data is shown in Figure 3.1d.

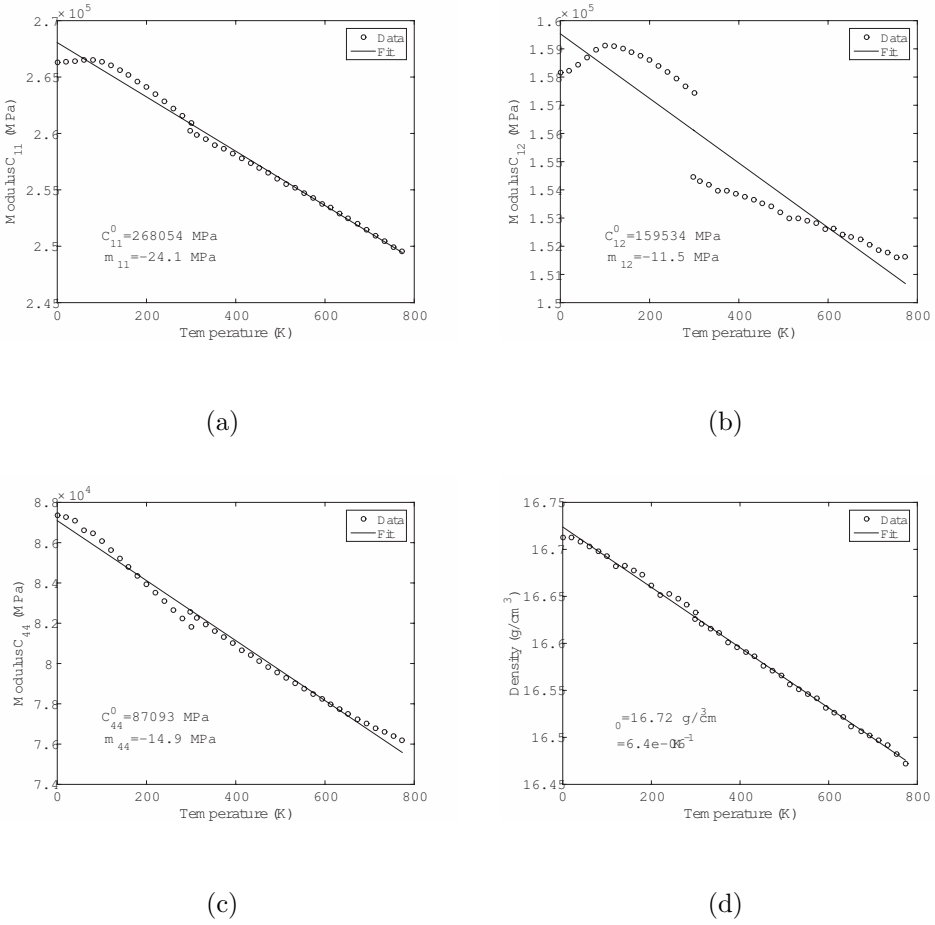

Figure 3.1: The thermoelastic material constants for tantalum.

3.2 Introduction to Slip Model

Deformation and ductile fracture of polycrystalline materials are complex processes involving various physical phenomena that are typically independently characterized across a hierarchy of disparate length and time scales. These characterizations depend on system parameters ranging from the local arrangement of atoms in the

crystal lattice to the orientation of the macroscopic loading path to the details of the structural configuration of the material. In order to model plasticity and failure in a robust and consistent way, a multiscale model must be developed to incorporate various characterizations of material behavior into a single coherent framework. As depicted in Figure 3.2, the slip behavior of atomistic systems can be transferred parametrically to a continuum crystal plasticity model of thermally activated slip that represents the atomistic behavior at each point.

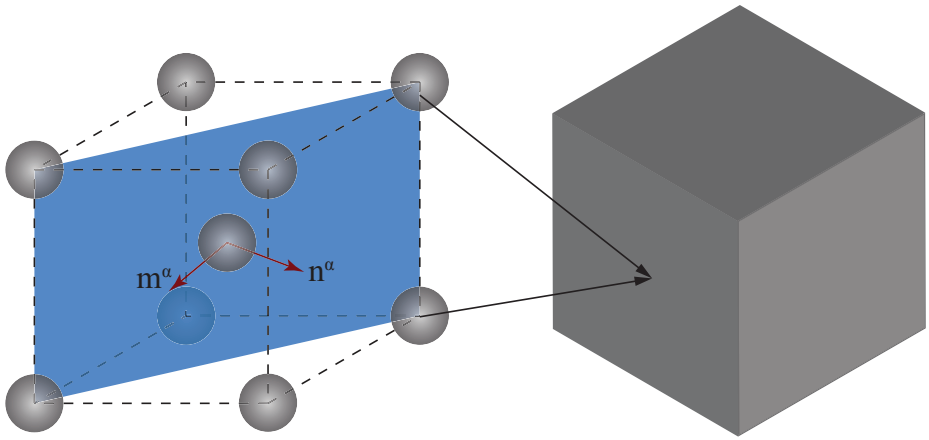

Figure 3.2: Information about slip is passed from the atomistic system to a continuum system as a parametric representation

By incorporating quantitative information from atomic-scale simulations into the crystal plasticity model, a more accurate, physics-based model can be derived. The atomic-scale characterization developed here includes effects on the critical resolved shear stress (CRSS) of body-centered cubic (BCC) Ta due to loading orientation, temperature, and strain rate.

The effect of loading orientation on plastic deformation of BCC metals has been a topic of significant interest to the research community dealing with deformation and damage in metals. The Schmid law has been conventionally used to characterize the dependence of the resolved shear stress on loading orientation in the form of a simple geometric formula [39]. While this law has been found to be widely applicable to face-centered cubic (FCC) materials, the relationship between the CRSS and the loading orientation suggested by the Schmid law is violated in BCC materials. This behavior has been attributed to the so-called non-Schmid effects, first observed experimentally by Taylor in his experiments [40, 41]. In the first paper [40], the orientation of shear bands in BCC iron was found to be dependent on the direction of the principal applied stress rather than the lattice orientation. In the second paper [41], an asymmetry was found in the resistance to shear when the sense of the shear was reversed in BCC brass. In general, these non-Schmid effects are characterized by the dependence of the CRSS on the sense of shear, as well as on stress components that do not give rise to a Peach-Koehler force acting on the dislocation [42]. These effects, intrinsic to the BCC crystal structure, are attributed to the lack of prescribed symmetry for slip in the $\langle 111 \rangle$ direction except on $\{110\}$ planes and on the non-planar core configurations of screw dislocations.

A number of experimental results have confirmed the presence of non-Schmid ef-

fects in BCC metals in general and specifically in Ta. Cogent reviews of these effects are given in, for example, [43, 44]. Experiments at 4.2K in [45], and at 77K and 273K in [46, 47] have demonstrated that orientation dependence of the yield stress for single crystal Ta specimens does not conform to the Schmid law across a range of temperatures. Results of these experiments assert that the orientation dependence is due partly to the asymmetry of the Peierls potential for movement in the $\{112\}$ planes. However, it has been concluded that this effect is insufficient to explain the orientation dependence in isolation [47]. Tensile tests performed on Ta single crystals across a range of temperatures from 77K to 483K at rates of $\dot{\epsilon} \approx 10^{-5}s^{-1}$ and $10^{-6}s^{-1}$ indicate a breakdown of the Schmid law and suggest that apparent $\{112\}\langle 111\rangle$ slip could actually be cooperative motion on two $\{110\}$ planes [48].

In addition to the loading orientation, temperature and strain rate play important roles in the determination of the CRSS for BCC metals. There is a characteristic timescale over which slip is thermally activated, and the applied strain rate determines the magnitude of the applied stress during this time. Since the applied stress affects the amount of thermal energy required to activate slip, the effects of temperature and strain rate on the CRSS are coupled. For example, experiments inducing $(\bar{1}01)\,[111]$ slip in Ta single crystal tensile specimens across a range of temperatures from 4.2K to 550K at strain rates of $\dot{\epsilon} \sim 10^{-4}s^{-1}$ and $10^{-2}s^{-1}$ show that the athermal limit (the temperature above which the flow stress is constant) varies with applied

strain rate [49]. This effect gives some indication of the interplay between temperature and strain rate in the thermal activation of dislocation motion, which is the dominant mechanism of slip at most temperatures and strain rates. The connection between temperature and strain rate is also revealed at the limits of the thermal activation model at extremely low temperatures or high strain rates, where slip becomes a stress-driven process.

A significant volume of numerical modeling work has been devoted to studying various aspects of single crystal slip in BCC materials. Early atomistic studies focused on the dissociation of a $\frac{1}{2}(111)$ screw dislocation [50], where quantification of the dissociation for a family of $\{110\}$ planes was performed. Subsequently, it was shown that while stable stacking faults were not likely to form in BCC materials [51], elastic anisotropy of the crystal could produce generalized stacking faults [52], inducing a stable dislocation core configuration spread onto a number of slip systems [53]. It has been found that asymmetry in the dislocation core relative to loading orientation produces an asymmetry in the stress required to move the dislocation [54]. More recent work has extended the analysis of dislocation behavior with atomistic studies as in, for example, [55].

Modeling work at higher scales, for example, in [56] has employed the mechanical threshold stress (MTS) model to conform to experimental results at 298K and 773K.

These results have shown that the yield and flow stresses of Ta polycrystals are very sensitive to the temperature and strain rate, but the hardening behavior is less sensitive to these loading parameters. The authors in [56] have argued that this points to the thermal activation of overcoming the Peierls barrier as the rate controlling mechanism for high strain-rate deformation. Further experiments on mildly textured polycrystalline Taylor cylinders [57] have shown that while the MTS model provides a reasonable fit to the data, it requires separate calibration for different ranges of temperature and strain-rate conditions. Modeling of some recent experiments on a tantalum top-hat sample in [2] has used a combination of the MTS model and a crystal plasticity model of thermally activated dislocation motion to study the formation of shear bands. Recent work in [58] has suggested that it is necessary to include non-Schmid effects in dislocation dynamics simulations to adequately model experimentally observed tension-compression asymmetry. The theory of crystal plasticity already incorporates much of the strain-rate and temperature sensitivity found in the experimental results mentioned above. However, numerical implementation of the theory for finite element simulation typically does not include the influence of non-Schmid effects. Additionally, there is still a need for a better physics-based informed understanding of the slip mechanisms to be incorporated in the crystal plasticity numerical models that can be extended to applications of extreme loading conditions.

The present study is motivated by the need to create a physical basis for the

functional forms and quantifications of slip system parameters for crystal plasticity finite element modeling. Section 3.3 outlines a basic framework of crystal plasticity theory. Section 3.4 describes the molecular dynamics model developed to provide the necessary tools for modeling along with validation studies with respect to various parameters. The crystal plasticity model parameters are extracted from MD simulation data and the rationale for the non-Schmid effects are discussed in Section 3.5. A finite element implementation of the model and simulation results are presented in Section 3.6.

3.3 The Crystal Plasticity Constitutive Modeling Framework

The crystal plasticity representation of slip behavior forms the basis for investigations performed in this study. Crystal plasticity theory is primarily concerned with the interpretation of plastic flow in crystalline materials as an aggregate of slip processes that proceed by the movement of dislocations on well-defined slip systems [59]. Plasticity thus conceived is anisotropic, with the form of anisotropy governed by the structure of the crystal lattice and the configuration of defects in the lattice. Some details and assumptions of the rate-dependent crystal plasticity model [2, 60, 61] that are examined in this study are described next.

The deformation gradient tensor $\mathbf{F}$ is taken as the fundamental representation of deformation in the crystal plasticity framework. This tensor is multiplicatively decomposed into thermo-elastic and plastic parts $\mathbf{F}^e$ and $\mathbf{F}^p$ respectively, as:

$$\mathbf{F} = \mathbf{F}^e\mathbf{F}^p \tag{3.4}$$

The thermo-elastic part of the Lagrangian strain tensor is then defined as:

$$\mathbf{E}^e = \frac{1}{2}\left[(\mathbf{F}^e)^{\mathrm{T}}\mathbf{F}^e - \mathbf{I}\right] \tag{3.5}$$

The Cauchy stress is related to the thermo-elastic strain $\mathbf{E}^e$ and the temperature T through the relation:

$$\boldsymbol{\sigma} = \frac{1}{\det(\mathbf{F}^e)}\mathbf{F}^e\mathbb{C} : \left[\mathbf{E}^e - \mathbf{A}_{\mathrm{th}}(T - T_0)\right]\mathbf{F}^{e\mathrm{T}} \tag{3.6}$$

where $\mathbb{C}$ is an anisotropic elasticity tensor with cubic symmetry, $\mathbf{A}_{\mathrm{th}}$ is a second order thermal expansion tensor, and T_0 is a reference temperature.

For the BCC crystal plasticity model, slip is assumed to occur in a $\langle 111\rangle$ direction along a $\{110\}$, $\{112\}$, or $\{123\}$ slip plane, for a total of up to 48 potential slip systems [59]. Each slip system α in the crystalline lattice is characterized by a slip plane with normal $\mathbf{n}^\alpha$ and a slip direction $\mathbf{m}^\alpha$. According to the Schmid law, the resolved shear stress driving slip on the system α is given by the projection of the Kirchhoff stress as:

$$\tau^\alpha = (\mathbf{m}^\alpha \otimes \mathbf{n}^\alpha) : \det(\boldsymbol{F})\,\boldsymbol{\sigma} \tag{3.7}$$

The resulting slip is characterized by the flow rule, which expresses the slip rate $\dot{\gamma}^\alpha$ as a function of the resolved shear stress τ^α and temperature T. The flow rule [2,61] is stated as:

$$\begin{aligned} \forall \;\; \tau^\alpha_{\text{eff}} &= |\tau^\alpha| - \frac{\mu}{\mu_0} s^\alpha_a > 0 \\ \dot{\gamma}^\alpha &= \dot{\gamma}_0 \exp\left(-\frac{\Delta G_{k_0}}{k_B T} \left\langle 1.0 - \left\langle \frac{\tau^\alpha_{\text{eff}}}{\frac{\mu}{\mu_0} s^\alpha_0} \right\rangle^p \right\rangle^q \right) \text{sign}\left(\tau^\alpha\right) \end{aligned} \tag{3.8}$$

where $\langle\rangle$ is the Macaulay bracket expressed as $\langle x \rangle = \frac{1}{2}(|x| + x)$. In this equation, s^α_0 is the intrinsic slip system resistance due to the Peierls barrier, and s^α_a is an evolving athermal slip system resistance due to long-range barriers such as dislocation density. The parameters μ and μ_0 are the temperature-dependent and reference (0K) shear moduli respectively, and the ratio μ/μ_0 scales the slip system resistances with temperature. The model parameters ΔG_{k_0}, p, q, and $\dot{\gamma}_0$ are generally empirically or phenomenologically derived from analyses of thermal activation. The deformation induced velocity gradient $\mathbf{L} = \dot{\mathbf{F}}\mathbf{F}^{-1}$ is additively decomposed into elastic and plastic parts as $\mathbf{L} = \mathbf{L}^e + \mathbf{L}^p$, where the plastic part is expressed as the summation of the slip-rates $\dot{\gamma}^\alpha$ due to dislocation glide on all systems as:

$$\mathbf{L}^p = \dot{\mathbf{F}}^p (\mathbf{F}^p)^{-1} = \sum_\alpha \dot{\gamma}^\alpha \mathbf{m}^\alpha \otimes \mathbf{n}^\alpha \tag{3.9}$$

The plastic deformation gradient $\mathbf{F}^p$ can be determined using Equation (3.9), while Equation (3.4) determines $\mathbf{F}^e$, from which the stresses are evaluated using Equation (3.6). Equations (3.4)-(3.9) thus form a closed set that can be solved, along with the appropriate boundary conditions, within a numerical scheme such as the finite

element method.

The flow rule in Equation (3.8) for thermally activated slip, which relates plastic slip-rate to temperature, resolved shear stress and lattice slip resistance, is used to create a link between the crystal plasticity model and the atomic-scale processes observed in the MD simulations performed in this study. The functional form of the flow rule is generally developed through characterization of a number of critical dependencies, which are each subjected to study via MD here to examine and re-evaluate this functional form. The flow rule is based on the Orowan equation, which relates the plastic slip rate $\dot{\gamma}^{\alpha}$ to the dislocation density ρ_m and the dislocation velocity v_d^{α} on a slip system α as:

$$\dot{\gamma}^{\alpha} = b\rho_m v_d^{\alpha} \tag{3.10}$$

where b is the magnitude of the Burger's vector. The dislocation velocity is characterized through an Arrhenius relation for thermal activation, and is expressed as the product of the jump length, the characteristic frequency v_0^* and the probability that at a given temperature T a particular thermal fluctuation attains a threshold energy ΔG_k^{α}, as:

$$v_d^{\alpha} = bv_0^* \exp\left(-\frac{\Delta G_k^{\alpha}}{k_B T}\right) \tag{3.11}$$

An empirical form has been used in [5] to model the dependence of the activation

energy ΔG_k^α on the effective resolved shear stress as:

$$\Delta G_k^\alpha = \Delta G_{k_0} \left\langle 1 - \left\langle \frac{\tau_{\text{eff}}^\alpha}{\tau_0} \right\rangle^p \right\rangle^q \tag{3.12}$$

where ΔG_{k_0} is the activation energy required to activate slip in the absence of an applied stress, and p and q are empirical parameters. The critical shear stress needed to initiate slip without thermal activation is $\tau_0 = \frac{\mu}{\mu_0} s_0^\alpha$, the intrinsic lattice resistance scaled by the temperature dependence of the shear modulus. The flow rule in Equation (3.8) results from a combination of equations (3.10), (3.11), and (3.12).

As a result of the evolving plastic deformation, the temperature and athermal slip resistance also evolve in the material. The rate of change in temperature induced by the plastic work is characterized by

$$\dot{T} = \frac{\eta}{\rho c_\rho} \sum_\alpha \tau^\alpha \dot{\gamma}^\alpha \tag{3.13}$$

where η is an efficiency factor that determines the amount of plastic work which is converted into heat. The athermal slip system resistance evolves as

$$\dot{s}_a^\alpha = \sum_\beta \left[r + (1-r)\, \delta^{\alpha\beta} \right] h^\beta \left| \dot{\gamma}^\beta \right| \tag{3.14}$$

This evolution equation takes into account self-hardening through dislocation pileup on the slip system α and latent hardening due to dislocation density on the other slip systems $\alpha \neq \beta$ via the material parameter r. The self-hardening rate is [6]

$$h^\beta = h_0 \left(\frac{s_s^\beta - s_a^\beta}{s_s^\beta - s_{a_0}^\beta} \right) \tag{3.15}$$

where $s^{\beta}_{a_0}$ is the initial athermal resistance, and the evolution of the saturation stress s^{β}_{s} is given by [62]

$$s^{\alpha}_{s} = s_{s_0} \left(\frac{\dot{\gamma}^{\alpha}}{\dot{\gamma}_0} \right)^{\frac{k_B T}{A}} \tag{3.16}$$

where A is an empirical parameter.

In the study presented in the following sections, MD simulations are performed to quantify the effects of: (i) temperature via parameters p and q in Equation (3.12), (ii) loading orientation via the functional form of τ^{α}, and (iii) strain rate via the probability of slip in Equation (3.11). The simulation procedures are discussed in detail in the next section followed by a presentation of the results.

3.4 Atomistic Simulations with MD: Model Details and Validations

Molecular dynamics simulations, using the software LAMPPS [63], are used to evaluate the crystal plasticity variables related to the CRSS at which dislocation motion is initiated. All simulations are carried out in the canonical ensemble (NVT) across a range of thermostat temperatures from 0.1K to 600K. An initial atomic configuration is shown in Figure 3.3. Slip in BCC Ta is primarily mediated by the motion of $\langle 111 \rangle$ screw dislocations [64], and hence the MD model is developed to manifest

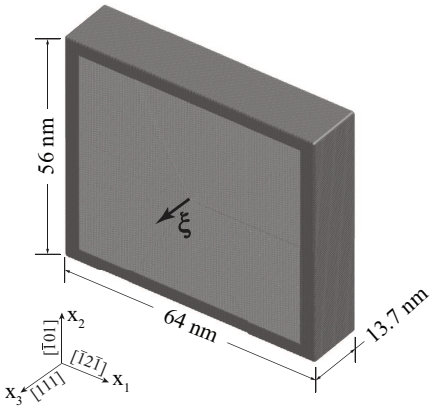

Figure 3.3: Illustration of MD simulation System 3 depicting dimensions and the crystal orientation. A velocity is applied to the dark gray atoms near the x_1 and x_2 boundaries. The vector $\vec{\xi}$ represents the orientation of the dislocation line.

this configuration. The crystal lattice is oriented so that the [111] crystal direction and dislocation line are parallel to the x_3 axis, $[\bar{1}2\bar{1}]$ is parallel to the x_1 axis, and $[\bar{1}01]$ is parallel to the x_2 axis. Dislocation motion in all the simulations proceeds along a combination of the $(\bar{1}01)$ and $(0\bar{1}1)$ planes. Due to the generally nonlinear nature of this motion due to finite temperature effects, slip cannot generally be assigned to a single slip system.

There are three simulation cells used in this study. For each, the simulation cell size is $(l_{x_1} = 64\text{nm}) \times (l_{x_2} = 56\text{nm})$ in the $x_1 - x_2$ plane. In the x_3 direction the cell sizes are $l_{x_3} = 3.4$nm (System 1), $l_{x_3} = 9.1$nm (System 2), and $l_{x_3} = 13.7$nm (System 3). The cells contain approximately 6.9×10^5, 1.8×10^6, and 2.8×10^6 atoms

of Ta, respectively. Periodic boundary conditions are applied in the x_3 direction to approximate a straight, infinitely long dislocation with the line direction shown in Figure 3.3. Displacement boundary conditions are applied in the x_1 and x_2 directions by moving atoms near the $|x_1| = 28$nm and $|x_2| = 32$nm boundaries at a constant velocity, corresponding to a displacement field prescribed in Equation (3.23) of section 3.4.4. Virial stresses, defined in section 3.4.2, near the dislocation core are evaluated in a prismatic region with dimensions $|x_1| \leq 16$nm, $|x_2| \leq 19$nm and $x_3 =$ depth of the simulation box. The MD simulations are conducted for total times of 2 to 10ns, using a constant time-step of 2.0fs each, resulting in $1 - 5 \times 10^6$ time-steps. Details of the simulation methodology are presented next.

3.4.1 Interatomic Potential for MD Simulations

At least three essential features must be considered for any empirical potential to be used in this study. The potential must:

1. accurately reproduce the elastic behavior of Ta, providing correct estimations of the anisotropic elastic moduli;

2. give a suitable result for the estimation of the relevant γ-surfaces for Ta that represent barriers to plastic flow.

3. produce the correct dislocation core configuration for a screw dislocation in Ta.

A number of central-force interatomic potentials have been developed for Ta, for which computational efficiency is gained by calculating only pairwise interactions. They include the Finnis-Sinclair potential in [65], and the embedded atom method or EAM potentials developed for Ta in [3, 4]. These potentials model interatomic interactions, accounting for the electron density [66] without characterizing any angular dependence of the density. Hence, they do not capture any directionality of the bonding in BCC materials. More sophisticated potentials have been proposed to account for directional bonding in BCC materials; for example, modified generalized pseudo-potential theory or MGPT in [1,67], angular-dependent interatomic potential or ADP in [68], modified embedded atom method or MEAM in [69] and the bond-order potentials or BOP in [70]. However, the computational cost for these potentials is much higher than for those without directionality, which restricts application to smaller molecular systems.

The following discussion will show that the central-force EAM potential developed in [3] satisfies the above three conditions with high efficiency and may be used for simulating larger systems. This potential has been used in atomistic simulations of the structure of small clusters [71], grain coalescence [72], collapse of nano-voids in Ta [73], and recently in the study of fracture behavior [74]. The larger simulation box size allowed by use of a simpler potential makes it less likely that spurious stresses introduced by the boundary conditions will influence the initiation of slip. Also, it

reduces the chances of suppressing slip mechanisms due to the imposition of a rigidly straight dislocation line through periodic boundary conditions with a very small dimension along the dislocation line length. It should be noted that the value of the Peierls stress estimated by each potential is different, and this deserves significant attention that is beyond the scope of the current investigation. Generally, none of the studies performed using these potentials have been able to reproduce empirically derived values of the Peierls stress in Ta [1, 75]. Consequently, the values obtained from the MD simulations need to be scaled to an appropriate value before being applied to a crystal plasticity framework.

The EAM model in [3] is used to model deformation in Ta in this study. The functional form of the interaction potential is:

$$U = \frac{1}{2}\sum_{i \neq j} V(r_{ij}) - \sum_{i} F(\rho_i), \qquad \text{where} \tag{3.17}$$

$$\rho_i = \sum_{j} \hat{\phi}(r_{ij}) \tag{3.18}$$

Here $V(r_{ij})$ is the pair-potential function and $F(\rho_i)$ is the embedding function. The electron density for atom i is obtained by summing the contributions of neighboring atoms j through the use of the distance-dependent density function $\hat{\phi}(r_{ij})$. Discrete values of the functions, used in MD simulations, are obtained by fitting cubic splines to match forces from the empirical potential to those from ab-initio calculations. In the following sections, MD model validation is carried out with respect to each of the three requirements above.

3.4.2 Validation of MD Model for Elastic Behavior

A displacement-controlled MD simulation is performed to create a deformation field that can aid in the evaluation of the critical stress required to move a dislocation and initiate slip. To achieve this deformation field, a constant strain rate $\dot{\epsilon}_0$ in the x_3 direction is applied through the imposition of the following atomic displacements on boundary atoms; that is,

$$\begin{aligned} x_1(t) &= X_1 \\ x_2(t) &= X_2 \\ x_3(t) &= \dot{\epsilon}_0 t \left[\sin(\phi) X_1 + \cos(\phi) X_2\right] + X_3 \end{aligned} \tag{3.19}$$

Here, the angle ϕ controls the orientation of the maximum resolved shear stress plane (MRSSP). It is possible to express the deformation gradient $\mathbf{F} = \frac{\partial \mathbf{x}}{\partial \mathbf{X}}$ in Equation (3.4) from the atomic displacements in Equation (3.19), assuming a homogeneous deformation field. Then, from Equation (3.5), the elastic Lagrangian strain tensor may be expressed as:

$$\mathbf{E}^e = \frac{1}{2} \begin{bmatrix} (\dot{\epsilon}_0 t)^2 \sin^2(\phi) & (\dot{\epsilon}_0 t)^2 \cos(\phi) \sin(\phi) & \dot{\epsilon}_0 t \sin(\phi) \\ (\dot{\epsilon}_0 t)^2 \cos(\phi) \sin(\phi) & (\dot{\epsilon}_0 t)^2 \cos^2(\phi) & \dot{\epsilon}_0 t \cos(\phi) \\ \dot{\epsilon}_0 t \sin(\phi) & \dot{\epsilon}_0 t \cos(\phi) & 0 \end{bmatrix} \tag{3.20}$$

The effects of temperature will be neglected in this derivation for simplicity of presentation. Components of the corresponding Cauchy stress tensor $\boldsymbol{\sigma}^c$ in a perfect lattice,

experiencing the strain field in Equation (3.20), may be written using Equation (3.6) as:

$$\begin{aligned}
\sigma^c_{11} &= \mu_2 \sin(\phi)\,(\dot{\epsilon}_0 t) + \mathcal{O}\left[(\dot{\epsilon}_0 t)^2\right] \\
\sigma^c_{22} &= -\mu_2 \sin(\phi)\,(\dot{\epsilon}_0 t) + \mathcal{O}\left[(\dot{\epsilon}_0 t)^2\right] \\
\sigma^c_{33} &= \mathcal{O}\left[(\dot{\epsilon}_0 t)^2\right] \\
\sigma^c_{23} &= \mu_1 \cos(\phi)\,(\dot{\epsilon}_0 t) + \mathcal{O}\left[(\dot{\epsilon}_0 t)^2\right] \\
\sigma^c_{13} &= \mu_1 \sin(\phi)\,(\dot{\epsilon}_0 t) + \mathcal{O}\left[(\dot{\epsilon}_0 t)^2\right] \\
\sigma^c_{12} &= \mu_2 \cos(\phi)\,(\dot{\epsilon}_0 t) + \mathcal{O}\left[(\dot{\epsilon}_0 t)^2\right]
\end{aligned} \tag{3.21}$$

where $\mu_i,\ i = 1, 2, 3$ are the anisotropic shear moduli in the appropriate directions. Additionally, the atomistic virial stress components σ^a_{ij} are assumed to be analogous to the Cauchy stress components in Equation (3.21), with the virial stress being defined for the simulation box as:

$$\sigma^a_{ij} = -\frac{1}{V_{box}}\left[\sum_k^N (m^k v^k_i v^k_j) + \sum_k^N (r^k_i f^k_j)\right] \tag{3.22}$$

Here, $i, j = 1, 2, 3$ correspond to the x_i directions and k is the identifier of an atom in the ensemble containing N atoms in a simulation box of volume V_{box}. The components of velocity and position vector for atom k are v^k_i and r^k_i respectively, while f^k_j is the force on the atom of mass m^k resulting from pairwise interaction. Figure 3.4 compares the evolution of the atomistic virial stress σ^a in Equation (3.22) with the continuum stress measure σ^c in Equation (3.21) for crystal plasticity simulations. The stresses are plotted as a function of the applied strain $\dot{\epsilon}_0 t$. A very good agreement is seen between

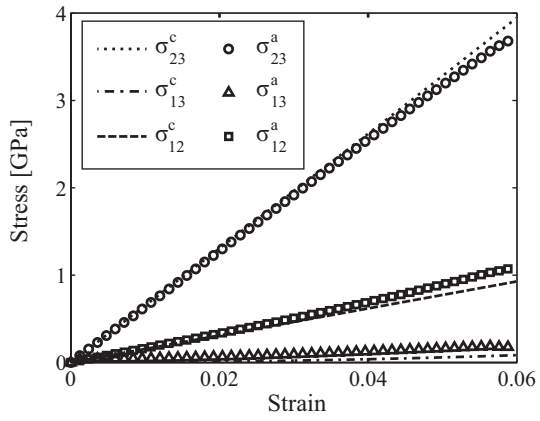

Figure 3.4: Comparing the evolution of the atomistic virial stress σ^a from Equation (3.22) and the Cauchy stress σ^c from Equation (3.21) as a function of the applied strain $\dot{\epsilon}_0 t$

the MD and crystal plasticity measures of the elastic stress-strain response. This indicates that the elastic behavior of the MD model, especially the elastic constants produced by the potential correspond to the experimentally determined, temperature-dependent elastic constants in [38]. These constants are similar to those used in previous crystal plasticity simulations of [2, 61].

3.4.3 Validation of MD Model with Respect to $\langle 111 \rangle$ Gamma-Surface Prediction

The γ-surfaces and corresponding generalized stacking fault energies reveal an important characteristic that governs the plastic behavior of a model material, viz.

the resistance to plastic flow on a given slip system in a perfect crystal. In this study, the relevant γ-surfaces are explored by displacing two halves of a perfect lattice split by a given slip plane and along a given slip direction. During the motion, the atoms are allowed to relax normal to the plane into the equilibrium configuration dictated by the MD potential employed.

There are two EAM potentials for Ta available in the literature. The EAM potential of Guellil and Adams [4] is a modification of the analytical EAM potential developed by Johnson and Oh [76], while the EAM potential of Li et. al. [3] is developed by the force-matching method. To determine if either potential is suited for this study, a test is performed to determine their effectiveness in accurately representing the generalized stacking fault energies predicted from the ab-initio work of [1]. The $\{112\}/\langle 111\rangle$ and $\{110\}/\langle 111\rangle$ γ-surfaces produced by MD simulations using these EAM potentials are shown in Figure 3.5. The generalized stacking fault energies represented by the maxima of the curves for the $\{110\}$ and $\{112\}$ slip systems are evaluated for the two EAM potentials and are compared against ab-initio results from the literature in Table 3.1. As seen in Table 3.1, the EAM potential in [3] matches more closely the maximum energies and separation between the maxima for the $\{110\}/\langle 111\rangle$ slip system found in the ab-initio work of [1]. The error is lower for the $\{112\}/\langle 111\rangle$ slip system for the potential in [4], but that potential significantly underestimates the difference between the two slip system families. Based on the

results of this test, the EAM potential of [3] is chosen for this study based on its favorable comparison to the ab-initio results of [1].

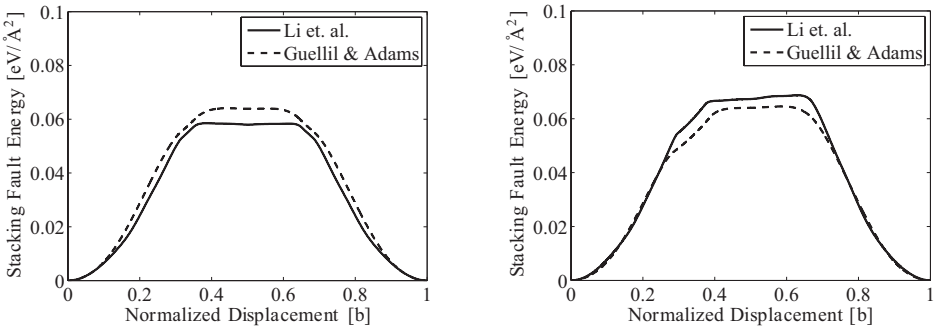

(a) (b)

Figure 3.5: γ-surfaces for Tantalum generated by two different potential functions for slip systems: (a) $\{110\}/\langle 111\rangle$; and (b) $\{112\}/\langle 111\rangle$. The solid and the dashed curves correspond to the EAM potential of [3] (used in this study) and [4] respectively.

3.4.4 Validation of MD Model with Respect to Screw Dislocation Core

Changes in the material symmetry near screw dislocation cores play an important role in the asymmetric behavior of BCC Ta with respect to the CRSS. To study these effects, the atomic configuration in the MD simulation volume is set up to represent an otherwise perfect Ta lattice containing a single screw dislocation as shown in Figure

Method [Ref.]			Difference from [1]	
	$\{110\}/\langle 111\rangle$	$\{112\}/\langle 111\rangle$		
Ab initio [68]	0.0524	0.0591	-	-
Ab initio [1]	0.054*	0.062*	-	-
ADP [68]	0.0482	0.0574	11%	8%
MGPT [1]	0.046*	0.055*	15%	11%
EAM [3]	0.0585	0.0687	8%	11%
EAM [4]	0.0614	0.0646	14%	4%

Table 3.1: Stacking fault energies in eV/Å^2 (* estimated from figures in the references). Relative errors compared to the values in [1] are also given.

3.3. The configuration of a screw dislocation in an isotropic medium is given by the displacement field derived in [59] as:

$$u_1 = u_2 = 0, u_3 = \frac{b}{2\pi}\tan^{-1}\left(\frac{x_2}{x_1}\right) \tag{3.23}$$

Atoms in the simulation volume are displaced according to this field and then relaxed using energy minimization. After energy minimization, the core configuration changes into a relaxed configuration by displacement of atoms near the core, including displacement in the x_1-x_2 plane. The relaxed core configuration is found to be spread symmetrically on three $\{110\}$ planes, producing a core configuration as shown in Figure 3.6.

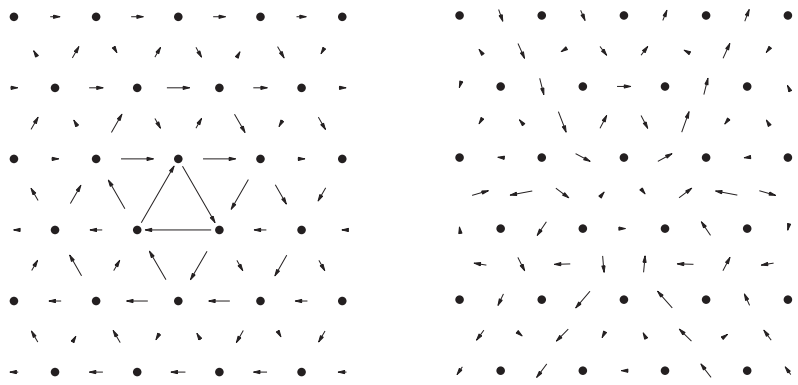

(a) (b)

Figure 3.6: Differential displacement maps for a $\frac{1}{2}[111]$ screw dislocation core: (a) out-of-plane displacements, normalized by $b/3$; (b) inplane displacements, magnified by a factor of 10.

The out-of-plane displacements in the dislocation core shown in Figure 3.6a are in good agreement with those in [42, 75] using a Finnis-Sinclair model for Ta [65], and those using the MGPT potential simulations in [67]. While the in-plane displacements for each potential reveal small variations in the core produced by various potentials, the same symmetry is exhibited.

3.5 Crystal Plasticity Model Parameters from MD Simulation Results

In this section, the effects of temperature, load orientation, and strain rate on the CRSS are studied and quantified. Connections are made between the quantitative analysis of the MD results and parameter values in the continuum scale crystal plasticity model. The resulting model is thus physically grounded in the results of dislocation transport that is measured directly in the atomistic simulations.

3.5.1 Thermal Effects on Critical Resolved Shear Stress (CRSS)

Driving plastic slip by thermally activated dislocation motion results in a strong temperature dependence of the CRSS. Molecular dynamics simulations can provide a characterization of this dependence, and correspondingly a suite of simulations is carried out at a constant strain rate $\dot{\epsilon}_0 = 5 \times 10^6 \text{s}^{-1}$ across a range of loading angles $-25^\circ \leq \phi \leq 25^\circ$ (cf. Equation (3.19)) and temperatures $1\text{K} \leq T \leq 600\text{K}$. The CRSS is identified from the simulations from the stress state in the system when the dislocation begins to move.

Thermal effects at the atomic scale are related to the crystal plasticity framework,

for which the CRSS is expressed as a function of temperature. This relation is obtained by inverting the relation in Equation (3.12) and substituting $\hat{\tau}^\alpha$ from Equation (3.35), yielding

$$\hat{\tau}^\alpha = \frac{\mu}{\mu_0}\left\{ s_a^\alpha + s_0^\alpha \left[1 - \left(\frac{\Delta G_k}{\Delta G_{k_0}} \right)^{\frac{1}{q}} \right]^{\frac{1}{p}} \right\} \tag{3.24}$$

Single crystal tantalum experiments at a range of temperatures $0.7\text{K} \leq T \leq 40\text{K}$ in [77] show that the value of the factor $\frac{\Delta G_k}{k_B T}$ at the critical stress remains nearly constant for a fixed strain rate. Experimental strain rates result in a value of $\frac{\Delta G_k}{k_B T} = 24$, except below 20K, where it reaches a minimum value of approximately $\frac{\Delta G_k}{k_B T} \approx 10$ at 2K [77]. This low temperature behavior has been attributed to quantum effects on the vibrational frequencies of dislocations in the thermal activation process. For models that operate at room temperature and above, the ratio is generally taken to be constant, yielding:

$$\hat{\tau}_{cr}^\alpha = \frac{\mu}{\mu_0}\left\{ s_a^\alpha + s_0^\alpha \left[1 - \left(C\frac{k_B T}{\Delta G_{k_0}} \right)^{\frac{1}{q}} \right]^{\frac{1}{p}} \right\} \tag{3.25}$$

Above the athermal limit $T = \frac{\Delta G_{k_0}}{C k_B}$, where Equation (3.25) cannot be used, the CRSS is taken to be constant. Using this relation, the dependence of the CRSS $\hat{\tau}_{cr}^\alpha$ on temperature can be parametrized by fitting to the data as shown in Figure 3.7.

It is assumed that the temperature dependence of $\hat{\tau}_{cr}^\alpha$ does not depend on loading orientation. Thus, the values of the slip resistances s_0^α and s_a^α and the parameters p and q are fit to the entire set of MD data. As $\hat{\tau}_{cr}^\alpha$ appears in both Equation (3.25) and

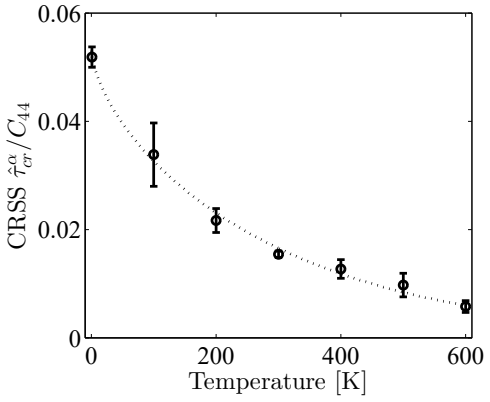

Figure 3.7: Temperature dependence of $\hat{\tau}^{\alpha}_{cr}$ for System 3. Error bars represent the standard deviation across the range of loading angles $-25° \leq \phi \leq 25°$. The dashed line is fit from Equation (3.25).

Equation (3.35), these equations are fit simultaneously to obtain a consistent value. The values of the parameters in Equation (3.25) are tabulated in Table 3.2.

The system size l_{x_3} is seen to have some effect on the parameter values as evaluated from the simulation results. The behavior is qualitatively very similar, but for the larger systems at high temperatures the slip process requires lower applied stress, indicated by the smaller values of s^{α}_{a}. At finite applied stress, the two mechanisms of thermally activated dislocation bow-out and kink-pair nucleation are in competition for dislocation movement [78]. For the high critical stresses observed in this study, it is expected that dislocation bow-out is the dominant mechanism, with the limiting case of the motion of a straight dislocation line, where the activation barrier approaches a maximum. To compare the system size l_{x_3} to the length scales

Method	s_0^α (MPa)	s_a^α (MPa)	p	q	C	ΔG_{k_0} (J)
MD System 1	4387	409	0.38	1.50	16.2	
MD System 2	4299	259	0.47	1.55	16.7	
MD System 3	4361	260	0.47	1.48	17.1	
CP Model [2]	550	50	0.34	1.66		2.1×10^{-19}
CP Model [61]	400	22	0.28	1.34		2.77×10^{-19}

Table 3.2: Values of coefficients in Equation (3.25). Values of C are not incorporated in the crystal plasticity models, and the ΔG_{k_0} values used in this study are not fit from the MD data, but taken from [2].

operative in the thermal activation process, it is noted that in [79], the kink-pair formation energy is found approach an asymptotic value at separations of greater than 5.7nm. The line length in System 3 is more than twice this value. Thus, the range of system sizes used in this study spans the lower range of the length scales required for kink-pair generation. Since there is no obvious changeover observed in the system behaviors, it is argued that the operative mechanism is dislocation bow-out for all the MD simulation systems. The lower critical stress values in the larger systems at high temperatures is consistent with larger line lengths imposing a more relaxed constraint on the straightness of the moving dislocation. The MD results indicate an upper bound for the activation barrier to dislocation motion where thermally activated bow-out is the dominant mechanism.

While the values of p and q are, in general, in the same range as those used in crystal plasticity models of [2, 61], the values of s_a^α and s_0^α are significantly higher. Such higher values are commonly observed in MD studies. They scale with the higher values of τ_{cr}, and are typically $\sim 2-10$ times higher for MD simulations than experiments, as noted in [1]. In the finite element crystal plasticity model, the parameter s_a^α is interpreted as the effect of long-range elastic interaction of dislocations. In the MD study, the value of s_a^α represents athermal slip resistance that is due to constraints on the atomistic system that do not necessarily correspond to physical phenomena present in the continuum description. As such, the values of s_a^α used in the crystal plasticity model are determined from empirical and theoretical considerations at that scale. Similarly, the value of s_0^α employed in the finite element simulations is derived to provide agreement with experimental results.

The value of C is also significantly different than the experimental value due to strain-rate effects discussed in section 3.5.3. Briefly, C is inversely proportional to the athermal limit, or the temperature beyond which the CRSS is approximately independent of temperature. This temperature limit demarcates a point of changeover in behavior. Beyond this temperature, the timescale of thermal activation is sufficiently shorter than the timescale of stress application that stress does not have time to develop beyond an intrinsic lower threshold. Thus, it should be expected that higher

strain rates produce lower values of C, i.e. higher athermal limits.

3.5.2 Load-Orientation Effects on CRSS

Load orientation is defined as the angle between a reference plane and the MRSSP. The load-orientation dependence of the CRSS in a crystal plasticity model for BCC crystals is explored next using atomistic simulations. Let θ denote the angle between the normal $\mathbf{n}^{\alpha}(\theta)$ to a potential slip plane α, and the normal $\mathbf{n}$ to the reference slip plane oriented in the x_2 direction. The Schmid tensor $\mathbf{S}^{\alpha}(\theta)$ for the system α in the deformed configuration is expressed as:

$$\mathbf{S}^{\alpha}(\theta) = \mathbf{m}^{\alpha}(\theta) \otimes \mathbf{n}^{\alpha}(\theta) \tag{3.26}$$

In the undeformed configuration, the slip direction $\mathbf{m}_0^{\alpha}(\theta)$ and the slip-plane normal $\mathbf{n}_0^{\alpha}(\theta)$ are respectively written as:

$$\mathbf{m}_0^{\alpha}(\theta) = \begin{bmatrix} 0 \\ 0 \\ 1 \end{bmatrix}, \mathbf{n}_0^{\alpha}(\theta) = \begin{bmatrix} \sin(\theta) \\ \cos(\theta) \\ 0 \end{bmatrix} \tag{3.27}$$

In the current configuration corresponding to the displacement field in Equation (3.19), the updated slip direction and plane normal are derived to be:

$$\mathbf{m}^{\alpha}(\theta) = \mathbf{F}^{e}\mathbf{m}_0^{\alpha}(\theta) = \begin{bmatrix} 0 \\ 0 \\ 1 \end{bmatrix}, \mathbf{n}^{\alpha}(\theta) = \mathbf{F}^{e-T}\mathbf{n}_0^{\alpha}(\theta) = \begin{bmatrix} \sin(\theta) \\ \cos(\theta) \\ 0 \end{bmatrix} \tag{3.28}$$

Here, they are unchanged by the displacement field given by Equation (3.19). The Schmid tensor in the deformed configuration is:

$$\mathbf{S}^{\alpha}(\theta) = \begin{bmatrix} 0 \\ 0 \\ 1 \end{bmatrix} \otimes \begin{bmatrix} \sin(\theta) \\ \cos(\theta) \\ 0 \end{bmatrix} = \begin{bmatrix} 0 & 0 & 0 \\ 0 & 0 & 0 \\ \sin(\theta) & \cos(\theta) & 0 \end{bmatrix} \tag{3.29}$$

The resolved shear stress for the slip system defined by the angle θ is derived as:

$$\begin{aligned} \tau^{\alpha}(\theta) &= \det(\mathbf{F})\,\boldsymbol{\sigma} : \mathbf{S}^{\alpha}(\theta) \\ &= \det(\mathbf{F}^{e})\,\boldsymbol{\sigma} : \mathbf{S}^{\alpha}(\theta) \\ &= \sin(\theta)\,\sigma_{13} + \cos(\theta)\,\sigma_{23} \end{aligned} \tag{3.30}$$

In Equation (3.30), $\det(\mathbf{F})\boldsymbol{\sigma}$ is the Kirchhoff stress. Since $\det(\mathbf{F}^{p}) = 1$, $\det(\mathbf{F}) = \det(\mathbf{F}^{e})$ and the Kirchhoff stress reduces to $\det(\mathbf{F}^{e})\,\boldsymbol{\sigma}$. Additionally, for the loadings characterized by Equation (3.19), $\det(\mathbf{F}^{e})\,\boldsymbol{\sigma} = \boldsymbol{\sigma}$, since $\det(\mathbf{F}^{e}) = 1$. The orientation of the MRSSP, defined by the angle χ, is obtained from the maximum condition of the resolved shear stress with respect to θ as:

$$\left.\frac{\partial \tau^{\alpha}(\theta)}{\partial \theta}\right|_{\theta=\chi} = \cos(\chi)\,\sigma_{13} - \sin(\chi)\,\sigma_{23} = 0 \quad \Longrightarrow \quad \tan(\chi) = \frac{\sigma_{13}}{\sigma_{23}} \tag{3.31}$$

In the MD system, the angle ϕ is used to control the orientation of the MRSSP through the displacement field specified in Equation (3.19). A first order approximation in $\dot{\epsilon}_0 t$ leads to:

$$\tan(\chi) = \frac{\sigma_{13}}{\sigma_{23}} \approx \tan(\phi) \tag{3.32}$$

The angle χ representing the orientation of the MRSSP in MD simulations is calculated from the atomic stresses and is used to assess orientation dependence of the

CRSS in the crystal plasticity model.

Under the Schmid law, typically employed in crystal plasticity models, the resolved shear stress that drives dislocation motion on a given slip system is simply the projection of the stress tensor onto the slip system, given by Equation (3.7). The spreading of the dislocation core, however, introduces a dependence on the non-glide stresses that are not represented by the Schmid law. This non-Schmid behavior is represented generally by a modification of the resolved shear stress given in [80, 81] as:

$$\hat{\tau}^{\alpha} = \tau^{\alpha} + \sum_{i=1}^{N_{ns}} a_i^{\alpha} \tau_i^{\alpha} \tag{3.33}$$

where τ^{α} is the resolved shear stress from the Schmid law, and the additional N_{ns} non-Schmid terms in Equation (3.33) can be interpreted as non-glide stresses corresponding to the resolved shear stresses on N_{ns} additional slip systems. The specific form of sum of tensor projections used in this study is given in [82, 83] as:

$$\begin{aligned} \hat{\tau}_{cr}^{\alpha} = \quad & (\mathbf{m}^{\alpha} \otimes \mathbf{n}^{\alpha}) : \boldsymbol{\sigma}_{cr} + a_1 (\mathbf{m}^{\alpha} \otimes \mathbf{n}_1^{\alpha}) : \boldsymbol{\sigma}_{cr} + \\ & a_2 \left[(\mathbf{n}^{\alpha} \times \mathbf{m}^{\alpha}) \otimes \mathbf{n}^{\alpha} \right] : \boldsymbol{\sigma}_{cr} + a_3 \left[(\mathbf{n}_1^{\alpha} \times \mathbf{m}^{\alpha}) \otimes \mathbf{n}_1^{\alpha} \right] : \boldsymbol{\sigma}_{cr} \end{aligned} \tag{3.34}$$

This form of the effective resolved shear stress includes the standard Schmid law resolved shear stress $\tau^{\alpha} = (\mathbf{m}^{\alpha} \otimes \mathbf{n}^{\alpha}) : \boldsymbol{\sigma}$, as well as the non-Schmid contributions from shear stresses on the slip plane $\mathbf{n}^{\alpha}$ perpendicular to the slip direction, $a_2 \left[(\mathbf{n}^{\alpha} \times \mathbf{m}^{\alpha}) \otimes \mathbf{n}^{\alpha} \right] : \boldsymbol{\sigma}$, and from resolved shear stresses on an additional $\{110\}$ plane with normal n_1^{α}. There are contributions from shear stresses on this additional

slip plane both parallel to the slip direction, $a_1 \left(\mathbf{m}^\alpha \otimes \mathbf{n}_1^\alpha\right) : \boldsymbol{\sigma}$, and perpendicular to the slip direction, $a_3 \left[\left(\mathbf{n}_1^\alpha \times \mathbf{m}^\alpha\right) \otimes \mathbf{n}_1^\alpha\right] : \boldsymbol{\sigma}$. For $\mathbf{m} = (111)$, $\mathbf{n} = (\bar{1}01)$, and $\mathbf{n_1} = (1\bar{1}0)$,

$$\hat{\tau}^\alpha = \sigma_{23} + a_1 \left(-\frac{\sqrt{3}}{2}\sigma_{13} + \frac{1}{2}\sigma_{23} \right) + a_2\sigma_{12} + a_3 \left[\frac{\sqrt{3}}{4} \left(\sigma_{22} - \sigma_{11}\right) - \frac{1}{2}\sigma_{12} \right] \tag{3.35}$$

The values of the coefficients a_1-a_3 in Equation (3.35) are fit to the entire MD data ensemble, with the value of $\hat{\tau}_{cr}^\alpha$ for each temperature fit from Equation (3.25). The results of this fitting procedure are given in Table 3.3 for the three systems simulated. It is noted that the changes in the values of the parameters across the systems do not appear to indicate significantly different non-Schmid behaviors. As pertains to the finite element simulations performed in this study, all of the sets of parameter values in Table 3.3 produce effective Schmid factors with a maximum difference of 5% for all the load orientations studied. The parameter values obtained from System 3 are taken to be most representative of the non-Schmid behavior and are used in the finite element simulations presented in Section 3.6.These parameters, along with the functional form in Equation (3.34) fully characterize the load-orientation effects of the atomic scale in the crystal plasticity framework when used in Equation (3.8). The data for System 3 is shown in Figure 3.8.

System	a_1	a_2	a_3
1	0.58	0.19	0.26
2	0.57	0.13	0.18
3	0.56	0.15	0.14

Table 3.3: Values of the non-Schmid coefficients in Equation (3.35).

3.5.3 Strain-rate Dependence of the CRSS

To analyze the strain-rate dependence, a range of strain rates that are plausible within the short timescale of MD simulations are applied at temperatures of 0.1K, 300K, and 600K for System 1. The essentially stress-driven process by which slip occurs at 0.1K results in a critical stress value that is nearly identical to the result of a quasi-static loading at 0K. This low (zero) temperature behavior is depicted as a constant value for the critical stress across the entire range of strain rates in Figure 3.9. Values obtained for quasi-static loading at 0K and the value obtained with a strain rate of $5 \times 10^6 \text{s}^{-1}$ agree to within 1%. For finite temperatures, where slip is a thermally activated process, strain rate affects the value of the critical stress. The time taken for thermal activation is assumed to be a function of temperature only, i.e. independent of strain rate. Also, higher strain rates produce higher values of shear stress that will be developed over any given period of time. Thus, higher strain rates will lead to higher values of CRSS. This trend is illustrated in Figure 3.9 for

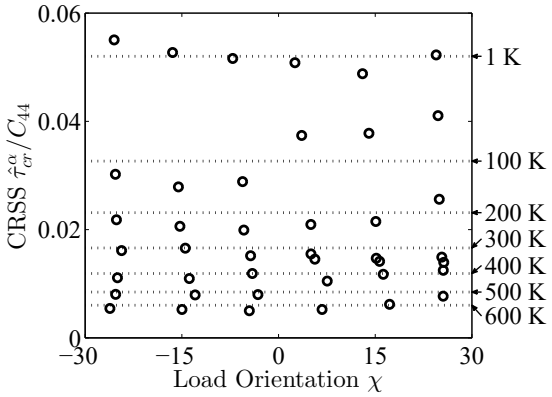

Figure 3.8: Normalized values of CRSS $\hat{\tau}^{\alpha}_{cr}/C_{44}$ for the MD results for System 3. Dashed lines are fit from Equation (3.25).

loading at 300K and 600K respectively. These results are in qualitative agreement with results for tungsten in [84].

The effect of strain rate on the CRSS is analyzed in terms of a discrete probability of slip occurring at each thermal fluctuation event in the lattice. The probability is based on the amount of thermal energy required to overcome the energetic barrier to slip. This perspective on the initiation of slip in dynamic deformation connects strain rate and temperature in the thermal activation process. The probability of a slip event B occurring on the m-th attack is approximated by the discrete product

$$P\left(B \in [t_{m-1}, t_m]\right) = P_m \prod_{j=1}^{m-1} \left(1 - P_j\right) \tag{3.36}$$

where $[t_{m-1}, t_m]$ corresponds to the time interval of the m-th attack and P_i is the probability of success at the i-th attack. It is assumed that the probability of success

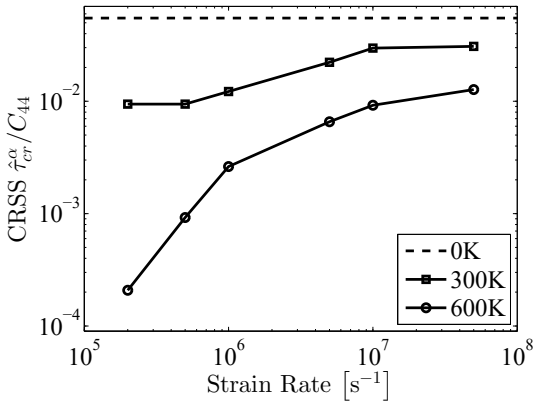

Figure 3.9: Strain-rate dependence of $\hat{\tau}^{\alpha}_{cr}$ with applied loading at 0K, 300K, and 600K. Lines are a guide to the eye.

does not change appreciably over the duration of the discrete time increment from t_{m-1} to t_m. The time increment is defined by the characteristic attack time, as derived below.

The shear modulus μ_1 (in GPa) is given as:

$$\mu_1 = \frac{1}{3}\left(C_{11} - C_{12} + C_{44}\right) = 65.23 - 0.0092\,T \tag{3.37}$$

where T(K) is the absolute temperature. For the rest of the MD-based development, a temperature $T = 0$K is used for illustration. Finite temperature values are obtained by substituting the corresponding value of the shear modulus. The relevant transverse wave speed and the corresponding frequency in Ta are respectively calculated as:

$$v_s = \sqrt{\frac{\mu_1}{\rho}} \approx 1.98 \times 10^3 \frac{m}{s} \qquad v_D = \left(\frac{3N}{4\pi V}\right)^{\frac{1}{3}} v_s \approx 4.69 \times 10^{12} s^{-1} \tag{3.38}$$

where N is the number of atoms in a given volume V. The attack frequency is then calculated to be

$$v_0^* = v_D \left(\frac{b}{l}\right) \approx 3.12 \times 10^{11} s^{-1} \tag{3.39}$$

where the critical length $l = V_{\text{act}}/b^2$ is approximated as $15b$ from discussions in [85]. A similar value of $17b$ has been determined by Cuitiño and co-workers [86] using first-principles calculations involved in the development of the EAM force field [87]. The characteristic attack time is

$$t_A = \frac{1}{v_0^*} \approx 3.20 \times 10^{-12} s \tag{3.40}$$

The probability of success for an attack at a particular state of stress and temperature is expressed as:

$$P(\tau, T) = \exp\left[-\frac{\Delta G_k(\tau)}{k_B T}\right] \tag{3.41}$$

Substituting the stress-dependence of the activation energy in Equation (3.12) into Equation (3.41) yields:

$$P\left(\tau_{\text{eff}}^{\alpha}, T\right) = \exp\left\{-\frac{\Delta G_{k_0}}{k_B T}\left[1 - \left(\frac{\tau_{\text{eff}}^{\alpha}}{\tau_0}\right)^p\right]^q\right\} \tag{3.42}$$

Finally, the probability of a slip event B occurring on the m-th attack in Equation (3.36) is given explicitly in terms of the applied stress and temperature as

$$P\left(\hat{\tau}_{cr}^{\alpha} \in (\tau_{m-1}, \tau_m]\right) = \prod_{j=1}^{m-1}\left\{1 - \exp\left[-\frac{\Delta G_{k_0}}{k_B T}\left[1 - \left(\frac{\tau_j}{\tau_0}\right)^p\right]^q\right]\right\} \exp\left[-\frac{\Delta G_{k_0}}{k_B T}\left[1 - \left(\frac{\tau_m}{\tau_0}\right)^p\right]^q\right] \tag{3.43}$$

The approximation to the stress τ_j applied at step j is:

$$\tau_j = \tau_{\text{eff}}^{\alpha}\left(t = j\Delta t\right) = \frac{1}{\Delta t}\int_{t=(j-1)\Delta t}^{t=j\Delta t}\int_{\hat{t}=0}^{\hat{t}=t}\dot{\tau}_{\text{eff}}^{\alpha}\left(\hat{t}\right)d\hat{t}dt \tag{3.44}$$

Here, the time t_A in Equation (3.40) is used as $\Delta t = t_m - t_{m-1}$. For subsequent analysis, the probability of a slip event in Equation (3.43) is approximated by a lognormal probability distribution function as:

$$f(X = x) = \frac{1}{x\sqrt{2\,\pi\,\beta}}\exp\left[-\frac{\left(\ln x - \alpha\right)^2}{2\,\beta^2}\right] \tag{3.45}$$

where $X = \tau_{\text{ref}} - \tau$ and α and β are parameters of the distribution. The distribution parameters α and β can be calculated from sample estimates for the mean and variance equations as:

$$\begin{aligned}\alpha &= \ln\frac{\mu_X^2}{\sqrt{\sigma_X^2 + \mu^2}}\\ \beta &= \sqrt{\ln\frac{\sigma_X^2}{\mu_X^2} + 1}\end{aligned} \tag{3.46}$$

In Figure 3.10, the cumulative probability of slip initiation is plotted as a function of the resolved shear stress for simulations carried out at 300K. The stress, which increases nearly linearly in time according to Equation (3.21), determines the probability of slip. At stresses that are relatively low for a given applied strain rate and system temperature, the probability of slip is near zero. This indicates that the system does not have enough thermal energy to overcome the Peierls barrier. Near the critical stress, the probability of slip increases in the range of stress where the energetic barrier to dislocation motion is commensurate with the thermal energy available

to the system.

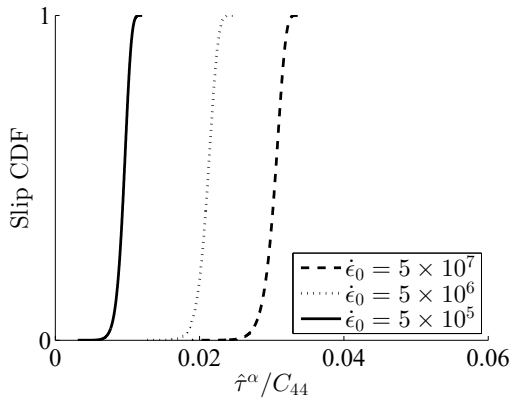

Figure 3.10: Cumulative probability of slip initiation as a function of the resolved shear stress for loading at different strain rates and at a temperature of 300K.

Lognormal distributions are fit to the MD simulation data at 300K and 600K such that the distribution means coincide with the simulation results. This is done by varying the parameters p and q to achieve suitable agreement. Results of the fitting procedure are plotted in Figure 3.11. As shown in the figure and seen in Table 3.4, the values of p and q are changing slowly and appear to be converging asymptotically to the empirical values at low strain rates. This indicates that the model for stress-dependence of the activation energy in Equation (3.12) is likely valid in this regime. At higher strain rates, the predicted values of the parameters diverge from their low strain-rate values with increasing strain rate. This indicates that the stress dependence model for activation energy cannot be consistently parametrized

across all the strain rates studied. While the parameter values are within the ranges of $0 < p < 1$ and $1 < q < 2$ derived in [5], the high rate results suggest significant changes in the effective barrier shape that these values represent. This high rate behavior corresponds to a range of strain rates where significant changes are exhibited by the CRSS-temperature profiles due to the changing balance of stress and thermal activation of slip. To account for the changing nature of the visco-plastic deformation, an additional strain-rate dependence needs to be accounted for in the model to accurately represent the very high strain-rate behavior.

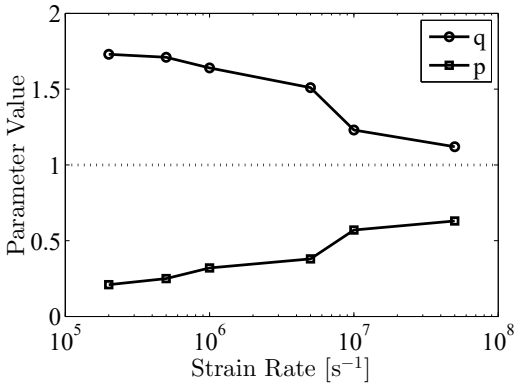

Figure 3.11: Strain-rate effects on the values of the parameters p and q. Connecting lines are a guide to the eye. The dashed line represents the upper bound on the value of p and the lower bound on the value of q given in [5].

$\dot{\epsilon}$ (s^{-1})	p	q
5×10^7	0.63	1.12
1×10^7	0.57	1.23
5×10^6	0.38	1.50
1×10^6	0.32	1.64
5×10^5	0.25	1.71
2×10^5	0.21	1.73

Table 3.4: Values of parameters p and q at various strain rates.

3.6 Finite Element Implementation and Simulations Using the Crystal Plasticity Model

The parametrized crystal plasticity model, developed in sections 3.3 and 3.5, is implemented in an ABAQUS Explicit user-defined material subroutine (VUMAT). Functional forms and parameter values in the crystal plasticity model that are not related to non-Schmid effects are obtained from [2]. The complete set of crystal plasticity parameters is listed in Table 3.5. A value of 800 MPa for s_0^α is used for the simulations employing the non-Schmid formulation. This value is chosen so that the average yield stress in tension and compression for the non-Schmid simulations equals

the symmetric yield stress for the simulations employing the Schmid Law formulation. Dynamic simulations are carried out for a 1mm $\times$ 1mm $\times$ 1mm cubic specimen of specified orientation, subjected to uniaxial tension and compression tests at 298K. A constant logarithmic strain-rate of $1s^{-1}$ is applied by specifying a spatially uniform velocity boundary condition on the $x_3 = 0.5$mm face. Symmetry boundary conditions are applied on the $x_1 = 0$, $x_2 = 0$, $x_3 = 0$ faces. Initial velocities are prescribed on all nodes to avoid the introduction of stress waves and to approximate the Poisson effects in the x_1 and x_2 directions. Slip is considered on the $\{011\}\,[111]$ slip systems, alternatively with and without non-Schmid effects.

The effect of the non-Schmid formulation is analyzed for loading in uniaxial tension and compression. As seen in Figure 3.12a, the stress-strain curves are identical in tension and compression for [001] loading in the absence of non-Schmid effects. This symmetric behavior is quantified in Figure 3.12b, where it is seen that the amount of accumulated slip is identical for tension and compression. In Figure 3.12a, including the non-Schmid effects results in a significant tension-compression asymmetry, consistent with the experimental results in [88, 89] for specimen dimensions $>\sim 1$ μm, and the analysis in [90]. In [58], an opposite trend has been found using dislocation dynamics (DD) simulations of Ta. The authors of that study note that their simulation results represent the experimental results in [91]. They evaluated a parameter, which controlled the strength of the non-Schmid effect from the MD simulations in [75].

The non-Schmid formulation developed in the study performed here also reproduces the MD results in [75], correctly predicting the direction of the tension-compression asymmetries found for loading in all the directions presented in [75]. Differences in the observed tension-compression asymmetry between the work in [58] and that reported here could be due to differences in boundary conditions and strain magnitudes.

The tension-compression asymmetry in the [001] loading simulations is directly attributable to changes in the effective Schmid factor. In the absence of non-Schmid effects, all of the active slip systems have an identical Schmid factor of 0.41. With the non-Schmid effects, the Schmid factors for all of the active systems are 0.63 in tension and 0.37 in compression. This results in a delayed onset of plasticity for compressive loading. The corresponding change in the accumulation of slip on the active systems is shown in Figure 3.12b. The lower slip-rate for the non-Schmid formulation observed in tension is due to the lower stresses that are developed. The small increase in slip for compression in the non-Schmid formulation versus the Schmid Law formulation is due to higher stresses that are partially offset by the higher value of s_0^α used in the non-Schmid formulation.

To study the impact of the non-Schmid effects on the asymmetry of yield, a number of load cases are modeled. The orientation of the loading axis is varied to study the behavior for tension and compression along [001], [012], [011], [$\bar{1}$22],

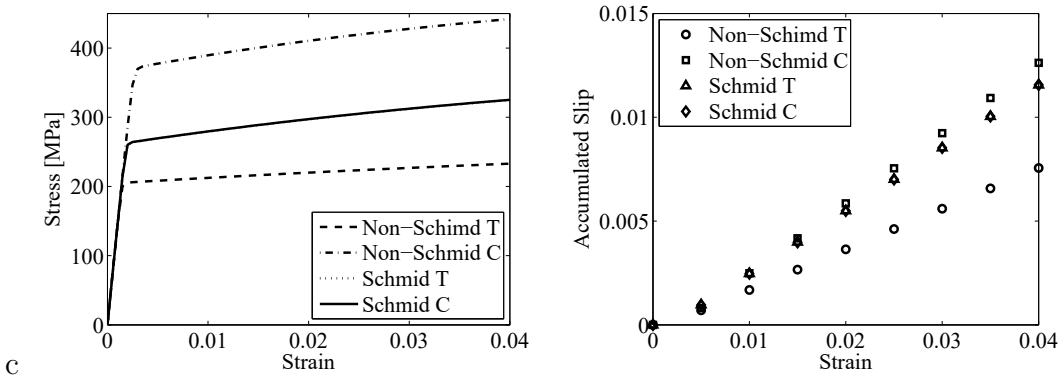

(a) (b)

Figure 3.12: Material response for loading axis oriented along [001]: (a) stress-strain, (b) accumulated slip on the primary slip system.

$[\bar{1}11]$, and $[\bar{1}12]$. A comparison of the yield stresses at 0.5% strain obtained from each of the non-Schmid formulation simulations is presented in Figure 3.13. In the figure, the yield stress for each orientation is normalized by the yield stress from the Schmid Law formulation simulation for that orientation. From the figure, it is clear that the yield stress in compression is higher for the [001] and [012] orientations, and the yield stress in tension is higher for the rest of the simulations. This is consistent with [88]. In comparison to the results in [47], there is agreement on the direction of the tension-compression asymmetry for the [011], $[\bar{1}22]$, and $[\bar{1}11]$ loading orientations, with yield in tension occurring at a higher stress than in compression. For the [001] and [012] orientations, the current study predicts lower yield stresses in tension, whereas in [47], the opposite trend is observed. Given that the results in [47] contradict those in [88] for the [001] orientation, it is argued that the difference

could be explained by heterogeneity in the experimental specimens and method of load application. Further experiments are necessary to investigate the source of the conflicting results.

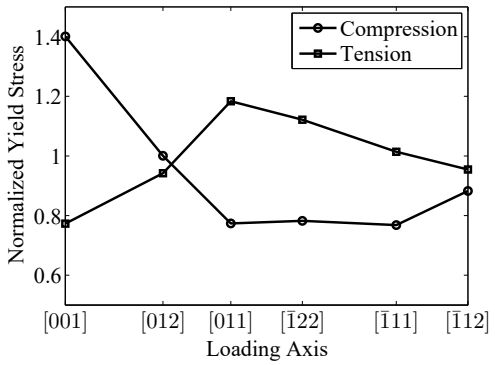

Figure 3.13: Yield stresses in tension and compression from simulations including non-Schmid effects for a range of loading orientations. Stresses are normalized by the yield stresses for each orientation from simulations employing the Schmid Law formulation. Lines are a guide to the eye.

3.7 Dislocation Density Based Hardening

In the flow rule (3.8), the athermal slip resistance s^α on slip system α was previously taken to evolve via the phenomenological relation (3.14), which implicitly depends on the dislocation density. In the crystal plasticity model used in the remainder of the study, this dependence is made explicit through the following relation,

$$s^\alpha = c_1 \mu b \sqrt{\rho_M^\alpha + \rho_P^\alpha} \tag{3.47}$$

where ρ_M^α is the density of mobile dislocations on slip system α, ρ_P^α is the part of the immobile dislocation density that is parallel to the mobile dislocation population on this system, and c_1 is a geometric constant. This is represented pictorially in Figure 3.14, where a dislocation moving from the source at the left encounters thermal resistance from the Peierls barrier and athermal resistance from the long-range stress fields of the mobile dislocations on the same slip system and the parallel projection of dislocations on other slip systems.

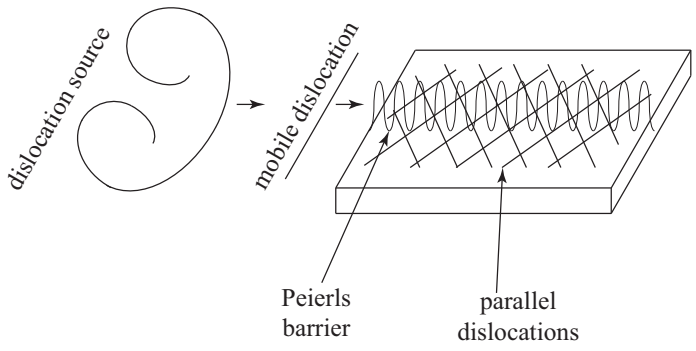

Figure 3.14: Representation of dislocation densities and slip resistance

The evolution of the slip resistance is given by

$$\dot{s}^\alpha = c_1 b \left(\sqrt{\rho_M^\alpha + \rho_P^\alpha}\dot{\mu} + \frac{\mu}{\sqrt{\rho_M^\alpha + \rho_P^\alpha}}\dot{\rho}_M^\alpha + \frac{\mu}{\sqrt{\rho_M^\alpha + \rho_P^\alpha}}\dot{\rho}_P^\alpha \right) \tag{3.48}$$

The rate of change of the shear modulus μ is given by the time derivative of Equation (3.37),

$$\dot{\mu} = \frac{1}{3}\left(\dot{C}_{11} - \dot{C}_{12} + \dot{C}_{44}\right) = \frac{1}{3}\left(m_{11} - m_{12} + m_{44}\right)\dot{T} \tag{3.49}$$

where $\dot{T}$ is given by Equation (3.13). The rates of the dislocation densities are governed by equations originally developed by [92]. First, based on the principle of maximum dissipation, the mobile part of the dislocation population is written as a function of the immobile part,

$$\rho_M^\alpha = \frac{2k_B T}{c_1 c_3 \mu b^4} \sqrt{\rho_P^\alpha} \tag{3.50}$$

so that the rate of change of the mobile dislocation density is

$$\dot{\rho}_M^\alpha = \frac{2k_B T}{c_1 c_3 \mu b^4 \sqrt{\rho_P^\alpha}} \dot{\rho}_P^\alpha - \frac{2k_B T}{c_1 c_3 \mu^2 b^4 \sqrt{\rho_P^\alpha}} \dot{\mu} \tag{3.51}$$

Next, the parallel part of the immobile dislocation density is a projection of dislocation lines from all slip systems onto a line in the system α as

$$\rho_P^\alpha = \sum_\beta \rho_I^\beta \sin\left(\mathbf{n}^\alpha, \mathbf{t}^\beta\right) \tag{3.52}$$

where ρ_I^β is the density of immobile dislocations on slip system β, and $\sin\left(\mathbf{n}^\alpha, \mathbf{t}^\beta\right)$ is the sine of the angle between the slip system normal $\mathbf{n}^\alpha$ and the tangent vector $\mathbf{t}^\beta$. The time derivative of Equation (3.52) is

$$\dot{\rho}_P^\alpha = \sum_\beta \dot{\rho}_I^\beta \sin\left(\mathbf{n}^\alpha, \mathbf{t}^\beta\right) \tag{3.53}$$

so that the rate of change of the slip resistance can be written explicitly in terms of the evolution of the immobile dislocation densities. Neglecting climb, and assuming that the relative densities between slip systems is roughly constant, the evolution of these populations can be written as

$$\dot{\rho}_I^\alpha = \left(c_4 \sqrt{\rho_I^\alpha} - c_5 \rho_I^\alpha\right) \dot{\gamma}^\alpha \tag{3.54}$$

where c_4 is a material constant combining the effects of dipole and lock formation, c_5 is a material constant related to athermal annihilation, and $\dot{\gamma}^\alpha$ is the slip rate on system α.

This framework is set in place to handle realistic evolution of dislocation densities based on phenomena that could potentially be measured, in order to obtain an experimentally validated model. In the absence of the necessary experimental data and techniques, calibration of the parameters in the dislocation density evolution model is carried out to reproduce the response of the phenomenological model [6] described above, as shown in Figure 3.15.

In future work, this hardening model should be investigated in detail, so that observed material behavior can be translated into material constants that can predict the hardening response of different materials. This will provide a significant improvement over phenomenological hardening models, which still require calibration of empirical parameters that do not correspond directly to physical processes.

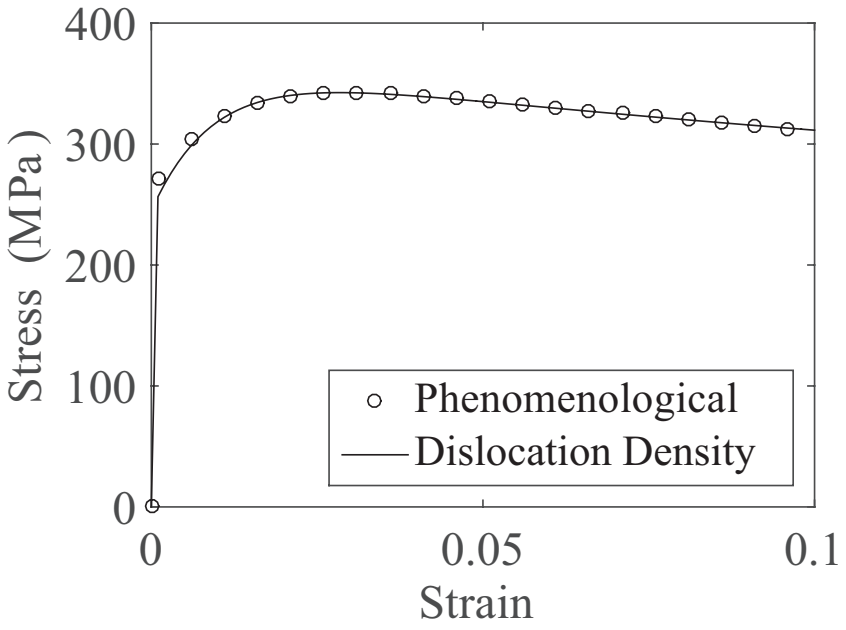

Figure 3.15: Stress-strain response for two hardening models - a phenomenolgical model [6], and the dislocation-density based approach developed in this study.

Parameter	Value
ΔG_{k_0}	2.1×10^{-19}J
s_0^α	550MPa, 800MPa
p	0.34
q	1.66
ρ	1.664×10^4kg/m^3
c_ρ	150 J/kgK
$s_{a_0}^\alpha$	50MPa
r	1.4
$\dot{\gamma}_0$	10^7s^{-1}
s_{s_0}	125MPa
h_{s_0}	300MPa
A	10^{-18}J
a_1	0.56
a_2	0.15
a_3	0.14

Table 3.5: Values of parameters used in the crystal plasticity model. The s_0^α values of 550MPa and 800MPa are used in the simulations without and with non-Schmid effects, respectively.

Chapter 4

Unit Cell Calculations of Crystal Plasticity and Damage Evolution

To simulate the coupled evolution of plastic deformation and crystal plasticity, finite element analysis is performed on a unit cell geometry. The initial discretization approximates an initially spherical void centered within a cubic matrix. An example is shown in Figure 4.1.

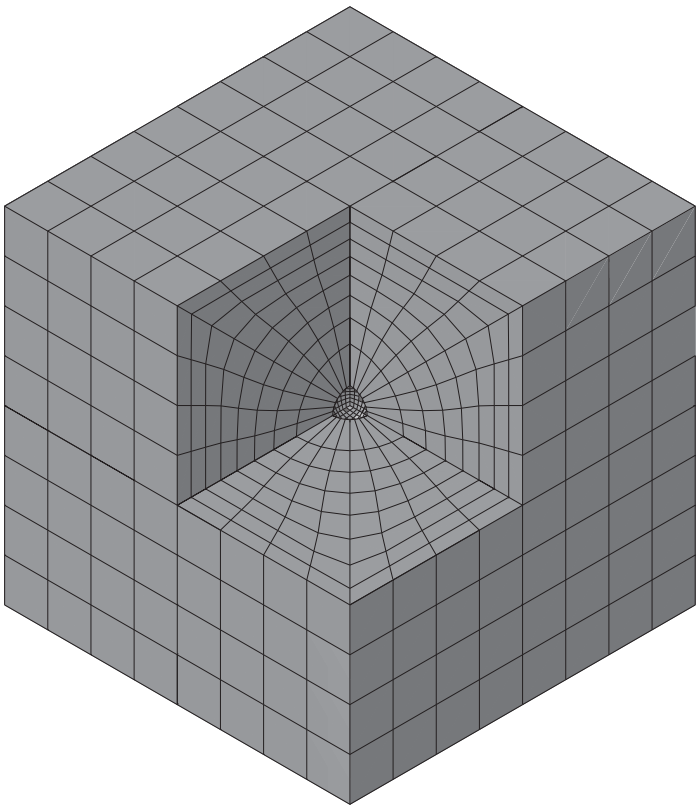

Figure 4.1: Finite element discretization of the damage unit cell. The matrix is composed of a set of hexahedral elements surrounding a spherical void.

The mesh is produced by an algorithm that subdivides concentric superellipsoid shells into elements with approximately equal areas on the surfaces of the shells. The surfaces for a given shell are parametrized by the axes a, b, and c, and the exponent n as

$$\left(\frac{x}{a}\right)^n + \left(\frac{y}{b}\right)^n + \left(\frac{z}{c}\right)^n = 1 \tag{4.1}$$

The innermost surface of the inner shell forms the surface of the void. The void is initially spherical, so that $a = b = c = R$ and $n = 2$. The outermost surface is that of

a cube, so that $a = b = c = \frac{L}{2}$, where L is the side length, and $n \to \infty$. A particular discretization is then produced by specifying a number of shells and a number of subdivisions per quadrant in a planar section. For example, the mesh in Figure 4.1 has eight shells and eight subdivisions.

This geometric domain is a particular case of the more general class of uniform tessellations of three-dimensional space. Specifically, the class of geometries is restricted to only cell-transitive convex honeycombs, so that space is filled with periodically repeating identical unit cells. This choice is made to enable the application of periodic boundary conditions. For a member of this class of domains, there exists a unique mapping from any point $\mathbf{X}$ on the boundary to a corresponding point $\mathbf{Y} = \mathcal{I}(\mathbf{X})$, also on the boundary (its periodic image), such that $\mathbf{f}(\mathbf{X}) = \mathbf{f}(\mathbf{Y}) + \mathbf{C}$ ($\mathbf{C}$ constant) for members $\mathbf{f}$ of a class of functions $\mathcal{F}$ that represent the quantities of interest for thermomechanical IVBP's. In this type of domain, the boundary $\partial\Omega_0$ of the material domain Ω_0 can be partitioned as $\partial\Omega_0 = \partial\Omega_0^+ \cup \partial\Omega_0^-$, where there is an isomorphism $\mathcal{I} : \partial\Omega_0^+ \mapsto \partial\Omega_0^-$ such that if $\mathcal{I} : \mathbf{X} \mapsto \mathbf{Y}$, then

$$\mathbf{N}(\mathbf{X}) = -\mathbf{N}(\mathbf{Y}) \tag{4.2a}$$

$$\mathbf{u}(\mathbf{X}) - \mathbf{u}(\mathbf{Y}) = \mathbf{H}(\mathbf{X} - \mathbf{Y}) \tag{4.2b}$$

where $\mathbf{H}$ is the volume average of the displacement gradient, and $\mathbf{N}$ and $\mathbf{u}$ are members of $\mathcal{F}$. The set of equations (4.2) give a recipe for the imposition of periodic boundary conditions: the geometry, given by the boundary defined by $\mathbf{N}$ achieves a

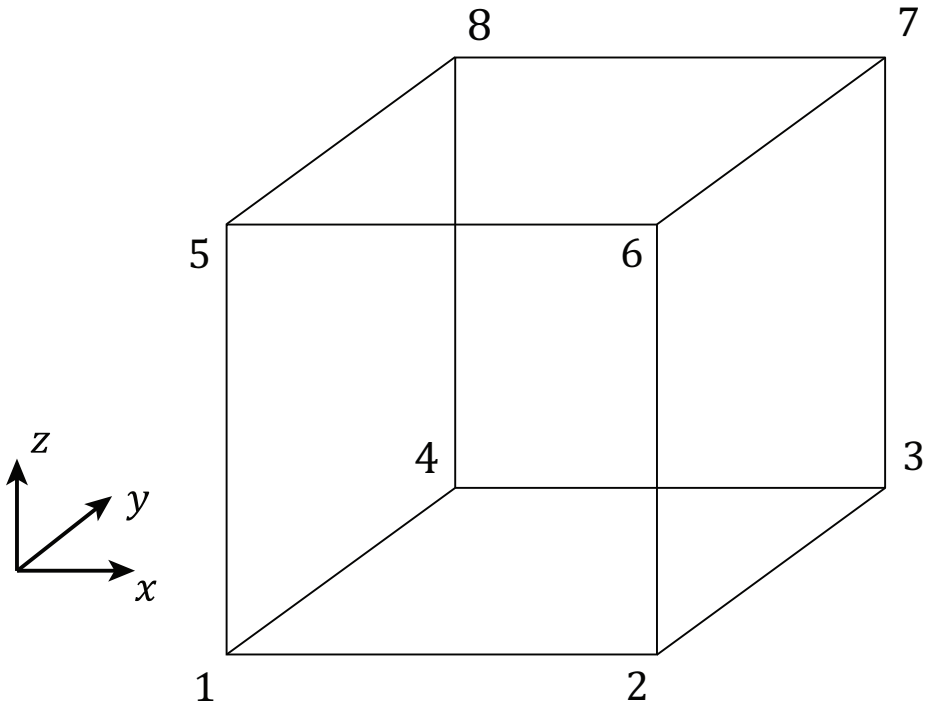

Figure 4.2: Hexahedral element.

deformation characterized by **H** given the appropriate boundary conditions **u**. The detailed prescription is derived in the following section.

4.1 Periodic Boundary Conditions in three dimensions

Periodic boundary conditions are developed for a three-dimensional unit cell defined as shown below,

The displacement gradient $\mathbf{H}$ is defined,

$$\mathbf{H} = \frac{1}{V}\int_V \frac{\partial \mathbf{u}}{\partial \mathbf{X}} dV = \frac{1}{V}\int_S \mathbf{u} \otimes \mathbf{N} dS \tag{4.3}$$

The integral (4.3) can be formulated as the sum of the integrals on the opposing faces

$$\mathbf{H} = \frac{1}{V}\sum_{\alpha}\left(\int_{\alpha^+} u \otimes \mathbf{N}_\alpha^+ dS + \int_{\alpha^-} \mathbf{u} \otimes \mathbf{N}_\alpha^- dS\right) \tag{4.4}$$

The cell is constructed as in Equation (4.2a) so that the normal to a given surface is equal to the negative of the normal vector for the opposing surface; that is,

$$\mathbf{N}_\alpha^- = -\mathbf{N}_\alpha^+ \tag{4.5}$$

Using (4.5), the sum in (4.4) reduces to

$$\mathbf{H} = \frac{1}{V}\sum_{\alpha}\left[\left(\int_{\alpha^+} \mathbf{u} dS - \int_{\alpha^-} \mathbf{u} dS\right) \otimes \mathbf{N}_\alpha^+\right] \tag{4.6}$$

Now, for an intially rectangular prismatic cell, such as that shown in Figure 4.2, the α^+-face ($\alpha = x, y, z$) of the cell, is defined by a normal vector whose components are all zero, except $x_\alpha = \frac{L_\alpha}{2}$. Similarly, the α^--face is characterized by $x_\alpha = -\frac{L_\alpha}{2}$. With the notation that $u_\beta^{\alpha^+}$ $\left(u_\beta^{\alpha^-}\right)$ refers to the β component ($\beta = 1, 2, 3$ for the x-, y-, and z-component, respectively) of the displacement vector evaluated on the positive (negative) α-face, the periodic boundary conditions are given,

$$\begin{aligned} u_\beta^{\alpha^+}(x_\gamma, x_\delta) - u_\beta^{\alpha^-}(x_\gamma, x_\delta) &= u_\beta\left(x_\alpha = \frac{L_\alpha}{2}, x_\gamma, x_\delta\right) - u_\beta\left(x_\alpha = -\frac{L_\alpha}{2}, x_\gamma, x_\delta\right) \\ &= L_\alpha H_{\alpha\beta} \end{aligned} \tag{4.7}$$

where γ and δ refer to the coordinates that span the $\alpha^{\pm}$ face.

The strain matrix H is then defined via the displacements of the nodes at the corners of the unit cell as

$$\begin{aligned}
H_{11} &= \frac{u_x^2 + u_x^3 + u_x^6 + u_x^7 - u_x^1 - u_x^4 - u_x^5 - u_x^8}{4L_x} \\
H_{22} &= \frac{u_y^3 + u_y^4 + u_y^7 + u_y^8 - u_y^1 - u_y^2 - u_y^5 - u_y^6}{4L_y} \\
H_{33} &= \frac{u_z^5 + u_z^6 + u_z^7 + u_z^8 - u_z^1 - u_z^2 - u_z^3 - u_z^4}{4L_z} \\
H_{12} &= \frac{u_x^3 + u_x^4 + u_x^7 + u_x^8 - u_x^1 - u_x^2 - u_x^5 - u_x^6}{4L_y} \\
H_{21} &= \frac{u_y^2 + u_y^3 + u_y^6 + u_y^7 - u_y^1 - u_y^4 - u_y^5 - u_y^8}{4L_x} \\
H_{13} &= \frac{u_x^5 + u_x^6 + u_x^7 + u_x^8 - u_x^1 - u_x^2 - u_x^3 - u_x^4}{4L_z} \\
H_{31} &= \frac{u_z^2 + u_z^3 + u_z^6 + u_z^7 - u_z^1 - u_z^4 - u_z^5 - u_z^8}{4L_x} \\
H_{23} &= \frac{u_y^5 + u_y^6 + u_y^7 + u_y^8 - u_y^1 - u_y^2 - u_y^3 - u_y^4}{4L_z} \\
H_{32} &= \frac{u_z^3 + u_z^4 + u_z^7 + u_z^8 - u_z^1 - u_z^2 - u_z^5 - u_z^6}{4L_u}
\end{aligned} \tag{4.8}$$

where the integrals in the definition of H have been evaluated with the standard one-point quadrature. From the eight corner nodes, there are 24 degrees of freedom (DOF's). There are six strain degrees of freedom, so that constraints must be utilized to eliminate 18 DOF's.

4.1.1 Constraint relations for displacement periodicity

The periodic boundary conditions (PBC) constraints are used to eliminate 12 DOF's as follows. From the x^+ and x^- faces, there are three constraint equations involving the corner nodes

$$u_x^2 - u_x^1 = u_x^3 - u_x^4 \tag{4.9a}$$

$$= u_x^6 - u_x^5 \tag{4.9b}$$

$$= u_x^7 - u_x^8 \tag{4.9c}$$

This leaves one additional x DOF that must be constrained. From the y^+ and y^- faces, there are four constraints that would form a linearly independent set with the first three:

$$u_x^4 - u_x^1 = u_x^8 - u_x^5 \tag{4.10a}$$

$$u_x^4 - u_x^1 = u_x^7 - u_x^6 \tag{4.10b}$$

$$u_x^3 - u_x^2 = u_x^8 - u_x^5 \tag{4.10c}$$

$$u_x^3 - u_x^2 = u_x^7 - u_x^6 \tag{4.10d}$$

Equation (4.10b) is chosen from this set to include in the final set of equations.

Similarly for the z^+ and z^- faces:

$$u_x^5 - u_x^1 = u_x^7 - u_x^3 \tag{4.11a}$$

$$u_x^5 - u_x^1 = u_x^8 - u_x^4 \tag{4.11b}$$

$$u_x^6 - u_x^2 = u_x^7 - u_x^3 \tag{4.11c}$$

$$u_x^6 - u_x^2 = u_x^8 - u_x^4 \tag{4.11d}$$

The constraints from (4.11) are not used in the following, but one of these could be used in place of Equation (4.10b) for an equivalent formulation.

From the four constraints (4.9) and (4.10b), four nodal degrees of freedom are eliminated,

$$u_x^6 = -u_x^1 + u_x^2 + u_x^5 \tag{4.12a}$$

$$u_x^4 = u_x^1 - u_x^2 + u_x^3 \tag{4.12b}$$

$$u_x^8 = -u_x^2 + u_x^3 + u_x^5 \tag{4.12c}$$

$$u_x^7 = -u_x^1 + u_x^3 + u_x^5 \tag{4.12d}$$

This set is chosen for the properties they yield in the complete set of constraint equations.

The y-displacement degree of freedom constraints are similarly formulated:

$$u_y^4 - u_y^1 = u_y^3 - u_y^2 \tag{4.13a}$$

$$= u_y^8 - u_y^5 \tag{4.13b}$$

$$= u_y^7 - u_y^6 \tag{4.13c}$$

One constraint is chosen from the periodic relationships between points on the x^+ and x^- faces,

$$u_y^2 - u_y^1 = u_y^6 - u_y^5 \tag{4.14a}$$

$$u_y^2 - u_y^1 = u_y^7 - u_y^8 \tag{4.14b}$$

$$u_y^3 - u_y^4 = u_y^6 - u_y^5 \tag{4.14c}$$

$$u_y^3 - u_y^4 = u_y^7 - u_y^8 \tag{4.14d}$$

Just as before, Equation (4.14a) is chosen for the current formulation, but equivalent formulations could be developed from the other equations.

From the periodic relationships between points on the z^+ and z^- faces,

$$u_y^5 - u_y^1 = u_y^6 - u_y^2 \tag{4.15a}$$

$$u_y^5 - u_y^1 = u_y^7 - u_y^3 \tag{4.15b}$$

$$u_y^6 - u_y^2 = u_y^8 - u_y^4 \tag{4.15c}$$

$$u_y^7 - u_y^3 = u_y^8 - u_y^4 \tag{4.15d}$$

Again, no constraints are used from Equation (4.15), but an equivalent formulation could be developed by replacing the constraint from (4.14a) with any of these constraints.

As before, four y-displacement degrees of freedom are with the constraints in

Equations (4.13) and (4.14a),

$$u_y^8 = -u_y^1 + u_y^4 + u_y^5 \tag{4.16a}$$

$$u_y^7 = -u_y^1 + u_y^4 + u_y^6 \tag{4.16b}$$

$$u_y^2 = u_y^1 - u_y^5 + u_y^6 \tag{4.16c}$$

$$u_y^3 = u_y^4 - u_y^5 + u_y^6 \tag{4.16d}$$

Finally, the z-displacement degree of freedom constraints are similarly formulated,

$$u_z^5 - u_z^1 = u_z^6 - u_z^2 \tag{4.17a}$$

$$= u_z^7 - u_z^3 \tag{4.17b}$$

$$= u_z^8 - u_z^4 \tag{4.17c}$$

From the periodicity relationships between z-displacement degrees of freedom on the x^+ and x^- faces,

$$u_z^2 - u_z^1 = u_z^3 - u_z^4 \tag{4.18a}$$

$$u_z^2 - u_z^1 = u_z^7 - u_z^8 \tag{4.18b}$$

$$u_z^3 - u_z^4 = u_z^6 - u_z^5 \tag{4.18c}$$

$$u_z^6 - u_z^5 = u_z^7 - u_z^8 \tag{4.18d}$$

As before, Equation (4.18a) is chosen to form one of the four equivalent sets of constraints.

From the periodicity relationships between z-displacement degrees of freedom on the y^+ and y^- faces,

$$u_z^4 - u_z^1 = u_z^3 - u_z^2 \tag{4.19a}$$

$$u_z^4 - u_z^1 = u_z^7 - u_z^6 \tag{4.19b}$$

$$u_z^3 - u_z^2 = u_z^8 - u_z^5 \tag{4.19c}$$

$$u_z^8 - u_z^5 = u_z^7 - u_z^6 \tag{4.19d}$$

As before, no constraints are used from Equation (4.19), but an equivalent formulation could be developed by replacing the constraint from (4.18a) with any of these constraints.

As before, four z-displacement degrees of freedom are with the constraints in Equations (4.17) and (4.18a),

$$u_z^7 = -u_z^1 + u_z^3 + u_z^5 \tag{4.20a}$$

$$u_z^6 = -u_z^1 + u_z^2 + u_z^5 \tag{4.20b}$$

$$u_z^4 = u_z^1 - u_z^2 + u_z^3 \tag{4.20c}$$

$$u_z^8 = u_z^2 - u_z^3 + u_z^5 \tag{4.20d}$$

The strain matrix entries (4.8) can then be simplified by substituting for the eliminated degrees of freedom:

$$\begin{aligned} H_{11} &= \frac{u_x^2 - u_x^1}{L_x} \\ H_{22} &= \frac{u_y^4 - u_y^1}{L_y} \\ H_{33} &= \frac{u_z^5 - u_z^1}{L_z} \\ H_{12} &= \frac{u_x^3 - u_x^2}{L_y} \\ H_{21} &= \frac{u_y^6 - u_y^5}{L_x} \\ H_{13} &= \frac{u_x^5 - u_x^1}{L_z} \\ H_{31} &= \frac{u_z^2 - u_z^1}{L_x} \\ H_{23} &= \frac{u_y^5 - u_y^1}{L_z} \\ H_{32} &= \frac{u_z^3 - u_z^2}{L_y} \end{aligned} \tag{4.21}$$

In matrix form,

$$H = \begin{bmatrix} \frac{u_x^2 - u_x^1}{L_x} & \frac{u_x^3 - u_x^2}{L_y} & \frac{u_x^5 - u_x^1}{L_z} \\ \frac{u_y^6 - u_y^5}{L_x} & \frac{u_y^4 - u_y^1}{L_y} & \frac{u_y^5 - u_y^1}{L_z} \\ \frac{u_z^2 - u_z^1}{L_x} & \frac{u_z^3 - u_z^2}{L_y} & \frac{u_z^5 - u_z^1}{L_z} \end{bmatrix} \tag{4.22}$$

From the periodicity relationships among the displacement degrees of freedom for the unit cell, 12 constraint equations are formed, reducing the number of active degrees of freedom to 12. Of these remaining 12, six more are eliminated by constraining rigid body motion, as detailed in the following section.

4.1.2 Constraints enforcing conservation of momentum

During simulations involving the unit cell in this study, the linear and angular momentum of the cell is controlled by constraining the displacement degrees of freedom of the cell to eliminated rigid body motion. This ensures that the ensemble average of the momenta is zero. The linear and angular momenta are considered separately in the remainder of this section.

4.1.2.1 Constraint relations for linear momentum

To fix the center of mass of the unit cell, the ensemble average of the displacement degrees of freedom in the α-direction is set to zero,

$$\sum_i u_\alpha^i = 0 \tag{4.23}$$

where α is one of x, y, or z. In the x-direction,

$$u_x^1 + u_x^2 + u_x^3 + u_x^4 + u_x^5 + u_x^6 + u_x^7 + u_x^8 = 0 \tag{4.24}$$

Substituting for the previously eliminated degrees of freedom in Equation (4.24) yields,

$$u_x^5 = -u_x^3 \tag{4.25}$$

In the y-direction,

$$u_y^1 + u_y^2 + u_y^3 + u_y^4 + u_y^5 + u_y^6 + u_y^7 + u_y^8 = 0 \tag{4.26}$$

which simplifies to

$$u_y^6 = -u_y^4 \tag{4.27}$$

In the z-direction,

$$u_z^1 + u_z^2 + u_z^3 + u_z^4 + u_z^5 + u_z^6 + u_z^7 + u_z^8 = 0 \tag{4.28}$$

Simplifying as before,

$$u_z^3 = -u_z^5 \tag{4.29}$$

The constraints (4.25),(4.27), and (4.29) produce a simplified strain matrix,

$$H = \begin{bmatrix} \frac{u_x^2 - u_x^1}{L_x} & \frac{u_x^3 - u_x^2}{L_y} & \frac{-u_x^3 - u_x^1}{L_z} \\ \frac{-u_y^4 - u_y^5}{L_x} & \frac{u_y^4 - u_y^1}{L_y} & \frac{u_y^5 - u_y^1}{L_z} \\ \frac{u_z^2 - u_z^1}{L_x} & \frac{-u_z^5 - u_z^2}{L_y} & \frac{u_z^5 - u_z^1}{L_z} \end{bmatrix} \tag{4.30}$$

The nine displacement degrees of freedom in Equation (4.30) are further reduced to six, as follows.

4.1.2.2 Constraint relations for angular momentum

A set of three constraints are imposed to eliminate rigid body rotation of the unit cell by symmetrizing the displacement gradient. To enforce the constraint $H_{12} = H_{21}$,

$$\frac{u_x^3 - u_x^2}{L_y} = \frac{-u_y^4 - u_y^5}{L_x} \tag{4.31}$$

From Equation (4.31),

$$u_x^3 = -\frac{L_y}{L_x}\left(u_y^4 + u_y^5\right) + u_x^2 \tag{4.32}$$

To enforce the symmetry $H_{13} = H_{31}$,

$$\frac{-u_x^3 - u_x^1}{L_z} = \frac{u_z^2 - u_z^1}{L_x} \tag{4.33}$$

From Equation (4.33) and Equation (4.32),

$$\begin{aligned} u_z^2 &= -\frac{L_x}{L_z}\left(u_x^3 + u_x^1\right) + u_z^1 \\ &= \frac{L_y}{L_z}\left(u_y^4 + u_y^5\right) - \frac{L_x}{L_z}\left(u_x^2 + u_x^1\right) + u_z^1 \end{aligned} \tag{4.34}$$

Similarly, for $H_{23} = H_{32}$,

$$\frac{u_y^5 - u_y^1}{L_z} = \frac{-u_z^5 - u_z^2}{L_y} \tag{4.35}$$

Equations (4.35) and (4.34) yield the constraint,

$$\begin{aligned} u_y^5 &= \frac{L_z}{L_y}\left(-u_z^5 - u_z^2\right) + u_y^1 \\ &= \frac{1}{2L_y}\left[L_x\left(u_x^1 + u_x^2\right) + L_y\left(u_y^1 - u_y^4\right) - L_z\left(u_z^1 + u_z^5\right)\right] \end{aligned} \tag{4.36}$$

Finally, substituting back into Equation (4.32) yields,

$$u_x^3 = \frac{1}{2L_x}\left[L_x\left(-u_x^1 + u_x^2\right) - L_y\left(u_y^1 + u_y^4\right) + L_z\left(u_z^1 + u_z^5\right)\right] \tag{4.37}$$

and Equation (4.34) becomes

$$u_z^2 = \frac{1}{2L_z}\left[-L_x\left(u_x^1 + u_x^2\right) + L_y\left(u_y^1 + u_y^4\right) + L_z\left(u_z^1 - u_z^5\right)\right] \tag{4.38}$$

Then, from Equations (4.37), (4.36), and (4.38), the strain matrix entries are finally simplified to,

$$
\begin{aligned}
H_{11} &= \frac{u_x^2 - u_x^1}{L_x} \\
H_{22} &= \frac{u_y^4 - u_y^1}{L_y} \\
H_{33} &= \frac{u_z^5 - u_z^1}{L_z} \\
H_{12} = H_{21} &= \frac{1}{2L_xL_y}\left[-L_x\left(u_x^1 + u_x^2\right) - L_y\left(u_y^1 + u_y^4\right) + L_z\left(u_z^1 + u_z^5\right)\right] \\
H_{13} = H_{31} &= \frac{1}{2L_xL_z}\left[-L_x\left(u_x^1 + u_x^2\right) + L_y\left(u_y^1 + u_y^4\right) - L_z\left(u_z^1 + u_z^5\right)\right] \\
H_{23} = H_{32} &= \frac{1}{2L_yL_z}\left[L_x\left(u_x^1 + u_x^2\right) - L_y\left(u_y^1 + u_y^4\right) - L_z\left(u_z^1 + u_z^5\right)\right]
\end{aligned}
\tag{4.39}
$$

The six remaining degrees of freedom are u_x^1, u_x^2, u_y^1, u_y^4, u_z^1, u_z^5, as illustrated in Figure 4.3.

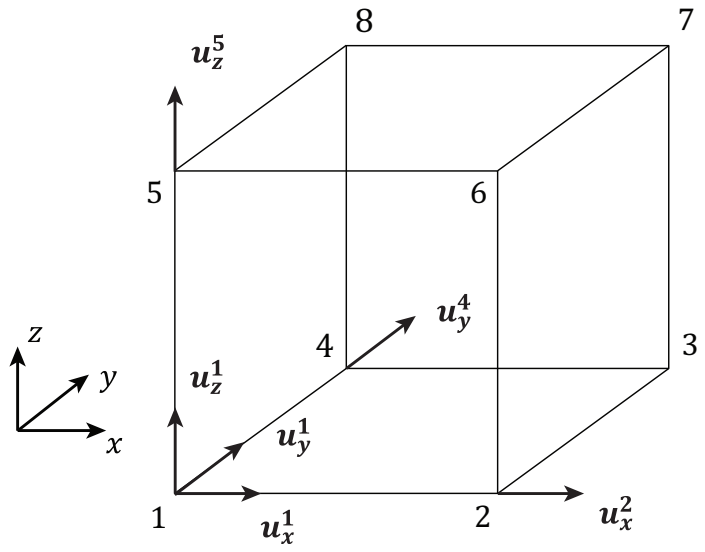

Figure 4.3: Periodic cell with illustration of the active degrees of freedom.

These six displacement degrees of freedom can be specified as boundary conditions to control the ensemble average (macroscale) strain, as described in Section 4.1.4. To apply this formulation to the unit cell, the periodic cell is implemented as a super-element for the geometric discretization, as shown in Figure 4.4.

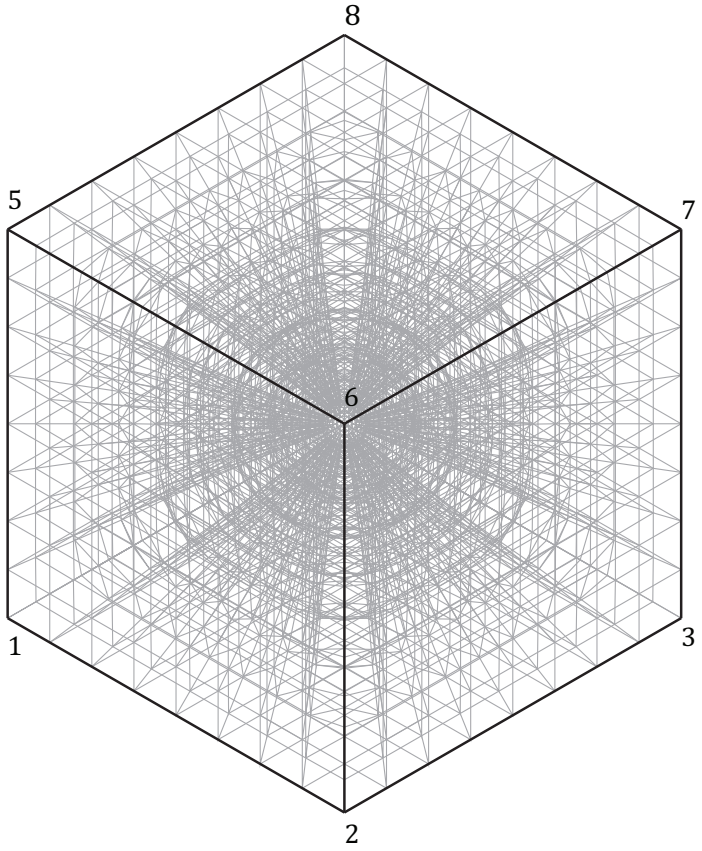

Figure 4.4: Finite element discretization: hexahedral mesh of voided unit cell with super-element for application of periodic boundary conditions.

In applying periodic boundary conditions to the unit cell, the corner nodes of the original mesh are identified with the nodes of the periodic super-element, adding one

new element to the mesh using the existing nodes. The rest of the boundary nodes in the unit cell are prescribed constraints according to the periodic relationships between the nodes. This is discussed in the following section.

4.1.3 Constraint equations for boundary nodes

For the nodes on the boundary of the unit cell, the set of imposed constraints depends on the identification of the nodes as belonging to a corner (vertex), an edge, or a face of the discretized cell. It is noted that corner, edge, and face are mutually exclusive designations. From the previous section, the nodes at the corners of the cell are subjected to the following constraints, written in terms of the six active degrees of freedom:

$$u_x^3 = \frac{1}{2L_x}\left[L_x\left(-u_x^1 + u_x^2\right) - L_y\left(u_y^1 + u_y^4\right) + L_z\left(u_z^1 + u_z^5\right)\right] \tag{4.40a}$$

$$u_x^4 = \frac{1}{2L_x}\left[L_x\left(u_x^1 - u_x^2\right) - L_y\left(u_y^1 + u_y^4\right) + L_z\left(u_z^1 + u_z^5\right)\right] \tag{4.40b}$$

$$u_x^5 = \frac{1}{2L_x}\left[L_x\left(u_x^1 - u_x^2\right) + L_y\left(u_y^1 + u_y^4\right) - L_z\left(u_z^1 + u_z^5\right)\right] \tag{4.40c}$$

$$u_x^6 = \frac{1}{2L_x}\left[L_x\left(-u_x^1 + u_x^2\right) + L_y\left(u_y^1 + u_y^4\right) - L_z\left(u_z^1 + u_z^5\right)\right] \tag{4.40d}$$

$$u_x^7 = -u_x^1 \tag{4.40e}$$

$$u_x^8 = -u_x^2 \tag{4.40f}$$

$$u_y^2 = \frac{1}{2L_y}\left[-L_x\left(u_x^1 + u_x^2\right) + L_y\left(u_y^1 - u_y^4\right) + L_z\left(u_z^1 + u_z^5\right)\right] \tag{4.40g}$$

$$u_y^3 = \frac{1}{2L_y}\left[-L_x\left(u_x^1 + u_x^2\right) + L_y\left(-u_y^1 + u_y^4\right) + L_z\left(u_z^1 + u_z^5\right)\right] \tag{4.40h}$$

$$u_y^5 = \frac{1}{2L_y}\left[L_x\left(u_x^1 + u_x^2\right) + L_y\left(u_y^1 - u_y^4\right) - L_z\left(u_z^1 + u_z^5\right)\right] \tag{4.40i}$$

$$u_y^6 = -u_y^4 \tag{4.40j}$$

$$u_y^7 = -u_y^1 \tag{4.40k}$$

$$u_y^8 = \frac{1}{2L_y}\left[L_x\left(u_x^1 + u_x^2\right) + L_y\left(-u_y^1 + u_y^4\right) - L_z\left(u_z^1 + u_z^5\right)\right] \tag{4.40l}$$

$$u_z^2 = \frac{1}{2L_z}\left[-L_x\left(u_x^1 + u_x^2\right) + L_y\left(u_y^1 + u_y^4\right) + L_z\left(u_z^1 - u_z^5\right)\right] \tag{4.40m}$$

$$u_z^3 = -u_z^5 \tag{4.40n}$$

$$u_z^4 = \frac{1}{2L_z}\left[L_x\left(u_x^1 + u_x^2\right) - L_y\left(u_y^1 + u_y^4\right) + L_z\left(u_z^1 - u_z^5\right)\right] \tag{4.40o}$$

$$u_z^6 = \frac{1}{2L_z}\left[-L_x\left(u_x^1 + u_x^2\right) + L_y\left(u_y^1 + u_y^4\right) + L_z\left(-u_z^1 + u_z^5\right)\right] \tag{4.40p}$$

$$u_z^7 = -u_z^1 \tag{4.40q}$$

$$u_z^8 = \frac{1}{2L_z}\left[L_x\left(u_x^1 + u_x^2\right) - L_y\left(u_y^1 + u_y^4\right) + L_z\left(-u_z^1 + u_z^5\right)\right] \tag{4.40r}$$

The remaining degrees of freedom for the corner nodes can be specified through boundary conditions or left free.

In addition to the 18 constraint equations for the corners of the unit cell, constraints are imposed for nodes on opposing faces that are not coincident with a corner or an edge of the unit cell as

$$u_\alpha^{x+} - u_\alpha^{x-} = u_\alpha^2 - u_\alpha^1 \tag{4.41a}$$

$$u_\alpha^{y+} - u_\alpha^{y-} = u_\alpha^4 - u_\alpha^1 \tag{4.41b}$$

$$u_\alpha^{z+} - u_\alpha^{z-} = u_\alpha^5 - u_\alpha^1 \tag{4.41c}$$

In terms of the six active degrees of freedom, Equation (4.41a) becomes

$$u_x^{x+} - u_x^{x-} = u_x^2 - u_x^1 \tag{4.42a}$$

$$u_y^{x+} - u_y^{x-} = \frac{1}{2L_y}\left[-L_x\left(u_x^1 + u_x^2\right) + L_y\left(u_y^1 - u_y^4\right) + L_z\left(u_z^1 + u_z^5\right)\right] - u_y^1 \tag{4.42b}$$

$$u_z^{x+} - u_z^{x-} = \frac{1}{2L_z}\left[-L_x\left(u_x^1 + u_x^2\right) + L_y\left(u_y^1 + u_y^4\right) + L_z\left(u_z^1 - u_z^5\right)\right] - u_z^1 \tag{4.42c}$$

The constraints in Equation (4.42) are applied to node pairs on opposing x-faces with identical y- and z-coordinates. Non-symmetric meshes can also be accommodated, for example, by substituting for the second node in a pair a degree of freedom tied to the average displacement of a patch of nodes around a given (y, z) point on the opposing face. In this study, the meshes are constructed symmetrically to avoid this complication. For node pairs on the $y+$ and $y-$ or $z+$ and $z-$ faces, similar calculations can be applied to Equations (4.41b) and (4.41c) to produce the appropriate constraints.

The constraints for nodes on opposing edges are formulated with reference to Figure 4.5 below. Three groups of edges are chosen by taking the three edges that meet at the corner node 1 as parent edges. These parent edges are grouped with child edges parallel to the parent and related by a rotation operation. For example, parent edge E_4 is related to children edges E_8, E_6, and E_2 in order rotating counter-clockwise about the positive y-axis. It is noted that this choice of grouping is for notational convenience; other groups can be formed to produce an equivalent formulation. On

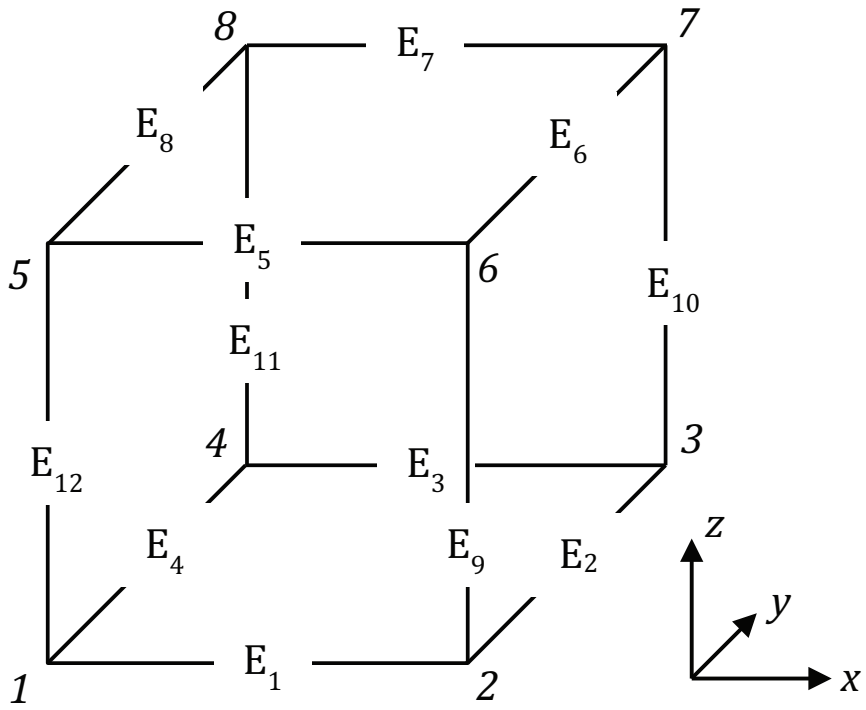

Figure 4.5: Corner and edge numbering for PBC constraints.

the E_4-related edges, the constraints are:

$$u_\alpha^{E_8} - u_\alpha^{E_4} = u_\alpha^5 - u_\alpha^1 \tag{4.43a}$$

$$u_\alpha^{E_6} - u_\alpha^{E_4} = u_\alpha^6 - u_\alpha^1 \tag{4.43b}$$

$$u_\alpha^{E_2} - u_\alpha^{E_4} = u_\alpha^2 - u_\alpha^1 \tag{4.43c}$$

On E_1-related edges, the constraints are:

$$u_\alpha^{E_3} - u_\alpha^{E_1} = u_\alpha^4 - u_\alpha^1 \tag{4.44a}$$

$$u_\alpha^{E_7} - u_\alpha^{E_1} = u_\alpha^8 - u_\alpha^1 \tag{4.44b}$$

$$u_\alpha^{E_5} - u_\alpha^{E_1} = u_\alpha^5 - u_\alpha^1 \tag{4.44c}$$

Finally, on E_{12}-related edges,

$$u_\alpha^{E_9} - u_\alpha^{E_{12}} = u_\alpha^2 - u_\alpha^1 \tag{4.45a}$$

$$u_\alpha^{E_{10}} - u_\alpha^{E_{12}} = u_\alpha^3 - u_\alpha^1 \tag{4.45b}$$

$$u_\alpha^{E_{11}} - u_\alpha^{E_{12}} = u_\alpha^4 - u_\alpha^1 \tag{4.45c}$$

Again, the appropriate substitutions should be made for the eliminated degrees of freedom in the final set of constraint equations so that the constraints are formulated entirely in terms of the six unconstrained degrees of freedom.

4.1.4 Relationships between macroscale strain components and displacement degrees of freedom

In the previous sections, the constrained degrees of freedom u_α^i are formulated in terms of the active degrees of freedom,

$$u_\alpha^i = u_\alpha^i \left(u_x^1, u_x^2, u_y^1, u_y^4, u_z^1, u_z^5\right) \tag{4.46}$$

These active degrees of freedom can, in turn, be defined in terms of the macroscale strain in the unit cell. Doing this allows the imposition of strain-control for simulations of the unit cell. In Equation (4.39) above, the displacement gradient is given as a function of the active displacement degrees of freedom as $\mathbf{H} = \mathbf{f}\left(u_x^1, u_x^2, u_y^1, u_y^4, u_z^1, u_z^5\right) = \mathbf{f}(\mathbf{u})$. This relationship can be inverted, as $\mathbf{u} = \mathbf{f}^{-1}(\mathbf{H})$. In component form,

$$u_x^1 = -\frac{1}{2}\left(L_x H_{11} + L_y H_{12} + L_z H_{13}\right) \tag{4.47a}$$

$$u_x^2 = \frac{1}{2}\left(L_x H_{11} - L_y H_{12} - L_z H_{13}\right) \tag{4.47b}$$

$$u_y^1 = -\frac{1}{2}\left(L_x H_{12} + L_y H_{22} + L_z H_{23}\right) \tag{4.47c}$$

$$u_y^4 = \frac{1}{2}\left(-L_x H_{12} + L_y H_{22} - L_z H_{23}\right) \tag{4.47d}$$

$$u_z^1 = -\frac{1}{2}\left(L_x H_{13} + L_y H_{23} + L_z H_{33}\right) \tag{4.47e}$$

$$u_z^5 = \frac{1}{2}\left(-L_x H_{13} - L_y H_{23} + L_z H_{33}\right) \tag{4.47f}$$

Thus, macroscale strain conditions can be imposed by specifying displacement boundary conditions on the active degrees of freedom. For example, macroscopic loading

with a uniaxial stress state is specified by

$$\begin{aligned} H_{11} &\neq 0 \\ \sigma_{ij} &= 0 \quad \text{for} \quad i \neq 1 \quad \text{and} \quad j \neq 1 \end{aligned} \tag{4.48}$$

For uncoupled shear and normal strain, as with cubic symmetry in the elastic tensor (for example, loading along a [001] axis in tantalum), Equation (4.48) can be satisfied in a simulation by specifying

$$H_{11} \neq 0 \tag{4.49a}$$

$$H_{ij} = 0 \quad \text{for} \quad i \neq j \tag{4.49b}$$

In terms of boundary conditions on the active displacement degrees of freedom, Equation (4.49a) gives

$$u_x^1 = -\frac{1}{2} H_{11} \tag{4.50a}$$

$$u_x^2 = \frac{1}{2} H_{11} \tag{4.50b}$$

Now, in Equation (4.49b), set $H_{12} = 0$ by taking

$$u_x^1 + u_x^2 + u_y^1 + u_y^4 - u_z^1 - u_z^5 = 0 \tag{4.51}$$

Using Equation (4.51), a constraint is imposed on u_z^5,

$$u_z^5 = u_x^1 + u_x^2 + u_y^1 + u_y^4 - u_z^1 \tag{4.52}$$

Next, setting $H_{13} = 0$ yields

$$-u_x^1 - u_x^2 + u_y^1 + u_y^4 + u_z^1 + u_z^5 = 0 \tag{4.53}$$

Equation (4.53) is used to constrain u_y^4,

$$u_y^4 = -u_y^1 \tag{4.54}$$

Similarly for $H_{23} = 0$,

$$u_x^1 + u_x^2 - u_y^1 - u_y^4 + u_z^1 + u_z^5 = 0 \tag{4.55}$$

and

$$u_x^2 = -u_x^1 \tag{4.56}$$

A simulation of deformation with a uniaxial stress state in a periodic unit cell can be performed by specifying the boundary conditions in Equation (4.50), along with the constraint equations from the previous sections and from Equations (4.52), (4.54), and (4.56). The degrees of freedom u_z^1 and u_z^1 are left free in this scenario, corresponding to the normal strains in the transverse directions that are determined according to the mechanics of the uniaxial stress state.

4.1.5 Average stresses in the unit cell

In order to determine the average stress values in the unit cell, the reaction forces for the constraints in Equation (4.47) are used, in the following manner. The virtual work is given in terms of the macroscopic nominal stress and virtual strain as

$$\delta W = \mathbf{P}^{\mathrm{T}} : \delta \mathbf{H} \tag{4.57}$$

In terms of the virtual displacements, Equation (4.57) becomes

$$dW = \left(-\frac{P_{11}}{L_x} - \frac{P_{12}+P_{21}}{2L_y} - \frac{P_{13}+P_{31}}{2L_z} + \frac{(P_{23}+P_{32})\,L_x}{2L_yL_z}\right)\delta u_x^1 + \tag{4.58}$$

$$\left(\frac{P_{11}}{L_x} - \frac{P_{12}+P_{21}}{2L_y} - \frac{P_{13}+P_{31}}{2L_z} + \frac{(P_{23}+P_{32})\,L_x}{2L_yL_z}\right)\delta u_x^2 + \tag{4.59}$$

$$\left(-\frac{P_{22}}{L_y} - \frac{P_{12}+P_{21}}{2L_x} + \frac{(P_{13}+P_{31})\,L_y}{2L_xL_z} - \frac{P_{23}+P_{32}}{2L_z}\right)\delta u_y^1 + \tag{4.60}$$

$$\left(\frac{P_{22}}{L_y} - \frac{P_{12}+P_{21}}{2L_x} + \frac{(P_{13}+P_{31})\,L_y}{2L_xL_z} - \frac{P_{23}+P_{32}}{2L_z}\right)\delta u_y^4 + \tag{4.61}$$

$$\left(-\frac{P_{33}}{L_z} + \frac{(P_{12}+P_{21})\,L_z}{2L_xL_y} - \frac{P_{13}+P_{31}}{2L_x} - \frac{P_{23}+P_{32}}{2L_y}\right)\delta u_z^1 + \tag{4.62}$$

$$\left(\frac{P_{33}}{L_z} + \frac{(P_{12}+P_{21})\,L_z}{2L_xL_y} - \frac{P_{13}+P_{31}}{2L_x} - \frac{P_{23}+P_{32}}{2L_y}\right)\delta u_z^5 \tag{4.63}$$

The virtual work can also be formulated in terms of the nodal reaction forces $\mathbf{r}$ and virtual displacements $\delta\mathbf{u}$ for the unconstrained degrees of freedom as

$$\delta W = \langle \mathbf{r}, \delta\mathbf{u} \rangle \tag{4.64}$$

In component form, Equation (4.64) becomes

$$\delta W = r_x^1\delta u_x^1 + r_x^2\delta u_x^2 + r_y^1\delta u_y^1 + r_y^4\delta u_y^4 + r_z^1\delta u_z^1 + r_z^5\delta u_z^5 \tag{4.65}$$

Equating the two expressions (4.63) and (4.65) for the virtual work yields

$$r_x^1 = -\frac{1}{L_x}P_{11} - \frac{1}{2L_y}(P_{12}+P_{21}) - \frac{1}{2L_z}(P_{13}+P_{31}) + \frac{L_x}{2L_yL_z}(P_{23}+P_{32}) \tag{4.66}$$

$$r_x^2 = \frac{1}{L_x}P_{11} - \frac{1}{2L_y}(P_{12}+P_{21}) - \frac{1}{2L_z}(P_{13}+P_{31}) + \frac{L_x}{2L_yL_z}(P_{23}+P_{32}) \tag{4.67}$$

$$r_y^1 = -\frac{1}{2L_x}(P_{12}+P_{21}) + \frac{L_y}{2L_xL_z}(P_{13}+P_{31}) - \frac{1}{L_y}P_{22} - \frac{1}{2L_z}(P_{23}+P_{32}) \tag{4.68}$$

$$r_y^4 = -\frac{1}{2L_x}(P_{12}+P_{21}) + \frac{L_y}{2L_xL_z}(P_{13}+P_{31}) + \frac{1}{L_y}P_{22} - \frac{1}{2L_z}(P_{23}+P_{32}) \tag{4.69}$$

$$r_z^1 = \frac{L_z}{2L_xL_y}\left(P_{12}+P_{21}\right) - \frac{1}{2L_x}\left(P_{13}+P_{31}\right) - \frac{1}{2L_y}\left(P_{23}+P_{32}\right) - \frac{1}{L_z}P_{33} \tag{4.70}$$

$$r_z^5 = \frac{L_z}{2L_xL_y}\left(P_{12}+P_{21}\right) - \frac{1}{2L_x}\left(P_{13}+P_{31}\right) - \frac{1}{2L_y}\left(P_{23}+P_{32}\right) + \frac{1}{L_z}P_{33} \tag{4.71}$$

Solving Equation (4.71) for the stress components,

$$P_{11} = \frac{1}{2}L_x\left(r_x^2 - r_x^1\right) \tag{4.72a}$$

$$P_{12}+P_{21} = -\frac{1}{2}\left[L_y\left(r_x^1+r_x^2\right) + L_x\left(r_y^1+r_y^4\right)\right] \tag{4.72b}$$

$$P_{13}+P_{31} = -\frac{1}{2}\left[L_z\left(r_x^1+r_x^2\right) + L_x\left(r_z^1+r_z^5\right)\right] \tag{4.72c}$$

$$P_{22} = \frac{1}{2}L_y\left(r_y^4 - r_y^1\right) \tag{4.72d}$$

$$P_{23}+P_{32} = -\frac{1}{2}\left[L_z\left(r_y^1+r_y^4\right) + L_y\left(r_z^1+r_z^5\right)\right] \tag{4.72e}$$

$$P_{33} = \frac{1}{2}L_z\left(r_z^5 - r_z^1\right) \tag{4.72f}$$

At this point, the constraints on the displacement degrees of freedom are defined in terms of the components of $\mathbf{H}$, and the stress components are defined in terms of the reaction forces associated with the displacements. A finite element simulation can be run, specifying $\mathbf{u}$ to achieve a given $\mathbf{H}$, and $\mathbf{P}$ can be obtained from the resulting reaction forces $\mathbf{r}$ to construct the effective macroscopic constitutive relation. Since the First Piola-Kirchhoff stress $\mathbf{P}$ is generally not symmetric, additional relations are needed to solve for the P_{ij} components where $i \neq j$. The symmetric Kirchhoff stress is defined

$$\boldsymbol{\tau} = \mathbf{P} \cdot \mathbf{F}^{\mathrm{T}} \tag{4.73}$$

with $\boldsymbol{\tau} = \boldsymbol{\tau}^{\mathrm{T}}$. This gives the additional constraints on $\mathbf{P}$,

$$\mathbf{P} \cdot \mathbf{F}^{\mathrm{T}} - \mathbf{F} \cdot \mathbf{P}^{\mathrm{T}} = \mathbf{0} \tag{4.74}$$

In component form,

$$\begin{aligned} P_{1j}F_{2j} - F_{1j}P_{2j} &= 0 \\ P_{1j}F_{3j} - F_{1j}P_{3j} &= 0 \\ P_{2j}F_{3j} - F_{2j}P_{3j} &= 0 \end{aligned} \tag{4.75}$$

with $F_{ij} = H_{ij} + \delta_{ij}$. The nine linear equations (4.75) in P_{ij} can be solved to derive a set of expressions for P in terms of r and u. The explicit expressions for the shear stresses P_{ij} are omitted here due to the complexity of the resulting formulae.

4.1.6 Application of PBC Formulae: Uniaxial Tension

An example is given here of the use the above formulation to apply a given deformation. For uniaxial stress plus equibiaxial lateral strain, the following prescription is used. To enforce an equibiaxial strain state in the transverse directions, set $H_{22} = H_{33}$, so that

$$-u_y^1 + u_y^4 + u_z^1 - u_z^5 = 0 \tag{4.76}$$

Then,

$$u_z^1 = u_y^1 \tag{4.77}$$

Eliminate u_x^2, u_y^4, u_z^1 in (4.52) to obtain

$$u_z^5 = -u_y^1 \tag{4.78}$$

The original constraint equations become simplified, and are written in terms of the two active degrees of freedom, u_x^1 and u_y^1 as

$$\begin{aligned}
u_x^3 &= u_x^6 = u_x^7 = -u_x^1 \\
u_x^4 &= u_x^5 = u_x^8 = u_x^1 \\
u_y^2 &= u_y^5 = u_y^6 = u_y^1 \\
u_y^3 &= u_y^7 = u_y^8 = -u_y^1 \\
u_z^2 &= u_z^3 = u_z^4 = u_y^1 \\
u_z^6 &= u_z^7 = u_z^8 = -u_y^1
\end{aligned} \tag{4.79}$$

The strain control in the loading direction is achieved by applying a boundary condition to u_x^1, and u_y^1 is left free, to be determined by the mechanics of the uniaxial stress state.

In Figure 4.6, the results of applying the periodic boundary conditions for uniaxial stress are plotted. The stress-strain response is compared to the application of affine boundary conditions. It is noted that the periodic boundary conditions produce a slightly softer response due to the fact that this imposes less restrictions on the deformation that can be accomodated. The difference in the response between the two scenarios is small due to the fact that the fields are nearly uniform at the boundary

of the cell, so that the imposition of affine boundary conditions only restricts the deformation by a small amount.

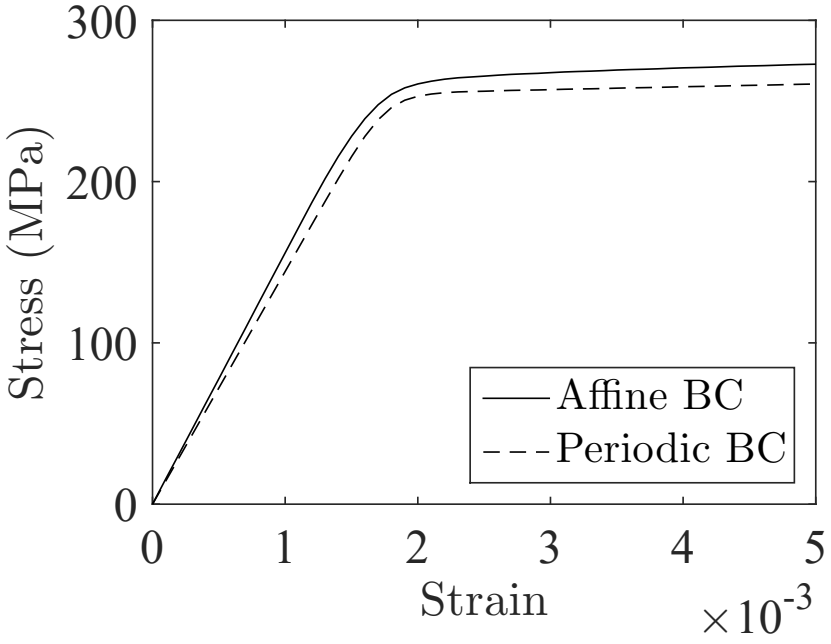

Figure 4.6: Stress-strain curves for uniaxial tension applying affine and periodic boundary conditions.

The periodic boundary conditions are used exclusively in the following sections, as the physical interpretation of a void in a periodic array of voids is more realistic than a void situated in a matrix that deforms homogeneously at the arbitrary cutoff of the cell boundary. The results of the unit cell analyses with periodic boundary conditions is examined in the next section.

4.2 Reults of the Direct Numerical Simulation of the Voided Microstructure

In this section, a summary is given of some key results from the direct numerical simulation of the damage unit cell. The mesh shown in Figure 4.1 is used in these simulations; the undeformed geometry consists of a spherical void with diameter 100μm centered in a cubic unit cell of side length 1mm. This configuration produces an initial void volume fraction of $f \approx 5 \times 10^{-3}$. Periodic boundary conditions are applied to the unit cell, as detailed in Section 4.1. A strain rate of 10^3s^{-1} is applied in the loading (-33) direction, and the stresses in the transverse directions $(-11$ and $-22)$ are controlled to achieve a given stress triaxiality χ, where

$$\chi = \frac{1}{3}\frac{\sigma_{11} + 2\sigma_{22}}{\sigma_{11} - \sigma_{22}} \tag{4.80}$$

This result is derived in Appendix C. A range of triaxiality is considered, from $\chi = 1/3$ (uniaxial stress) at one extreme, to $\chi \approx \infty$ (hydrostatic stress) at the other. Figure 4.7 shows some of the deformed geometries at 1% strain in the loading direction, along with contours of the von Mises equivalent stress.

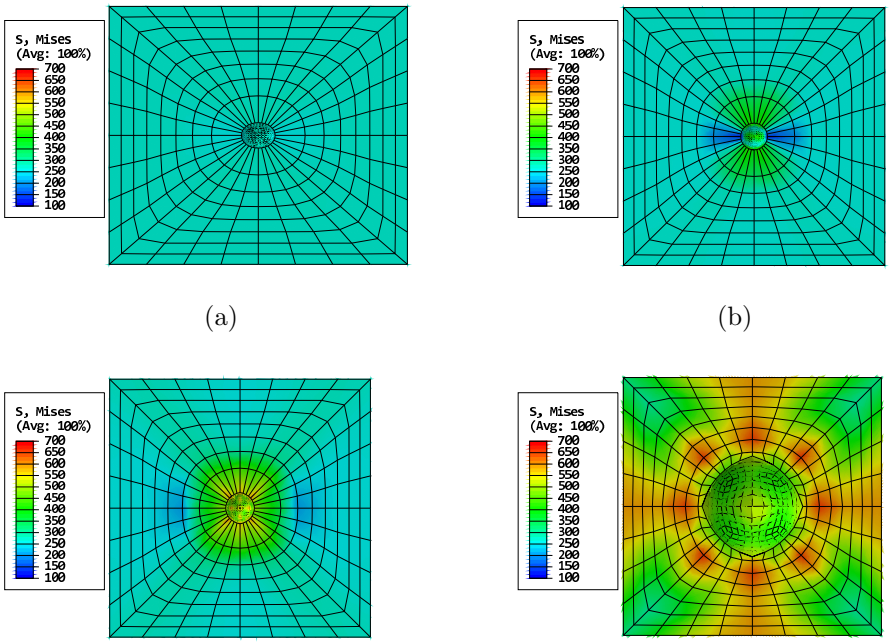

Figure 4.7: Deformed geometry at 1% strain, with contours of von Mises equivalent stresses: (a) $\chi = 1/3$ (deformation magnified 10x), (b) $\chi = 4$, (c) $\chi = 8$, (d) $\chi \approx \infty$.

It is noted that the deformed shape of the void changes from ellipsoidal (e.g., Figure 4.7a) to spherical (Figure 4.7d) with increasing stress triaxiality. It is also significant that the deformation of the void at low triaxiality is relatively small, while the deformation of the void at $\chi \approx \infty$ is much greater. This is in spite of the fact that the average deviatoric stresses are all zero at $\chi \approx \infty$. To simulate this effect, Gurson-type damage models include a contribution of the hydrostatic stress to the plasticity. This is an effective strategy for idealized materials at high triaxiality, but it works less well for varying triaxiality and is not as well suited for materials modeled with

rate-dependent crystal plasticity formulations. On the other hand, DEHF naturally maps equitriaxial macroscale deformation of the damage unit cell to the appropriate plastic driving forces within the cell, as demonstrated in Chapter 5.

The stress-strain curves for the various unit cell simulations are shown in Figure 4.8.

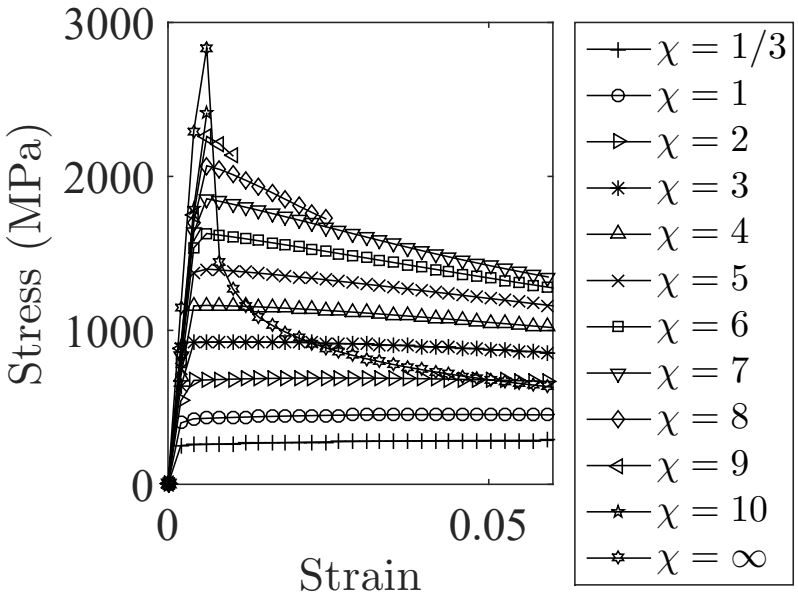

Figure 4.8: Stress-strain curves for unit cell calculations with varying triaxiality.

The stress values in Figure 4.8 are the volume averages of the Second Piola-Kirchhoff stress T_{33} in the unit cells. Similarly, the strains in the figure are the volume averages of the Lagrangian strain. It is noted that the material behavior of the crystal is single-stage hardening for all simulations; however, there is evident soft-

ening for certain cases. For low triaxiality ($\chi < 3$), the ensemble behavior exhibits a hardening trend. For the middle of the triaxiality range ($3 \leq \chi \leq 5$), there is an initial hardening phase followed by softening. For higher triaxialities ($\chi > 5$), there is almost no hardening, with increasingly rapid softening with increasing triaxiality. At the highest finite triaxialities, ($\chi > 7$), the simulations fail due to breakdown of the stress control mechanism in the presence of rapid, severe mesh distortion. The hydrostatic simulation employs only displacement control, so this effect is mitigated, and the simulation progresses, although the results with the severely distorted mesh are not meaningful.

The growth of the void is shown in Figure 4.9a for various triaxialities.

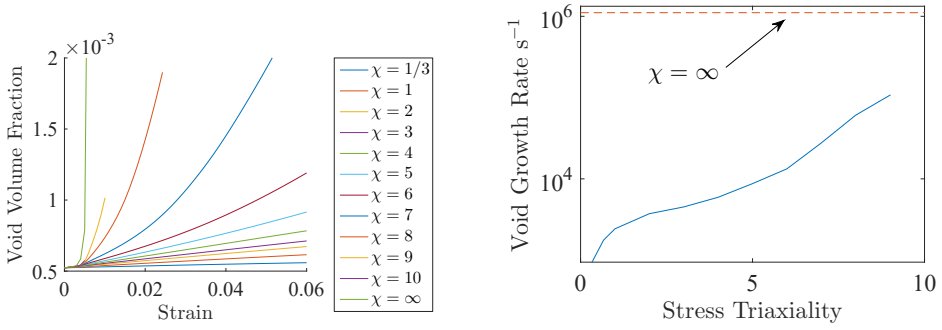

(a) (b)

Figure 4.9: Void growth for varying triaxialities: (a) history of the void volume fraction as a function of strain; and (b) exponential growth rate of void.

In the figure, it is clear that increasing triaxiality produces more rapid growth of

the void volume fraction. At low triaxiality, there is little void growth, up to $chi > 3$. Beyond this level of triaxiality, there is increasingly rapid void growth, up to the limit of $\chi \approx \infty$, where the void growth covers orders of magnitude within the intial 0.1% of the plastic strain. A quantitative analysis of this trend is shown graphically in Figure 4.9b. A least-squares fit is performed to determine the exponential growth rate a, as in

$$f(t) = f_0 \exp(at) \tag{4.81}$$

The trend toward increasing growth rate with increasing triaxiality is clearly evident in Figure 4.9b, with a fairly consistent pattern for $\chi \geq 3$. It is also clear that accurately measuring such a growth rate is increasingly difficult at high triaxiality, where the states of interest lie. This casts some doubt on the efficacy of the method of parametric homogenization from microscale numerical simulations for this problem. Alternatively, issues of non-convergent mesh sensitivity and numerical instability of the microscale finite element discretization can be avoided completely when DEHF is employed, as evidenced in the following chapter.

Chapter 5

Application of DEHF to Crystal Plasticity

In this chapter, the application of DEHF to the problem of coupled crystal plasticity and damage evolution is examined. First, a few examples are given elucidating the importance of considering the higher-order moments of the microscale mechanical fields. Next, the correspondence of the macroscale quantities to the microstructural characterization as given by the Eshelby solution for an ellipsoidal inhomogeneity is considered, and the relevant expressions are derived.

5.1 Distribution-Enhanced Treatment of the Microscale Mechanical Fields

In this section, several examples of inhomogeneous microscale mechanical fields and their macroscale representations are examined. It is shown that higher-order moments are significant to the elastic and plastic response of the material. The significance of the absence of higher-order descriptions of these fields ranges from inaccuracy in the prediction of the magnitude of the stress with increasing heterogeneity in Section 5.1.2, to errors of arbitrary scale in the prediction of the dissipation and qualitatively incorrect predictions of the plastic driving forces with increasing void volume fraction in Section 5.1.3.

5.1.1 Application: Lagrangian Strain

For a simple example of the importance of higher-order descriptors of the mechanical fields, the Lagrangian strain is studied first. In the voided microstructure, the displacement and displacement gradient fields are microscopically inhomogeneous. The Lagrangian strain, being a nonlinear function of the displacement gradient, requires a higher-order description to be consistent with the microscale. The details are given in what follows.

For a given microscale displacement field,

$$\mathbf{u}(\mathbf{X}) = \mathbf{x}(\mathbf{X}) - \mathbf{X} \tag{5.1}$$

where $\mathbf{x}$ is the position at time t of the material point $\mathbf{X}$. The gradient of this field is given

$$\mathbf{H} = \frac{\partial \mathbf{u}}{\mathbf{X}} = \frac{\partial \mathbf{x}}{\partial \mathbf{X}} - \frac{\partial \mathbf{X}}{\partial \mathbf{X}} = \mathbf{F} - \mathbf{I} \tag{5.2}$$

The symmetric part of the displacement gradient $\mathbf{H}$ defines a strain measure; a component of this tensor gives the *engineering strain* in a uniaxial deformation test. The finite deformation Lagrangian strain is a nonlinear function of $\mathbf{H}$,

$$\begin{aligned} \mathbf{E} &= \frac{1}{2}\left(\mathbf{F}^{\mathrm{T}} \cdot \mathbf{F} - \mathbf{I}\right) \\ &= \frac{1}{2}\left(\mathbf{H} + \mathbf{H}^{\mathrm{T}} + \mathbf{H}^{\mathrm{T}} \cdot \mathbf{H}\right) \end{aligned} \tag{5.3}$$

The deformation gradient is multiplicatively decomposed into elastic and plastic parts, with

$$\mathbf{F} = \mathbf{F}^e \cdot \mathbf{F}^p \tag{5.4}$$

The elastic Lagrangian strain is defined,

$$\begin{aligned} \mathbf{E}^e &= \frac{1}{2}\left(\mathbf{F}^{e\mathrm{T}} \cdot \mathbf{F}^e - \mathbf{I}\right) \\ &= \frac{1}{2}\left(\mathbf{H}^e + \mathbf{H}^{e\mathrm{T}} + \mathbf{H}^{e\mathrm{T}} \cdot \mathbf{H}^e\right) \end{aligned} \tag{5.5}$$

with $\mathbf{F}^e = \mathbf{H}^e + \mathbf{I}$.

The derivatives of $\mathbf{E}^e$ with respect to $\mathbf{H}^e$ evaluated at $\mathbf{H}^e = \mathbf{0}$ are zero, except

$$\left.\frac{\partial E^e_{ij}}{\partial H^e_{ij}}\right|_{\mathbf{H}^e=\mathbf{0}} = \left.\frac{\partial E^e_{ij}}{\partial H^e_{ji}}\right|_{\mathbf{H}^e=\mathbf{0}} = \frac{1}{2} \tag{5.6}$$

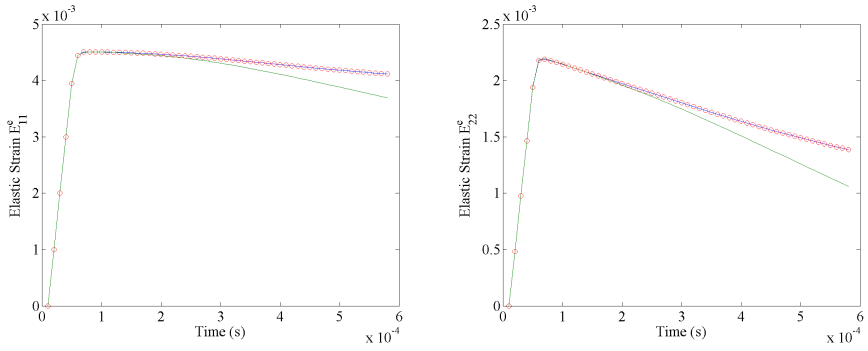

(a) (b)

Figure 5.1: $\mu^1_{E^e_{ji}}$ via volume integration (blue line), via Equation (5.9) (red circles), and $\hat{E}^e_{ij}\,(\mu^1_{\mathbf{H}^e})$ via Equation (5.10) (green line)

.

$$\left.\frac{\partial^2 E^e_{ij}}{\partial H^e_{ki}\partial H^e_{kj}}\right|_{\mathbf{H^e=0}} = \left.\frac{\partial^2 E^e_{ij}}{\partial H^e_{kj}\partial H^e_{ki}}\right|_{\mathbf{H^e=0}} = \frac{1}{2} \tag{5.7}$$

The first moment of E^e_{ij} is

$$\begin{aligned}\mu^1_{E^e_{ij}} =& E^e_{ij}\,(0) + \mu^1_{H^e_{ij}}\left(\left.\frac{\partial E^e_{ij}}{\partial H^e_{ij}}\right|_{\mathbf{H^e=0}} + \left.\frac{\partial E^e_{ij}}{\partial H^e_{ji}}\right|_{\mathbf{H^e=0}}\right)\\ &+ \frac{1}{2}\left(\mu^2_{H^e_{ki}H^e_{kj}}\left.\frac{\partial^2 E^e_{ij}}{\partial H^e_{ki}\partial H^e_{kj}}\right|_{\mathbf{H^e=0}} + \mu^2_{H^e_{kj}H^e_{ki}}\left.\frac{\partial^2 E^e_{ij}}{\partial H^e_{kj}\partial H^e_{ki}}\right|_{\mathbf{H^e=0}}\right)\end{aligned} \tag{5.8}$$

$$\mu^1_{E^e_{ij}} = \frac{1}{2}\left(\mu^1_{H^e_{ij}} + \mu^1_{H^e_{ji}} + \mu^2_{H^e_{kj}H^e_{ki}}\right) \tag{5.9}$$

It is noted that this expression can give rise to significantly different effective values of E^e_{ij} than if one were to calculate the effective value as

$$\hat{E}^e_{ij} = \frac{1}{2}\left(\mu^1_{H^e_{ij}} + \mu^1_{H^e_{ji}} + \mu^1_{H^e_{kj}}\mu^1_{H^e_{ki}}\right) \tag{5.10}$$

In Figure 5.1, the results of Equations (5.9) and (5.10) are plotted for illustration. It

is seen clearly in the figure that the effects of the nonlinearity of the elastic Lagrangian strain in the elastic displacement gradient can be significant, and that the evolution of the inhomogeneity in the elastic displacement gradient makes it infeasible to map the elastic Lagrangian strain to a function of only the average of the elastic displacement gradient. It is thus necessary to include the moment of order two in Equation (5.9) in order to accurately represent the average elastic Lagrangian strain as a function of the elastic displacement gradient.

5.1.2 Application: Stress

A more complicated example of the application of DEHF to crystal plasticity is the treatment of the stress. The Second Piola-Kirchhoff stress with respect to the intermediate configuration is given by,

$$\begin{aligned} T^*_{ij} =& L_{ijkl}\left(E^e_{kl} - A_{kl}\Delta\theta\right) \\ =& \left(L^0_{ijkl} + M_{ijkl}\Delta\theta\right)\left[\frac{1}{2}\left(F^e_{pk}F^e_{pl} - \delta_{kl}\right) - A_{kl}\Delta\theta\right] \\ =& \frac{1}{2}\left(L^0_{ijkl}F^e_{pk}F^e_{pl} - L^0_{ijkk}\right) - L^0_{ijkl}A_{kl}\Delta\theta \\ &+ \frac{1}{2}\left(M_{ijkl}\Delta\theta F^e_{pk}F^e_{pl} - M_{ijkk}\Delta\theta\right) - M_{ijkl}A_{kl}\left(\Delta\theta\right)^2 \end{aligned} \tag{5.11}$$

where $\mathbb{L}$ is the elasticity tensor, $\mathbf{A}$ is the thermal expansion tensor, and $\Delta\theta$ is the change in temperature from the reference state. The tensor $\mathbb{L}^0$ is the elasticity tensor at 0K, and $\mathbb{M}$ is the change in the elastic constants with temperature. To simplify

the development, the notation is introduced,

$$q^{T^*} = \left(\mathbb{L}^0, \mathbb{M}, \mathbf{A}, \mathbf{F}^e, \Delta\theta\right) \tag{5.12}$$

In order to compute the moment-expansion based approximations, all of the partial derivatives of the stress must be computed. The first-order partial derivatives of the stress are

$$\frac{\partial T^*_{ij}}{\partial L^0_{mnkl}} = \frac{1}{2}\left(F^e_{pk}F^e_{pl}\delta_{im}\delta_{jn} - \delta_{im}\delta_{jn}\delta_{kl}\right) - A_{kl}\Delta\theta\delta_{im}\delta_{jn} \tag{5.13}$$

$$\frac{\partial T^*_{ij}}{\partial M_{mnkl}} = \frac{1}{2}\left(F^e_{pk}F^e_{pl}\Delta\theta\delta_{im}\delta_{jn} - \Delta\theta\delta_{im}\delta_{jn}\delta_{kl}\right) - A_{kl}\left(\Delta\theta\right)^2\delta_{im}\delta_{jn} \tag{5.14}$$

$$\begin{aligned}\frac{\partial T^*_{ij}}{\partial F^e_{mn}} =& \frac{1}{2}L^0_{ijnk}F^e_{mk} + \frac{1}{2}L^0_{ijkn}F^e_{mk} + M_{ijnk}F^e_{mk}\Delta\theta + M_{ijkn}F^e_{mk}\Delta\theta \\ =& L^0_{ijnk}F^e_{mk} + M_{ijnk}F^e_{mk}\Delta\theta\end{aligned} \tag{5.15}$$

$$\frac{\partial T^*_{ij}}{\partial A_{kl}} = -L^0_{ijkl}\Delta\theta - M_{ijkl}\left(\Delta\theta\right)^2 \tag{5.16}$$

$$\frac{\partial T^*_{ij}}{\partial \Delta\theta} = -L^0_{ijkl}A_{kl} + \frac{1}{2}\left(M_{ijkl}F^e_{pk}F^e_{pl} - M_{ijkk}\right) - 2M_{ijkl}A_{kl}\Delta\theta \tag{5.17}$$

The nonzero second-order partial derivatives are

$$\begin{aligned}\frac{\partial^2 T^*_{ij}}{\partial L^0_{mnkl}\partial F^e_{qr}} =& \frac{1}{2}\left(F^e_{ql}\delta_{kr}\delta_{im}\delta_{jn} + F^e_{qk}\delta_{lr}\delta_{im}\delta_{jn}\right) \\ =& F^e_{qk}\delta_{lr}\delta_{im}\delta_{jn}\end{aligned} \tag{5.18}$$

$$\frac{\partial^2 T^*_{ij}}{\partial L^0_{mnkl}\partial A_{qr}} = -\Delta\theta\delta_{kq}\delta_{lr}\delta_{im}\delta_{jn} \tag{5.19}$$

$$\frac{\partial^2 T^*_{ij}}{\partial L^0_{mnkl}\partial \Delta\theta} = -A_{kl}\delta_{im}\delta_{jn} \tag{5.20}$$

$$\frac{\partial^2 T^*_{ij}}{\partial M_{mnkl}\partial F^e_{qr}} = F^e_{qk}\Delta\theta\delta_{lr}\delta_{im}\delta_{jn} \tag{5.21}$$

$$\frac{\partial^2 T^*_{ij}}{\partial M_{mnkl}\partial A_{qr}} = -\left(\Delta\theta\right)^2 \delta_{kq}\delta_{lr}\delta_{im}\delta_{jn} \tag{5.22}$$

$$\frac{\partial^2 T^*_{ij}}{\partial M_{mnkl}\partial \Delta\theta} = -2A_{kl}\Delta\theta\delta_{im}\delta_{jn} \tag{5.23}$$

$$\frac{\partial^2 T^*_{ij}}{\partial F^e_{mn}\partial F^e_{pq}} = \left(L^0_{ijnq} + M_{ijnq}\Delta\theta\right)\delta_{mp} \tag{5.24}$$

$$\frac{\partial^2 T^*_{ij}}{\partial F^e_{mn}\partial \Delta\theta} = M_{ijnk}F^e_{mk} \tag{5.25}$$

$$\frac{\partial^2 T^*_{ij}}{\partial A_{kl}\partial \Delta\theta} = -L^0_{ijkl} - 2M_{ijkl}\Delta\theta \tag{5.26}$$

$$\frac{\partial^2 T^*_{ij}}{\partial \left(\Delta\theta\right)^2} = -2M_{ijkl}A_{kl} \tag{5.27}$$

The nonzero third-order partial derivatives are

$$\frac{\partial^3 T^*_{ij}}{\partial L^0_{mnkl}\partial F^e_{qr}\partial F^e_{st}} = \delta_{qs}\delta_{kt}\delta_{lr}\delta_{im}\delta_{jn} \tag{5.28}$$

$$\frac{\partial^3 T^*_{ij}}{\partial L^0_{mnkl}\partial A_{qr}\partial \Delta\theta} = -\delta_{kq}\delta_{lr}\delta_{im}\delta_{jn} \tag{5.29}$$

$$\frac{\partial^3 T^*_{ij}}{\partial M_{mnkl}\partial F^e_{qr}\partial F^e_{st}} = \delta_{qs}\delta_{kt}\Delta\theta\delta_{lr}\delta_{im}\delta_{jn} \tag{5.30}$$

$$\frac{\partial^3 T^*_{ij}}{\partial M_{mnkl}\partial F^e_{qr}\partial \Delta\theta} = F^e_{qk}\delta_{lr}\delta_{im}\delta_{jn} \tag{5.31}$$

$$\frac{\partial^3 T^*_{ij}}{\partial M_{mnkl}\partial A_{qr}\partial \Delta\theta} = -2\Delta\theta\delta_{kq}\delta_{lr}\delta_{im}\delta_{jn} \tag{5.32}$$

$$\frac{\partial^3 T^*_{ij}}{\partial F^e_{mn}\partial F^e_{pq}\partial \Delta\theta} = M_{ijnq}\delta_{mp} \tag{5.33}$$

$$\frac{\partial^3 T^*_{ij}}{\partial A_{kl}\partial \left(\Delta\theta\right)^2} = -2M_{ijkl} \tag{5.34}$$

The nonzero fourth-order partial derivatives are

$$\frac{\partial^4 T^*_{ij}}{\partial M_{mnkl}\partial F^e_{qr}\partial F^e_{st}\partial \Delta\theta} = \delta_{qs}\delta_{kt}\delta_{lr}\delta_{im}\delta_{jn} \tag{5.35}$$

$$\frac{\partial^4 T^*_{ij}}{\partial M_{mnkl}\partial A_{qr}\left(\partial\Delta\theta\right)^2} = -2\delta_{kq}\delta_{lr}\delta_{im}\delta_{jn} \tag{5.36}$$

The moment expansion for the first moment of the stress is thus,

$$\begin{aligned}
\mu^1_{T^*_{ij}} = &\left(\mu^1_{L^0_{ijkl}} + \mu^1_{M_{ijkl}}\mu^1_{\Delta\theta}\right)\left[\frac{1}{2}\left(\mu^1_{F^e_{pk}}\mu^1_{F^e_{pl}} - \delta_{kl}\right) - \mu^1_{A_{kl}}\mu^1_{\Delta\theta}\right] \\
&+ \frac{1}{2}\left[\mu^1_{F^e_{qk}}\hat{\mu}^2_{L^0_{ijkl},F^e_{ql}} - \mu^1_{\Delta\theta}\hat{\mu}^2_{L^0_{ijkl},A_{kl}} - \mu^1_{A_{kl}}\hat{\mu}^2_{L^0_{ijkl},\Delta\theta}\right. \\
&+ \mu^1_{F^e_{qk}}\mu^1_{\Delta\theta}\hat{\mu}^2_{M_{ijkl},F^e_{ql}} - \left(\mu^1_{\Delta\theta}\right)^2\hat{\mu}^2_{M_{ijkl},A_{kl}} - \mu^1_{A_{kl}}\mu^1_{\Delta\theta}\hat{\mu}^2_{M_{ijkl},\Delta\theta} \\
&+ \left(\mu^1_{L^0_{ijnk}} + \mu^1_{M_{ijkl}}\mu^1_{\Delta\theta}\right)\hat{\mu}^2_{F^e_{mk},F^e_{ml}} + \mu^1_{M_{ijkl}}\mu^1_{F^e_{ml}}\hat{\mu}^2_{F^e_{mk},\Delta\theta} \\
&\left. - \left(\mu^1_{L^0_{ijkl}} + 2\mu^1_{M_{ijkl}}\mu^1_{\Delta\theta}\right)\hat{\mu}^2_{A_{kl},\Delta\theta} - 2\mu^1_{M_{ijkl}}\mu^1_{A_{kl}}\hat{\mu}^2_{\Delta\theta,\Delta\theta}\right] \\
&+ \frac{1}{6}\left[\hat{\mu}^3_{L^0_{ijkl},F^e_{ml},F^e_{mk}} - \hat{\mu}^3_{L^0_{ijkl},A_{kl},\Delta\theta} + \left(\hat{\mu}^3_{M_{ijkl},F^e_{ml},F^e_{mk}} - 2\hat{\mu}^3_{M_{ijkl},A_{kl},\Delta\theta}\right)\mu^1_{\Delta\theta}\right. \\
&\left. + \hat{\mu}^3_{M_{ijkl},F^e_{ml},\Delta\theta}\mu^1_{F^e_{mk}} + \left(\hat{\mu}^3_{F^e_{mk},F^e_{ml},\Delta\theta} - 2\hat{\mu}^3_{A_{kl},\Delta\theta,\Delta\theta}\right)\mu^1_{M_{ijkl}}\right] \\
&+ \frac{1}{24}\left(\hat{\mu}^4_{M_{ijkl},F^e_{ql},F^e_{qk},\Delta\theta} - 2\hat{\mu}^4_{M_{ijkl},A_{kl},\Delta\theta,\Delta\theta}\right)
\end{aligned} \tag{5.37}$$

Thus, the stress has a finite moment expansion in terms of its constituent variables, and can be calculated exactly. However, (5.37) is a complicated expression that would be very expensive to compute. The moment expansion can be truncated at any arbitrary order to construct an approximation that is computationally feasible. Two such truncations, of orders one and two, are plotted in Figure 5.2.

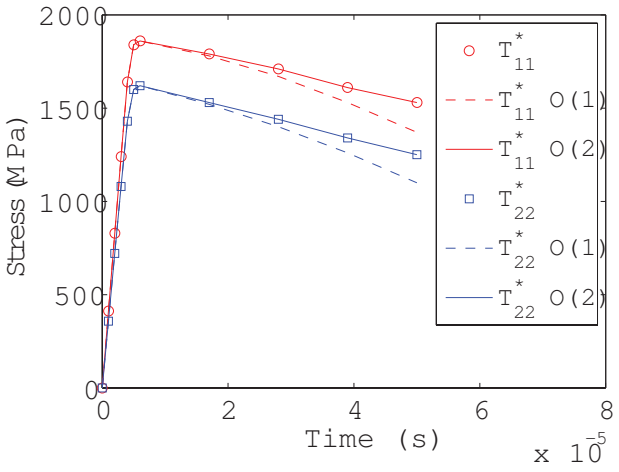

Figure 5.2: The first- and second-order moment expansion approximations of the components of the average stress T^* compared with the direct numerical calculation.

As seen in the figure, the first-order approximation of the stress departs from the actual value significantly, and is not a viable option. The second-order approximation, on the other hand, agrees quite well with the full field calculation, and could be used in this scenario with minimal error. Determination of the appropriate truncation for the moment expansion expressions is a straightforward task in this case. Given expressions for the higher order moment variables, the contributions of each term can be approximated to determine the relative weight of its contribution. This could be done adaptively during a simulation to maintain a compact expression throughout the history, expanding to a more complex approximation only as needed.

5.1.3 Plastic Dissipation

The treatment of the microscale distributions with higher-order descriptions has important implications for thermodynamics, as well. As an example, the plastic dissipation is considered next.

Given the multiplicative decomposition of the deformation gradient $\mathbf{F} = \mathbf{F}^e\mathbf{F}^p$, the time derivative of the deformation gradient can be written as,

$$\dot{\mathbf{F}} = \dot{\mathbf{F}}^e\mathbf{F}^p + \mathbf{F}^e\dot{\mathbf{F}}^p \tag{5.38}$$

The internal power is written in the intermediate configuration as

$$\dot{\mathcal{U}} = \int_{\Omega^*} \mathbf{T}^* : \left(\dot{\mathbf{E}}^e + \mathbf{C}^e\mathbf{L}^{p*}\right) d\mathbf{X}^* \tag{5.39}$$

Given the expression for the stress in Equation (5.11),

$$\begin{aligned}
\dot{\mathcal{U}} &= \int_{\Omega_0} \left(\mathbb{L}^0 + \mathbb{M}\Delta\theta\right) : \left(\dot{\mathbf{E}}^e + \mathbf{C}^e\mathbf{L}^{p*}\right) \otimes \left(\mathbf{E}^e - \mathbf{A}\Delta\theta\right) d\mathbf{X} \\
&= \int_{\Omega_0} \Big(\mathbb{L}^0 : \dot{\mathbf{E}}^e \otimes \mathbf{E}^e + \mathbb{L}^0 : \mathbf{C}^e\mathbf{L}^{p*} \otimes \mathbf{E}^e \\
&\qquad -\mathbb{L}^0 : \dot{\mathbf{E}}^e \otimes \mathbf{A}\Delta\theta - \mathbb{L}^0 : \mathbf{C}^e\mathbf{L}^{p*} \otimes \mathbf{A}\Delta\theta \\
&\qquad +\mathbb{M}\Delta\theta : \dot{\mathbf{E}}^e \otimes \mathbf{E}^e + \mathbb{M}\Delta\theta : \mathbf{C}^e\mathbf{L}^{p*} \otimes \mathbf{E}^e \\
&\qquad -\mathbb{M}\Delta\theta : \dot{\mathbf{E}}^e \otimes \mathbf{A}\Delta\theta - \mathbb{M}\Delta\theta : \mathbf{C}^e\mathbf{L}^{p*} \otimes \mathbf{A}\Delta\theta\Big)\, d\mathbf{X}
\end{aligned} \tag{5.40}$$

The power is then additively decomposed into elastic and plastic parts,

$$\dot{\mathcal{U}} = \dot{W}^e + \dot{W}^p \tag{5.41}$$

Using the shorthand for the variables appearing in the expression for the elastic power,

$$\mathbf{q}^e = \left(\mathbb{L}^0, \mathbb{M}, \mathbf{A}, \mathbf{F}^e, \dot{\mathbf{F}}^e, \Delta\theta\right) \tag{5.42}$$

the moment expansion of the elastic power is

$$\dot{W}^e = \dot{W}^e\left(\mu^1_{\mathbf{q}^e}\right) + \left.\frac{\partial^2 \dot{W}^e}{\partial \mathbf{q}^e \otimes \partial \mathbf{q}^e}\right|_{\mathbf{q}^e = \mu^1_{\mathbf{q}^e}} : \hat{\mu}^2_{\mathbf{q}^e \otimes \mathbf{q}^e} + \text{h.o.t.} \tag{5.43}$$

Similarly for the plastic power, the notation for the variables is

$$\mathbf{q}^p = \left(\mathbb{L}^0, \mathbb{M}, \mathbf{A}, \mathbf{F}^e, \mathbf{F}^p, \dot{\mathbf{F}}^p, \mu^1_{\Delta\theta}\right) \tag{5.44}$$

The expression for the moment expansion of the plastic power is

$$\dot{W}^p = \dot{W}^p\left(\mu^1_{\mathbf{q}^p}\right) + \left.\frac{\partial^2 \dot{W}^p}{\partial \mathbf{q}^p \otimes \partial \mathbf{q}^p}\right|_{\mathbf{q}^p = \mu^1_{\mathbf{q}^p}} : \hat{\mu}^2_{\mathbf{q}^p \otimes \mathbf{q}^e} + \text{h.o.t.} \tag{5.45}$$

The inadequacy of representing the elastic, plastic, and total energy densities by a function of the averages of the constituents is demonstrated in Figure 5.3. In the figure, it is clearly seen that the energy densities predicted by the first-order approximation are significantly different than those of the full-field solution. Furthermore, these differences are growing in time, suggesting that the error in the approximation may be unbounded. The approximation of the total internal energy is even qualitatively incorrect for the first-order approximation, which predicts a decrease beyond a certain point in the history, while the full-field solution clearly exhibits the correct monotonic increase. Part of the error comes from an over-prediction of the decrease in the elastic energy due to the prediction of lower elastic strains and stresses, as

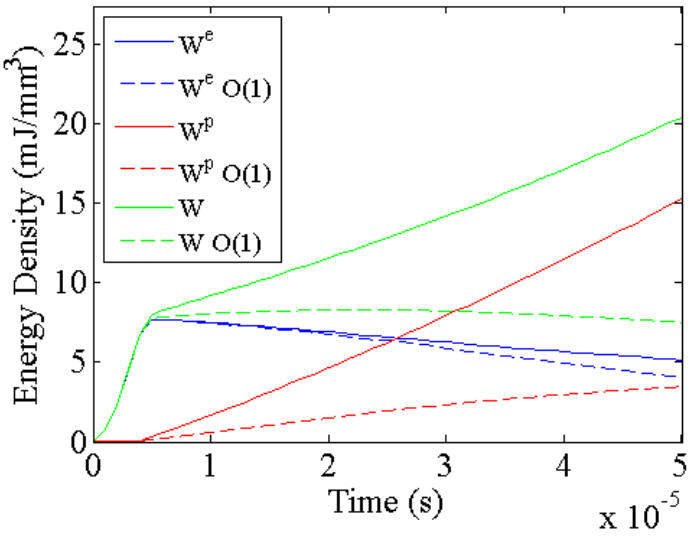

Figure 5.3: The first-order moment expansion approximations of the elastic, plastic, and total energy densities compared with the direct numerical calculations.

described in the previous sections. An even larger discrepancy is seen in the plastic dissipation, evidenced by the diverging curves in Figure 5.3. This is due to the approximation of the plastic slip rate. This rate is given by

$$\dot{\gamma}^{\alpha} = \rho_M^{\alpha} b^2 \nu_0 \exp\left\{ -\frac{\Delta G}{k_B \theta}\left[1 - \left(\frac{\tau^{\alpha} - s_a^{\alpha}\frac{\mu}{\mu_0}}{s_t^{\alpha}\frac{\mu}{\mu_0}}\right)^{p}\right]^{q}\right\} \tag{5.46}$$

The partial derivatives of Equation (5.46), with respect to, for example, the resolved shear stress τ^{α} are nonzero for all orders. This means that as the heterogeneity of the microscale stress field changes over time, there are significant contributions from higher-order moments even beyond order two. To handle these contributions, a new scheme is introduced, whereby the flow function is approximated by a Bernstein polynomial expansion,

$$\dot{\gamma}^{\alpha} \approx \sum_{k=0}^{m} a_k \tau^{\alpha k} \tag{5.47}$$

The expressions for the coefficients a_k are derived in Appendix A. In short, the Bernstein polynomial approximation of order m of the flow rule requires $m+1$ evaluations of the flow function. This approximation then supports a moment expansion of order m, as well.//

To underscore the importance of the higher-order moment variables, normalized values of the variables $\tau^{\alpha k}$ appearing in Equation (5.47) are plotted in Figure 5.4 as a function of void radius for a spherical void. The figure shows that the contribution of the first-order moment variable decreases with increasing void volume. Thus, the first-order approximation predicts a decrease in the plastic dissipation for a given stress with increasing void volume, as opposed to the full-field solution, wherein the

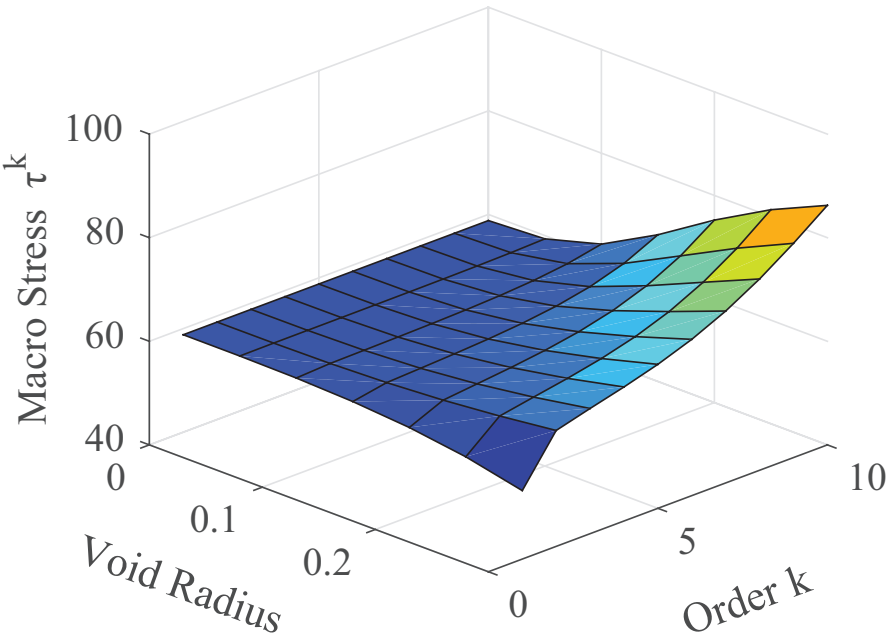

Figure 5.4: Average resolved shear stress as a function of void radius and expansion order

plastic dissipation increases with increasing void volume for a given applied stress. In Figure 5.4, it is noted that the moment variables of higher order increase for increasing void volume, and including these variables enables prediction of the correct trend.

5.2 Calculation of the Macroscale Mechanical Variables

5.2.1 Eshelby Solution

In the implementation of DEHF in Chapter 2, expressions were derived that gave the higher-order moment variables in terms of the microstructure and the first-order (applied) fields. A similar strategy is presented in this section for the case of the voided microstructure. The crux of the method is to apply the Eshelby solution [7] for an ellipsoidal inhomogeneity, such as that shown in Figure 5.5, where the inhomogeneity is taken to have elastic constants equal to zero to model a void.

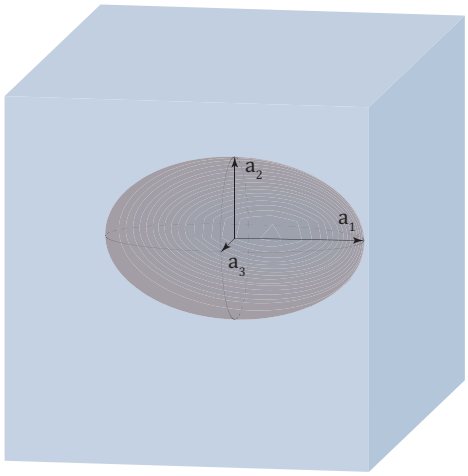

Figure 5.5: Ellipsoidal inhomogeneity with major semi-axes a_1, a_2, and a_3.

In the inhomogeneity problem, given a macroscale elastic strain $\boldsymbol{\Xi}^e$, an *eigenstrain* field $\tilde{\mathbf{E}}$ is sought such that

$$\mathbb{L}_{\text{matrix}} : \left[\boldsymbol{\Xi}^e + \mathbf{E}^e\left(\mathbf{X}\right) - \tilde{\mathbf{E}}\right] = \mathbb{L}_{\text{inhom}} : \left[\boldsymbol{\Xi}^e + \mathbf{E}^e\left(\mathbf{X}\right)\right] \tag{5.48}$$

The elastic constitutive relation is

$$\mathbf{T}^* = \mathbb{L} : \mathbf{E}^e \tag{5.49}$$

where the elastic strain is defined by

$$\mathbf{E}^e = \frac{1}{2}\left(\mathbf{F}^{e\mathrm{T}} \cdot \mathbf{F}^e - \mathbf{I}\right) \tag{5.50}$$

The *consistency condition* (5.48) implicitly defines the eigenstrain $\tilde{\mathbf{E}}$ as a fictitious strain defined within an heterogeneity such that when this strain is subtracted from the total strain, the resulting difference can be multiplied by the matrix elasticity tensor to give the stress in the homogeneity.

For an ellipsoidal inhomogeneity, the eigenstrain is constant, and the Eshelby tensor $\mathbb{S}$ is implicitly defined as the tensor that ensures

$$\mathbf{E}^e(\mathbf{X}) \equiv \mathbb{S} : \tilde{\mathbf{E}} \tag{5.51}$$

Substituting from Equation (5.51) into Equation (5.48),

$$(\mathbb{L}_{\text{matrix}} - \mathbb{L}_{\text{inhom}}) : \left[\boldsymbol{\Xi}^e + \mathbb{S} : \tilde{\mathbf{E}}^e\right] = \mathbb{L}_{\text{matrix}} : \tilde{\mathbf{E}} \tag{5.52}$$

Taking the inhomogeneity to be a void, so that $\mathbb{L}_{\text{inhom}} = \mathbf{0}$,

$$\tilde{\mathbf{E}} = (\mathbb{I} - \mathbb{S})^{-1} : \boldsymbol{\Xi}^e \tag{5.53}$$

In the void, from equations (5.51) and (5.53), the elastic strain is $\mathbf{E}^e = \left[\mathbb{I} + (\mathbb{S}^{-1} - \mathbb{I})^{-1}\right] : \boldsymbol{\Xi}^e$, and of course $\mathbf{T}^* = \mathbf{0}$. In the matrix, the elastic strain is

$$\mathbf{E}^e(\mathbf{X}) \triangleq \left[\mathbb{I} + \mathbb{D}(\mathbf{X}) : \left(\mathbb{S}^{-1} - \mathbb{I}\right)^{-1}\right] : \boldsymbol{\Xi}^e \tag{5.54}$$

Equation (5.54) implicitly defines the tensor $\mathbb{D}(\mathbf{X})$, which determines the heterogeneous microscale strain field. To simplify the notation, define

$$\mathbb{M}(\mathbf{X}) \triangleq \mathbb{I} + \mathbb{D}(\mathbf{X}) : \left(\mathbb{S}^{-1} - \mathbb{I}\right)^{-1} \tag{5.55}$$

With the definition in Equation (5.55), Equation (5.54) can be written

$$\mathbf{E}^e(\mathbf{X}) = \mathbb{M}(\mathbf{x}) : \boldsymbol{\Xi}^e \tag{5.56}$$

From equations (5.49) and (5.56), the stress in the matrix can be calculated from

$$\mathbf{T}^*(\mathbf{X}) = \mathbb{L} : \mathbb{M}(\mathbf{X}) : \mathbf{E}^e_\infty \tag{5.57}$$

Then, the resolved shear stress can be calulated as

$$\tau^{\alpha} = \mathbf{C}^{e} \cdot \mathbf{Z}^{\alpha} : \mathbf{T}^{*} = \mathbf{P}^{\alpha} : \mathbf{T}^{*} \tag{5.58}$$

where $\mathbf{Z}^{\alpha} = \mathbf{m}_0^{\alpha} \otimes \mathbf{n}_0^{\alpha}$ is the dyad of the slip system vectors $\mathbf{m}_0^{\alpha}$ and $\mathbf{n}_0^{\alpha}$ in the reference or intermediate configurations, and $\mathbf{P}^{\alpha} = \mathbf{m}^{\alpha} \otimes \mathbf{n}^{\alpha}$ is the dyad of the slip system vectors $\mathbf{m}^{\alpha}$ and $\mathbf{n}^{\alpha}$ in the current configuration.

5.2.2 Evaluation of the Eshelby Tensor

For an ellipsoidal inhomogeneity, ϵ^{*} is constant, so that

$$u_i(\mathbf{x}) = \frac{a_1 a_2 a_3}{4\pi} \epsilon_{pq}^{*} \int_{S(\bar{\xi})} \left(\bar{\xi} \cdot \mathbf{x}\right) L_{mnpq} N_{im}\left(\bar{\xi}\right) D^{-1}\left(\bar{\xi}\right) \bar{\xi}_n \zeta^{-3} dS\left(\bar{\xi}\right) \tag{5.59}$$

and

$$u_{i,j}(\mathbf{x}) = \frac{a_1 a_2 a_3}{4\pi} \epsilon_{pq}^{*} \int_{S(\bar{\xi})} L_{mnpq} N_{im}\left(\bar{\xi}\right) D^{-1}\left(\bar{\xi}\right) \bar{\xi}_j \bar{\xi}_n \zeta^{-3} dS\left(\bar{\xi}\right) \tag{5.60}$$

Using $dS\left(\bar{\xi}\right) = a_1 a_2 a_3 \zeta^{-3} dS\left(\bar{\zeta}\right)$, Equations (5.59) and (5.60) become, respectively,

$$u_i(\mathbf{x}) = \frac{1}{4\pi} \epsilon_{pq}^{*} \int_{S(\bar{\xi})} \left(\bar{\xi} \cdot \mathbf{x}\right) L_{mnpq} N_{im}\left(\bar{\xi}\right) D^{-1}\left(\bar{\xi}\right) \bar{\xi}_n dS\left(\bar{\zeta}\right) \tag{5.61}$$

and

$$u_{i,j}(\mathbf{x}) = \frac{1}{4\pi} \epsilon_{pq}^{*} \int_{S(\bar{\xi})} L_{mnpq} N_{im}\left(\bar{\xi}\right) D^{-1}\left(\bar{\xi}\right) \bar{\xi}_j \bar{\xi}_n dS\left(\bar{\zeta}\right) \tag{5.62}$$

Writing the surface element $dS\left(\bar{\zeta}\right)$ as $d\bar{\zeta}_3 d\theta$, Equations (5.61) and (5.62) become, respectively,

$$u_i(\mathbf{x}) = \frac{1}{4\pi} \epsilon_{pq}^{*} x_m \int_{-1}^{1} d\bar{\zeta}_3 \int_{0}^{2\pi} L_{mnpq} N_{im}\left(\bar{\xi}\right) D^{-1}\left(\bar{\xi}\right) \bar{\xi}_n d\theta \tag{5.63}$$

and

$$u_{i,j}\left(\mathbf{x}\right)=\frac{1}{4\pi}\epsilon_{pq}^{*}\int_{-1}^{1}d\bar{\zeta}_{3}\int_{0}^{2\pi}L_{mnpq}N_{im}\left(\bar{\xi}\right)D^{-1}\left(\bar{\xi}\right)\bar{\xi}_{j}\bar{\xi}_{n}d\theta \tag{5.64}$$

$$\epsilon_{ij}=\frac{1}{2}\left(\frac{\partial u_{i}}{\partial x_{j}}+\frac{\partial u_{j}}{\partial x_{i}}\right) \tag{5.65}$$

Using Equation (5.65), the strain is written as,

$$u_{i,j}\left(\mathbf{x}\right)=\frac{1}{8\pi}\epsilon_{pq}^{*}\int_{-1}^{1}d\bar{\zeta}_{3}\int_{0}^{2\pi}L_{mnpq}\left[N_{im}\left(\bar{\xi}\right)\bar{\xi}_{j}+N_{jm}\left(\bar{\xi}\right)\bar{\xi}_{i}\right]D^{-1}\left(\bar{\xi}\right)\bar{\xi}_{n}d\theta \tag{5.66}$$

Defining

$$G_{imjn}\left(\bar{\xi}\right)=\bar{\xi}_{j}\bar{\xi}_{n}N_{im}\left(\bar{\xi}\right)D^{-1}\left(\bar{\xi}\right) \tag{5.67}$$

Equation (5.66) becomes,

$$\epsilon_{ij}\left(\mathbf{x}\right)=\frac{1}{8\pi}\epsilon_{pq}^{*}\int_{-1}^{1}d\bar{\zeta}_{3}\int_{0}^{2\pi}L_{mnpq}\left[G_{imjn}\left(\bar{\xi}\right)+G_{jmin}\left(\bar{\xi}\right)\right]d\theta \tag{5.68}$$

Thus, the strain can be written in terms of the eigenstrain as,

$$\epsilon_{ij}=S_{ijpq}\epsilon_{pq}^{*} \tag{5.69}$$

where

$$S_{ijpq}=\frac{1}{8\pi}\int_{-1}^{1}d\bar{\zeta}_{3}\int_{0}^{2\pi}L_{mnpq}\left[G_{imjn}\left(\bar{\xi}\right)+G_{jmin}\left(\bar{\xi}\right)\right]d\theta \tag{5.70}$$

The following changes of variables are used (no summation on indices):

$$y_{i}=\frac{x_{i}}{a_{i}} \tag{5.71a}$$

$$y_{i}'=\frac{x_{i}'}{a_{i}} \tag{5.71b}$$

$$\zeta_{i}=a_{i}\bar{\xi}_{i} \tag{5.71c}$$

$$\bar{\zeta}_i = \frac{\zeta_i}{\zeta} \tag{5.71d}$$

with

$$\zeta = \left(\zeta_1^2 + \zeta_2^2 + \zeta_3^2\right)^{1/2} \tag{5.72}$$

and

$$z = \bar{\zeta} \cdot \mathbf{y}' \tag{5.73}$$

From Equation (5.71),

$$\bar{\xi}_i = \zeta \frac{\bar{\zeta}_i}{a_i} \tag{5.74}$$

However, since

$$\bar{\xi}_j \bar{\xi}_n N_{im}\left(\bar{\xi}\right) D^{-1}\left(\bar{\xi}\right) = \frac{\bar{\xi}_j \bar{\xi}_n \epsilon_{ikl} \epsilon_{mpq} L_{krps} \bar{\xi}_r \bar{\xi}_s L_{ltqu} \bar{\xi}_t \bar{\xi}_u}{\epsilon_{vwa} L_{vb1c} \bar{\xi}_b \bar{\xi}_c L_{wd2e} \bar{\xi}_d \bar{\xi}_e L_{af3g} \bar{\xi}_f \bar{\xi}_g} \tag{5.75}$$

$G_{imjn}\left(\bar{\xi}\right)$ is homogeneous of degree zero in $\bar{\xi}$; that is, $G_{imjn}\left(\bar{\xi}\right) = G_{imjn}\left(\alpha\bar{\xi}\right)$ for any $\alpha \in \mathbb{R}\backslash 0$, and the following change of variables can be made:

$$\bar{\xi}_i = \frac{\bar{\zeta}_i}{a_i} \tag{5.76}$$

The components of $\bar{\zeta}$ can be expressed as,

$$\bar{\zeta}_1 = \left(1 - \bar{\zeta}_3^2\right)^{1/2} \cos\left(\theta\right) \tag{5.77a}$$

$$\bar{\zeta}_2 = \left(1 - \bar{\zeta}_3^2\right)^{1/2} \sin\left(\theta\right) \tag{5.77b}$$

$$\bar{\zeta}_3 = \bar{\zeta}_3 \tag{5.77c}$$

Substituting from Equation (5.77) into Equation (5.70),

$$S_{ijpq} = \frac{1}{8\pi} \int_{-1}^{1} d\bar{\zeta}_3 \int_0^{2\pi} L_{mnpq} \left[G_{imjn}\left(\bar{\zeta}_3, \theta\right) + G_{jmin}\left(\bar{\zeta}_3, \theta\right)\right] d\theta \tag{5.78}$$

In order to evaluate the integral in Equation (5.78) for a general case, numerical quadrature is employed. In this context, numerical quadrature is being used to evaluate integrals of the form,

$$I(g) = \int_a^b w(x) f(x) \, dx \tag{5.79}$$

where $w(x)$ is a non-negative function on $[a, b]$, $f(x)$ is well approximated by a polynomial, and $g(x) = w(x) f(x)$ is the function to be integrated. To approximate $I(g)$, Gauss quadrature employs a set of weights ϕ_i and points x_i that seek to minimize

$$R = \left| I(g) - \sum_{i=1}^{n} \phi_i g(x_i) \right| \tag{5.80}$$

In order to determine the appropriate weights, the following theoretical aspects are considered, following the development in [93]. First, there exists a unique set of mutually orthogonal monic polynomials such that $(p_i, p_k) = 0$ for $i \neq k$, where

$$(f, g) = \int_a^b w(x) f(x) g(x) \, dx \tag{5.81}$$

These polynomials can be defined by the recursion,

$$p_0(x) = 1 \tag{5.82a}$$

$$p_1(x) = x - \frac{(xp_0, p_0)}{(p_0, p_0)} \tag{5.82b}$$

$$p_{i+1}(x) = \left[x - \frac{(xp_i, p_i)}{(p_i, p_i)} \right] p_i(x) - \frac{(p_i, p_i)}{(p_{i-1}, p_{i-1})} p_{i-1}(x), \; i \geq 1 \tag{5.82c}$$

Let ϕ_i be the solutions of the system of equations

$$\sum_{i=1}^{n} \phi_i p_k(x_i) = \begin{cases} (p_0, p_0) & \text{if } k = 0, \\ 0 & \text{if } k = 1, 2, \ldots, n-1 \end{cases} \tag{5.83}$$

where x_i are the n zeros of the polynomial $p_n(x)$. Then, for any polynomial $p(x)$ of degree $2n-1$, $R \equiv 0$; that is,

$$\int_a^b w(x)\, p(x)\, dx = \sum_{i=1}^{n} \phi_i p(x_i) \tag{5.84}$$

Taking $w(x) \equiv 1$, and $[a,b] = [-1,1]$ yields

$$p_k(x) = \frac{k!}{(2k)!} \frac{d^k}{dx^k} \left[\left(x^2 - 1\right)^k \right] \tag{5.85}$$

The *Legendre polynomials* are obtained by normalization of the polynmials generated by Equation (5.85) such that $p_k(1) = 1$. The weights associated with the k-th Legendre polynomial are

$$\phi_i = \frac{1}{(1 - x_i^2)\left[\frac{dp_k}{dx}(x_i)\right]^2} \tag{5.86}$$

For computational purposes, the Legendre polynomials are constructed via

$$p_k(x) = 2^n \sum_{j=1}^{k} \binom{k}{j} \binom{\frac{k+j-1}{2}}{k} x^j \tag{5.87}$$

and the weights are computed as

$$\phi_i = \frac{1}{(1 - x_i^2)\left[2^n \sum_{j=1}^{k} \binom{k}{j} \binom{\frac{k+j-1}{2}}{k} j x_i^{j-1}\right]^2} \tag{5.88}$$

It is noted that the accuracy of the Guass quadrature procedure using the Legendre polynomials depends on the accuracy of the approximation of the function $g(x)$ by an order $2n-1$ polynomial. To evaluate the integral over a general interval $[a,b]$, the limits of integration have to be transformed using the change of variables $x = \frac{b-a}{2} z + \frac{a+b}{2}$, so that

$$\int_a^b g(x)\, dx = \frac{b-a}{2} \int_a^b g\left(\frac{b-a}{2} z + \frac{a+b}{2}\right) dz \tag{5.89}$$

and

$$\int_a^b g(x)\,dx \approx \frac{b-a}{2}\sum_{i=1}^{n}\phi_i g\left(\frac{b-a}{2}z_i+\frac{a+b}{2}\right)dz \tag{5.90}$$

Thus, the n-point Gauss quadrature approximation of $I(x)$ is a weighted summation of the values of the function $g(x)$ evaluated at the zeros of the n-th order Legendre polynomial given as in Equation (5.87), with the weights given by Equation (5.88). The numerical approximation of $I(g)$ is accordingly,

$$I^n(g) = \frac{b-a}{2}\sum_{i=1}^{n}\phi_i g\left(\frac{b-a}{2}z_i+\frac{a+b}{2}\right)dz \tag{5.91}$$

An examination of the numerical properties of the approximation of the Eshelby tensor is given in Appendix D.

5.2.3 Exterior Fields

For points exterior to the void, the fields are non-uniform and are given by

$$\epsilon_{ij}(x) = \epsilon_{ij}^{\infty} + D_{ijkl}(x)\,\epsilon_{kl}^{*} \tag{5.92}$$

$$\sigma_{ij}(x) = \sigma_{ij}^{\infty} + C_{ijkl}D_{klmn}(x)\,\epsilon_{mn}^{*} \tag{5.93}$$

The components of the fourth-order tensor $\mathbb{D}(x)$ are given by Mura [9]

$$8\pi(1-\nu)D_{ijkl} = \psi_{,klij} - 2\nu\delta_{kl}\phi_{,ij} - (1-\nu)\left[\phi_{,kj}\delta_{il}+\phi_{,ki}\delta_{jl}+\phi_{,lj}\delta_{ik}+\phi_{,li}\delta_{jk}\right]$$

The displacement field is given by

$$u_i(x) = \frac{1}{8\pi(1-\nu)}\left[\epsilon_{jl}^{*}\psi_{,jli} - 2\nu\epsilon_{mm}^{*}\phi_{,i} - 4(1-\nu)\,\epsilon_{il}^{*}\phi_{,l}\right]$$

The displacement gradient is thus

$$u_{i,k}(x) = \frac{1}{8\pi(1-\nu)}\left[\epsilon^*_{jl}\psi_{,jlik} - 2\nu\epsilon^*_{mm}\phi_{,ik} - 4(1-\nu)\epsilon^*_{il}\phi_{,lk}\right]$$

and

$$\epsilon_{ik}(x) = \frac{1}{8\pi(1-\nu)}\left[\epsilon^*_{jl}\psi_{,jlik} - 2\nu\epsilon^*_{mm}\phi_{,ik} - 2(1-\nu)(\epsilon^*_{kl}\phi_{,li} + \epsilon^*_{il}\phi_{,lk})\right] \tag{5.94}$$

The scalar potentials ψ and ϕ are defined as

$$\psi(x) = \int_\Omega |x - x'|\, dx' \tag{5.95}$$

$$\phi(x) = \int_\Omega \frac{1}{|x - x'|} dx' \tag{5.96}$$

The derivatives of the potential function ψ are

$$\begin{aligned}
\psi_{,i} =& \frac{1}{2}x_i\left\{I(\lambda) - x_n x_n I_N(\lambda) - a_I^2\left[I_I(\lambda) - x_n x_n I_{IN}(\lambda)\right]\right\} \\
\psi_{,ijl} =& -\delta_{ij}x_l\left[I_L(\lambda) - a_I^2 I_{IL}(\lambda)\right] - x_i x_j\left[I_J(\lambda) - a_I^2 I_{IJ}(\lambda)\right]_{,l} \\
& -(\delta_{il}x_j + \delta_{jl}x_i)\left[I_J(\lambda) - a_I^2 I_{IJ}(\lambda)\right] \\
\psi_{,ijkl} =& -\delta_{ij}\delta_{kl}\left[I_K(\lambda) - a_I^2 I_{IK}(\lambda)\right] - (\delta_{ik}\delta_{jl} + \delta_{jk}\delta_{il})\left[I_J(\lambda) - a_I^2 I_{IJ}(\lambda)\right] \\
& -\delta_{ij}x_k\left[I_K(\lambda) - a_I^2 I_{IK}(\lambda)\right]_{,l} - (\delta_{ik}x_j + \delta_{jk}x_i)\left[I_J(\lambda) - a_I^2 I_{IJ}(\lambda)\right]_{,l} \\
& -(\delta_{il}x_j + \delta_{jl}x_i)\left[I_J(\lambda) - a_I^2 I_{IJ}(\lambda)\right]_{,k} - x_i x_j\left[I_J(\lambda) - a_I^2 I_{IJ}(\lambda)\right]_{,kl}
\end{aligned} \tag{5.97}$$

The derivatives of the potential function ϕ are

$$\phi_{,i} = -x_i I_I(\lambda)$$

and

$$\phi_{,ij} = -\delta_{ij}I_I(\lambda) - x_i I_{I,J}(\lambda)$$

where λ is the largest positive solution of

$$\frac{x_1^2}{a_1^2+\lambda}+\frac{x_2^2}{a_2^2+\lambda}+\frac{x_3^2}{a_3^2+\lambda}=1$$

The so-called *I-integrals* that appear in the above equations are given by

$$I(\lambda)=2\pi a_1a_2a_3\int_\lambda^\infty\frac{ds}{\Delta(s)}$$

$$I_j(\lambda)=2\pi a_1a_2a_3\int_\lambda^\infty\frac{ds}{\left(a_j^2+s\right)\Delta(s)}$$

$$I_{jk}(\lambda)=2\pi a_1a_2a_3\int_\lambda^\infty\frac{ds}{\left(a_j^2+s\right)\left(a_k^2+s\right)\Delta(s)}$$

where

$$\Delta(x)=\left(a_1^2+x\right)^{1/2}\left(a_2^2+x\right)^{1/2}\left(a_3^2+x\right)^{1/2}$$

The first-order I-integrals I_j have the property

$$I_1(\lambda)+I_2(\lambda)+I_3(\lambda)=\frac{4\pi a_1a_2a_3}{\Delta(\lambda)}$$

The second-order I-integrals I_{jk} have the properties

$$I_{12}(\lambda)=\frac{I_2(\lambda)-I_1(\lambda)}{a_1^2-a_2^2}$$

$$I_{11}(\lambda)=\frac{4\pi}{3}\frac{a_1a_2a_3}{\left(a_1^2+\lambda\right)\Delta(\lambda)}-\frac{1}{3}\left[I_{12}(\lambda)+I_{13}(\lambda)\right]$$

The third-order I-integrals I_{jkl} have the properties

$$I_{123}(\lambda)=\frac{I_{23}(\lambda)-I_{13}(\lambda)}{a_1^2-a_2^2}$$

$$I_{112}(\lambda)=\frac{I_{12}(\lambda)-I_{11}(\lambda)}{a_1^2-a_2^2}$$

$$I_{113}(\lambda) = \frac{I_{13}(\lambda) - I_{11}(\lambda)}{a_1^2 - a_3^2}$$

$$I_{111} = \frac{4\pi}{5}\frac{a_1 a_2 a_3}{(a_1^2+\lambda)^2 \Delta(\lambda)} - \frac{1}{5}\left[I_{112}(\lambda) + I_{113}(\lambda)\right]$$

The I-integrals above suffer from numerical instabilities when major semi-axes of the ellipsoid approach each other in magnitude. Thus, it is necessary to provide explicit forms for the cases when some or all of the axes are equal in length. For the degenerate case of a sphere, $a_1 = a_2 = a_3 = a$, and

$$I(\lambda) = \frac{4\pi a^3}{\sqrt{a^2+\lambda}}$$

$$I_J(\lambda) = \frac{4\pi a^3}{3(a^2+\lambda)^{3/2}}$$

$$I_{\underbrace{JK\cdots L}_{n}}(\lambda) = \frac{4\pi a^3}{(2n+1)(a^2+\lambda)^{n+1/2}}$$

For the degenerate case of a prolate spheroid, $a_1 > a_2 = a_3$, and

$$I(\lambda) = \frac{4\pi a_1 a_3^2}{\sqrt{a_1^2 - a_3^2}} \ln\left(\frac{\sqrt{a_1^2+\lambda} - \sqrt{a_1^2 - a_3^2}}{\sqrt{a_1^2+\lambda} + \sqrt{a_1^2 - a_3^2}}\right) \tag{5.98}$$

$$I_1(\lambda) = \frac{4\pi a_1 a_3^2}{(a_1^2 - a_3^2)^{3/2}}\left[\ln\left(\frac{\sqrt{a_1^2+\lambda} - \sqrt{a_1^2 - a_3^2}}{\sqrt{a_1^2+\lambda} + \sqrt{a_1^2 - a_3^2}}\right) - \frac{(a_1^2 - a_3^2)^{1/2}}{(a_1^2+\lambda)^{1/2}}\right] \tag{5.99}$$

$$I_2(\lambda) = I_3(\lambda) = \frac{2\pi a_1 a_3^2}{(a_1^2 - a_3^2)^{3/2}}\left[\frac{(a_1^2+\lambda)^{1/2}(a_1^2 - a_3^2)^{1/2}}{a_3^2+\lambda} - \ln\left(\frac{\sqrt{a_1^2+\lambda} - \sqrt{a_1^2 - a_3^2}}{\sqrt{a_1^2+\lambda} + \sqrt{a_1^2 - a_3^2}}\right)\right] \tag{5.100}$$

For the degenerate case of an oblate spheroid $a_1 = a_2 > a_3$, and

$$I(\lambda) = \frac{4\pi a_1 a_2 a_3}{(a_1^2 - a_3^2)^{1/2}} F(\alpha, k) \tag{5.101}$$

$$I_1(\lambda) = \frac{4\pi a_1 a_2 a_3}{(a_1^2 - a_2^2)(a_1^2 - a_3^2)^{1/2}}\left[F(\alpha,k) - E(\alpha,k)\right] \tag{5.102}$$

$$I_2(\lambda) = 4\pi a_1 a_2 a_3 \left[\frac{\left(a_1^2 - a_3^2\right)^{1/2}}{\left(a_1^2 - a_2^2\right)\left(a_2^2 - a_3^2\right)} E(\alpha, k) - \frac{1}{\left(a_1^2 - a_2^2\right)\left(a_1^2 - a_3^2\right)^{1/2}} F(\alpha, k) - \frac{\left(a_3^2 + \lambda\right)^{1/2}}{\left(a_2^2 - a_3^2\right)\left(a_1^2 + \lambda\right)^{1/2}\left(a_2^2 + \lambda\right)^{1/2}} \right] \tag{5.103}$$

$$I_3(\lambda) = \frac{4\pi a_1 a_2 a_3}{\left(a_2^2 - a_3^2\right)\left(a_1^2 - a_3^2\right)^{1/2}} \left[\frac{\left(a_2^2 + \lambda\right)^{1/2}\left(a_1^2 - a_3^2\right)^{1/2}}{\left(a_1^2 + \lambda\right)^{1/2}\left(a_3^2 + \lambda\right)^{1/2}} - E(\alpha, k) \right] \tag{5.104}$$

For ellipsoids ($a_1 > a_2 > a_3$), the integrals are

$$I(\lambda) = \frac{4\pi a_1 a_2 a_3}{\left(a_1^2 - a_3^2\right)^{1/2}} F(\alpha, k) \tag{5.105}$$

$$I_1(\lambda) = \frac{4\pi a_1 a_2 a_3}{\left(a_1^2 - a_2^2\right)\left(a_1^2 - a_3^2\right)^{1/2}} \left[F(\alpha, k) - E(\alpha, k) \right] \tag{5.106}$$

$$I_2(\lambda) = 4\pi a_1 a_2 a_3 \left[\frac{\left(a_1^2 - a_3^2\right)^{1/2}}{\left(a_1^2 - a_2^2\right)\left(a_2^2 - a_3^2\right)} E(\alpha, k) - \frac{1}{\left(a_1^2 - a_2^2\right)\left(a_1^2 - a_3^2\right)^{1/2}} F(\alpha, k) - \frac{\left(a_3^2 + \lambda\right)^{1/2}}{\left(a_2^2 - a_3^2\right)\left(a_1^2 + \lambda\right)^{1/2}\left(a_2^2 + \lambda\right)^{1/2}} \right] \tag{5.107}$$

$$I_3(\lambda) = \frac{4\pi a_1 a_2 a_3}{\left(a_2^2 - a_3^2\right)\left(a_1^2 - a_3^2\right)^{1/2}} \left[\frac{\left(a_2^2 + \lambda\right)^{1/2}\left(a_1^2 - a_3^2\right)^{1/2}}{\left(a_1^2 + \lambda\right)^{1/2}\left(a_3^2 + \lambda\right)^{1/2}} - E(\alpha, k) \right] \tag{5.108}$$

Where F and E are the incomplete elliptic integrals of the first and second kind, respectively:

$$F(\alpha, k) = \int_0^\alpha \frac{dw}{\left[1 - k^2 \sin^2(w)\right]^{1/2}}$$

$$E(\alpha, k) = \int_0^\alpha \left[1 - k^2 \sin^2(w)\right]^{1/2} dw$$

with

$$\alpha = \sin^{-1}\left(\frac{a_1^2 - a_3^2}{a_1^2 + \lambda} \right)^{1/2}$$

and

$$k = \left(\frac{a_1^2 - a_2^2}{a_1^2 - a_3^2} \right)^{1/2}$$

The numerical calculation of the incomplete elliptic integrals is covered in Appendix B. The derivatives of the I-integrals are given by

$$I_{i\cdots jk,p}(\lambda) = \frac{-2\pi a_1 a_2 a_3}{(a_i^2+\lambda)\cdots\left(a_j^2+\lambda\right)(a_k^2+\lambda)(a_1^2+\lambda)^{1/2}(a_2^2+\lambda)^{1/2}(a_3^2+\lambda)^{1/2}}\lambda_{,p}$$

Thus,

$$I_{i,j}(\lambda) = \frac{-2\pi a_1 a_2 a_3}{(a_i^2+\lambda)(a_1^2+\lambda)^{1/2}(a_2^2+\lambda)^{1/2}(a_3^2+\lambda)^{1/2}}\lambda_{,j}$$

$$I_{ij,k}(\lambda) = \frac{-2\pi a_1 a_2 a_3}{(a_i^2+\lambda)\left(a_j^2+\lambda\right)(a_1^2+\lambda)^{1/2}(a_2^2+\lambda)^{1/2}(a_3^2+\lambda)^{1/2}}\lambda_{,k}$$

$$I_{i,jk}(\lambda) = \frac{-2\pi a_1 a_2 a_3}{(a_i^2+\lambda)(a_1^2+\lambda)^{1/2}(a_2^2+\lambda)^{1/2}(a_3^2+\lambda)^{1/2}}\left[\lambda_{,jk} - \left(\frac{1}{a_i^2+\lambda} + \frac{1}{2}\sum_n \frac{1}{a_n^2+\lambda}\right)\lambda_{,j}\lambda_{,k}\right]$$

$$I_{ij,kl}(\lambda) = \frac{-2\pi a_1 a_2 a_3}{(a_i^2+\lambda)\left(a_j^2+\lambda\right)(a_1^2+\lambda)^{1/2}(a_2^2+\lambda)^{1/2}(a_3^2+\lambda)^{1/2}}\left[\lambda_{,kl} - \left(\frac{1}{a_I^2+\lambda} + \frac{1}{a_J^2+\lambda} + \frac{1}{2}\sum_n \frac{}{a_n^2}\right.\right.$$

The derivatives of λ are given by

$$\lambda_{,l} = \frac{2x_l}{a_L^2+\lambda}\frac{\left(a_I^2+\lambda\right)^2}{x_i x_i}$$

$$\lambda_{,ij} = \frac{F_{i,j} - \lambda_{,i}C_{,j}}{C}$$

where

$$F_i = \frac{2x_i}{a_I+\lambda}$$

$$C = \frac{x_i x_i}{\left(a_I^2+\lambda\right)^2}$$

$$C_{,j} = 2x_j \sum_k \frac{1}{\left(a_k^2+\lambda\right)^2} - 2\frac{x_i x_i}{\left(a_I^2+\lambda\right)^3}\lambda_{,j}$$

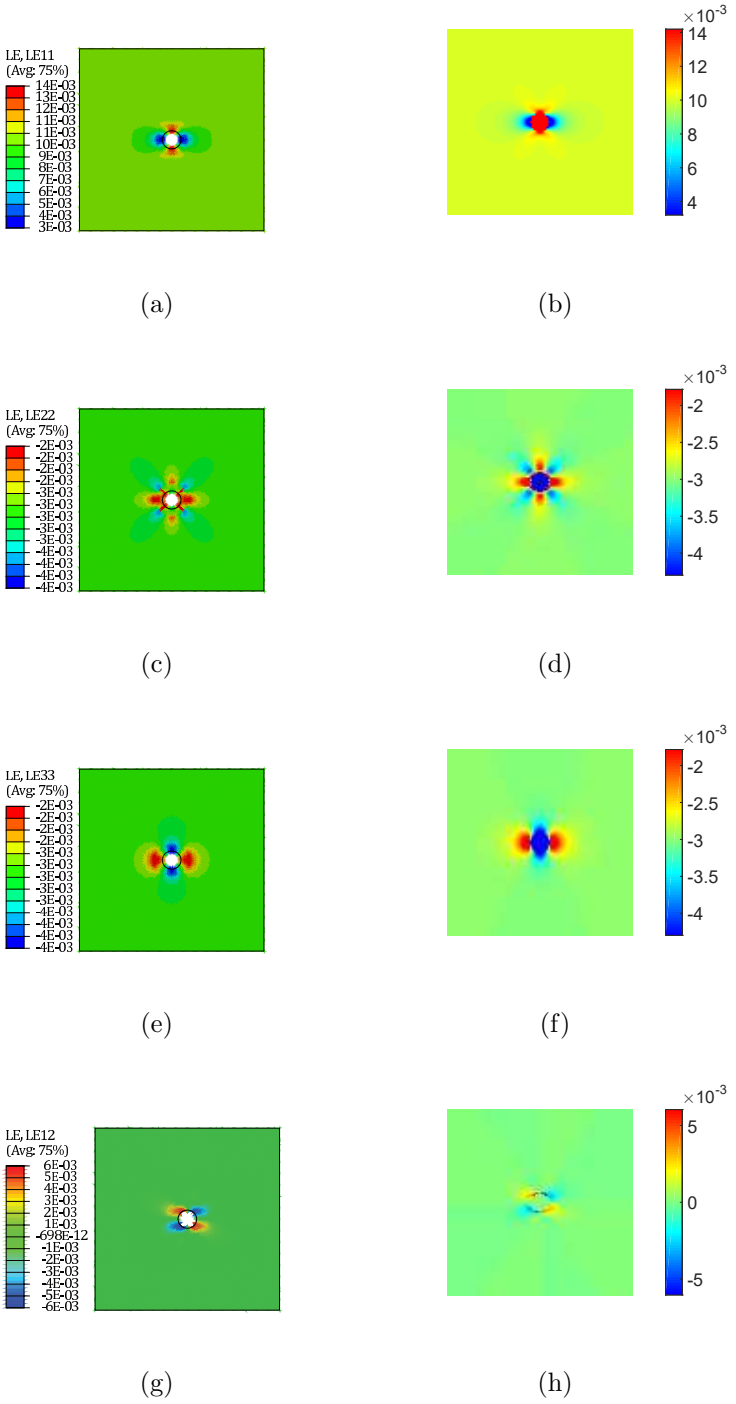

Figure 5.6: Strain fields for the DNS and homogenized calculations

The application of the above equations is shown in Figure 5.6. In the figure, the strain contours computed from direct numerical simulation of the void unit cell are shown in the left column. In the right column, the corresponding strain contours as calculated by the Eshelby formulation are shown. Visually, the two sets of results are very similar. A quantitative comparison of the two solutions is given in Section 5.3, where the deformation of the void under each solution is compared. It is shown that the agreement is quite good.

5.2.4 Approximation of the Effective Elasticity Tensor

Using the Eshelby tensor $\mathbb{S}$, it is possible to construct a number of approximations to the effective elasticity tensor $\mathbb{L}_{\text{eff}}$, where

$$\mathbf{T}^* = \mathbb{L}_{\text{eff}} : \mathbf{\Xi}^e \tag{5.109}$$

A class of approximations use the Eshelby tensor $\mathbb{S}$ to derive an interaction tensor $\mathbb{A}$ that produces the effective elasticity tensor through

$$\mathbb{L}_{\text{eff}} = \sum_{i=0}^{N} c_i \mathbb{L}_i \mathbb{A}_i \tag{5.110}$$

In Equation (5.110), the index i ranges over the phases, from 0 for the matrix, and through $1, \ldots, N$ for N inhomogeneities. Then c_i is the volume fraction of the inhomogeneity i, while $\mathbb{L}_i$ is the elasticity tensor, and $\mathbb{A}_i$ is the interaction tensor. The

$\mathbb{A}_i$ are constrained so that

$$\sum_{i=0}^{N} c_i \mathbb{L}_i \mathbb{A}_i = \mathbb{I} \tag{5.111}$$

Given (5.111), the interaction tensor for the matrix can be determined a priori as

$$\mathbb{A}_0 = \frac{1}{c_0} \left(\mathbb{I} - \sum_{i=1}^{N} c_i \mathbb{L}_i \mathbb{A}_i \right) \tag{5.112}$$

For a two-phase problem, Equations (5.110) and (5.112) can be combined to yield

$$\mathbb{L}_{\text{eff}} = \mathbb{L}_0 + c_1 \left(\mathbb{L}_1 - \mathbb{L}_0 \right) \mathbb{A}_1 \tag{5.113}$$

For the void problem, there is just one inhomogeneity, and the components of its elasticity tensor are 0. One such approximation, introduced by Mori and Tanaka, is

$$\mathbb{L}_{\text{eff}} \approx \mathbb{L} : \left\{ \mathbb{I} - f \left[\mathbb{I} - (1 - f) \, \mathbb{S} \right]^{-1} \right\} \tag{5.114}$$

where f is the void volume fraction. As shown in Figure 5.7, this approximation yields good agreement with DNS results obtained by FEM solution of the elastic micromechanics problem.

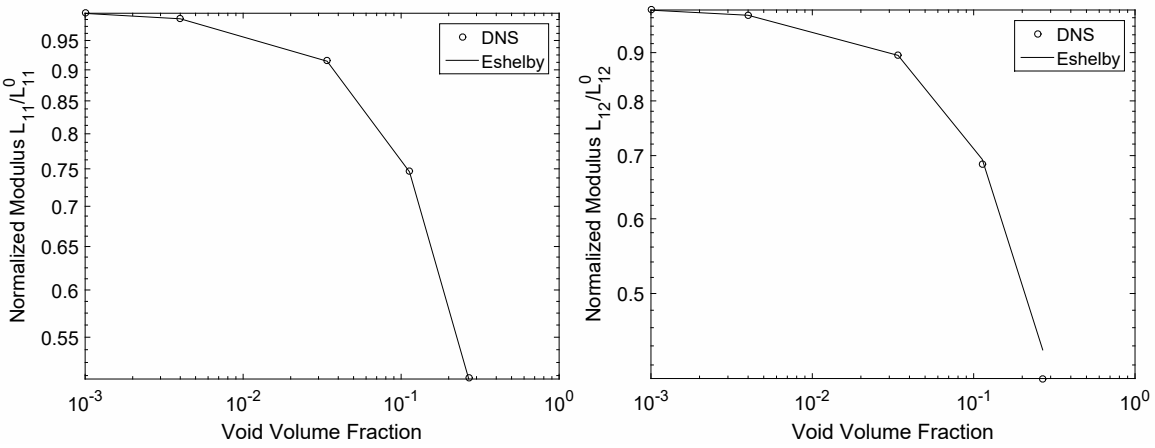

Figure 5.7: Mori-Tanaka approximation of effective elastic moduli as a function of void volume fraction.

5.3 Coupled Damage Crystal Plasticity Model

In order to capture the coupled damage-crystal plasticity at the macroscale, DEHF is applied to a microstructure consisting of ellipsoidal voids. The exterior Eshelby solution is exploited to approximate the microscale distribution of stress in the microstructure, and DEHF is applied to determine the enhanced plasticity occurring due to the presence of the void. In the case of evolving damage, the mapping from the microscale fields to the macroscale moments is varying in time according to the evolution of the void. Under the assumption that the voids of interest remain ellipsoidal, the void evolution is characterized by the time-history of the ellipsoidal major semi-axes a, b, and c. In order to capture this behavior, a novel damage evolution

relation is developed that relates changes in the circumference of the void in the principal planes to change in the major semi-axes. The development begins with a brief outline of the theory behind this relation.

5.3.1 Void Evolution Based on the Arc Length Integral

Given a smooth parametrization $\mathbf{X}(s)$ in the reference configuration, the length of this curve for $0 \leq s \leq R$ is given by

$$L = \int_0^R \sqrt{\frac{d\mathbf{X}}{ds} \cdot \frac{d\mathbf{X}}{ds}} ds \tag{5.115}$$

With $d\mathbf{x}(s) = \mathbf{F}(s) \cdot d\mathbf{X}(s)$, the length of the deformed curve is

$$\begin{aligned} l &= \int_0^R \sqrt{\mathbf{F}(s) \cdot \frac{d\mathbf{X}}{ds} \cdot \mathbf{F}(s) \cdot \frac{d\mathbf{X}}{ds}} ds \\ &= \int_0^R \sqrt{\frac{d\mathbf{X}}{ds} \cdot \mathbf{C}(s) \cdot \frac{d\mathbf{X}}{ds}} ds \end{aligned} \tag{5.116}$$

Assuming that the curve is a circle with radius R in the X_1, X_2 plane in the reference configuration, a parametrization is

$$\mathbf{X} = \begin{bmatrix} s \\ \sqrt{R^2 - s^2} \\ 0 \end{bmatrix} \tag{5.117}$$

In the current configuration, the circle is transformed into an ellipse. Substituting from (5.117) into (5.116),

$$l = \int_0^R \sqrt{C_{11}(s) - 2C_{12}(s)\frac{s}{\sqrt{R^2 - s^2}} + C_{22}(s)\frac{s^2}{R^2 - s^2}}ds \tag{5.118}$$

The circumference of the ellipse in the current configuration is then $4l = 4aE\left(1 - \frac{b^2}{a^2}\right)$, where a and b are the major semi-axes of the ellipse, and $E(x)$ is the complete elliptic integral of the second kind. Assuming that the curve $\mathbf{X}(s)$ is a plane section of a sphere, taking the X_1, X_3 and X_2, X_3 plane sections yields two additional equations in the major semi-axes of the ellipse, resulting in the system

$$\begin{aligned} l(X_1, X_2) &= aE\left(1 - \frac{b^2}{a^2}\right) \\ l(X_1, X_3) &= aE\left(1 - \frac{c^2}{a^2}\right) \\ l(X_2, X_3) &= bE\left(1 - \frac{c^2}{b^2}\right) \end{aligned} \tag{5.119}$$

This system of equations is solved by Newton iteration, with $a_0 = b_0 = c_0 = R$, and

$$\begin{Bmatrix} a \\ b \\ c \end{Bmatrix}^{(n+1)} = \begin{Bmatrix} a \\ b \\ c \end{Bmatrix}^{(n)} - \begin{bmatrix} \frac{b^2}{a^2-b^2}\Delta_{ab} & \frac{c^2}{a^2-c^2}\Delta_{ac} & 0 \\ \frac{ab}{b^2-a^2}\Delta_{ab} & 0 & \frac{c^2}{b^2-c^2}\Delta_{bc} \\ 0 & \frac{ac}{a^2-c^2}\Delta_{ac} & \frac{bc}{c^2-b^2}\Delta_{bc} \end{bmatrix}^{-1} \times \begin{Bmatrix} aE\left(1 - \frac{b^2}{a^2}\right) - l(X_1, X_2) \\ aE\left(1 - \frac{c^2}{a^2}\right) - l(X_1, X_3) \\ bE\left(1 - \frac{c^2}{b^2}\right) - l(X_2, X_3) \end{Bmatrix} \tag{5.120}$$

where $\Delta_{xy} = E\left(1 - \frac{y^2}{x^2}\right) - K\left(1 - \frac{y^2}{x^2}\right)$, and $K(m)$ is the complete elliptic integral of the first kind.

Thus, given the lengths of the major semi-axes at step n, and the increment in the deformation C from step n to step $n+1$, the model predicts the lengths of the major semi-axes at step $n+1$, as required. The application of the model to an elastic step is considered first.

5.3.2 Applications

For an elastic step, the exterior Eshelby tensor field can be determined directly from the total deformation gradient. To determine the increments in the major semi-axes of the void, this field is sampled at points along each of the ellipsoidal circumferences in the principal planes, and Gauss-Legendre numerical quadrature is applied to evaluate the integral in (5.118).

To validate the model, elastic deformations are applied to a single hexahedral element consisting of a tantalum single crystal microstructure containing a single, intitially spherical void. The principal axis of the deformation is aligned with the [001] direction for all of the tests, and the transverse stress varies for each simulation so that a target stress triaxiality is achieved in the deformed configuration. The triaxiality varies from 1/3 (uniaxial stress) to 1000 (approximately hydrostatic stress). Figure 5.8 shows the results of these simulations, with an initially spherical void of radius 0.05mm deformed elastically to 0.1% strain.

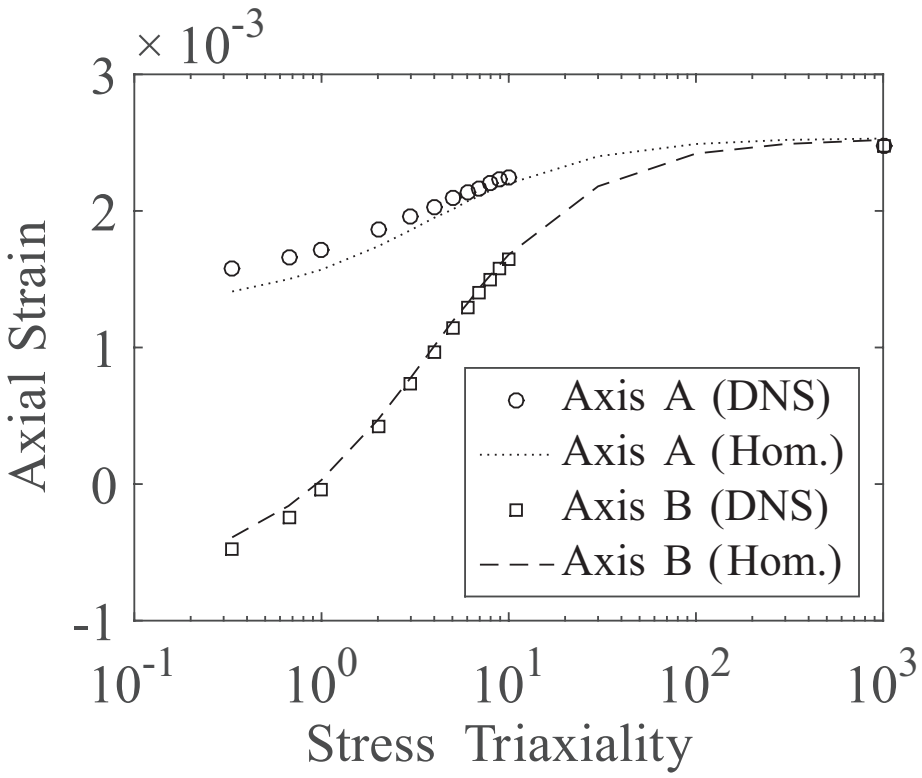

Figure 5.8: Axial strain in void due to elastic deformation, as calculated by Abaqus (open symbols) and DEHF (dashed lines).

The results of the DEHF calculations are compared to the unit cell calculations performed in Abaqus, and as seen in Figure 5.8, the DEHF results agree quite well with those of the direct numerical simulations across a wide range of stress triaxiality, validating the DEHF model for the elastic case.

For a general plastic deformation, the damage evolution model is applied incrementally, so that the incremental deformation gradient is used to calculate the defor-

mation $\mathbf{C}$ in Equation (5.118). That is,

$$\mathbf{C} = \mathbf{F}^{\mathrm{T}} \cdot \mathbf{F} \tag{5.121}$$

with

$$\mathbf{F} = \mathbf{F}_{n+1} \cdot \mathbf{F}_n^{-1} \tag{5.122}$$

Figure 5.9 shows the results of this relation applied to an initially spherical void of radius 0.05mm deformed plastically to 0.7% strain.

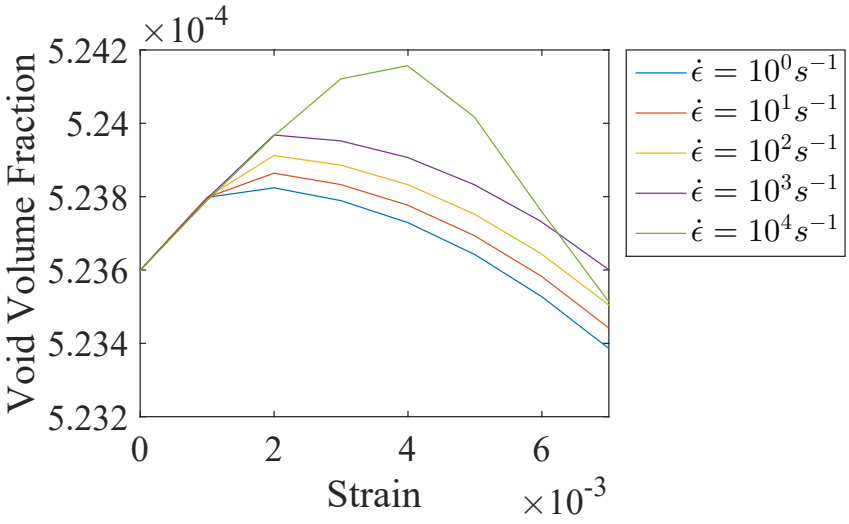

Figure 5.9: Void volume evolution for various strain rates.

The specimens in these tests are subjected to a uniaxial stress loading, with $\chi = 1/3$. It is seen from the figure that the evolution follows the same general trend as the uniaxial loading of the unit cell simulations in Section 4.2. In each case, the void undergoes a very brief initial growth phase, before beginning to shrink in volume during plastic deformation. It is also clear from Figure 5.9, that this phenomenon

is strain rate dependence. It is not possible to draw general conclusions about the damage process from this limited test suite, but future work will focus on testing the model across a range of stress triaxiality, strain rate, and other loading parameters.

Chapter 6

Conclusions and Future Work

This study is focused on developing a framework for the multiscale modeling of materials with heterogeneous microstructures. Part of this work is dedicated to creating a physical basis for functional parametric forms in crystal plasticity constitutive models for materials with a BCC lattice structure. This effort is detailed in Chapter 3. The second main part of this work is the development and application of a new method of homogenization for nonlinear constitutive relations, the *distribution-enhanced homogenization framework* (DEHF). In addition, a novel damage evolution law is formulated to study the process of ductile damage within DEHF. In this summary, a few highlights from these efforts are outlined.

6.1 Tantalum Material Model

This methodology is applied to develop a physically-based model for tantalum. Specifically, the model identifies an effective measure of the critical stress required for thermally activated slip. The model accounts for the dependence of this effective critical resolved stress for slip initiation on temperature, strain rate, and load orientation as observed in atomistic simulations. It is therefore able to provide a direct link between relevant atomistic processes and their crystal plasticity counterpart representations.

It is found that temperature effects are well characterized by the established functional form in [5], where MD simulations have identified the values of the parameters. The strain-rate effects are explained through a probabilistic framework within which thermal activation is modeled as a discrete process controlled by the frequency of thermal fluctuation and the probability associated with reaching the thermal activation energy required to move a dislocation. The load orientation effects are quantified by parametrization of the effects of non-glide stresses with reference to the general functional form in [82, 83]. Analysis of the MD simulation results relates the relative magnitudes of non-glide stresses contributing to the effective resolved shear stress.

The new crystal plasticity model including non-Schmid effects is implemented in a commercial finite element code and simulations are conducted to validate the

effectiveness of this model. The improved physics captured in this model produces realistic finite element simulations, consistent with experimental observations in [88] and in substantial agreement with the results in [47] except where those observations contradict those in [88]. Specifically, the orientation-dependent tension-compression asymmetry experimentally observed in BCC metals is reproduced by the new model.

6.2 DEHF Theory and Applications

In this chapter, a new approach to hierarchical multi-scale modeling in the form of the *distribution-enhanced homogenization framework* or DEHF is proposed. The framework does not make any a priori assumption on the macroscale constitutive behavior being represented by a homogeneous effective medium theory. Instead, the evolution of macroscale variables are governed by the moments of microscale distribution of evolving field variables. The macroscale constitutive relations are formulated in terms of a series expansion that is based on the microscale constitutive relations and the moments (of arbitrary order) of microscale field variables. This approach demonstrates excellent accuracy in representing the microscale fields through their distributions. Also, an approximate characterization of the microscale heterogeneity is accounted for explicitly in the macroscale constitutive behavior. Increasing the order of this approximation results in increased fidelity of the macroscale approximation of the microscale constitutive behavior.

CHAPTER 6. CONCLUSIONS AND FUTURE WORK

In the applications studied here, the macroscale DEHF model is shown to capture the microscale response of the material without parametrization of the macroscale constitutive relations. The higher-order moments of the mechanical field variables are written in terms of their evolving first moments (from microscale equilibrium conditions) and moments related to the microstructure. While closed form expressions relating the moments of the mechanical fields are not available for all cases, semi-analytical methods or numerical analysis may be used to determine these relationships. The inclusion of higher-order moments allows the DEHF to approximate the microscale results to an arbitrary degree of accuracy, so that the homogenized constitutive relations give the approximate evolution at every point in the history. Thus it does not require matching specific characteristics of the history, which may not be representative of the overall behavior. The macroscale behavior is represented naturally as a function of the microstructure via the higher-order moments in the microscale fields, captured in the homogenized relations.

Additionally, there are two fundamental outcomes of the DEHF that have practical implications for micromechanical analyses. First, by including higher-order moments of the microscale fields in the macroscale problem, micromechanical analyses do not require boundary conditions to ensure satisfaction of the original form of Hill's lemma. This is because the analysis of the macroscale problem includes the energet-

ics of the higher-order terms. There is no requirement that the macroscopic power be written only in terms of the average stresses and strain-rates and thus no need to restrict the micromechanical analyses to eliminate the contribution of terms other than these averages. For problems such as those considered in this work, satisfaction of microscale equilibrium requires that certain relationships are maintained for given sets of microstructural descriptors between the first-order and higher-order variables, so that no additional conservation laws or boundary conditions are required for the higher-order terms. Second, the moment approximations can give insight into the significance of microscale features with respect to the macroscale response. For example, applying microscale stress fields with identical first moments to different microstructures will generally produce different higher-order moments. By analyzing the magnitude of the contributions of these higher-order moments to the constitutive response, the equivalence of two microstructures with respect to a particular constitutive response can be assessed when the significant higher-order moments of the two microscale stress fields are comparable.

6.3 Future Work

In the near term, the DEHF simulations of crystal plasticity and ductile damage will be carried further to examine the coupling of the two phenomena. Questions of particular interest for this study include probing the effects of stress triaxiality and

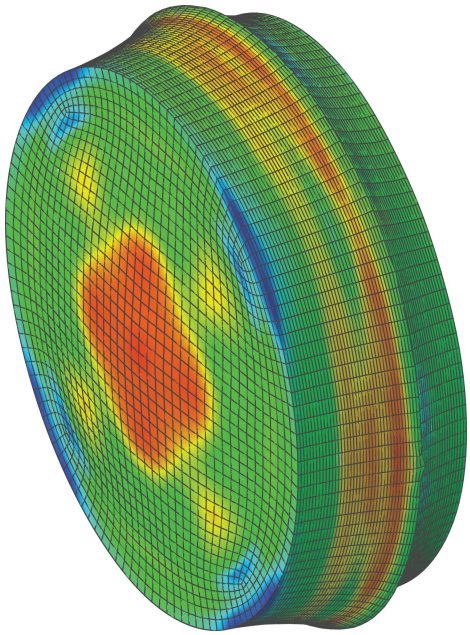

Figure 6.1: Elasto-viscoplastic deformation of a tantalum target under impact from a tantalum flyer plate traveling at 300 ms.

strain rate. After the fundamental study of damage evolution for a single void, the model will be used to simulate plasticity and failure in high rate deformations such as those produced by flyer plate impacts, as shown in Figure 6.1.

Beyond the near term, there are a number of interesting directions into which further research based on the ideas in this study could be developed. First, there is a large body of work which focuses on treating the macroscale response of polycrystalline material in a computationally tractable way; that is, without directly computing the crystal plasticity response at each point within the microstructure. There has also been extensive study into characterization of the microstructure it-

self through evaluation of various morphological parameters such as average grain size, number of neighbors, grain aspect ration, and many others. The methods developed in this study open an avenue of investigation into the connections between the macroscale mechanical response and the macroscale characterization of the material morphology. For example, establishing the appropriate connection between the moments of the stress distribution and the moments of the distribution of crystal orientations would allow a DEHF computation of the macroscale response for a given microstructure and microscale constitutive behavior. Successful implementation of such a formulation would allow, for example, new investigation of equivalence among microstructures according to mechanical response, whereas current methods generally identify equivalent microstructures based on morphological parameters. Such a shift in analysis would be an important step toward answering a wide array of questions about the sensitivity of mechanical response to various morphological features; for example, the relative importance of grain size, grain boundary type, etc. in determining the yield strength of the material.

Appendix A

Bernstein Polynomial Basis and Approximation

The n-th order Bernstein polynomial approximation of a function $f(x)$ is

$$B_n^f(x) = \sum_{k=0}^{n} f\left(\frac{k}{n}\right) b_{k,n}(x) \tag{A.1}$$

where the Bernstein basis polynomials are

$$b_{k,n}(x) = \frac{n!}{k!\,(n-k)!} x^k (1-x)^{n-k} \tag{A.2}$$

The derivatives of the basis functions can be written in terms of lower-order basis functions. For example, the first derivative is easily shown to be

$$\begin{aligned} \frac{d}{dx} b_{k,n}(x) &= \frac{n!}{(k-1)!\,(n-k)!} x^{k-1} (1-x)^{n-k} - \frac{n!}{k!\,(n-1-k)!} x^k (1-x)^{n-1-k} \\ &= n\left[b_{k-1,n-1}(x) - b_{k,n-1}(x)\right] \end{aligned} \tag{A.3}$$

By recursion, derivatives of order m are given as

$$\begin{aligned}\frac{d^m}{dx^m}b_{k,n}(x) &= \frac{n!}{(n-m)!}\sum_{j=\max(0,m-k)}^{\min(m,n-k)}\frac{(-1)^j m!}{j!\,(m-j)!}b_{k-m+j,n-m}(x)\\ &= \frac{n!}{(n-m)!}\sum_{j=\max(0,m-k)}^{\min(m,n-k)}\frac{(-1)^j m!}{j!\,(m-j)!}\frac{(n-m)!}{(k-m+j)!\,(n-k-j)!}x^{k-m+j}(1-x)^{n-k-j}\\ &= n!m!\sum_{j=\max(0,m-k)}^{\min(m,n-k)}\frac{(-1)^j x^{k-m+j}(1-x)^{n-k-j}}{j!\,(m-j)!\,(k-m+j)!\,(n-k-j)!}\end{aligned} \tag{A.4}$$

According to Equations (A.2) and (A.4), derivatives of B_n^f can be written as

$$\begin{aligned}\frac{d^m}{dx^m}B_n^f(x) &= \sum_{k=0}^{n} f\left(\frac{k}{n}\right)\frac{d^m}{dx^m}b_{k,n}(x)\\ &= n!m!\sum_{k=0}^{n} f\left(\frac{k}{n}\right)\sum_{j=\max(0,m-k)}^{\min(m,n-k)}\frac{(-1)^j x^{k-m+j}(1-x)^{n-k-j}}{j!\,(m-j)!\,(k-m+j)!\,(n-k-j)!}\end{aligned} \tag{A.5}$$

If these derivatives are evaluated at $x = 0$, the inner summand is 0 unless $j = m - k$, and $j \geq 0$ implies $k \leq m$, so that

$$\begin{aligned}\frac{d^m}{dx^m}B_n^f(x=0) &= \frac{n!m!}{(n-m)!}\sum_{k=0}^{m} f\left(\frac{k}{n}\right)\frac{(-1)^{m-k}}{k!\,(m-k)!}\\ &= \frac{n!m!}{(n-m)!}\sum_{k=0}^{m} f\left(\frac{m-k}{n}\right)\frac{(-1)^k}{k!\,(m-k)!}\end{aligned} \tag{A.6}$$

Similarly, for $x = 1$, the inner summand is 0 unless $j = n - k$, and $j \leq m$ implies $k \geq n - m$, so that

$$\begin{aligned}\frac{d^m}{dx^m}B_n^f(x=1) &= \frac{n!m!}{(n-m)!}\sum_{k=n-m}^{n} f\left(\frac{k}{n}\right)\frac{(-1)^{n-k}}{(m-n+k)!\,(n-k)!}\\ &= \frac{n!m!}{(n-m)!}\sum_{k=0}^{m} f\left(\frac{n-k}{n}\right)\frac{(-1)^k}{k!\,(m-k)!}\end{aligned} \tag{A.7}$$

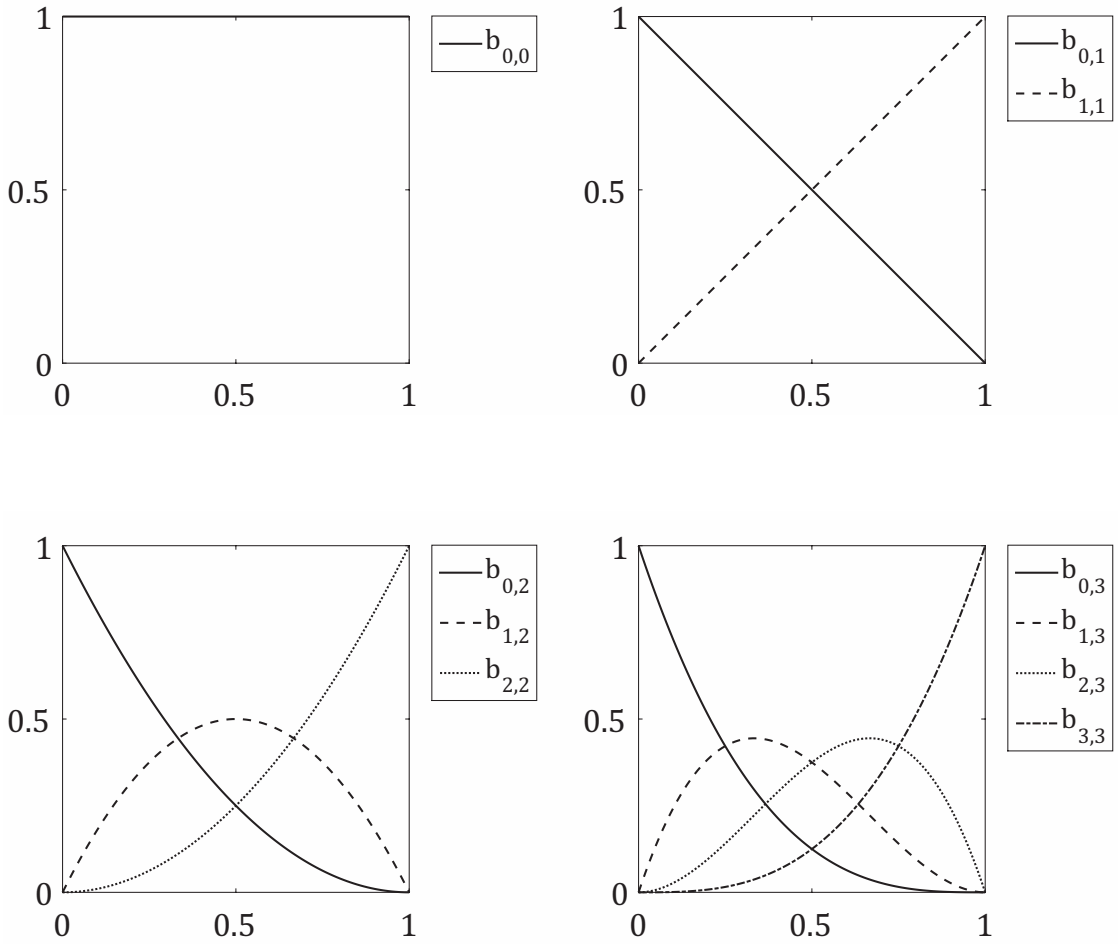

Figure A.1: Sets of Bernstein polynomial bases for order-0 up to order-3.

Appendix B

Numerical Evaluation of Elliptic Integrals

The arithmetic-geometric mean algorithm produces a set of sequences:

$$a_{n+1} = \frac{1}{2}(a_n + b_n) \quad b_{n+1} = \sqrt{a_n b_n} \quad c_{n+1} = \frac{1}{2}(a_n - b_n) \tag{B.1}$$

with $a_n \geq b_n$. As $n \to \infty$, $a_n \to b_n$. The numerical procedure terminates when $a_n - b_n \leq \text{tol}$. With $a_0 = 1$, $b_0 = \cos\alpha$, $c_0 = \sin\alpha$, the complete elliptic integral of the first kind is

$$K(m) = \lim_{n\to\infty} \frac{\pi}{2a_n} \tag{B.2}$$

where $m = \sin^2\alpha$. The descending Landen transformation produces a sequence:

$$\phi_{n+1} = \phi_n + \tan^{-1}\left(\frac{b_n}{a_n}\tan\phi_n\right) + \pi\left\lceil\frac{\phi_n}{\pi} - \frac{1}{2}\right\rceil \tag{B.3}$$

where the range of $\tan^{-1}$ is $\left[-\frac{\pi}{2}, \frac{\pi}{2}\right]$, and the ceiling function $\lceil\rceil$ prevents ϕ_{n+1} from being constrained to this interval. Defining,

$$\Phi = \lim_{n\to\infty} \frac{\phi}{2^n} \tag{B.4}$$

The incomplete elliptic integral of the first kind can be written

$$F(\phi, m) = \frac{2\Phi}{\pi} K(m) = \lim_{n\to\infty} \frac{\phi_n}{2^n a_n} \tag{B.5}$$

Taking n as before, the numerical procedure produces an estimate of $F(\phi, m)$. The corresponding approximation of the incomplete elliptic integral of the second kind is computed as

$$E(\phi, m) = F(\phi, m)\left(1 - \frac{1}{2}\sum_{j=0}^{n} 2^j c_j^2\right) + \sum_{j=1}^{n} c_j \sin\phi_j \tag{B.6}$$

Appendix C

Derivations Related to Stress Triaxiality

The deviatoric stress is defined

$$\mathbf{s} = \boldsymbol{\sigma} - \frac{1}{3}\mathrm{tr}\left(\boldsymbol{\sigma}\right)\, I$$

The deviatoric stress matrix is

$$[\mathbf{s}] = \begin{bmatrix} \frac{2}{3}\sigma_{11} - \frac{1}{3}\left(\sigma_{22} + \sigma_{33}\right) & \sigma_{12} & \sigma_{13} \\ \sigma_{12} & \frac{2}{3}\sigma_{22} - \frac{1}{3}\left(\sigma_{11} + \sigma_{33}\right) & \sigma_{23} \\ \sigma_{13} & \sigma_{23} & \frac{2}{3}\sigma_{33} - \frac{1}{3}\left(\sigma_{11} + \sigma_{22}\right) \end{bmatrix}$$

The inner product is defined for the deviatoric stress

$$s_{ij}s_{ij} = \frac{2}{3}\left[\sigma_{11}^2 + \sigma_{22}^2 + \sigma_{33}^2 - \sigma_{11}\sigma_{22} - \sigma_{11}\sigma_{33} - \sigma_{22}\sigma_{33}\right] + \sigma_{12}^2 + \sigma_{13}^2 + \sigma_{23}^2$$

For

$$\sigma_{22} = \sigma_{33}$$

with

$$\sigma_{12} = \sigma_{13} = \sigma_{23} = 0$$

the inner product above becomes

$$s_{ij}s_{ij} = \frac{2}{3}\left[\sigma_{11}^2 - 2\sigma_{11}\sigma_{22} + \sigma_{22}^2\right]$$

The trace of the stress tensor is

$$\sigma_{kk} = \sigma_{11} + 2\sigma_{22}$$

The stress triaxiality is defined

$$\chi = \frac{\frac{1}{3}\sigma_{kk}}{\sqrt{\frac{3}{2}s_{ij}s_{ij}}}$$

From above,

$$\chi = \frac{1}{3}\frac{\sigma_{11} + 2\sigma_{22}}{\sigma_{11} - \sigma_{22}}$$

$$\chi = \frac{1}{3}\frac{1 + 2\frac{\sigma_{22}}{\sigma_{11}}}{1 - \frac{\sigma_{22}}{\sigma_{11}}}$$

The stress triaxiality is plotted as a function of the stress ratio in Figure C.1. The stress triaxiality goes asymptotically to $\pm\infty$ as the stress ratio approaches 1; this corresponds to a hydrostatic stress state. A stress ratio of 0 occurs in uniaxial stress; the corresponding stress triaxiality is $\chi = 1/3$. The triaxiality goes asymptotically to $\chi = -2/3$ as the stress ratio goes to $\pm\infty$, but stress ratios outside the interval $[-1, 1]$ are not studied, as a reorientation of the principle axes will produce a stress ratio within the interval.

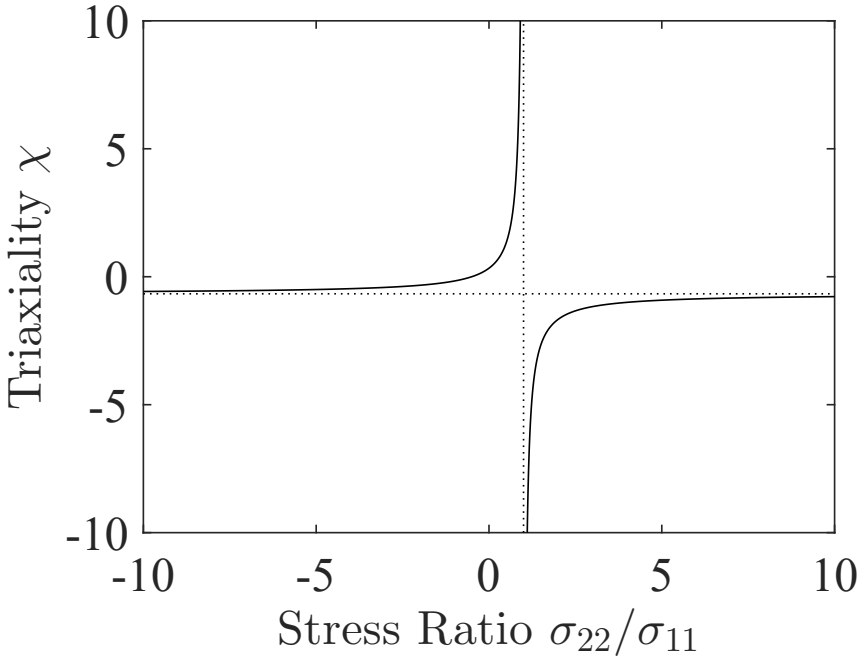

Figure C.1: Stress triaxiality χ as a function of the stress ratio σ_{22}/σ_{11}.

The stress ratio can also be taken as a function of the triaxiality via

$$\frac{\sigma_{22}}{\sigma_{11}} = \frac{3\chi - 1}{3\chi + 2} \tag{C.1}$$

This representation is more useful for applying constant triaxiality loading, as the stress boundary conditions can be formulated for a given χ. The stress ratio is plotted as a function of the stress triaxiality in Figure C.2 The following relationships hold:

The uniaxial stress state is characterized by either

$$\left.\frac{\sigma_{22}}{\sigma_{11}}\right|_{\chi=\frac{1}{3}} = 0 \rightarrow \sigma_{22} = 0$$

or

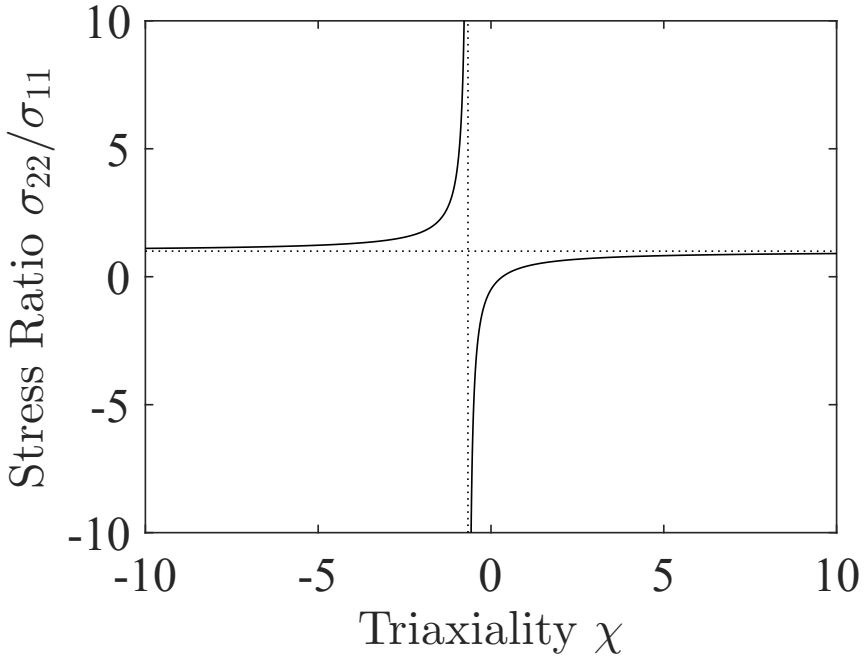

Figure C.2: The stress ratio σ_{22}/σ_{11}as a function of the stress triaxiality χ .

$$\lim_{\chi \to -\frac{2}{3}^{\pm}} \left(\frac{\sigma_{22}}{\sigma_{11}} \right) = \pm\infty \rightarrow \sigma_{11} = 0$$

The hydrostatic stress state is characterized by

$$\lim_{\chi \to \pm\infty} \left(\frac{\sigma_{22}}{\sigma_{11}} \right) = 1$$

The linearized stresses are given by

$$\sigma_{11} = C_{11}\epsilon_{11} + 2C_{12}\epsilon_{22}$$

$$\sigma_{22} = C_{12}\epsilon_{11} + (C_{11} + C_{12})\,\epsilon_{22}$$

for axisymmetric loading, where $\epsilon_{22} = \epsilon_{33}$. The ratio of the transverse to the longitudinal stress is

$$\frac{\sigma_{22}}{\sigma_{11}} = r_s$$

Substituting $\sigma_{22} = r_s\sigma_{11}$ and rearranging,

$$\sigma_{11} = \frac{C_{12}}{r_s}\epsilon_{11} + \frac{(C_{11} + C_{12})}{r_s}\epsilon_{22}$$

Equating the two expressions for σ_{11},

$$C_{11}\epsilon_{11} + 2C_{12}\epsilon_{22} = \frac{C_{12}}{r_s}\epsilon_{11} + \frac{(C_{11} + C_{12})}{r_s}\epsilon_{22}$$

$$\left(C_{11} - \frac{C_{12}}{r_s}\right)\epsilon_{11} = \left(\frac{C_{11} + C_{12}}{r_s} - 2C_{12}\right)\epsilon_{22}$$

$$\left(\frac{r_sC_{11} - C_{12}}{r_s}\right)\epsilon_{11} = \left(\frac{C_{11} + C_{12} - 2r_sC_{12}}{r_s}\right)\epsilon_{22}$$

The ratio of the transverse and longitudinal strains is

$$\frac{\epsilon_{22}}{\epsilon_{11}} = \frac{r_sC_{11} - C_{12}}{C_{11} + (1 - 2r_s)\,C_{12}}$$

The stress ratio is defined in terms of the stress triaxiality,

$$r_s = \frac{3\chi - 1}{3\chi + 2}$$

so that

$$\frac{\epsilon_{22}}{\epsilon_{11}} = \frac{\frac{3\chi-1}{3\chi+2}C_{11} - C_{12}}{C_{11} + \left(1 - 2\frac{3\chi-1}{3\chi+2}\right)C_{12}}$$

$$\frac{\epsilon_{22}}{\epsilon_{11}} = \frac{(3\chi - 1)\,C_{11} - (3\chi + 2)\,C_{12}}{(3\chi + 2)\,C_{11} + (-3\chi + 4)\,C_{12}}$$

Appendix D

Approximation of the Eshelby tensor

For a perfect cubic crystal, the quantities $\boldsymbol{N}(\xi)$ and $D(\xi)$ have the form [9]

$$D(\xi) = \mu^2(\lambda + 2\mu + \mu')\xi^6 + \tag{D.1a}$$

$$\mu\mu'(2\lambda + 2\mu + \mu')\xi^2\left(\xi_1^2\xi_2^2 + \xi_1^2\xi_3^2 + \xi_2^2\xi_3^2\right) + \tag{D.1b}$$

$$\mu'^2(3\lambda + 3\mu + \mu')\xi_1^2\xi_2^2\xi_3^2 \tag{D.1c}$$

$$N_{11}(\xi) = \mu^2\xi^4 + \beta\xi^2\left(\xi_2^2 + \xi_3^2\right) + \gamma\xi_2^2\xi_3^2 \tag{D.1d}$$

$$N_{22}(\xi) = \mu^2\xi^4 + \beta\xi^2\left(\xi_1^2 + \xi_3^2\right) + \gamma\xi_1^2\xi_3^2 \tag{D.1e}$$

$$N_{33}(\xi) = \mu^2\xi^4 + \beta\xi^2\left(\xi_1^2 + \xi_2^2\right) + \gamma\xi_1^2\xi_2^2 \tag{D.1f}$$

$$N_{12}(\xi) = -(\lambda + \mu)\xi_1\xi_2\left(\mu\xi^2 + \mu'\xi_3^2\right) \tag{D.1g}$$

$$N_{13}(\xi) = -(\lambda + \mu)\xi_1\xi_3\left(\mu\xi^2 + \mu'\xi_2^2\right) \tag{D.1h}$$

$$N_{23}(\xi) = -(\lambda+\mu)\,\xi_2\xi_3\left(\mu\xi^2+\mu'\xi_1^2\right) \tag{D.1i}$$

$$N_{ij}(\xi) = N_{ji}(\xi) \tag{D.1j}$$

where

$$\begin{aligned}
\xi^2 &= \xi_1^2+\xi_2^2+\xi_3^2 \\
\beta &= \mu(\lambda+\mu+\mu') \\
\gamma &= \mu'(2\lambda+2\mu+\mu') \\
\lambda &= C_{12} \\
\mu &= C_{44} \\
\mu' &= C_{11}-C_{12}-2C_{44}
\end{aligned} \tag{D.2}$$

The code used in this study passes the verification test that these values are accurately reproduced. The integral in Equation (5.70) can be expressed as

$$S_{ijpq} = \frac{1}{8\pi} L_{mnpq}\left(\bar{G}_{imjn}+\bar{G}_{jmin}\right) \tag{D.3}$$

where

$$\bar{G}_{imjn} = 2\pi\int_{-1}^{1} R\left[G_{imjn}/Z\right] d\bar{\zeta}_3 \tag{D.4}$$

where $R\left[G_{imjn}/Z\right]$ is a sum of residues. For a spheroid with $a_1 = a_2$, $\rho = a_1/a_3$, in a cubic crystal, with the principal spheroid axes aligned with the principal crystal vectors, the entries of $\bar{\mathbf{G}}$ are given by

$$\bar{G}_{1111} = \bar{G}_{2222} \tag{D.5a}$$

$$
\begin{aligned}
&= \frac{\pi}{a}\int_0^1 \left\{ 2\frac{1-x^2}{pq} s\left[\mu^2 s + \beta\rho^2 x^2\right] + \frac{\left(1-x^2\right)^2}{p\left(p+q\right)}\left[\beta s + \gamma\rho^2 x^2\right] \right\} dx \\
\bar{G}_{3333} =& \frac{4\pi}{a}\int_0^1 \frac{\rho^2 x^2}{pq} s\left[\mu^2 s + \beta\left(1-x^2\right)\right] dx \qquad \text{(D.5b)} \\
&+ \frac{\pi\gamma}{a}\int_0^1 \frac{\rho^2 x^2\left(1-x^2\right)^2}{p\left(p+q\right)} dx \\
\bar{G}_{1122} =& \bar{G}_{2211} \qquad \text{(D.5c)} \\
=& \frac{2\pi}{a}\int_0^1 \frac{1-x^2}{pq}\left\{ s\left[\mu^2 s + \beta\rho^2 x^2\right] + \left(1-x^2\right)\left[\beta s + \gamma\rho^2 x^2\right] \right\} dx \\
&- \frac{\pi}{a}\int_0^1 \frac{\left(1-x^2\right)^2}{p\left(p+q\right)}\left[\beta s + \gamma\rho^2 x^2\right] dx \\
\bar{G}_{1133} =& \bar{G}_{2233} \qquad \text{(D.5d)} \\
=& \frac{2\pi}{a}\int_0^1 \frac{\rho^2 x^2}{pq}\left\{ 2s\left[\mu^2\left(1-x^2+\rho^2 x^2\right) + \beta\rho^2 x^2\right] \right. \\
&\qquad \left. + \left(1-x^2\right)\left[\beta s + \gamma\rho^2 x^2\right] \right\} \\
\bar{G}_{1212} =& -\frac{\pi\left(\lambda+\mu\right)}{a}\int_0^1 \frac{\left(1-x^2\right)^2}{p\left(p+q\right)}\left[\mu s + \mu'\rho^2 x^2\right] dx \qquad \text{(D.5e)} \\
\bar{G}_{1313} =& \bar{G}_{2323} \qquad \text{(D.5f)} \\
=& -\frac{\pi\left(\lambda+\mu\right)}{a}\int_0^1 \left[2\mu\frac{\rho^2 x^2\left(1-x^2\right)s}{pq} + \mu'\frac{\rho^2 x^2\left(1-x^2\right)^2}{p\left(p+q\right)} \right] dx \\
\bar{G}_{3311} =& \bar{G}_{3322} \qquad \text{(D.5g)} \\
=& \frac{\pi}{a}\int_0^1 \left\{ 2\frac{1-x^2}{pq} s\left[\mu^2 s + \beta\left(1-x^2\right)\right] + \frac{\gamma}{2}\frac{\left(1-x^2\right)^3}{p\left(p+q\right)} \right\} dx
\end{aligned}
$$

Here,

$$
\begin{aligned}
a =& \mu^2\left(\lambda + 2\mu + \mu'\right) \\
b =& a^{-1}\mu\mu'\left(2\lambda + 2\mu + \mu'\right)
\end{aligned}
$$

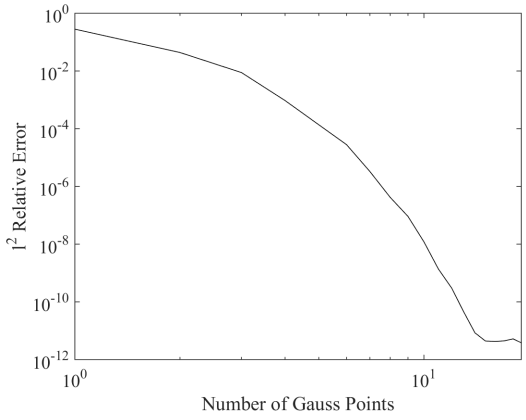

Figure D.1: The l^2 norm of the relative error in the approximation of S_{ijpq} as a function of the number of integration points used is plotted on a log scale.

$$
\begin{aligned}
c =& a^{-1}\mu'^{2}\left(3\lambda + 3\mu + \mu'\right) \\
\beta =& \mu\left(\lambda + \mu + \mu'\right) \\
\gamma =& \mu'\left(2\lambda + 2\mu + \mu'\right) \\
p =& \left\{ s^3 + b\rho^2 x^2\left(1 - x^2\right)s + \frac{1}{4}\left(1 - x^2\right)^2\left[bs + c\rho^2 x^2\right] \right\}^{1/2} \\
q =& \left[s^3 + b\rho^2 x^2\left(1 - x^2\right)s \right]^{1/2} \\
s =& \left(1 - x^2 + \rho^2 x^2\right)
\end{aligned}
\tag{D.6}
$$

Gauss quadrature is used to numerically evaluate the integrals in Equation (D.5). The l^2 norm of the relative error in the calculation, given by

$$
e^n = \sqrt{\sum_{i,j,p,q} \left(S^n_{ijpq} - S^{n_{\max}}_{ijpq}\right)^2} \tag{D.7}
$$

is plotted in Figure D.1, where $n_{\max} = 20$. Following [94], the integral in Equation

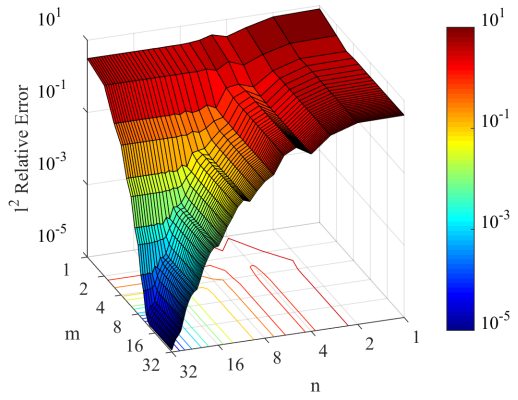

Figure D.2: The l^2 norm of the relative error in the approximation of S_{ijpq} by the summation in Equation (D.8) for varying m and n is plotted on a log scale.

(5.78) is approximated by the sum

$$S^n_{ijpq} = \frac{1}{8} L_{mnpq} \sum_{\alpha=1}^{n(\bar{\zeta}_3)} \phi_\alpha \left\{ \sum_{\beta=1}^{m(\theta)} \phi_\beta \left[G_{imjn}\left(\bar{\zeta}_{3\alpha}, \theta_\beta\right) + G_{jmin}\left(\bar{\zeta}_{3\alpha}, \theta_\beta\right) \right] \right\} \tag{D.8}$$

Define the l^2 norm of the relative error in the approximation of S_{ijpq} by the summation in Equation (D.8) as

$$\sqrt{\sum_{i,j,p,q} \left(S^n_{ijpq} - S_{ijpq}\right)^2} \tag{D.9}$$

The error is plotted as a function of m and n in Figure D.2. For the calculations in this study, values of $m = 32$ and $n = 32$ were used for the numerical approximation of the Eshelby tensor.

Appendix E

Numerical Implementation of Crystal Plasticity

E.1 Rate Tangent Formulation

$$\dot{\gamma}^{\alpha} = f\left(\mu_{\tau}^{k}, g^{\alpha}, \theta\right) \tag{E.1}$$

$$\dot{\gamma}_{n+1}^{\alpha} = \dot{\gamma}_{n}^{\alpha} + \frac{\partial f}{\partial \mu_{\tau}^{k}} \cdot \frac{d}{dt}\mu_{\tau}^{k} + \frac{\partial f}{\partial g^{\alpha}}\dot{g}^{\alpha} + \frac{\partial f}{\partial \theta}\dot{\theta} \tag{E.2}$$

Based on an existing code authored by D.J. Luscher and C. A. Bronkhorst, a rate-dependent crystal plasticity model was implemented in an ABAQUS Explicit VUMAT as described in the following sections. The code admits full parallelization via the ABAQUS domain-level parallelization scheme using MPI. [95] Within the

VUMAT, two versions of the plastic updates are implemented:

1. A fully explicit method based on a modification of the rate tangent scheme [96]

2. An iterative implicit method based on a modification [96] of the Cuitiño-Ortiz method [97]

In the following section, the crystal plasiticity model for thermally activated slip is presented. [2] In Section E.3, the results of a simple numerical experiment are presented. Finally, in Section E.4 the parallel efficiency of the code is discussed.

E.2 The Crystal Plasticity Model

The elastic part of the deformation is governed by an anisotropic linear elastic constitutive law. The elastic constants depend linearly on temperature as:

$$\begin{aligned} C^{11} &= C_0^{11} + X_M^{11}\theta \\ C^{12} &= C_0^{12} + X_M^{12}\theta \\ C^{44} &= C_0^{44} + X_M^{44}\theta \end{aligned} \tag{E.3}$$

In the local crystal coordinate system, the stresses are given by

$$\begin{bmatrix} T_{11}^C \\ T_{22}^C \\ T_{33}^C \\ T_{12}^C \\ T_{13}^C \\ T_{23}^C \end{bmatrix} = \begin{bmatrix} C_{11} & C_{12} & C_{12} & 0 & 0 & 0 \\ C_{12} & C_{11} & C_{12} & 0 & 0 & 0 \\ C_{12} & C_{12} & C_{11} & 0 & 0 & 0 \\ 0 & 0 & 0 & 2C_{44} & 0 & 0 \\ 0 & 0 & 0 & 0 & 2C_{44} & 0 \\ 0 & 0 & 0 & 0 & 0 & 2C_{44} \end{bmatrix} \begin{bmatrix} E_{11}^C \\ E_{22}^C \\ E_{33}^C \\ E_{12}^C \\ E_{13}^C \\ E_{23}^C \end{bmatrix} \tag{E.4}$$

The rotation matrix representing the transformation from global to local crystal coordinates is given by

$$Q = \begin{bmatrix} c_\phi c_\omega - s_\phi s_\omega c_\theta & s_\phi c_\omega + c_\phi s_\omega c_\theta & s_\omega s_\theta \\ -c_\phi s_\omega - s_\phi c_\omega c_\theta & -s_\phi s_\omega + c_\phi c_\omega c_\theta & c_\omega s_\theta \\ s_\phi s_\theta & -c_\phi s_\theta & c_\theta \end{bmatrix} \tag{E.5}$$

The velocity gradient is calculated as

$$L = \frac{1}{dt} \left\{ \left(F_\tau F_t^{-1} - I \right) \left[\frac{1}{2} \left(F_\tau F_t^{-1} + I \right) \right]^{-1} \right\} \tag{E.6}$$

with symmetric part

$$D = \frac{1}{2} \left(L + L^T \right) \tag{E.7}$$

On a given slip plane α, the Schmid tensor in the reference configuration is given by

$$S_0^\alpha = m_0^\alpha \otimes n_0^\alpha \tag{E.8}$$

The Schmid tensor is rotated into the crystal coordinate system and updated into the current configuration via the relation,

$$S^{\alpha} = F_t^* \left\{ \left[Q \left(S_0^{\alpha} Q^T \right) \right] F_t^{*-1} \right\} \tag{E.9}$$

The RHS in Equation E.9 is due to the orthogonality requirement on m^{α} and s^{α}, where

$$s^{\alpha} = F^* s_0^{\alpha} \quad m^{\alpha} = m_0^{\alpha} F^{*-1} \tag{E.10}$$

The symmetric part of the Schmid tensor in the current configuration is given by

$$P^{\alpha} = \frac{1}{2} \left(S^{\alpha} + S^{\alpha T} \right) \tag{E.11}$$

The shear stress rate is calculated as

$$\dot{\tau}^{\alpha} = R^{\alpha} : D^* \tag{E.12}$$

where

$$R^{\alpha} = P^{\alpha} : \mathbb{C} + \beta^{\alpha} \tag{E.13}$$

and

$$\beta^{\alpha} = P^{\alpha} \check{T} + \left(P^{\alpha} \check{T} \right)^T \tag{E.14}$$

where $\check{T}$ is the second Piola-Kirchoff stress.

The explicit plastic update method is based on a Taylor expansion approximation of the current slip rates,

$$\dot{\gamma}_{n+1}^{\alpha} = \dot{\gamma}_n^{\alpha} + \left. \frac{\partial \dot{\gamma}^{\alpha}}{\partial \tau^{\alpha}} \right|_n \dot{\tau}^{\alpha} \Delta t + \left. \frac{\partial \dot{\gamma}^{\alpha}}{\partial g^{\alpha}} \right|_n \dot{g}^{\alpha} \Delta t \tag{E.15}$$

The slip rate for a given slip system α, is given by

$$\dot{\gamma}^{\alpha} = \text{sign}\left(\tau^{\alpha}\right)\dot{\gamma}_0 \exp\left(-\frac{F_0}{k_B\theta_t}\left\langle 1.0 - \left\langle \frac{|\tau^{\alpha}| - s_T^{\alpha}\cdot\frac{C_t^{44}}{C_0^{44}}}{s_0^{\alpha}\cdot\frac{C_t^{44}}{C_0^{44}}}\right\rangle^{p}\right\rangle^{q}\right) \tag{E.16}$$

where $\langle\rangle$ are Macaulay brackets, and $\dot{\gamma}_0$ is a flow rule parameter. On a given slip plane α, the derivative of the slip rate with respect to the slip resistance is given by

$$\frac{d\dot{\gamma}^{\alpha}}{ds^{\alpha}} = -\text{sign}\left(\tau^{\alpha}\right)\frac{\dot{\gamma}^{\alpha}F_0\cdot q\cdot p}{k_B\theta_t SL}\left\langle 1.0 - \left\langle \frac{|\tau^{\alpha}| - s_T^{\alpha}\cdot\frac{C_t^{44}}{C_0^{44}}}{s_0^{\alpha}\cdot\frac{C_t^{44}}{C_0^{44}}}\right\rangle^{p}\right\rangle^{q-1.0}\left\langle \frac{|\tau^{\alpha}| - s_T^{\alpha}\cdot\frac{C_t^{44}}{C_0^{44}}}{s_0^{\alpha}\cdot\frac{C_t^{44}}{C_0^{44}}}\right\rangle^{p-1.0} \tag{E.17}$$

Similarly, the derivative of the slip rate with respect to the resolved shear stress on a given slip plane α is given by

$$\frac{d\dot{\gamma}^{\alpha}}{d\tau^{\alpha}} = \frac{C_0^{44}}{C_t^{44}}\frac{\dot{\gamma}^{\alpha}F_0\cdot q\cdot p}{k_B\theta_t SL}\left\langle 1.0 - \left\langle \frac{|\tau^{\alpha}| - s_T^{\alpha}\cdot\frac{C_t^{44}}{C_0^{44}}}{s_0^{\alpha}\cdot\frac{C_t^{44}}{C_0^{44}}}\right\rangle^{p}\right\rangle^{q-1.0}\left\langle \frac{|\tau^{\alpha}| - s_T^{\alpha}\cdot\frac{C_t^{44}}{C_0^{44}}}{s_0^{\alpha}\cdot\frac{C_t^{44}}{C_0^{44}}}\right\rangle^{p-1.0} \tag{E.18}$$

The updated slip rates f are calculated from the previous rates by

$$f = N^{-1}\left[\dot{\gamma} + dt\frac{d\gamma}{d\tau}\cdot(R:D)\right] \tag{E.19}$$

where R is the nslip×3×3 matrix comprised of the 3×3 matrices R^{α} for each slip system α, and

$$N_{\alpha\beta} = \Delta t\frac{d\dot{\gamma}^{\alpha}}{d\tau^{\alpha}}\left[R^{\alpha}:P^{\beta} - \frac{d\dot{\gamma}^{\alpha}}{ds^{\alpha}}h^{\alpha\beta}\text{sign}\left(\tau^{\alpha}\right)\right] + \delta_{\alpha\beta} \tag{E.20}$$

The values of $\dot{\gamma}_{n+1}^{\alpha}$ are then estimated as

$$\dot{\gamma}_{n+1}^{\alpha} = \frac{1}{2}\left(\dot{\gamma} + f\right) \tag{E.21}$$

The entries $h^{\alpha\beta}$ in the hardening matrix are given by

$$h^{\alpha\beta} = h^{\beta}\left[r + (1-r)\,\delta_{\alpha\beta}\right] \tag{E.22}$$

In the implicit plastic update method, the shear stresses τ^{α} and slip resistances g^{α} are iteratively updated based on trial values for the current slip rates $\dot{\gamma}^{\alpha}_{n+1}$. The residuals f^{α}, given by

$$f^{\alpha} = \dot{\gamma}^{\alpha}_{n+1} - \operatorname{sign}\left(\tau^{\alpha}\right)\dot{\gamma}_0 \exp\left(-\frac{F_0}{k_B\theta_t}\left\langle 1.0 - \left\langle \frac{|\tau^{\alpha}| - s^{\alpha}_T \cdot \frac{C^{44}_t}{C^{44}_0}}{s^{\alpha}_0 \cdot \frac{C^{44}_t}{C^{44}_0}} \right\rangle^{p} \right\rangle^{q}\right) \tag{E.23}$$

are computed, and the procedure continues until these values are below a given tolerance.

The plastic velocity gradient is then given by

$$L^{p}_0 = \dot{\gamma}_{n+1} \cdot S_0 = \dot{\gamma}^{\alpha}_{n+1}\left(QSQ^{T}\right) \tag{E.24}$$

The plastic deformation gradient is subsequently calculated via

$$F^{p}_{\tau} = \exp(L^{p}_0 \Delta t) F^{p}_t \tag{E.25}$$

This enables the update of the elastic deformation gradient as

$$F^{*}_{\tau} = F_{\tau} F^{p-1}_{\tau} \tag{E.26}$$

The strain and stress in the crystal coordinate system are determined by

$$E_C = Q^{T}\left[\frac{1}{2}\left(F^{*T}_{\tau} F^{*}_{\tau} - I\right)\right] Q - A_{11}\left(\theta_t - \theta_0\right) I \tag{E.27}$$

and Equation E.4, respectively. The stress in the global coordinates is thus

$$T^{*}_{\tau} = Q T_C Q^{T} \tag{E.28}$$

The updated Cauchy stress at time τ is given by

$$\sigma_\tau = (\det F_\tau^*)^{-1} F_\tau^* T_\tau^* F_\tau^{*T} \tag{E.29}$$

The accumulated slip for the timestep is

$$\Delta\gamma = \frac{dt}{2}(f + \dot{\gamma}) \tag{E.30}$$

The hardening rates are updated

$$h^\beta = h_0 \frac{S_{S_0}\left(\frac{|\Delta\gamma^\beta|}{\dot{\gamma}_0 dt}\right)^{\frac{k_B\theta_t}{A}} - S_\rho^\beta}{SB - S0} \tag{E.31}$$

as well as the slip system resistances

$$s_\tau = s_t + h^{\alpha\beta}|\Delta\gamma| \tag{E.32}$$

Finally, the temperature is updated via

$$\dot{\theta} = \frac{\eta}{\rho c_p}\sum \tau^\alpha \dot{\gamma}^\alpha \tag{E.33}$$

$$\theta_\tau = \theta_t + \dot{\theta}\Delta t \tag{E.34}$$

E.3 Numerical Experiment: High Strain-Rate Deformation of Tantalum

To test the algorithm, two test problems are investigated. The specimen in both cases is a tantalum cube with edge length 6.35 mm. Material parameters for tantalum are taken from the work of Bronkhorst et. al. [2]

In the first problem, the spatial domain is meshed with 8000 8-noded reduced integration brick elements. In the second problem, the mesh contains 1.25×10^5 elements of the same type. The orientation of the crystal lattice is specified separately for each element, with each Euler angle sampled from a normal distribution centered on $\pi/2$ with a standard deviation of $\pi/6$. The Euler angle θ is plotted on the undeformed elements of the 1.25×10^5 problem.

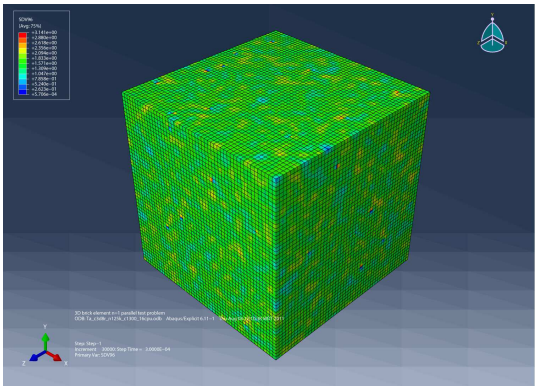

The planarity of the negative z face is maintained throughout the simulations, and a constant velocity of -1300/s is applied to the nodes on the positive z face up to $\epsilon \approx 0.65$. The resulting deformation is shown in the following figure, with the mises stress plotted on each element.

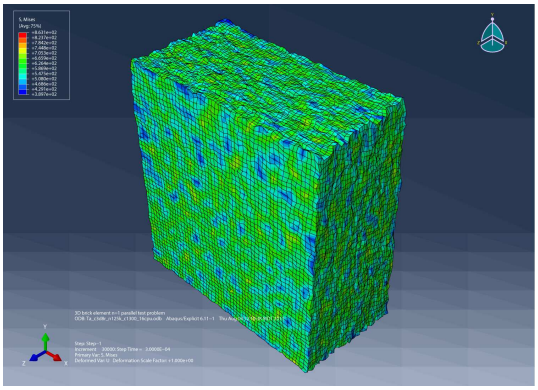

The resulting stress-strain curve for the 8000 element test case is compared to the previously published data of Bronkhost et. al. [2] in the figure below.

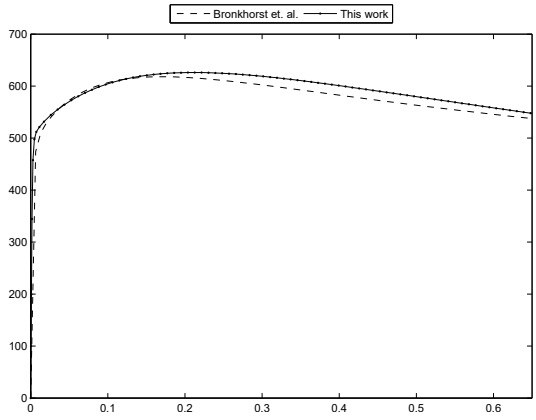

The difference in the deformation is attributable to the difference in the initial crystallographic textures of the two samples.

E.4 Parallel Efficiency of the Code: Scaling up to 32 Processors

The parallel efficiency of the algorithm is tested on the LANL bering cluster with 1-32 processors for each test. In the figure below, efficiencies for the rate tangent-based algorithm, given by the number of element-steps per second, are plotted for the two test problems.

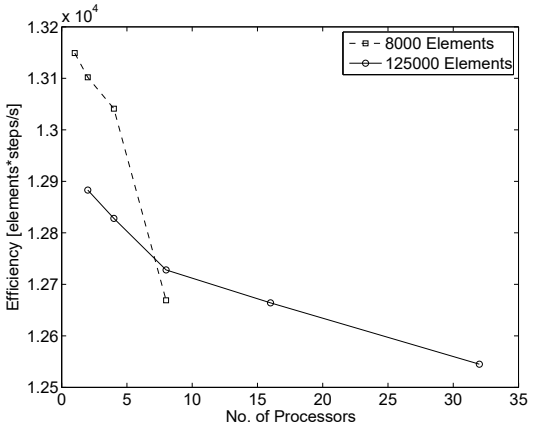

It is noted that the larger 125000 element problem scales well up to 32 processors, while the smaller 8000 element problem is efficiently parallelized up to 4 processors. For the implicit method, the efficiency is 3.4×10^3 element-steps per second for the 8000 element problem on 8 processors, or 2.4 times slower than the rate tangent-based method.

The preceeding computations were carried out on a bering compute node. If, instead, the computations are carried out on the bering frontend node, the efficiencies for the 125000 element problem on 4 and 8 processors are 1.97×10^4 and 1.91×10^4, respectively. These values represent a speedup of approximately 1.5 times over the compute node calculations.

Bibliography

[1] L. H. Yang, P. Söderlind, and J. A. Moriarty, "Accurate atomistic simulation of $(a/2)\langle 111\rangle$ screw dislocations and other defects in bcc tantalum," *Philos. Mag. A*, vol. 81, no. 5, pp. 1355–1385, 2001.

[2] C. A. Bronkhorst, B. L. Hansen, E. K. Cerreta, and J. F. Bingert, "Modeling the microstructural evolution of metallic polycrystalline materials under localization conditions," *J. Mech. Phys. Solids*, vol. 55, no. 11, pp. 2351 – 2383, 2007.

[3] Y. Li, D. J. Siegel, J. B. Adams, and X. Y. Liu, "Embedded-atom-method tantalum potential developed by the force-matching method," *Phys. Rev. B*, vol. 67, p. 125101, Mar 2003.

[4] A. M. Guellil and J. B. Adams, "The application of the analytic embedded atom method to bcc metals and alloys," *J. Mater. Res.*, vol. 7, no. 03, pp. 639–652, 1992.

[5] U. F. Kocks, A. S. Argon, and M. F. Ashby, *Thermodynamics and kinetics of slip*, ser. Prog. Mater Sci. Pergamon Press, 1975, vol. 19.

BIBLIOGRAPHY

[6] A. Acharya and A. J. Beaudoin, "Grain-size effect in viscoplastic polycrystals at moderate strains," *J. Mech. Phys. Solids*, vol. 48, no. 10, pp. 2213 – 2230, 2000.

[7] J. Eshelby, "The determination of the elastic field of an ellipsoidal inclusion, and related problems," *Proc. Royal Soc. Lond. Ser. A*, vol. 241, no. 1226, pp. 376–396, 1957.

[8] T. Mori and K. Tanaka, "Average stress in matrix and average elastic energy of materials with misfitting inclusions," *Acta Metall.*, vol. 21, no. 5, pp. 571 – 574, 1973.

[9] T. Mura, *Micromechanics of defects in solids*, ser. Mechanics of Elastic and Inelastic Solids. Dordrecht, The Netherlands: Martinus Nijhoff Publishers, 1987, vol. 3, reprinted with minor corrections 1991.

[10] P. Ponte Castañeda, "The effective mechanical properties of nonlinear isotropic composites," *J. Mech. Phys. Solids*, vol. 39, no. 1, pp. 45–71, Jan. 1991.

[11] P. Ponte Castañeda, "New variational principles in plasticity and their application to composite materials," *J. Mech. Phys. Solids*, vol. 40, no. 8, pp. 1757 – 1788, 1992.

[12] E. Kröner, "Berechnung der elastischen konstanten des vielkristalls aus den konstanten des einkristalls," *Z. Phys.*, vol. 151, no. 4, pp. 504–518, 1958.

[13] B. Budiansky and T. T. Wu, "Theoretical prediction of plastic strains of polycrystals," *Proc. 4th U.S. Nat. Congr. Appl. Mech.*, pp. 1175–1185, 1962.

[14] R. Lebensohn and C. Tomé, "A self-consistent anisotropic approach for the simulation of plastic deformation and texture development of polycrystals: Application to zirconium alloys," *Acta Metall. Mater.*, vol. 41, no. 9, pp. 2611 – 2624, 1993.

[15] F. Feyel and J.-L. Chaboche, "FE^2 multiscale approach for modelling the elasto-viscoplastic behaviour of long fibre SiC/Ti composite materials," *Comput. Methods Appl. Mech. Eng.*, vol. 183, no. 34, pp. 309 – 330, 2000.

[16] V. Kouznetsova, W. A. M. Brekelmans, and F. P. T. Baaijens, "An approach to micro-macro modeling of heterogeneous materials," *Comput. Mech.*, vol. 27, no. 1, pp. 37–48, 2001.

[17] S. Ghosh, J. Bai, and P. Raghavan, "Concurrent multi-level model for damage evolution in microstructurally debonding composites," *Mech. Mater.*, vol. 39, no. 3, pp. 241 – 266, 2007.

[18] S. Keshavarz and S. Ghosh, "Hierarchical crystal plasticity FE model for nickel-based superalloys: Sub-grain microstructures to polycrystalline aggregates," *Int. J. Solids Struct.*, vol. 55, no. 0, pp. 17 – 31, 2015.

[19] J. M. Guedes and N. Kikuchi, "Preprocessing and postprocessing for materials

based on the homogenization method with adaptive finite element methods," *Comput. Methods Appl. Mech. Eng.*, vol. 83, no. 2, pp. 143 – 198, 1990.

[20] S. Ghosh, K. Lee, and S. Moorthy, "Multiple scale analysis of heterogeneous elastic structures using homogenization theory and voronoi cell finite element method," *Int. J. Solids Struct.*, vol. 32, no. 1, pp. 27–62, 1995.

[21] S. Ghosh, *Micromechanical Analysis and Multi-Scale Modeling Using the Voronoi Cell Finite Element Method*. Florida: CRC Press/Taylor & Francis, 2011.

[22] J. Fish, K. Shek, M. Pandheeradi, and M. S. Shephard, "Computational plasticity for composite structures based on mathematical homogenization: Theory and practice," *Comput. Methods Appl. Mech. Eng.*, vol. 148, no. 12, pp. 53 – 73, 1997.

[23] A. Bensoussan, J.-L. Lions, and G. Papanicolaou, *Asymptotic Analysis for Periodic Structures*, ser. Studies in Mathematics and Its Applications. Elsevier, 1978, vol. 5.

[24] E. Sanchez-Palencia, "Homogenization method for the study of composite media," in *Asymptotic Analysis II*, ser. Lecture Notes in Mathematics, F. Verhulst, Ed. Springer Berlin Heidelberg, 1983, vol. 985, pp. 192–214.

[25] S. Swaminathan, S. Ghosh, and N. J. Pagano, "Statistically equivalent repre-

sentative volume elements for unidirectional composite microstructures: Part I - without damage," *J. Composite Mater.*, vol. 40, no. 7, pp. 583–604, 2006.

[26] V. Kouznetsova, M. G. D. Geers, and W. A. M. Brekelmans, "Multi-scale constitutive modelling of heterogeneous materials with a gradient-enhanced computational homogenization scheme," *Int. J. Numer. Methods Eng.*, vol. 54, no. 8, pp. 1235–1260, 2002.

[27] F. Vernerey, W. K. Liu, and B. Moran, "Multi-scale micromorphic theory for hierarchical materials," *J. Mech. Phys. Solids*, vol. 55, no. 12, pp. 2603 – 2651, 2007.

[28] D. J. Luscher, D. L. McDowell, and C. A. Bronkhorst, "A second gradient theoretical framework for hierarchical multiscale modeling of materials," *Int. J. Plast.*, vol. 26, no. 8, pp. 1248 – 1275, 2010.

[29] S. Ghosh, K. Lee, and P. Raghavan, "A multi-level computational model for multi-scale damage analysis in composite and porous materials," *Int. J. Solids Struct.*, vol. 38, no. 14, pp. 2335 – 2385, 2001.

[30] D. Paquet, P. Dondeti, and S. Ghosh, "Dual-stage nested homogenization for rate-dependent anisotropic elasto-plasticity model of dendritic cast aluminum alloys," *Int. J. Plast.*, vol. 27, no. 10, pp. 1677–1701, Oct. 2011.

[31] L. Schwartz, *Théorie des Distributions, Tome I-II*, ser. Publications de l'Institut

de Mathématique de l'Université de Strasbourg. Paris: Hermann & Cie, 1950-51, vol. 9-10.

[32] J. J. Duistermaat and J. A. C. Kolk, *Distributions: Theory and Applications*. New York: Springer, 2010.

[33] M. E. Gurtin, E. Fried, and L. Anand, *The Mechanics and Thermodynamics of Continua*. New York: Cambridge University Press, 2010.

[34] J. C. Simo and T. J. R. Hughes, *Computational Inelasticity*, ser. Interdisciplinary Applied Mathematics. New York: Springer-Verlag, 1998, vol. 7.

[35] S. Keshavarz and S. Ghosh, "Multi-scale crystal plasticity finite element model approach to modeling nickel-based superalloys," *Acta Mater.*, vol. 61, no. 17, pp. 6549 – 6561, 2013.

[36] C. Alleman, S. Ghosh, D. Luscher, and C. A. Bronkhorst, "Evaluating the effects of loading parameters on single-crystal slip in tantalum using molecular mechanics," *Philos. Mag.*, vol. 94, no. 1, pp. 92–116, 2014.

[37] R. Hill, "Elastic properties of reinforced solids: Some theoretical principles," *J. Mech. Phys. Solids*, vol. 11, no. 5, pp. 357 – 372, 1963.

[38] G. Simmons and H. Wang, *Single Crystal Elastic Constants and Calculated Aggregate Properties: A Handbook*, 2nd ed. Cambridge, Massachusetts: The MIT Press, 1971.

BIBLIOGRAPHY

[39] E. Schmid and W. Boas, *Plasticity of Crystals: With Special Reference to Metals*. F. A. Hughes Co., 1950.

[40] G. I. Taylor and C. F. Elam, "The distortion of iron crystals," *Proc. R. Soc. London, Ser. A*, vol. 112, no. 761, pp. 337–361, September 1926.

[41] G. I. Taylor, "The deformation of crystals of β-brass," *Proc. R. Soc. London, Ser. A*, vol. 118, no. 779, pp. 1–24, March 1928.

[42] M. S. Duesberry and V. Vítek, "Plastic anisotropy in b.c.c. transition metals," *Acta Mater.*, vol. 46, no. 5, pp. 1481–1492, 1998.

[43] J. Christian, "Some surprising features of the plastic deformation of body-centered cubic metals and alloys," *Metall. Mater. Trans. A*, vol. 14, pp. 1237–1256, 1983.

[44] G. Taylor, "Thermally-activated deformation of bcc metals and alloys," *Prog. Mater Sci.*, vol. 36, no. 0, pp. 29 – 61, 1992.

[45] J. A. Shields, S. H. Goods, R. Gibala, and T. E. Mitchell, "Deformation of high purity tantalum single crystals at 4.2 K," *Mater. Sci. Eng.*, vol. 20, no. 0, pp. 71 – 81, 1975.

[46] J. F. Byron and D. Hull, "Plastic deformation of tantalum single crystals: I. the surface morphology of yield," *J. Less-Common Met.*, vol. 13, no. 1, pp. 71 – 84, 1967.

BIBLIOGRAPHY

[47] J. F. Byron, "Plastic deformation of tantalum single crystals: II. the orientation dependence of yield," *J. Less-Common Met.*, vol. 14, no. 2, pp. 201 – 210, 1968.

[48] R. T. Sato and A. K. Mukherjee, "The asymmetric temperature dependence of yield stress in tantalum single crystals at low temperatures," *Mater. Sci. Eng.*, vol. 8, no. 2, pp. 74 – 82, 1971.

[49] S. S. Lau, S. Ranji, A. K. Mukherjee, G. Thomas, and J. E. Dorn, "Dislocation mechanisms in single crystals of tantalum and molybdenum at low temperatures," *Acta Metall.*, vol. 15, no. 2, pp. 237 – 244, 1967.

[50] V. Vítek, "Dissociation of dislocations on {110} planes in anisotropic b.c.c. metals," *Phys. Status Solidi B*, vol. 15, no. 2, pp. 557–566, 1966.

[51] V. Vitek, "Intrinsic stacking faults in body-centred cubic crystals," *Philos. Mag.*, vol. 18, no. 154, pp. 773–786, 1968.

[52] V. Vítek and F. Kroupa, "Generalized splitting of dislocations," *Philos. Mag.*, vol. 19, no. 158, pp. 265–284, 1969.

[53] V. Vítek, R. C. Perrin, and D. K. Bowen, "The core structure of $\frac{1}{2}\langle 111\rangle$ screw dislocations in b.c.c. crystals," *Philos. Mag.*, vol. 21, no. 173, pp. 1049–1073, 1970.

[54] M. S. Duesbery, V. Vítek, and D. K. Bowen, "The effect of shear stress on the

screw dislocation core structure in body-centred cubic lattices," *Philos. Trans. R. Soc. London, Ser. A*, vol. 332, no. 1588, pp. 85–111, 1973.

[55] A. Koester, A. Ma, and A. Hartmaier, "Atomistically informed crystal plasticity model for body-centered cubic iron," *Acta Mater.*, vol. 60, no. 9, p. 38943901, 2012.

[56] S. Chen and G. Gray, "Constitutive behavior of tantalum and tantalum-tungsten alloys," *Metall. Mater. Trans. A*, vol. 27, pp. 2994–3006, 1996.

[57] P. J. Maudlin, J. F. Bingert, J. W. House, and S. R. Chen, "On the modeling of the taylor cylinder impact test for orthotropic textured materials: experiments and simulations," *Int. J. Plast.*, vol. 15, no. 2, pp. 139 – 166, 1999.

[58] Z. Q. Wang and I. J. Beyerlein, "An atomistically-informed dislocation dynamics model for the plastic anisotropy and tension-compression asymmetry of bcc metals," *Int. J. Plast.*, vol. 27, no. 10, pp. 1471 – 1484, 2011, conventional and Emerging Materials.

[59] J. P. Hirth and J. Lothe, *Theory of Dislocations*. John Wiley & Sons, 1982.

[60] E. P. Busso and F. A. McClintock, "A dislocation mechanics-based crystallographic model of a B2-type intermetallic alloy," *Int. J. Plast.*, vol. 12, no. 1, pp. 1–28, 1996.

[61] M. Kothari and L. Anand, "Elasto-plastic constitutive equations for polycrystal

metals: application to tantalum," *J. Mech. Phys. Solids*, vol. 46, no. 1, pp. 51–83, 1997.

[62] U. F. Kocks, "Laws for work-hardening and low-temperature creep," *J. Eng. Mater. Technol.*, vol. 98, no. 1, pp. 76 – 85, 1976.

[63] S. Plimpton, "Fast parallel algorithms for short-range molecular dynamics," *J. Comput. Phys.*, vol. 117, pp. 1–19, 1995.

[64] R. J. Arsenault, "Investigation of the mechanism of thermally activated deformation in tantalum and tantalum-base alloys," *Acta Metall.*, vol. 14, pp. 831–838, 1966.

[65] G. J. Ackland and R. Thetford, "An improved n-body semi-empirical model for body-centred cubic transition metals," *Philos. Mag. A*, vol. 56, no. 1, pp. 15–30, 1987.

[66] M. S. Daw and M. I. Baskes, "Semiempirical, quantum mechanical calculation of hydrogen embrittlement in metals," *Phys. Rev. Lett.*, vol. 50, pp. 1285–1288, Apr 1983.

[67] C. Woodward and S. I. Rao, "Ab-initio simulation of isolated screw dislocations in bcc Mo and Ta," *Philos. Mag. A*, vol. 81, no. 5, pp. 1305–1316, 2001.

[68] Y. Mishin and A. Y. Lozovoi, "Angular-dependent interatomic potential for tantalum," *Acta Mater.*, vol. 54, no. 19, pp. 5013–5026, 2006.

[69] B. J. Lee, M. I. Baskes, H. Kim, and Y. K. Cho, "Second nearest-neighbor modified embedded atom method potentials for bcc transition metals," *Phys. Rev. B*, vol. 64, p. 184102, Oct 2001.

[70] M. Mrovec, V. Vitek, D. Nguyen-Manh, D. G. Pettifor, L. G. Wang, and M. Sob, "Study of the mechanical behavior of bcc transition metals using bond-order potentials," *MRS Proc.*, vol. 578, pp. 199–204, 1999.

[71] A. Jiang, T. A. Tyson, and L. Axe, "The structure of small ta clusters," *J. Phys. Condens. Matter*, vol. 17, pp. 6111–6121, 2005.

[72] A. J. Detor, "Atomistic simulations of grain coalescence," *Phys. Rev. B*, vol. 78, no. 14, p. 144113, 2008.

[73] J. Marian, J. Knap, and G. H. Campbell, "A Quasicontinuum study of nanovoid collapse under uniaxial loading in Ta," *Acta Mater.*, vol. 56, pp. 2389–2399, 2008.

[74] J. Mei, Y. Ni, and J. Li, "The effect of crack orientation on fracture behavior of tantalum by multiscale simulation," *Int. J. Solids Struct.*, vol. 48, no. 21, pp. 3054 – 3062, 2011.

[75] K. Ito and V. Vitek, "Atomistic study of non-schmid effects in the plastic yielding of bcc metals," *Philos. Mag. A*, vol. 81, no. 5, pp. 1387–1407, 2001.

[76] R. A. Johnson and D. J. Oh, "Analytic embedded atom method model for bcc metals," *J. Mater. Res.*, vol. 4, no. 5, pp. 1195–1201, 1989.

[77] S. Takeuchi and K. Maeda, "Slip in high purity tantalum between 0.7 and 40 K," *Acta Metall.*, vol. 25, no. 12, pp. 1485 – 1490, 1977.

[78] R. Gröger and V. Vítek, "Multiscale modeling of plastic deformation of molybdenum and tungsten. III. effects of temperature and plastic strain rate," *Acta Materialia*, vol. 56, no. 19, pp. 5426 – 5439, 2008.

[79] L. Yang and J. Moriarty, "Kink-pair mechanisms for a/2 111 screw dislocation motion in bcc tantalum," *Mater. Sci. Eng., A*, vol. 319321, no. 0, pp. 124 – 129, 2001.

[80] Q. Qin and J. L. Bassani, "Non-schmid behavior in single crystals," *J. Mech. Phys. Solids*, vol. 40, no. 4, pp. 813–833, 1992.

[81] Q. Qin and J. Bassani, "Non-associated plastic flow in single crystals," *J. Mech. Phys. Solids*, vol. 40, no. 4, pp. 835–862, 1992.

[82] R. Gröger, "Development of physically based plastic flow rules for body-centered cubic metals with temperature and strain rate dependencies," Ph.D. dissertation, University of Pennsylvania, 2007.

[83] R. Gröger, V. Racherla, J. Bassani, and V. Vitek, "Multiscale modeling of plastic deformation of molybdenum and tungsten: II. yield criterion for single crystals based on atomistic studies of glide of screw dislocations," *Acta Materialia*, vol. 56, no. 19, pp. 5412 – 5425, 2008.

[84] D. Brunner and V. Glebovsky, "Analysis of flow-stress measurements of high-purity tungsten single crystals," *Mater. Lett.*, vol. 44, pp. 144–52, 2000.

[85] M. Tang, L. P. Kubin, and G. R. Canova, "Dislocation mobility and the mechanical response of b.c.c. single crystals: A mesoscopic approach," *Acta Mater.*, vol. 46, no. 9, pp. 3221 – 3235, 1998.

[86] A. M. Cuitiño, L. Stainier, G. Wang, A. Strachan, T. Çağin, W. A. G. III, and M. Ortiz, "A multiscale approach for modeling crystalline solids," *J. Comput.-Aided Mater.*, vol. 8, pp. 127–149, 2001.

[87] A. Strachan, T. Çağin, O. Gülseren, S. Mukherjee, R. E. Cohen, and W. A. G. III, "First principles force field for metallic tantalum," *Modell. Simul. Mater. Sci. Eng.*, vol. 12, pp. 445–459, 2004.

[88] P. J. Sherwood, F. Guiu, H. C. Kim, and P. L. Pratt, "Plastic anisotropy of tantalum, niobium, and molybdenum," *Can. J. Phys.*, vol. 45, no. 2, pp. 1075–1089, 1967.

[89] J. Y. Kim, D. Jang, and J. R. Greer, "Tensile and compressive behavior of tungsten, molybdenum, tantalum and niobium at the nanoscale," *Acta Mater.*, vol. 58, no. 7, pp. 2355 – 2363, 2010.

[90] C. Lu, B. Remington, B. Maddox, B. Kad, H. Park, S. Prisbrey, and M. Mey-

ers, "Laser compression of monocrystalline tantalum," *Acta Materialia*, vol. 60, no. 19, pp. 6601 – 6620, 2012.

[91] D. Hull, J. F. Byron, and F. W. Noble, "Orientation dependence of yield in body-centered cubic metals," *Can. J. Phys.*, vol. 45, no. 2, pp. 1091–1099, 1967.

[92] A. Ma, F. Roters, and D. Raabe, "A dislocation density based constitutive model for crystal plasticity {FEM} including geometrically necessary dislocations," *Acta Materialia*, vol. 54, no. 8, pp. 2169 – 2179, 2006.

[93] J. Stoer, R. Bulirsch, R. H. Bartels, W. Gautschi, and C. Witzgall, *Introduction to numerical analysis*, ser. Texts in applied mathematics. New York: Springer, 2002.

[94] A. Gavazzi and D. Lagoudas, "On the numerical evaluation of eshelby's tensor and its application to elastoplastic fibrous composites," *Computational Mechanics*, vol. 7, no. 1, pp. 13–19, 1990.

[95] *Abaqus Documentation*, Dassault Syst'emes, Providence, RI, 2012.

[96] X. Ling, M. F. Horstmeyer, and G. P. Potirniche, "On the numerical implementation of 3d rate-dependent single crystal plasticity formulations," *Int. J. Numer. Methods Eng.*, vol. 63, pp. 548–568, 2005.

[97] A. M. C. no and M. Ortiz, "Computational modelling of single crystals," *Mod-*

BIBLIOGRAPHY

elling and Simulation in Materials Science and Engineering, vol. 1, no. 3, p. 225, 1993.

Vita

Coleman Alleman received a Bachelor of Arts degree with honors in Philosophy from The Ohio State University in 2005. He subsequently studied Mechanical Engineering at The Ohio State University under the advising of Professor Somnath Ghosh, and he received a Master of Science degree in Mechanical Engineering from The Ohio State University in 2011. His Master's research focused on the molecular modeling of polymer composite systems for manufacturing of nano-biomedical devices. Coleman then joined the Civil Engineering Department at The Johns Hopkins University in 2011 under the advising of Professor Ghosh. His PhD research focused on multiscale constitutive modeling of the mechanical behavior of crystalline metals. Starting in October, 2015, Coleman will Join Sandia National Laboratories Livermore, where he will work as a postdoctoral researcher in the Mechanics of Materials group.